Analytical and Numerical Contact Analyses of Semi-Infinite Media With Patterned and Rough Surfaces

by

Zhong-Qing Gong

B.S. (Peking University, China) 1996
M.S. (University of Houston) 1998

A dissertation submitted in partial satisfaction of the

requirements for the degree of

Doctor of Philosophy
in

Engineering–Mechanical Engineering

in the

GRADUATE DIVISION

of the

UNIVERSITY OF CALIFORNIA, BERKELEY

Committee in charge:

Professor Kyriakos Komvopoulos, Chair
Professor David B. Bogy
Professor Gregory L. Fenves

Spring 2004

The dissertation of Zhong-Qing Gong is approved:

Chair	Date
	Date
	Date

University of California, Berkeley

Spring 2004

Analytical and Numerical Contact Analyses of Semi-Infinite Media With Patterned and Rough Surfaces

By

Zhong-Qing Gong

Abstract

Analytical and Numerical Contact Analyses of Semi-Infinite Media With Patterned and Rough Surfaces

by

Zhong-Qing Gong

Doctor of Philosophy in Engineering–Mechanical Engineering

University of California, Berkeley

Professor Kyriakos Komvopoulos, Chair

Contact analyses of semi-infinite media with patterned and rough surfaces were performed in order to examine the effects of surface patterning, frictional heating, and surface cracking on the resulting deformation and stresses in the media. Stress and plastic strain results for layered media possessing meandered and sinusoidal surface patterns were compared with those of a layered medium with a smooth (flat) surface and identical layer thickness and material properties subjected to the same normal and tangential loading. Two- and three-dimensional finite element results for the contact stress and deformation fields were obtained for patterned media in terms of coefficient of friction, spherical indenter radius, and sliding repetitions. In addition, a fully coupled thermomechanical finite element analysis was carried out to obtain solutions for the surface temperature distribution and to elucidate the effect of the Peclet number on the maximum temperature rise and subsurface plasticity.

In addition to the studies involving smooth surfaces, a plane-strain model was developed for a layered medium in contact with a rough surface characterized by fractal geometry. A constitutive relation between the mean contact pressure and a representative strain was obtained based on finite element results for a rigid cylindrical asperity in normal contact with an elastic layered medium. The real contact area was obtained as a function of mechanical properties, layer thickness, truncated half-contact width, and asperity radius. These relations were incorporated into a numerical algorithm to determine the contact pressure profiles and stress state based on the distribution of asperity microcontacts. Numerical results revealed that crack initiation is more likely to occur at both the surface and the interface in the case of a stiff layer, while they are more likely to occur at the surface in the case of a compliant layer.

A thermomechanical analysis was conducted for semi-infinite elastic solid in sliding contact with a rough (fractal) surface. The model accounts for effect of thermal and mechanical coupling through the normal surface displacement caused by the contact pressure, shear traction, and thermoelastic distortion due to frictional heating. The effect of frictional heating on the contact pressure, temperature rise, and stress field is examined in terms of the Peclet number and topography (fractal) parameters.

Surface cracking in a multi-layered medium due to repetitive sliding of a rigid asperity was analyzed using linear elastic fracture mechanics and the finite element method. The stress intensity factor and crack propagation results are presented in terms of coefficient of friction at the contact region and crack interface and initial crack length. Numerical results show that the surface crack propagates toward the layer interface at an angle of ~57 deg. from the original crack plane, independent of crack growth increment,

in fair agreement with experimental observations. This analysis was extended to surface cracking in layered media in sliding contact with a rough (fractal) surface. The significance of topography (fractal) parameters on the crack growth behavior is interpreted in terms of finite element results for the contact pressure, stress intensity factors, and maximum equivalent plastic strain.

The main findings in this dissertation provide insight into the significance of surface patterning, overcoat properties, frictional heating, and surface cracking on the mechanical and thermomechanical behavior of half-space media with patterned and rough surfaces. The obtained results advance the current state in contact mechanics of thin-film mechanical systems with contact interfaces, such as microelectromechanical devices and hard disk drives, and enhance the understanding about the underlying reasons leading to mechanical failure of contacting surfaces and layered media.

_____

Professor Kyriakos Komvopoulos

Dissertation Chair

TABLE OF CONTENTS

LIST OF FIGURES

Chapter 2

Chapter 3

Chapter 5

Chapter 6

Chapter 7

LIST OF TABLES

ACKNOWLEDGEMENTS

I would like to express my most sincere gratitude to my research advisor, Professor Kyriakos Komvopoulos, for his intellectual support, guidance, encouragement, enthusiasm, and endless patience, which made this dissertation possible. The time I spent with him at Berkeley is very enjoyable. I am grateful to Professor David B. Bogy and Professor Gregory L. Fenves for serving on my dissertation committee; Professor Panayiotis Papadopoulos, Professor David J. Steigmann, Professor Lisa A. Pruitt, and Professor Chenming Calvin Hu for serving on my qualifying exam committee. Their valuable advice and comments help me finish my study at Berkeley.

I would like to thank my fellow students in the lab, Dr. Ning Ye, Dr. Lior Kogut, Dr. Wei Lu, Jian Yang, Dujiang Wan, Rui Xu, Jing Zhou, Xiao-Guang Ma, Satomi Ohno, Vinh Do, and Ari Lumbantobing, who have offered the helpful discussion and assistance for this work.

I am deeply indebted to my family for the support they provided me through my entire life and in particular, I must acknowledge my wife, Di, without whose love, encouragement and patience, I would not have finished this thesis.

Last but not the least, this research would not have been possible without the financial support from the Information Storage Industry Consortium (INSIC), Extremely High Density Recording (EHDR) Program, and the Computer Mechanics Laboratory at the University of California at Berkeley.

CHAPTER 1

INTRODUCTION

Contact mechanics is a sub-field of applied mechanics that deals with the deformation, stresses, and frictional heating of contacting solid bodies. Historically, contact mechanics evolved from the study of Heinrich Hertz (1882), who obtained solutions for the frictionless contact of two elastic bodies with ellipsoidal profiles. Since then, progress in contact mechanics resulted in extension of the Hertz theory to problems involving contacting bodies of various geometries and different constitutive laws. The incorporation of friction at the interface of contacting bodies led to mechanics studies of sliding and rolling contact. Furthermore, the interdependence of mechanical and thermal fields in the presence of frictional heating necessitated the development of fully coupled thermomechanical theories. Progress in contact mechanics has been motivated by numerous applications where surface interaction affects the operation and durability of mechanical systems. From macroscopic sliding systems, such as brakes, clutches, and seals, to microscopic contact systems, such as microgears and microgrippers in MEMS and the head-disk interface in hard disk drives, accurate failure analysis depends strongly on detailed knowledge of the deformation and stress fields, as well as generation of frictional heat and conduction/dissipation in the interacting bodies.

Coatings are often used to protect components subjected to contact stresses and to enhance the tribological performance and functionality of interacting surfaces. A coating modifies the contact pressure distribution at the contact interface. A compliant coating

reduces the contact pressure by spreading the contact area while a stiffer coating produces an opposite effect. Consequently, the coating modifies the stress distribution below the contact interface. The enhanced wear resistance of hard protective coatings, such as ceramics, cemented carbides, and diamond-like carbon, which is due to their high hardness, greatly affects the reliability of many mechanical systems. Hence, analysis of the stresses and deformation in layered media due to sliding contact is critical to the design of various mechanical components.

Contact mechanics of layered media with flat surfaces has been investigated both analytically and numerically. However, surface features of various length scales play a significant role in the elastic-plastic deformation and temperature rise due to frictional heating in layered media. For example, patterned layered media are used in many leading-edge technologies, such as high-density data storage and magnetic random access memory media. The surface microfeatures are typically produced by achromatic interferometric lithography and electron beam techniques. Contact analysis of patterned media with various surface features presents major difficulties due to the complexity of the analytical solutions for the surface and subsurface deformation and stress fields. Thus, numerical techniques, such as the finite element method, must be employed to analyze contact between solid bodies with real surface topographies.

Engineering surfaces exhibit roughness over a wide range of length scales, thus resulting in a number of microscopic contact spots, referred to as asperity contacts. The effect of surface roughness on contact deformation has been the reason for most friction and wear models. Traditional statistical techniques have been adopted to characterize rough surfaces by assuming an asperity height distribution. However, because of the

multi-scale nature of surfaces, surface roughness parameters depend strongly on the sample size, instrument resolution, and experimental filter used to acquire the topography data. Fractal geometry has been used in contemporary contact mechanics studies to characterize engineering surfaces in order to avoid the scale-dependence of statistical models. The fractal description of surfaces provides more insight into the roughness effect on the deformation and stresses of contacting rough surfaces.

In sliding mechanical systems, friction causes mechanical energy to be dissipated in the form of heat within the vicinity of the real contact area. The frictional heat dissipated is responsible for the temperature rise at the surface and in the substrate. Frictional heating and the resulting temperature rise may affect significantly the tribological behavior of sliding components, especially at high sliding speeds. The surface temperature rise could be high enough to change the properties of the sliding materials, promote surface oxidation, degrade the lubricant functionality, and even cause melting of the solid lubricant or the surface of the interacting materials. The interfacial temperature rise leads to the development of thermal stresses and induces variations in the real contact area and contact pressure distribution due to thermal expansion. Since these changes in the contact conditions affect the heat generation rate and heat conduction across the contact interface, the thermal and mechanical stress/strain fields are fully coupled and, therefore, must be determined simultaneously rather than sequentially. Thus, knowledge of the surface temperature and thermoelastic stresses in sliding solid bodies with rough surfaces is essential in failure analysis of mechanical systems.

Traditionally, hard and stiff coatings have been used to protect components subjected to contact stresses and to enhance the wear resistance of interacting surfaces.

The inherent high hardness of these materials is obtained at the expense of low fracture toughness. Consequently, contact fatigue and/or fracture of hard coatings are dominant failure mechanisms in many mechanical systems subjected to continuous sliding contact, such as gear flanks, bearing surfaces, and head-disk interface in hard disk drives. Analysis of surface cracking in layered media is necessary in order to fully understand the underlying mechanisms of wear particle generation and overcoat delamination. Furthermore, knowledge of the effect of surface cracking on the accumulation of plastic deformation in the elastic-plastic substrate is also important to the identification of the failure mechanism(s) in the substrate medium.

From the aforementioned, it is apparent that contact analysis of layered media possessing realistic surface topographies presents serious difficulties (both analytical and numerical). Therefore, the objective of this dissertation is to provide comprehensive contact analyses of semi-infinite media with patterned and rough surfaces. Mechanical and thermomechanical analyses of homogenous and/or layered media with rough surface are performed analytically, while contact analyses of layered media with patterned surfaces and surface cracking in elastic-plastic layered media are performed with the finite element method due to the complexity induced by the surface topography and the constitutive relationships.

The dissertation has been organized as following. Chapter 2 presents a plane-strain finite element analysis of patterned elastic-plastic layered media that elucidates the effect of surface geometry on the deformation and stress fields arising due to normal and sliding contact. The significance of surface patterning on the deformation behavior is interpreted in terms of stress and strain results illustrative of the tendency for crack

initiation and plastic deformation in the media. Relations for the contact pressure concentration factor and onset of yielding in the first (hard) layer are derived from finite element results for indented layered media with sinusoidal surface patterns. The contact analysis of patterned media is extended to a three-dimensional analysis in Chapter 3 by introducing an elastic-plastic finite element model of a sphere in normal and sliding contact with a layered medium with a patterned surface characterized by regularly spaced rectangular pads. Three complete loading cycles, involving indentation, sliding, and unloading of the rigid sphere, are simulated to assess the effect of repeated sliding on the stresses in the first (hard) layer and plastic deformation in the underlying (soft) layer. Thermomechanical sliding contact simulations of an elastic-plastic layered medium with a patterned surface and an elastic-plastic sphere are carried out to examine the effect of frictional heating on the deformation behavior of the medium. The likelihood of thermal cracking in the wake of microcontacts during sliding is interpreted in the context of the thermal tensile stress due to temperature gradients in the layered medium.

Chapter 4 describes a two-dimensional contact model for layered elastic media with rough surfaces characterized by fractal geometry. A finite element model of a rigid cylindrical asperity in normal contact with an elastic layered medium is used to obtain a constitutive relationship between the mean contact pressure and a representative strain. The real contact area is found to be a function of mechanical properties, layer thickness, truncated half-contact width, and asperity radius. These relationships are incorporated into a numerical algorithm to determine the contact pressure profiles and stress state according to the distribution of asperity contacts. Solutions for the total contact load and contact area show the significance of material properties, layer thickness, and surface

topography on the global parameters of this contact system. The contact pressure and local stress fields are discussed in terms of the effect of friction coefficient, layer thickness, and material properties on the pressure profile, surface stress, interface stress, von Mises equivalent stress, and maximum principal stress.

Chapter 5 provides a thermomechanical analysis for semi-infinite elastic solid sliding against a rigid rough surface characterized by fractal geometry. A piecewise-linear distribution of the contact pressure is obtained by superposition of overlapping triangular pressure elements. The normal surface displacements due to the effects of contact pressure, shear traction, and thermoelastic distortion caused by frictional heating are incorporated in the influence coefficients of the matrix inversion method. The effects of surface topography and interaction between neighboring asperity contacts on the surface and subsurface temperature rise and stress field of the elastic semi-infinite solid are discussed in the context of numerical results. The significance of frictional heating on the contact pressure, temperature rise, and stresses is interpreted in terms of the Peclet number and topography (fractal) parameters. The results provide insight into the likelihood for cracking and plastic flow at the surface due to the combined effects of mechanical and thermal surface tractions.

In Chapter 6, surface cracking in a multi-layered medium due to sliding of a rigid asperity is examined using linear elastic fracture mechanics and the finite element method. The crack propagation direction is predicted based on the maximum (tensile or shear) stress intensity factor (SIF) range. The effects of the crack length, sliding friction, and crack-face friction on the SIF and crack propagation direction are discussed in the context of finite element solutions. Simulation results demonstrate the effects of crack

growth in the elastic surface layer on the accumulation of plastic strain in the elastic-plastic underlying layer and the significance of crack growth increment on the propagation path. Based on the obtained results, a general fatigue approach for surface cracking is derived for multi-layered media subjected to repetitive sliding contact. This study is extended in Chapter 7 to examine surface cracking in a layered medium due to sliding contact with a rough surface. A contact algorithm is used to determine the critical segment of the rough surface for fracture analysis. The significance of topography (fractal) parameters on the crack growth behavior are interpreted in terms of results for the contact pressure, stress intensity factors, and maximum equivalent plastic strain.

The dissertation is concluded in Chapter 8 by summarizing the main findings of this research.

CHAPTER 2

EFFECT OF SURFACE PATTERNING ON CONTACT DEFORMATION OF ELASTIC-PLASTIC LAYERED MEDIA

2.1 Introduction

Surface layers (overcoats) are often used to protect components subjected to contact stresses and to enhance the tribological performance and functionality of interacting surfaces. The contact mechanics literature is rich in both theoretical and numerical elastic-plastic contact analyses of layered media. King (1987) analyzed indentation of elastic layered media and obtained a relation for the effective elastic modulus in terms of the layer thickness and elastic properties of the layer and substrate materials. O'Sullivan and King (1988) obtained analytical solutions for the stress field due to sliding of a spherical indenter on a layered elastic medium. Komvopoulos (1988, 1989) performed finite element analyses of normal contact on elastic and elastic-plastic layered media. Tian and Saka (1991) used the finite element method to study sliding contact on an elastic-plastic two-layer half-space. Kral and Komvopoulos (1996, 1997) obtained finite element results for the surface and subsurface stress and strain fields occurring in elastic-plastic layered media due to indentation and sliding contact. A common objective in these studies has been the investigation of the effects of coefficient of friction and overcoat thickness and mechanical properties on the contact stress and deformation fields. However, in all the previous studies the layered medium was modeled

as a half-space with a flat surface. Therefore, very little is known about the role of surface geometry features (patterning) on the elastic-plastic deformation of layered media.

Contact of elastic bodies possessing small-amplitude sinusoidal surfaces has been the central theme of several earlier analyses on the effect of surface geometry on contact stresses. Westergaard (1939) used complex variables in two-dimensional elasticity to analyze contact between a sinusoidal and a flat surface. Dundurs et al. (1973) implemented a Fourier analysis in a stress function approach to solve the latter problem. Elastic contact analysis of half-spaces with two-dimensional, sinusoidal, isotropic surfaces is fairly cumbersome. Experimental results suggest that it is difficult to predict the shape of microscopic contact areas (Johnson et al., 1985), hereafter referred to as microcontacts. A change from approximately circular to square-shaped microcontacts occurred in the apparent contact region with increasing normal load, leading eventually to the development of discontinuous contact zones separated by noncontacting small circular regions. Johnson et al. (1985) used a numerical method to determine the pressure distribution and contact area, and obtained closed-form asymptotic solutions for both light and heavy loads, which resulted in almost full contact. Seabra and Berthe (1987) used a variational formulation to study normal contact of an infinitely long wavy cylinder with a flat plane and reported that both the pressure concentration factor and the change of the contact area are strong functions of wavelength, amplitude, and normal load. In addition, the effect of surface roughness on the contact behavior was shown to be qualitatively similar to that of surface waviness. Komvopoulos and Choi (1992) analyzed normal contact of regularly spaced rigid asperities with an elastic half-space using the finite element method and obtained results for the maximum contact pressure, normal

load, and subsurface stresses in terms of asperity distribution and indentation depth. Undulated (textured) surfaces have been shown to yield low electrical conduct resistance (Saka et al., 1984) and low sliding friction (Tian et al., 1989) due to the entrapment of oxidized wear debris in the surface cavities. Ramachandra and Ovaert (2000) examined the effect of coating discontinuities on the surface elastic deformation and stresses, and observed a significant decrease in pressure singularities at coating discontinuities with crowned edges.

The previous studies have provided useful insight into the contact stress and strain fields of elastic-plastic layered media and the role of surface geometry on contact deformation of homogeneous media. However, elastic-plastic deformation of layered media with different surface patterns subjected to both normal and tangential (friction) surface loadings has not been analyzed to date, probably due to the highly complex analytical relations. Therefore, a principal objective of this study is to elucidate the concomitant effect of surface pattern geometry, coefficient of friction, and normal load (or indentation depth) on the evolution of deformation and stresses in elastic-plastic layered media. This is accomplished by performing finite element simulations of normal and sliding contact of a rigid cylindrical asperity on layered media with different surface patterns and layer material properties. The finite element method is suitable for such type of complex contact problems because analytical solutions for the surface and subsurface deformation and stress fields are extremely difficult to obtain. Another goal of this work is to derive relations for the contact pressure concentration factor and the inception of yielding in the first (hard) layer of indented layered media possessing sinusoidal surface patterns.

2.2 Modeling Procedures

2.2.1 Surface Modeling and Finite Element Mesh

To examine the effect of the surface pattern geometry on the deformation and stresses in elastic-plastic layered media, meandered surfaces consisting of undulations (pads) of height b and width and lateral spacing a (Fig. 2.1(a)) and sinusoidal surfaces of wavelength l and amplitude d (Fig. 2.1(b)) were analyzed using the finite element method. The surface pattern shown in Fig. 2.1(a) is typical of undulated surfaces, used to minimize friction through the entrapment of wear debris (Tian et al., 1989), and patterned media for ultra-high density magnetic recording produced by ion beam lithography (Ross, 2001). The wavy surface shown in Fig. 2.1(b) is similar to the topography of micromachined (lapped) surfaces, where the average grit size and lateral spacing control the amplitude and wavelength of the generated pattern. Different surface patterns were modeled by varying the dimensionless ratios b/a and d/l. The radius of the rigid asperity R was fixed in all simulations.

Normal and sliding contact simulations were performed with the two-dimensional finite element mesh shown in Fig. 2.2(b), based on the usual plane strain assumption. The mesh consists of approximately 10,000 eight-node, isoparametric, quadrilateral elements (depending on the modeled surface pattern), and its dimensions are $x/R = 2.4$ and $y/R = 3.1$. The nodes at the bottom boundary of the mesh were constrained against displacement in the y-direction and the nodes at the left boundary against displacement in the x-direction. To accurately determine the contact pressure distribution, contact area, and stress and strain fields in the highly stressed region adjacent to the contact interface,

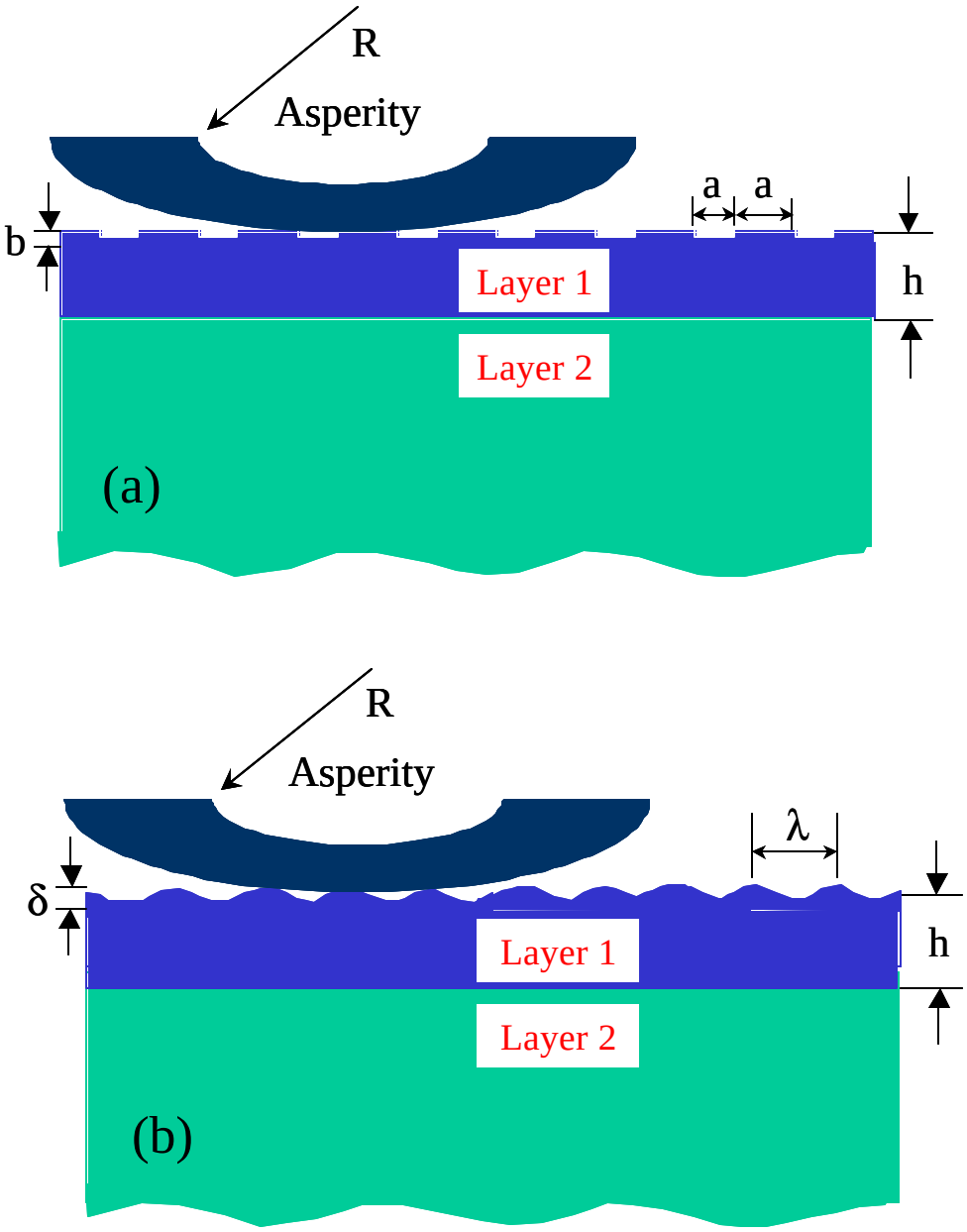

Fig. 2.1 Schematics of layered media with (a) meandered and (b) sinusoidal surfaces and pertinent nomenclature of geometry parameters.

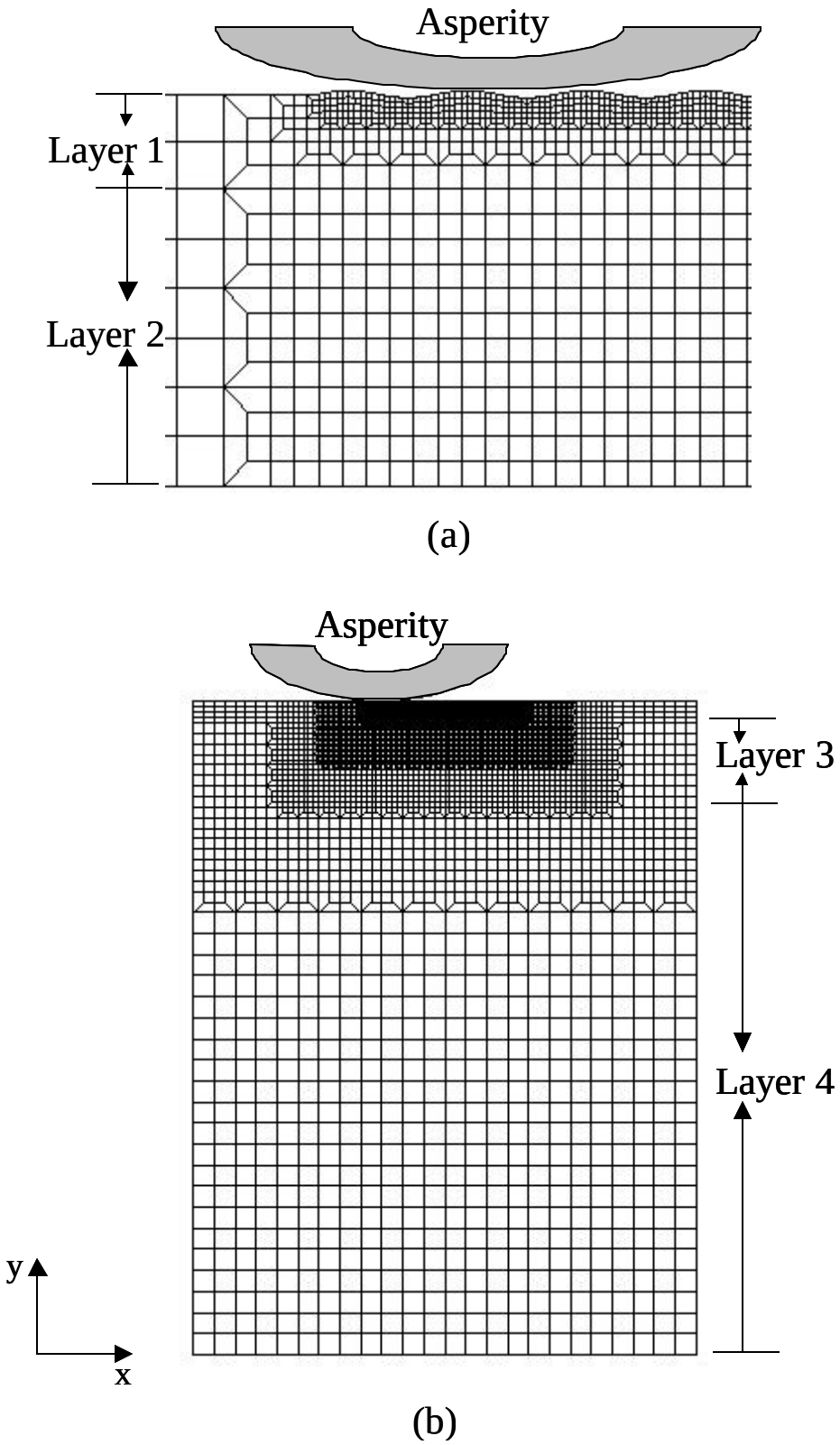

Fig. 2.2 Finite element mesh of layered medium with a sinusoidal surface: (a) mesh of first and second layers and (b) mesh of entire layered medium.

small square elements of sides equal to 1/32 of the thickness of the first layer were used to refine the mesh in the vicinity of the surface, as shown in Fig. 2.2(a) for a layered medium with a sinusoidal surface pattern. A 3 x 3 integration scheme was used in all simulations.

Contact between the layered media and the rigid asperity was detected with special contact elements. These elements are used to determine contact or separation between surface nodal points of the mesh and the rigid countersurface by measuring the local interfacial gap. If the obtained distance is less than a specified tolerance value, it is assumed that contact has been established and the appropriate force (contact pressure) is applied to the corresponding surface nodes of the mesh. Relative slip (sliding) was also modeled with the contact elements using the local overclosure, i.e., the specified tolerance for the penetration of nodal points on the mesh surface into the rigid surface. These kinematic measures were used together with a Lagrange multiplier to model surface interaction and, hence, calculate the associated normal and friction traction at the nodes of the contact region. Coulomb friction was assumed in all simulation cases. According to the adopted friction model, a shear stress, t, develops between the contacting surfaces upon the occurrence of a very small relative tangential displacement. Slip or stick commences when $t = \mu p$ or $t < \mu p$, respectively, where μ is the coefficient of friction, specified for the contact elements, and p is the local contact pressure. Thus, both normal and tangential tractions were applied simultaneously, and the produced friction force was proportional to the normal load.

2.2.2 Material Properties and Constitutive Models

The thickness, h, elastic modulus, E, and yield strength, s_Y, of each layer of the layered media analyzed in this study are given in Table 2.1. These thickness and material property values are typical of layers used in magnetic recording rigid disks, i.e., carbon overcoat (layer 1), CoCrPt magnetic medium (layer 2), CrV underlayer (layer 3), and NiP electroplated layer (layer 4). The material properties of layers 1 and 2 were obtained from nanoindentation experiments performed on carbon-coated rigid disks (Komvopoulos, 2000).

The von Mises yield criterion was used to check whether yielding occurred at a material point. According to this criterion, the yield condition, g, is expressed as

$$g = J_2 - k^2 = 0, \tag{2.1}$$

where k is a material constant and J_2 is the second deviatoric stress invariant, given by

$$J_2 = \frac{1}{2} S_{ij} S_{ij}, \tag{2.2}$$

where $S_{ij} = s_{ij} - d_{ij} s_m$, in which, s_{ij} is the stress tensor, d_{ij} is Kronecker's delta function, and s_m is the mean octahedral stress ($s_m = s_{ii}/3$).

Table 2.1. Thickness and material properties of layered medium

Medium	h/R	E (GPa)	s_Y (GPa)
Layer 1	0.025	168	13.0
Layer 2	0.078	130	2.67
Layer 3	0.4	140	2.58
Layer 4	2.6	160	2.67

For uniaxial stress state, the yield criterion can be written as

$$s_M = \left[\frac{3}{2} S_{ij} S_{ij}\right]^{1/2} = s_Y \tag{2.3}$$

where s_M is the von Mises equivalent stress. Plastic deformation was based on the usual associated flow rule, assuming negligible plastic volume change. An updated Lagrangian formulation was used in all contact simulations. Each layer was assumed to exhibit elastic-perfectly plastic material behavior. The equivalent plastic strain, $\bar{e}_p$, is defined as

$$\bar{e}_p = \int_\Omega [\frac{2}{3} de_{ij}^p de_{ij}^p]^{1/2} \tag{2.4}$$

where W is the strain path. The plastic flow rule was applied only to yielding material for which $s_M = s_Y$. The usual elastic constitutive equations were used when $s_M < s_Y$.

2.2.3 Finite Element Simulations

Quasi-static sliding contact simulations consisting of three sequential steps of loading, sliding, and unloading of a rigid asperity on layered media with different surface geometries were performed in an incremental fashion. Normal contact (indentation) was simulated by advancing the rigid asperity toward the elastic-plastic medium up to a specified penetration depth, d (or normal load, L). Subsequently, the asperity was displaced laterally to a maximum distance, S, of about eight times the half-contact width at maximum normal load. The coefficient of friction and normal load were maintained constant throughout all simulations. Finally, the asperity was unloaded following the same steps as for the loading. All simulations were performed with the multipurpose finite element code ABAQUS. A total of eight sliding and four normal contact simulation cases were examined, i.e., b/a = 0 and d/l = 0 (flat surfaces), b/a = 0.5, 1, and 2

(meandered surfaces, Table 2.2), and d/l = 0.008, 0.016, and 0.032 (sinusoidal surfaces, Table 2.3). The assumed friction coefficient values of 0.1 and 0.5 are typical of boundary-lubricated and dry (or poorly lubricated) surfaces, respectively.

2.3 Results and Discussion

To elucidate the effect of surface patterning on the contact deformation behavior, elastic-plastic finite element results for the surface and subsurface stresses and strains in

Table 2.2. Sliding contact simulations for layered media with meandered surface patterns

b/a	$L/s_{Y1}a_0$	m	S/R
0.0	0.57	0.1/0.5	0.5
0.5	0.57	0.1/0.5	0.5
1.0	0.57	0.1/0.5	0.5
2.0	0.57	0.1/0.5	0.5

Table 2.3. Sliding and normal contact simulations for layered media with sinusoidal surface patterns

d/l	Sliding			Indentation	
	$L/s_{Y1}a_0$	m	S/R	d/R	m
0.0	0.57	0.1, 0.5	0.5	0.0025-0.015	0.5
0.008	0.57	0.1, 0.5	0.5	0.0025-0.015	0.5
0.016	0.57	0.1, 0.5	0.5	0.0025-0.015	0.5
0.032	0.57	0.1, 0.5	0.5	0.0025-0.015	0.5

layered media with meandered and sinusoidal surface patterns in sliding contact with a rigid asperity are presented in this section. For the geometry, material, and load parameters considered in this study, deformation was found to occur mainly in the first two layers. Thus, results illustrating the evolution of stress and deformation in the first (hard/stiff) and second (soft/compliant) layers of the medium are presented first, followed by an analysis for the contact pressure concentration factor and a general yield criterion for the first layer of indented layered media with sinusoidal surfaces.

2.3.1 Sliding Contact Simulations

2.3.1.1 Contact Pressure

Figures 2.3 and 2.4 show contact pressure distributions on layered media with meandered and sinusoidal surfaces, respectively, obtained for sliding distance S/R = 0.125, dimensionless normal load $L/s_{Y1}a_0$ = 0.57, and different pattern geometry parameters b/a and d/l. The x coordinate was normalized by the half-contact width, a_0, and the contact pressure, p, by the maximum contact pressure, p_0^{max}, corresponding to a layered medium with a flat surface and similar layer thickness and material properties subjected to the same loading. The contact pressure of this flat-layered medium is also plotted in Fig. 2.3 (b/a = 0) and Fig. 2.4 (d/l = 0) for comparison. The pressure profiles of the patterned surfaces are distinctly different from those of the flat surface. Five microcontacts with peak pressures occurring at the trailing edges of the pads (with respect to the direction of sliding) can be seen in Fig. 2.3. The local pressure spikes are evidently due to the sharp corners of the pads. Comparison of Figs. 2.3(a)-2.3(c) shows that the pressure spikes intensify significantly with increasing b/a. The singularity of the

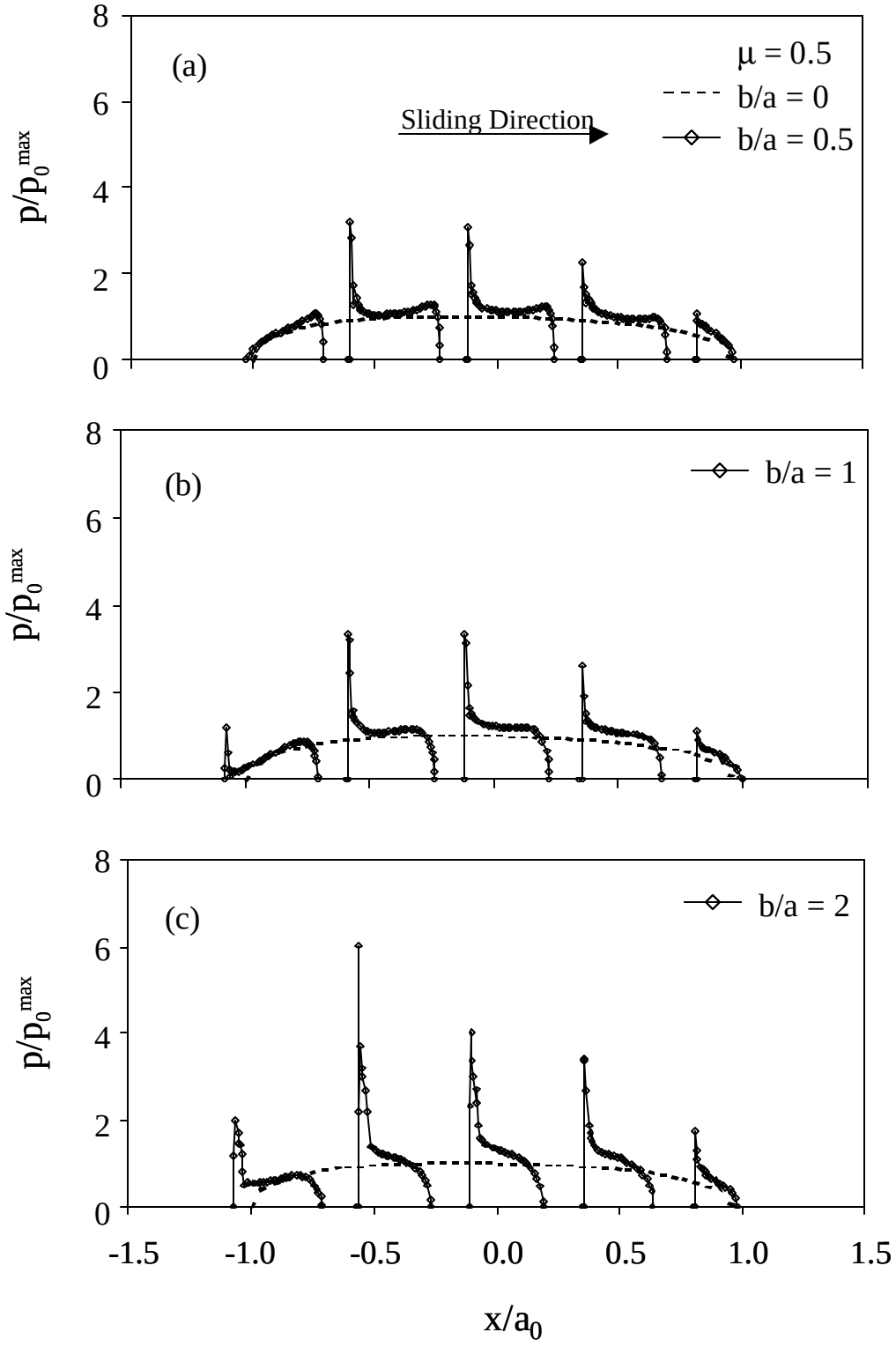

Fig. 2.3 Contact pressure profiles of layered media with meandered surfaces (S/R = 0.125 and m = 0.5): (a) b/a = 0.5, (b) b/a = 1, and (c) b/a = 2. (The pressure profile of a layered medium with a flat surface (b/a = 0) is shown by a discontinuous curve.)

problem at the sharp corners is somewhat mitigated by the immediate yielding of the corners of the pads, thus bounding the solutions. To check the convergence of the pressure profiles, a two times finer mesh was used for the pad corners of the meandered surface with b/a = 0.5. The peak contact pressure obtained with this refined mesh was found to differ from the maximum peak pressure shown in Fig. 2.3(a) by 7.7 percent. Further mesh refinement was not possible due to convergence problems associated with excessive distortion of the very small elements at the pad corners.

The effect of surface texturing (roughening) on the contact pressure distribution can be interpreted by comparing the pressure profiles obtained for d/l = 0.008, 0.016, and 0.032 and identical normal load and coefficient of friction (Fig. 2.4). For the relatively rougher surfaces, i.e., d/l = 0.016 (Fig. 2.4(b)) and d/l = 0.032 (Fig. 2.4(c)), the contact interface consists of five distinct microcontacts, similar to the layered media with meandered surface patterns (Fig. 2.3). However, pressure spikes do not occur with sinusoidal surfaces. For the smoother surface (d/l = 0.008), the contact pressure varies less abruptly and the pressure profile is continuous at the center of the contact interface due to the merger of the three microcontacts in this region. A similar behavior was observed in a previous contact analysis of two-dimensional discontinuous coatings (Ramachandra and Ovaert, 2000). The results shown in Fig. 2.4 indicate that both the distribution and the peak value of the contact pressure are very sensitive to the surface pattern geometry, especially the peak contact pressure that increases rapidly with increasing amplitude-to-wavelength ratio.

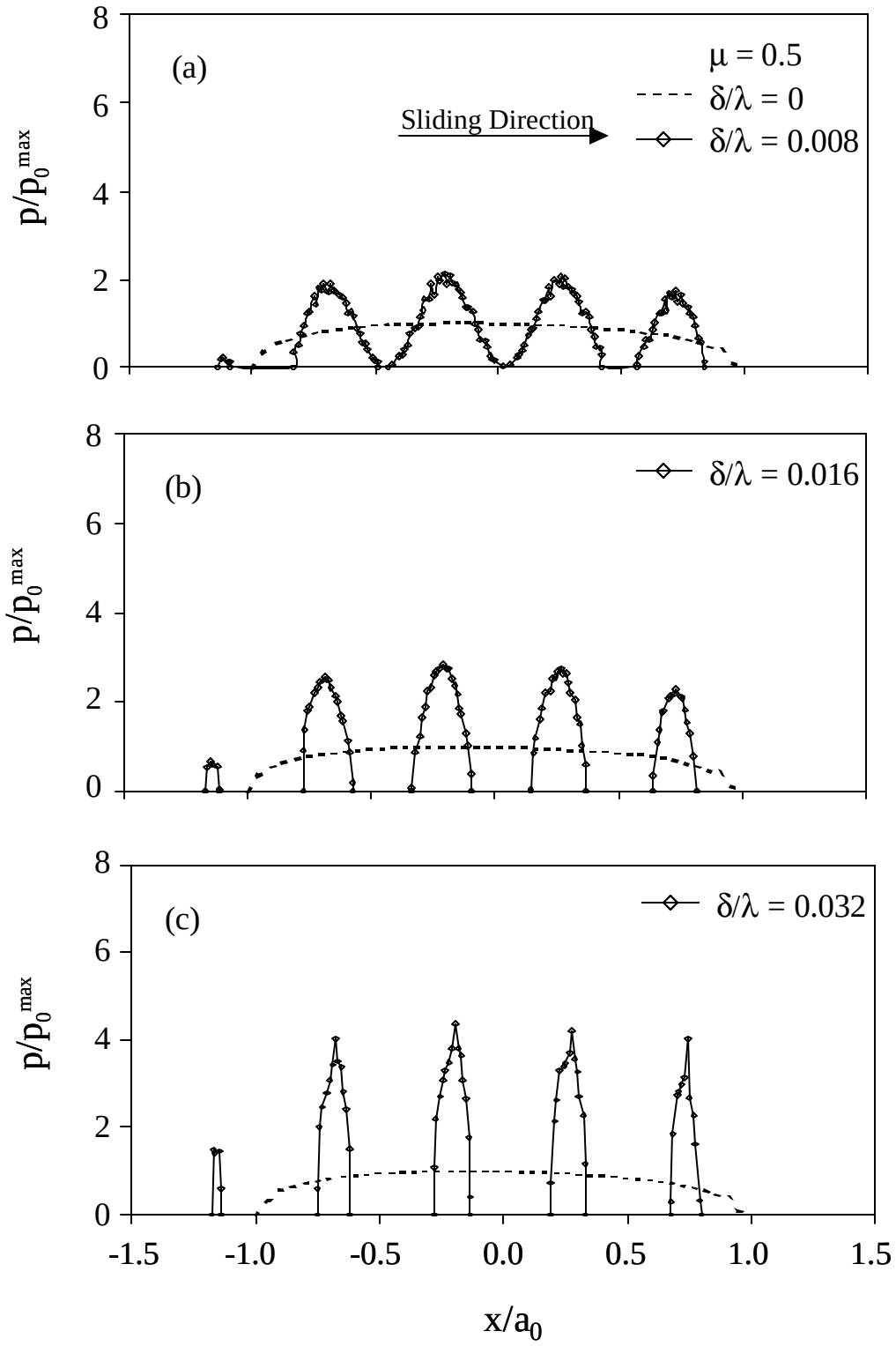

Fig. 2.4 Contact pressure profiles of layered media with sinusoidal surfaces (S/R = 0.125 and m = 0.5): (a) d/l = 0.008, (b) d/l = 0.016, and (c) d/l = 0.032. (The pressure profile of a layered medium with a flat surface (d/l = 0) is shown by a discontinuous curve.)

2.3.1.2 Surface Stresses

The von Mises equivalent stress is often used to interpret material failure induced by large plastic deformation. However, it is not possible to differentiate between failures associated with predominantly compressive and tensile stress states based on this yield criterion. Furthermore, the high material hardness (or yield strength) is obtained at the expense of low fracture toughness. Consequently, fracture and delamination of hard and stiff protective coatings are the dominant failure mechanisms in many tribological contacts. The susceptibility to cracking of relatively hard and stiff coatings strongly depends on the magnitude of the maximum tensile stress, such as the surface normal stress s_{xx}. Figure 2.5 shows the evolution of s_{xx} stress obtained from the nodes at the surface of layered media with flat (d/l = 0) and rough (d/l = 0.008, 0.016, and 0.032) surfaces for m = 0.5. (Stress results in Fig. 2.5, as well as in subsequent figures, are normalized by the yield strength s_Y of corresponding layer material.) Four distinct regions of tensile stress occur at the sliding interface of the media having rough surfaces. Maximum tensile stresses arise at the trailing edges of microcontacts within the contact zone, unlike the smooth (flat) surface, in which the contact stresses are compressive throughout the contact region. The magnitude of the peak tensile s_{xx} stress increases with d/l, indicating that rougher surfaces produce higher surface tensile stresses. For d/l = 0.032, the maximum tensile s_{xx} stress at the contact interface is very close to the yield strength of the layer material. Moreover, the significant residual tensile stress in the wake of the sliding path observed for d/l = 0.032 supports the view that rough surfaces are generally more vulnerable to contact fatigue due to repetitive sliding.

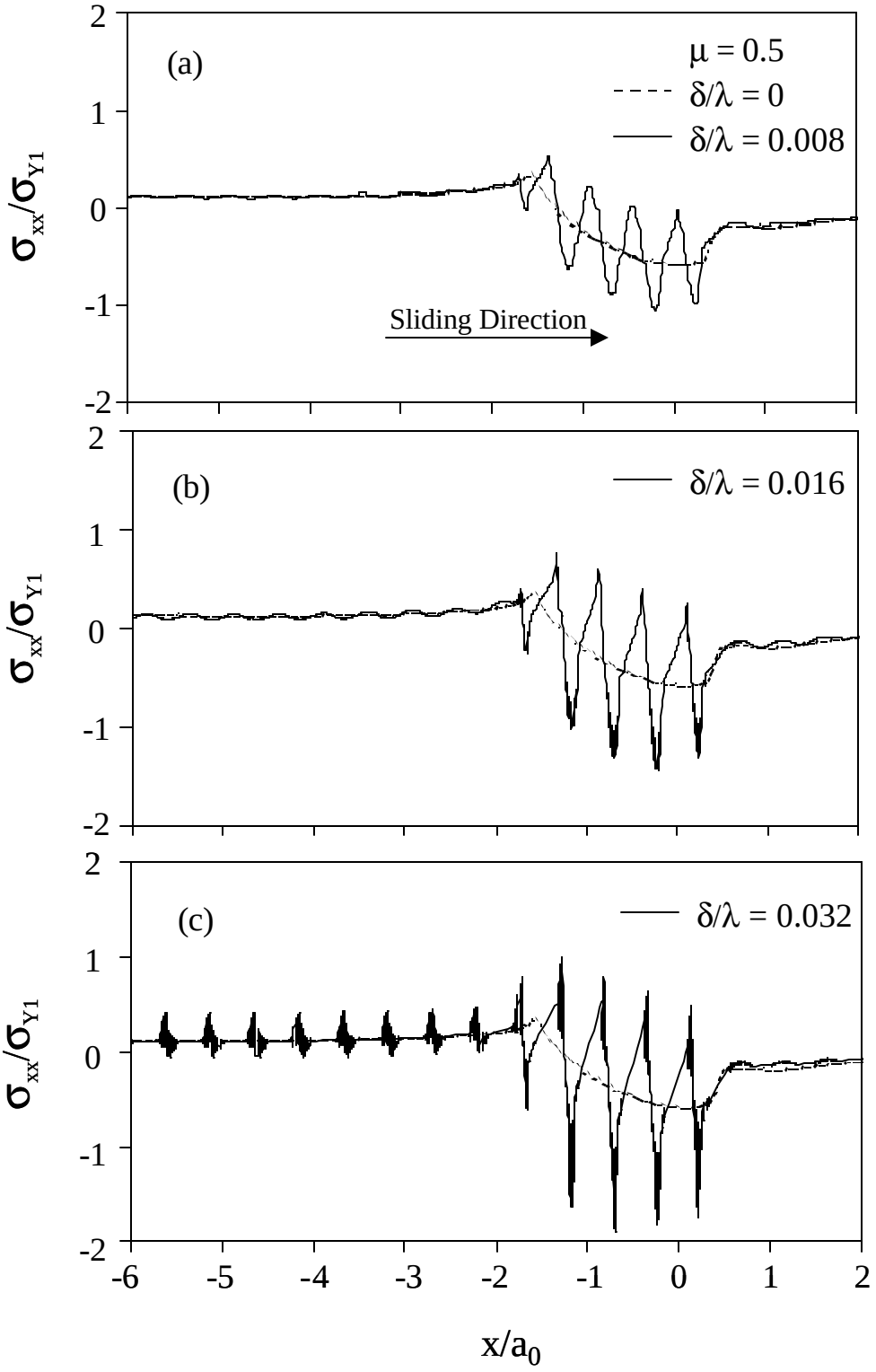

Fig. 2.5 Variation of s_{xx} stress at the surface of layered media with sinusoidal surfaces (S/R = 0.5 and m = 0.5): (a) d/l = 0.008, (b) d/l = 0.016, and (c) d/l = 0.032. (The surface stress distribution for a layered medium with a flat surface (d/l = 0) is shown by a discontinuous curve.)

Since the surface tensile stress σ_{xx} is the first principal stress in the layer, it controls the initiation of transverse surface cracks in the wake of sliding microcontacts, a phenomenon often encountered when rigid indenters are traversed over brittle materials. Formation of ring cracks on carbon-coated hard disks has been observed in scratching experiments (Wu, 1991). This type of surface cracking has been the main objective of several contact mechanics studies (Keer and Worden, 1990; Keer and Kuo, 1992; Chen et al., 1991; Bower and Fleck, 1994). Results from these analyses have confirmed that crack initiation at the surfaces of homogeneous media commences immediately behind the contact region of the sliding indenter, where the tensile stress reaches a maximum.

To evaluate the effect of friction on the propensity for surface cracking, the stress results shown in Fig. 2.5 (μ = 0.5) are compared with those shown in Fig. 2.6 (μ = 0.1). Although the low-friction simulation results reveal a similar trend, i.e., peak tensile stresses also arise at the trailing edges of microcontacts within the contact region, the magnitudes of the maximum tensile stresses are significantly lower than those obtained for μ = 0.5. Moreover, the residual stress in the wake of sliding is negligibly small, similar to that obtained with the flat-surface layered medium. This suggests that the effect of surface patterning (texturing) on plastic deformation (reflected by the development of residual stress) is suppressed when friction at the sliding interface is low, such as in the case of boundary-lubricated surfaces, even for relatively rough surface topographies (i.e., high d/l values).

To further elucidate the effect of surface patterning on the maximum tensile stress at the surface, results showing the variation of the maximum first principal stress at the

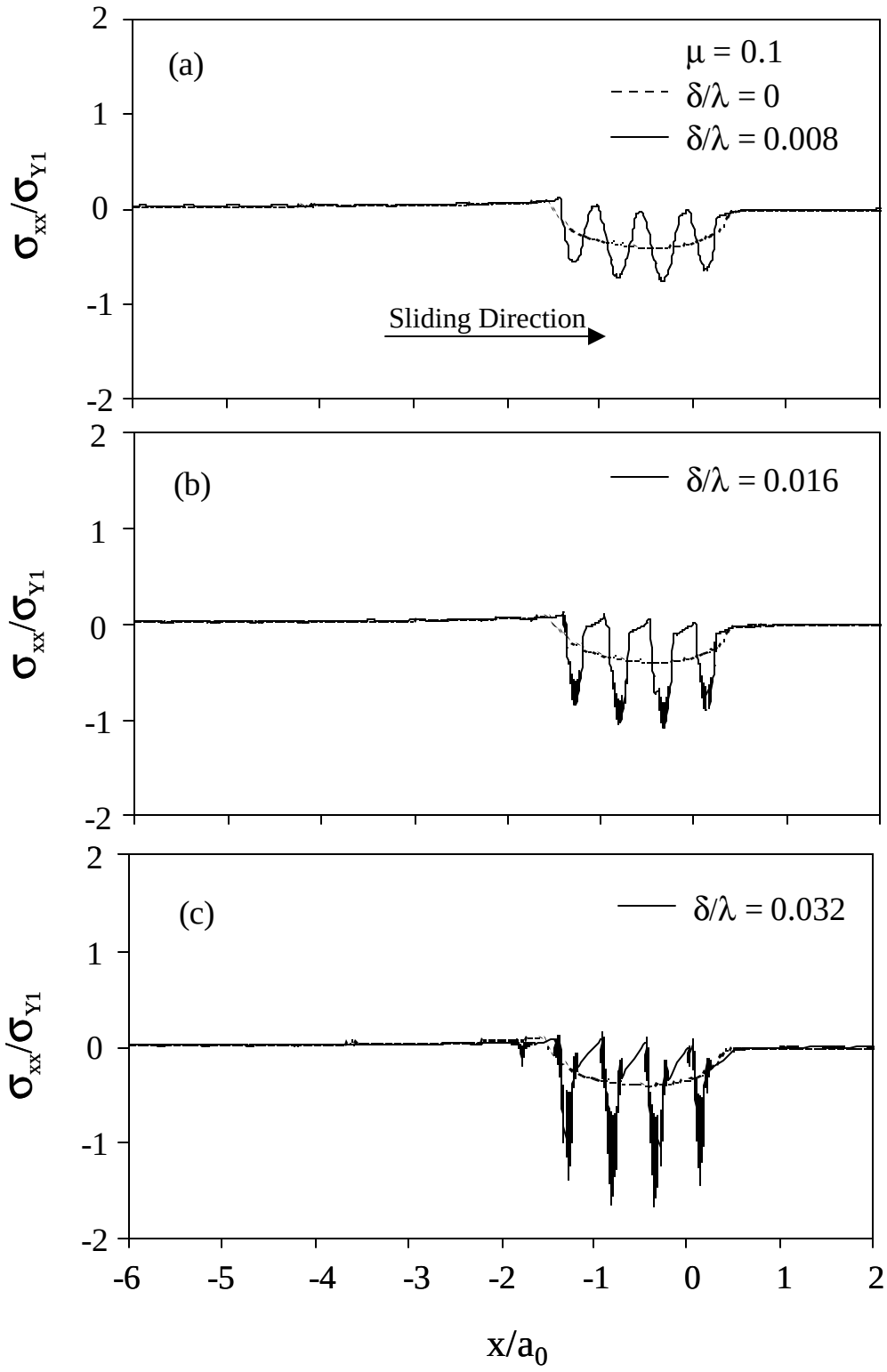

Fig. 2.6 Variation of s_{xx} stress at the surface of layered media with sinusoidal surfaces (S/R = 0.5 and m = 0.1): (a) d/l = 0.008, (b) d/l = 0.016, and (c) d/l = 0.032. (The surface stress distribution for a layered medium with a flat surface (d/l = 0) is shown by a discontinuous curve.)

surface of the first layer, σ_1^{max} (which is the surface tensile σ_{xx} stress in the wake of sliding) with sliding distance, S/R, for d/l between 0 and 0.032 and m = 0.5 are contrasted in Fig. 2.7(a). In all simulation cases, the maximum tensile stress increases rapidly with the initiation of sliding, reaching a steady state at a sliding distance S/R = 0.125, in agreement with previous finite element results (Kral and Komvopoulos, 1996). Furthermore, increasing the ratio d/l causes the maximum tensile stress in the hard layer to increase significantly. In fact, for d/l = 0.032, the stress is close to the yield strength of the layer material ($\sigma_1^{max}/\sigma_{Y1} \simeq 1$). As shown in Fig. 2.7(b), tensile stresses occur also in the underlying soft layer. While the effect of surface patterning is initially negligible (S/R < 0.2), a trend similar to that observed with the hard layer occurs thereafter, i.e., the maximum first principal stress increases with d/l, reaching a steady state value when S/R > 0.25. However, comparison of the results shown in Figs. 2.7(a) and 2.7(b) shows that the maximum tensile stress in the soft layer is much lower than that in the hard layer. Thus, the hard surface layer protects the underlying soft layer from high tensile stresses, which would otherwise occur under direct sliding contact, decreasing the likelihood for crack initiation in the soft layer.

2.3.1.3 Evolution of Plasticity in Layered Media

To examine the dependence of plasticity on sliding friction, equivalent plastic strain contours for m = 0.5 and 0.1, d/l = 0.032, and S/R = 0.5 are contrasted in Fig. 2.8. (Different contour levels are used to facilitate plotting of the much smaller plastic zones in Fig. 2.8(b).) For relatively high friction (m = 0.5), a continuous plastic zone is produced in the soft layer, with the maximum plastic strain occurring at the interface with the hard

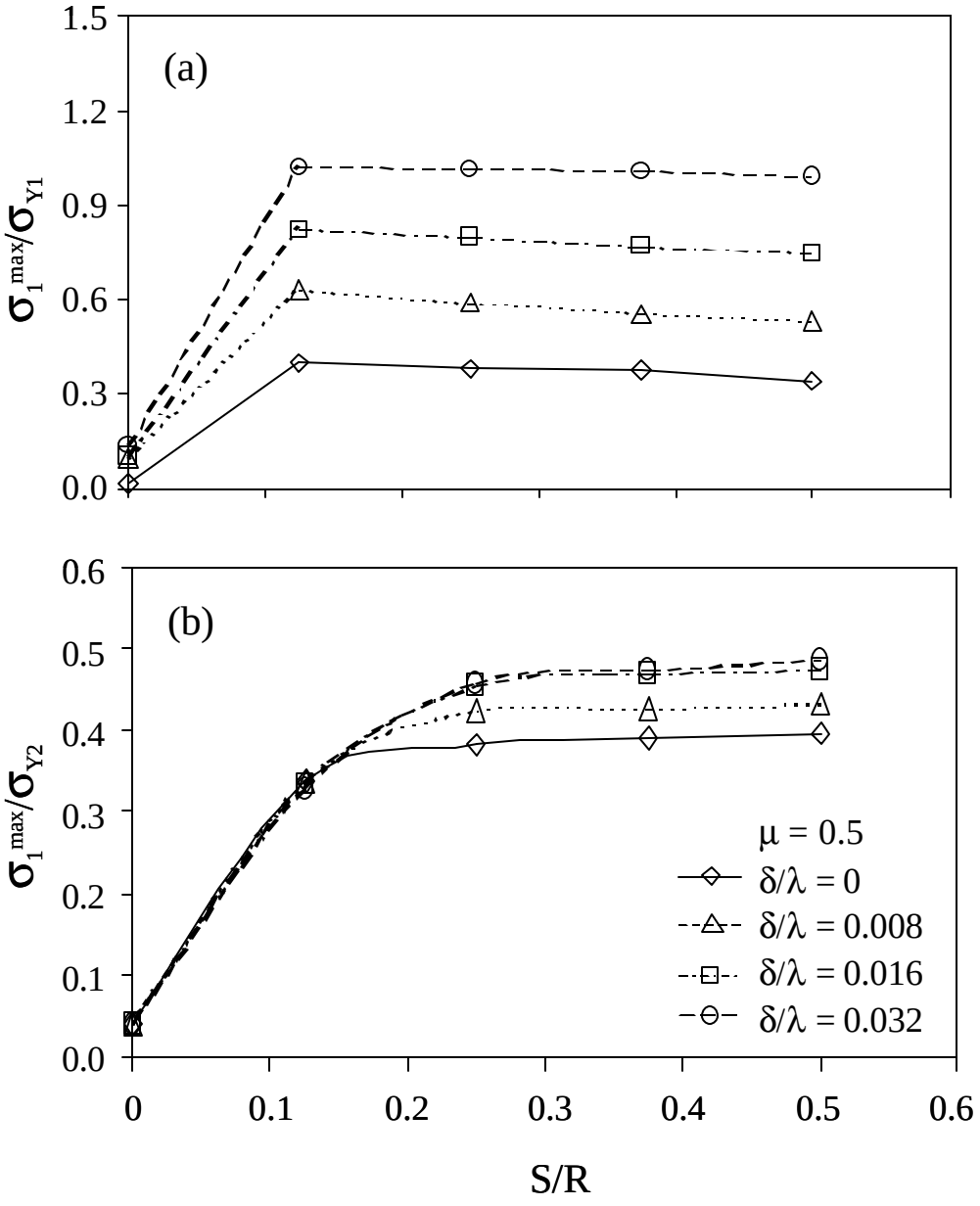

Fig. 2.7 Maximum first principal stress s_1^{max} versus sliding distance S/R in (a) first (hard) layer and (b) second (soft) layer of layered media with flat and sinusoidal surfaces (m = 0.5).

layer (Fig. 2.8(a)). Alternatively, for low-friction sliding (m = 0.1), a discontinuous plastic zone exhibiting periodicity similar to that of the surface pattern evolves in the soft layer (Fig. 2.8(b)). In addition, the maximum plastic strain is much lower than that in the high-friction case and the hard layer deforms only elastically, conversely to the high-friction case where very small plastic zones occur at surface peaks (Fig. 2.8(a)).

While the evolution of plasticity in the soft layer for d/l = 0.008 and 0.016 was found to be qualitatively similar to that shown in Fig. 2.8, the deformation of the hard

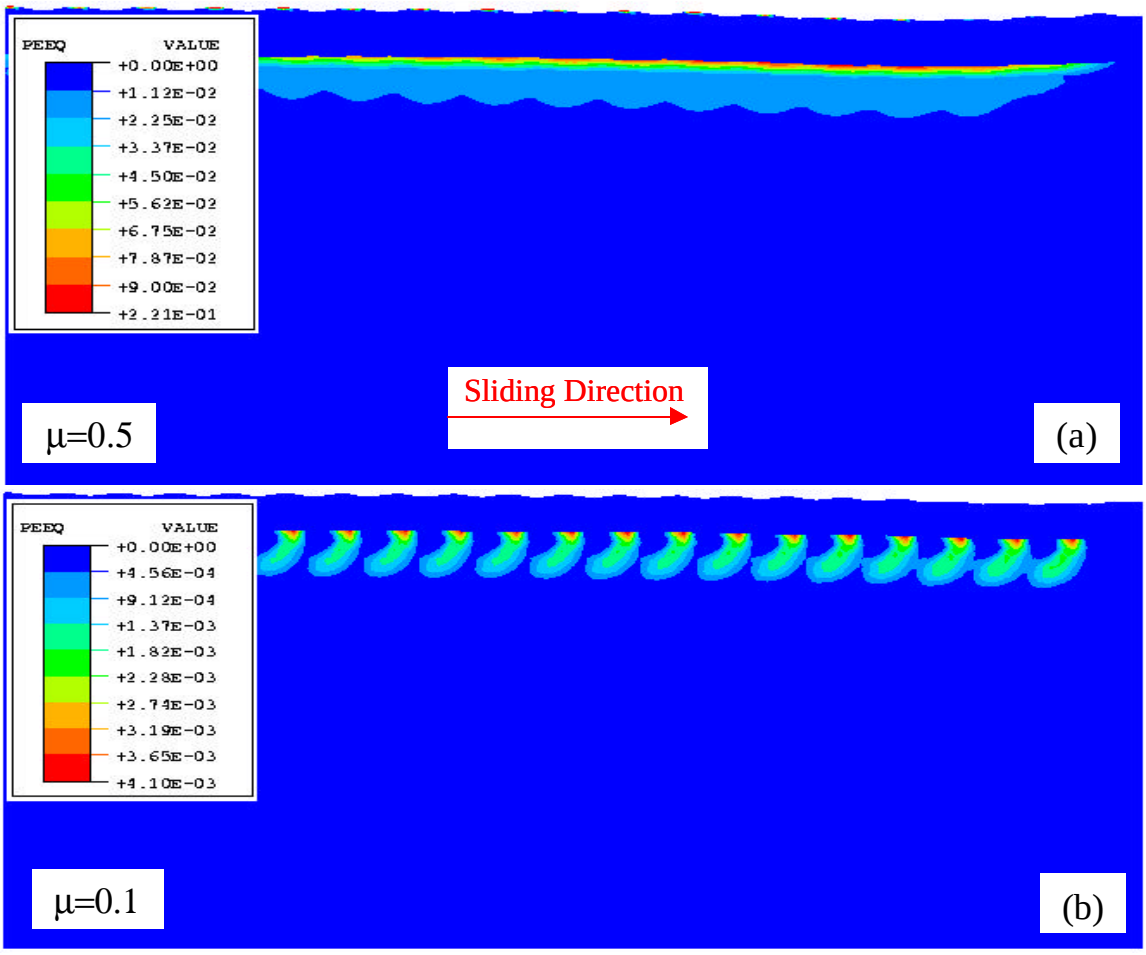

Fig. 2.8 Contours of equivalent plastic strain $\bar{e}_p$ in layered media with sinusoidal surfaces (d/l = 0.032) for different friction coefficients (S/R = 0.5): (a) m = 0.5 and (b) m = 0.1.

layer demonstrated a dependence on the magnitude of d/l. Plastic strain contours obtained for a layered medium with a sinusoidal surface (d/l = 0.016) and a flat-surface layered medium (d/l = 0), i.e., low-roughness and smooth surface, respectively, revealed the absence of plastic deformation in the hard layer during sliding, despite the high friction coefficient (m = 0.5), conversely to the rough-surface layered medium (Fig. 2.8(a)). This is due to the relatively high yield strength of the hard layer. These results demonstrate the pronounced effects of surface pattern geometry, coefficient of friction, and material properties on the development of plasticity in layered media.

Figures 2.9(a) and 2.9(b) show the maximum equivalent plastic strain, $\bar{e}_p^{\max}$, in the underlying soft layer of layered media with meandered and sinusoidal surface patterns, respectively, as a function of sliding distance S/R. Results for flat-surface layered media (b/a = 0 and d/l = 0) are also shown for comparison. The continuous decrease of the slopes of all strain curves indicates the approach to steady-state peak plastic strains in the range of 0.08-0.15. Nonetheless, the most important result is the decrease of plastic strain with increasing ratios b/a and d/l. This is more apparent for the sinusoidal surface patterns producing lower plastic strains, a consequence of the less pronounced stress concentration effect in the absence of sharp corners, as in the case of the meandered surfaces. For instance, at a sliding distance S/R = 0.5, the maximum plastic strain in the second layer for d/l = 0.032 is equal to ~60 percent of that obtained for d/l = 0. This is attributed to the effect of surface patterning on the compliance of the relatively stiffer surface layer. Increasing the magnitude of b/a (or d/l) produces a more compliant surface layer that can store more strain energy without undergoing plastic

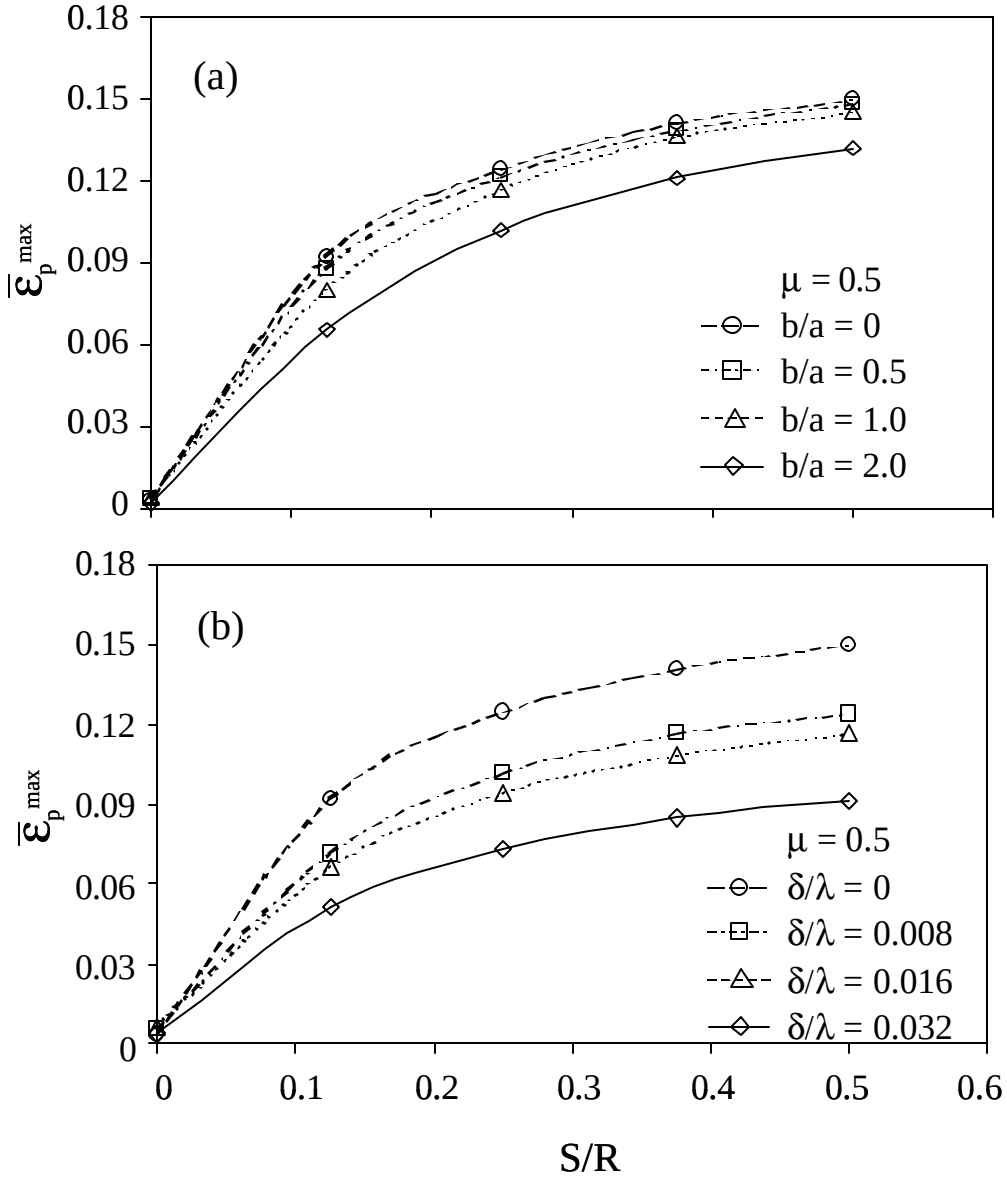

Fig. 2.9 Maximum plastic strain $\bar{e}_p^{max}$ in the second (soft) layer of layered media with (a) meandered and (b) sinusoidal surfaces versus siding distance S/R (m = 0.5). (Stress results for b/a = 0 and d/l = 0 in (a) and (b), respectively, are for a layered medium having a flat surface.)

deformation. Thus the reduced effective stiffness of the first layer lowers the subsurface stresses, thereby decreasing the likelihood of plastic flow in the soft layer. However, as discussed earlier, increasing d/l leads to a higher maximum first principal stress at the trailing edge of the contact region, while increasing b/a promotes the development of high pressure spikes, therefore indicating a greater likelihood for surface crack initiation and plastic flow, respectively. Consequently, an optimum range of d/l (or b/a) must be determined in order to minimize the probability for surface cracking and subsurface plastic deformation.

2.3.2 Normal Contact Simulations

In this section, semi-empirical relations for the contact pressure concentration factor and the inception of yielding in layered media with sinusoidal surface patterns are derived from finite element simulation results for the contact pressure and deformation fields resulting from normal contact with a rigid asperity.

2.3.2.1 Contact Pressure Concentration Factor

The contact pressure profiles of indented layered media with sinusoidal surface patterns are fairly similar to those for sliding contact (Fig. 2.4), except that the profiles for normal contact are symmetric. The dependence of contact pressure on surface pattern geometry and indentation depth is of particular interest since it affects the evolution of plasticity in the layers. The contact pressure concentration factor, K_p, is defined as the ratio of the maximum contact pressure of the patterned layered medium to that of the flat-layered medium. Figure 2.10 shows the variation of K_p with indentation depth, d/R, for different values of d/l and $m = 0.5$. In all cases, K_p decreases monotonically with increasing indentation depth (or normal load) and wavelength and increases with

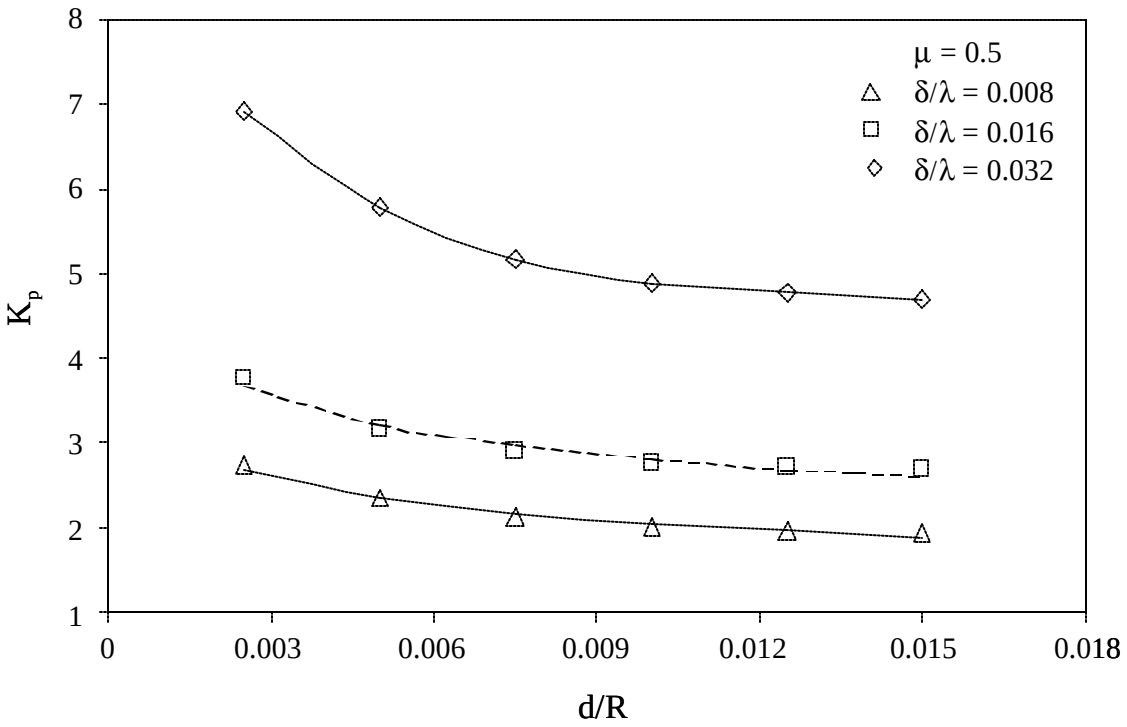

Fig. 2.10 Contact pressure concentration factor K_p for layered media with sinusoidal surfaces versus indentation depth d/R (m = 0.5).

increasing amplitude of surface waviness. This trend is in qualitative agreement with results for a plane in contact with a wavy cylinder obtained by Seabra and Berthe (1987).

The following relation of K_p was fitted to the finite element results obtained for d/l = 0.008 and 0.016. (Data for d/l = 0.032 were not used because plastic deformation occurred in some of these simulations.)

$$K_p = C(\frac{d}{l})^a (\frac{d}{R})^b , \tag{2.5}$$

where C = 2.0327, a = 0.4578, and b = -0.1978. The correlation factor for this fit is equal to 0.996. The values of a and b are fairly close to those of the pressure concentration factor obtained for a wavy cylinder indenting an elastic homogeneous half-space (Seabra and Berthe, 1987). Since the values of the material parameters and layer thickness used in

the finite element analysis affect the magnitudes of the parameters in Eq. (2.5), the values of C, a, and b are specific to the modeled media. However, the same approach can be repeated to obtain best-fit values for different material property and thickness values of the layers. Hence, the increase of the maximum contact pressure on layered media possessing sinusoidal surface patterns can be determined from Eq. (2.5).

2.3.2.2 Yield Criterion

Figure 2.11 shows that the normalized maximum von Mises equivalent stress in the first layer of layered media with sinusoidal surface patterns increases with increasing ratios d/l and d/R. However, the effect of the pattern geometry is significantly more

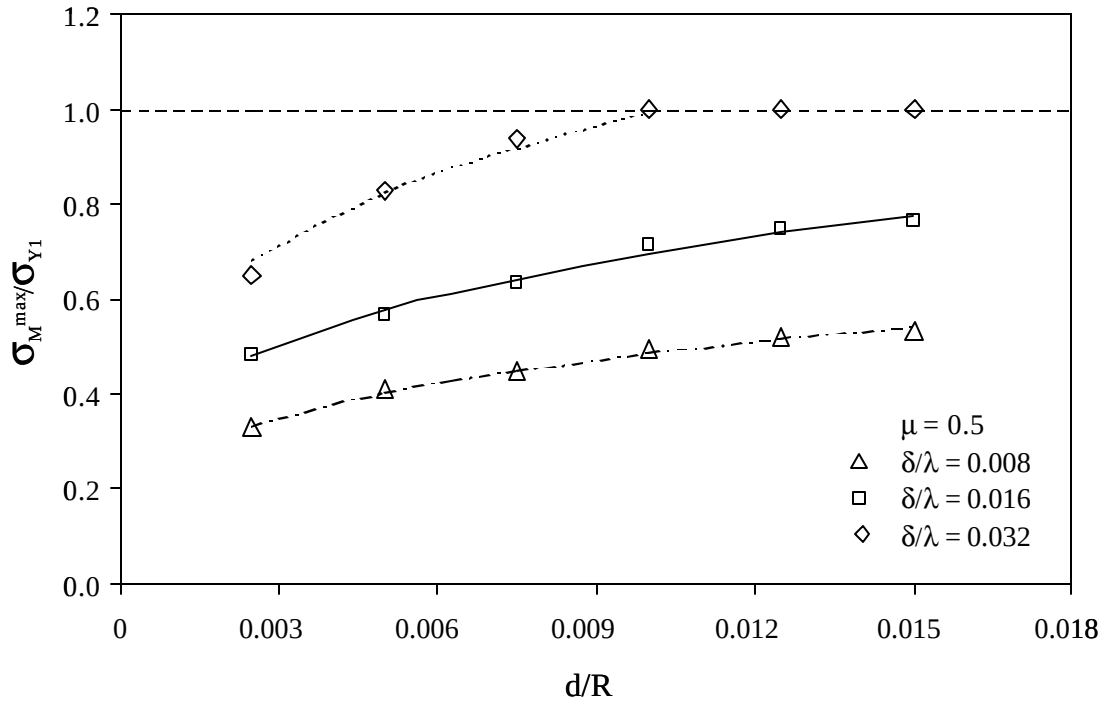

Fig. 2.11 Maximum von Mises equivalent stress $s_M^{\max}$ in the first (hard) layer of layered media with sinusoidal surfaces versus indentation depth d/R (m = 0.5).

pronounced than that of the indentation depth (or normal load). For d/l = 0.032, $s_M^{\max}$ reaches the yield stress of the layer when d/R = 0.01.

Based on the simulation results for d/l = 0.008 and 0.016, a yield criterion for layered media with sinusoidal surface patterns (d/l > 0) was obtained by fitting to the finite element results a relation of the form:

$$\frac{s_M^{\max}}{s_{Y1}} = C_1 (\frac{d}{l})^g (\frac{d}{R})^h \le 1. \tag{2.6}$$

Based on an iterative procedure, it was determined that g = 0.5173 and h = 0.2715. However, because C_1 is a function of material properties, finite element simulations for layered media with different elastic properties were performed in order to obtain a relation for C_1 in terms of the elastic modulus of the hard and soft layers. Figure 2.12 shows the variation of $s_M^{\max}$ in the first layer with indentation depth d/R for different values of the elastic modulus ratio of the first (hard) and second (soft) layers, E_1/E_2, d/l = 0.016, and μ = 0.5. These results demonstrate that $s_M^{\max}$ increases with both ratios E_1/E_2 and d/R. After fitting to the finite element results relation

$$C_1 = C_2 \left[\frac{E_1/(1-\nu_1^2)}{E_2/(1-\nu_2^2)} \right]^m, \tag{2.7}$$

it was found that C_2 = 17.1798 and m = 0.6935. (The correlation factor is equal to 0.998.) Substituting Eq. (2.7) into Eq. (2.6), the general yield criterion for layered media with sinusoidal surfaces can be written as

$$\frac{\sigma_M^{\max}}{\sigma_{Y1}} = C_2 \left[\frac{E_1/(1-\nu_1^2)}{E_2/(1-\nu_2^2)} \right]^m (\frac{\delta}{\lambda})^\gamma (\frac{d}{R})^\eta \le 1 , \quad (d/l > 0), \tag{2.8}$$

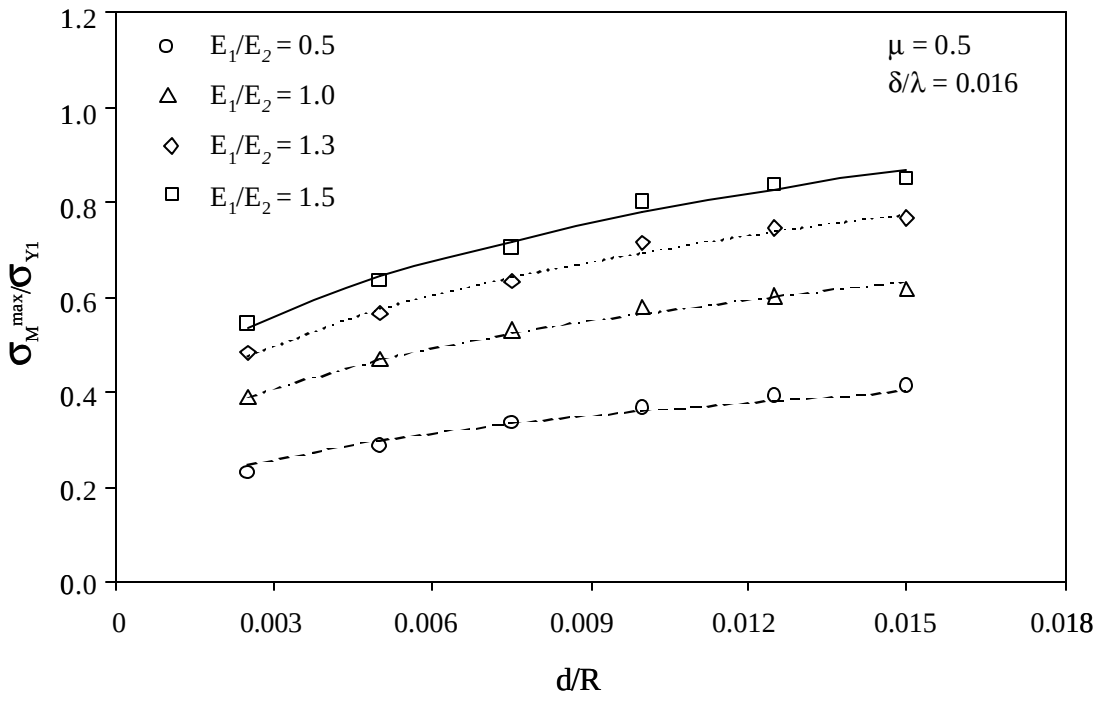

Fig. 2.12 Maximum von Mises equivalent stress $s_M^{\max}$ in the first (hard) layer of layered media with sinusoidal surfaces (d/l = 0.016) versus indentation depth d/R and elastic modulus ratio of first-to-second layer E_1/E_2 (m = 0.5).

where g, h, m, and C_2 are material constants. Based on this yield criterion, the normal load (indentation depth) at the inception of yielding in the first layer can be predicted for given material properties, layer thickness, and amplitude-to-wavelength ratio.

To evaluate the accuracy of the yield criterion (Eq. (2.8)), results for the indentation depth (normal load) at the onset of plasticity in the first layer calculated from Eq. (2.8) are compared in Fig. 2.13 with results determined directly from finite element simulations. (A comparison of results for d/l = 0.008 was not possible due to the excessive computation time required to reach yielding in this simulation case.) For d/l = 0.032, yielding is predicted from Eq. (2.8) to initiate at d/R = 0.01, which is equal to the value obtained from the finite element analysis. To examine the case of d/l = 0.016, the

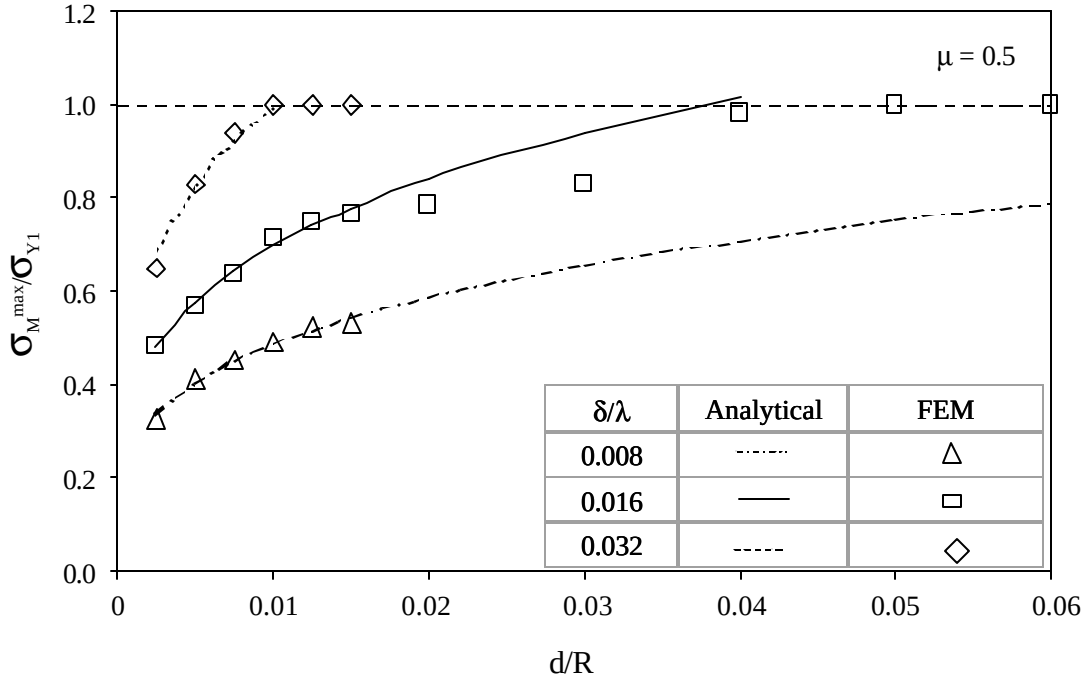

Fig. 2.13 Comparison of empirical and finite element results for the maximum von Mises equivalent stress $s_M^{\max}$ in the first (hard) layer of layered media with sinusoidal surfaces versus indentation depth d/R (m = 0.5).

asperity radius was reduced by a factor of 4 in order to reduce the indentation depth (i.e., computation time) required to initiate yielding. As shown in Fig. 2.13, Eq. (2.8) gives that yielding in the first layer commences at d/R = 0.038, while the finite element prediction is d/R = 0.04, i.e., the difference between the results of the two approaches is 5 percent. Hence, Eq. (2.8) can be used to determine the load at the onset of yielding in the first layer of patterned layered media in terms of surface geometry parameters and material properties.

2.4 Conclusions

A two-dimensional plane-strain finite element analysis of normal and sliding contact of elastic-plastic layered media was performed in order to elucidate the effect of

surface patterning on the resulting deformation behavior. Stress and plastic strain results for layered media possessing meandered and sinusoidal surface patterns were compared with those of a layered medium with a smooth (flat) surface and identical layer thickness and material properties subjected to the same normal and tangential loading. Based on the presented results and discussion, the following main conclusions can be drawn.

(1) The apparent contact area of layered media with patterned surfaces in contact with a rigid cylindrical asperity consists of several microcontacts exhibiting a trend to merge with each other with increasing indentation depth (or normal load). During sliding, high peak pressures occur at the trailing edges of microcontacts in the contact zone. The maximum contact pressure is a strong function of the pattern geometry. Significantly higher peak pressures occur at the sharp edges (stress raisers) of the meandered surfaces. In contrast, the contact pressure at the microcontacts within the contact zone of layered media possessing sinusoidal surface patterns increases smoothly due to the continuity of the surface profile.

(2) The magnitude of the surface tensile stress in the direction of sliding provides information about the likelihood for transverse (ring) crack initiation at the surface, in the wake of sliding. The maximum tensile residual stress on layered media with sinusoidal surface patterns occurs at the trailing edge of the contact region. This residual stress is much higher than that obtained with a layered medium having a flat surface and depends on the pattern geometry and friction coefficient. For patterned surfaces exhibiting high amplitude-to-wavelength ratio and high friction, a significant tensile residual stress develops in the wake of sliding. This residual tensile stress may continue to increase with the accumulation of sliding cycles leading to surface

cracking. Conversely to the flat surface that yields a purely compressive stress field, small regions of tensile stress occur at the contact region of layered media with sinusoidal surface patterns.

(3) The maximum plastic strain due to sliding contact decreases with increasing the amplitude-to-wavelength ratio of the sinusoidal surface patterns. Patterned surfaces produce lower plastic strains and smaller plastic zones than flat surfaces due to the lower stresses resulting from the increased compliance of the hard first layer that can store significant strain energy without undergoing plastic deformation. The decreased surface stiffness of the patterned layered media reduces the maximum plastic strain and size of plastic zone in the underlying soft layer. However, this arises at the expense of a higher surface tensile stress at the trailing edge of the contact interface, indicating a greater probability of surface crack initiation for patterned media.

(4) Relations for the contact pressure concentration factor and inception of yielding in the first layer of indented layered media with sinusoidal surface patterns were derived from finite element solutions using a best-fit approach. The contact pressure concentration factor decreases with increasing indentation depth (normal load) and wavelength-to-amplitude ratio. The yield criterion accounts for the effects of material properties, pattern geometry parameters, and contact load, and is in good agreement with finite element predictions. Yielding in the first layer is predominantly controlled by the geometry of the surface pattern and secondarily by the indentation depth.

CHAPTER 3

MECHANICAL AND THERMOMECHANICAL ELASTIC-PLASTIC CONTACT ANALYSIS OF LAYERED MEDIA WITH PATTERNED SURFACES

3.1 Introduction

An enhancement of the tribological performance and functionality of contacting surfaces is commonly achieved through deposition of thin surface layers (overcoats) exhibiting high hardness and low coefficient of friction. Analysis of the stresses and deformation in layered media due to sliding contact is critical to the design of various mechanical components. The primary objective of previous theoretical and numerical analyses has been the examination of the effect of the thickness and mechanical properties of protective overcoats on the contact stress and strain fields in the overcoat and underlying substrate media. However, relatively less is known about the role of surface microfeatures (typically produced by lithography and electron beam techniques) on the elastic-plastic deformation and temperature rise due to frictional heating in layered media. Patterned layered media are used in many leading-edge technologies, such as high-density data storage (Chou et al., 1996; White et al., 1997) and magnetic random access memory media (Savas et al., 1999). Achromatic interferometric lithography has been used to fabricate arrays of microstructures with spatial periodicity of ~100 nm for ultra-high density magnetic storage applications (Savas et al., 1999; Farhoud et al., 1998).

Contact of elastic bodies with small-amplitude sinusoidal surfaces has been examined in early analytical studies in order to determine the effect of surface geometry

on the contact stresses. Using complex variables, Westergaard (1939) obtained a closed form solution for the elastic contact of a sinusoidal surface and a smooth plane. Dundurs et al. (1973) implemented a Fourier analysis in a stress function approach to obtain solutions for the previous contact problem. Johnson et al. (1985) determined the pressure distribution and contact area, and derived closed-form asymptotic solutions for both light and heavy contact loads resulting in almost full contact. Komvopoulos and Choi (1992) analyzed normal contact between regularly spaced rigid asperities and an elastic half-space and obtained finite element solutions for the maximum contact pressure, normal load, and subsurface stresses in terms of the asperity distribution and indentation depth. Ramachandra and Ovaert (2000) examined the stresses produced in discontinuous coatings of different profiles and various mechanical properties of the coating and substrate materials, and observed a significant decrease of the contact pressure peaks in the case of discontinuous coatings with crowned edges. Gong and Komvopoulos (2003) analyzed normal and sliding contact of a rigid cylindrical asperity on patterned elastic-plastic layered media using the finite element method and examined the effect of pattern geometry on the resulting deformation and stress fields. While the maximum plastic strain due to sliding contact decreased with increasing amplitude-to-wavelength ratio of sinusoidal surface patterns, the high surface tensile stress at the trailing edge of the contact region indicated a greater probability for surface cracking in the case of the patterned medium.

The temperature rise at sliding interfaces due to frictional heating may affect significantly the tribological behavior of electromechanical components. Thermomechanical analysis of homogeneous half-spaces subjected to a fast moving heat

source have shown that the surface stress field is predominantly compressive (Ju and Huang, 1982) and that the maximum thermal tensile stress occurs slightly below the trailing edge of the contact region (Huang and Ju, 1985) at a depth where the temperature gradient begins to vanish (Ju and Liu, 1988). This critical depth depends on the Peclet number, which is a function of sliding speed, contact radius, and material diffusivity. Ju and Chen (1984) conducted a thermomechanical contact analysis for layered media under a moving friction load and a moving heat source and discussed crack initiation in the context of the determined stress field. Leroy et al. (1989) derived a two-dimensional model for a layered medium subjected to a moving heat source and reported high stresses in overcoats with thermomechanical properties significantly different from those of the substrate material. Cho and Komvopoulos (1997) performed a fracture mechanics analysis of subsurface crack propagation and showed that, although frictional heating exhibits a negligible effect on the crack propagation direction, it increases the in-plane crack growth rate and reduces the critical crack length at the onset of out-of-plane growth at the right crack tip. In a more recent study, Ye and Komvopoulos (2003) developed a finite element model to examine the simultaneous effects of mechanical and thermal surface traction on the deformation of elastic-plastic layered media, and interpreted the propensity for plastic flow and cracking in terms of the thickness and thermal properties of the layer, normal load, and Peclet number.

Despite important insight into thermomechanical contact deformation of elastic-plastic media derived from previous studies, a comprehensive three-dimensional contact analysis for elastic-plastic patterned layered media has not been reported yet. Therefore, the principal objective of this study was to examine the effects of pattern geometry,

coefficient of friction, indenter sharpness (radius), and sliding cycles on the stresses and strains arising in layered patterned media subjected to normal and shear (friction) surface tractions. Another objective was to analyze the effect of frictional heating on the surface temperature distribution and evolution of subsurface plasticity. This was accomplished by performing finite element simulations of normal and sliding contact of a sphere on layered media with patterned surfaces. The finite element method is suitable for such type of complex contact problems, for which it is extremely difficult to obtain analytical solutions for the surface and subsurface deformation and stress fields. Deformation and frictional heating in patterned layered media is discussed in the context of finite element results for the contact pressure distribution, subsurface stress/strain fields, and temperature rise at the contact surface obtained for different indentation depths, coefficient of friction, sliding cycles, indenter radius, and Peclet number.

3.2 Modeling Procedures

3.2.1 Finite Element Model

Figure 3.1 shows a three-dimensional finite element model of a sphere in contact with an elastic-plastic layered medium with a patterned surface. Due to symmetry, only one-half of the sphere and layered medium were modeled in order to reduce the computation time. The finite element mesh consists of 25,732 eight-node, linear interpolation elements having a total of 33,099 nodes. The normalized mesh dimensions are $x/H = 2.443$, $y/H = 0.260$, and $z/H = 1.0$, where H is the total thickness of the mesh. Four pads of constant height equal to $0.86b$, regularly spaced at lateral distances $l = 0.714b$, where b is the side of the square pad surfaces, were modeled at the surface of the finite element mesh (i.e., pad spatial periodicity equal to $b + l$). In these simulations, the

sphere was assumed to be rigid with a radius of curvature R/H = 0.763 and 1.526. Sliding was simulated by displacing the sphere along the positive x-direction in an incremental fashion. The nodes on planes x = 0, y = 0, and z = 0 were constrained against displacement in the x-, y-, and z-direction, respectively.

In the thermomechanical analysis, the length of the finite element mesh was reduced to x/H = 1.588 and the number of pads to three due to the excessive computation time in coupled thermal and mechanical contact analysis. Therefore, the mesh in the

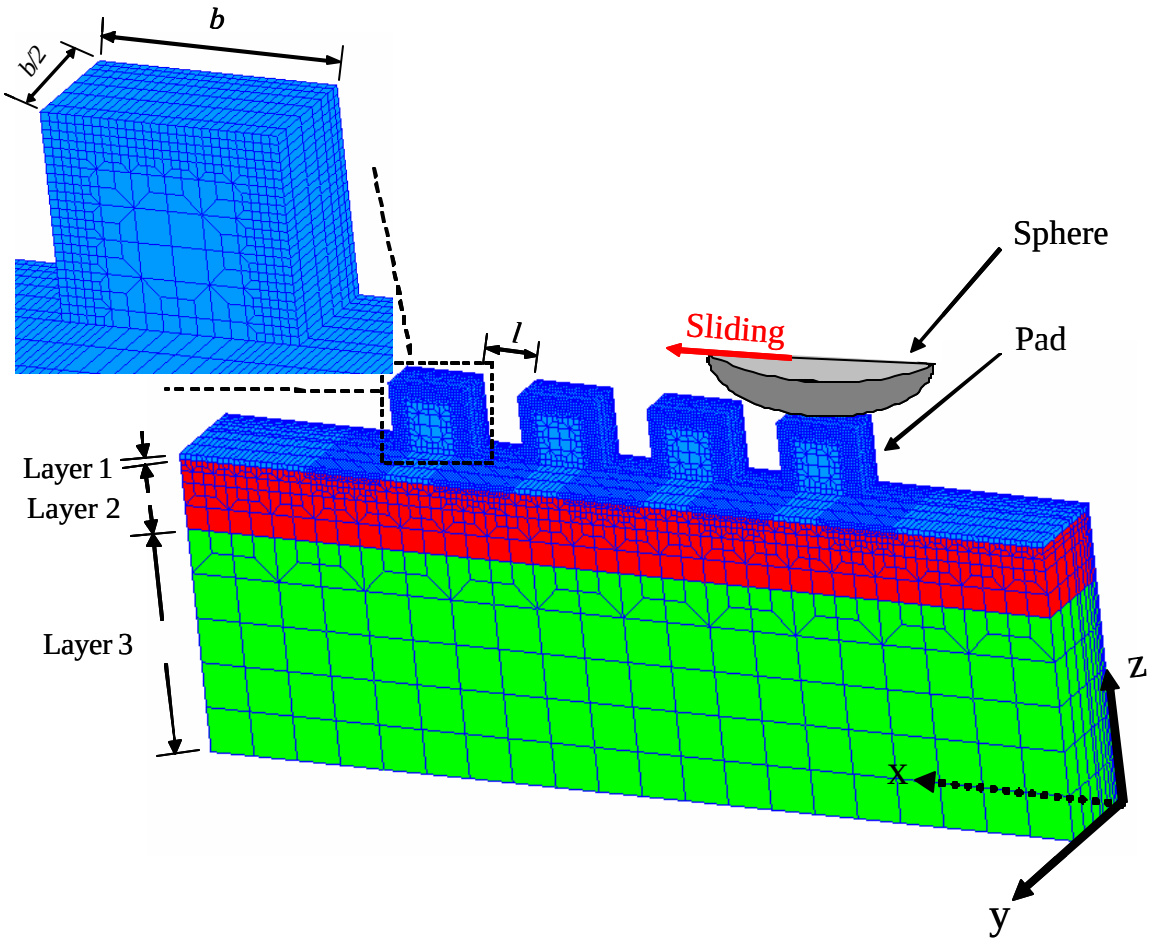

Fig. 3.1 Three-dimensional finite element mesh of a layered medium with a patterned surface. (The inset at the top shows the detail of the refined mesh of each pad.)

thermomechanical simulations consisted of 20,995 eight-node, coupled temperature-displacement finite elements comprising a total of 27,585 nodes. In addition, the sphere was assumed to be elastic-perfectly plastic with a radius of curvature R/H = 1.526 and thermomechanical properties identical to those of the first layer. The temperature at the nodes of planes y = 0, and x/H = 0 and 1.588 was set equal to 20 ^{o}C. Heat conduction was restricted across the sphere/layered medium contact interface.

3.2.2 Material Properties and Constitutive Models

The normalized thickness, h/H, and elastic-plastic properties of each layer material of the patterned layered medium are given in Table 3.1. These thickness and mechanical property values are typical of layers used in magnetic recording rigid disks consisting of carbon overcoat (layer 1), CoCrPt magnetic medium (layer 2), and CrV

Table 3.1. Thickness and thermomechanical properties of layers in the patterned layered medium

Medium	Layer 1	Layer 2	Layer 3
Thickness (h/H)	0.015	0.374	0.611
Elastic modulus (GPa)	168	130	140
Poisson's ratio	0.3	0.3	0.3
Yield strength (GPa)	13	2.67	2.58
Thermal expansion (K^{-1})	3.1×10^{-6}	13×10^{-6}	4.9×10^{-6}
Specific heat (J/g·K)	0.5	0.411	0.438
Conductivity (W/m·K)	5.2	105	96.5
Density (kg/m^3)	2.15×10^{3}	8.9×10^{3}	7.19×10^{3}
Diffusivity (m^2/s)	4.84×10^{-6}	28.7×10^{-6}	30.64×10^{-6}

underlayer (layer 3) deposited on NiP-coated Al-Mg substrate. The elastic modulus and yield strength of layers 1 and 2 have been determined from nanoindentation measurements (Komvopoulos, 2000). The specific heat, thermal conductivity, and density of the first layer are representative of carbon films (Graebner, 1996; Morath et al., 1994; Tsai and Bogy, 1987). All other density and thermal properties were obtained from tabulated data compiled by Kaye and Laby (1986). The von Mises yield criterion was used to determine whether yielding occurred at a material point. Each layer was modeled as an elastic-perfectly plastic material.

3.2.3 Thermal Model

Sliding friction at contact interfaces of mechanical components promotes energy dissipation in the form of heat within the vicinity of the real contact area. The dissipated frictional heat is responsible for the temperature rise at the contact interface of sliding bodies, causing the development of thermal stresses and variations in the real contact area and contact pressure distribution due to thermal expansion. Since these changes in the contact conditions affect the heat generation rate and heat conduction across the contact interface, the thermal and mechanical stress/strain fields are fully coupled and, therefore, must be determined simultaneously rather than sequentially. In this study, the temperature was integrated using a backward-difference scheme, and the coupled system was solved using the Newton method. A fully coupled thermal-mechanical stress analysis automatically invokes a nonsymmetic matrix storage and solution scheme to improve the computational efficiency. This is because the stiffness matrix is asymmetric due to friction and the convective term in the conduction-convection equation.

The heat flux density due to frictional heat, q, is given by (Ye and Komvopoulos, 2003)

$$q = \eta \mu p u \,, \tag{3.1}$$

where η is the fraction of mechanical work dissipated as heat, μ is the coefficient of friction, p is the contact pressure, and u is the sliding speed. In the present simulations, it is assumed that η = 1.0, which is consistent with the conclusion of Uetz and Föhl (1978) that nearly all the energy dissipated in a frictional contact is converted to heat. The amount of frictional heat that is instantaneously conducted into each body depends on the heat partition factor. The heat generated due to subsurface plastic flow is ignored in the present study as significantly less than the frictional heat generated at the contact region in the case of relatively high coefficient of friction (e.g., μ = 0.5).

Although the contact interface was modeled to have zero heat capacity, it was assigned properties for the exchange of heat by conduction and radiation, as in a previous study (Ye and Komvopoulos, 2003). However, heat flux due to radiation was neglected as secondary compared to that due to conduction. The flux density across the contact interface (from the sphere to the layered medium), q_c, is defined as

$$q_c = k_g (q_1 - q_2) \,, \tag{3.2}$$

where q_1 and q_2 are temperatures at surface nodes of the contacting bodies (i.e., the sphere and patterned layered medium, respectively), and k_g is the gap conductance, defined as k/Dl, where k is the thermal conductivity of the first layer, and Dl is the size of the smallest finite element.

The heat flux density into each contacting body, q_1 and q_2, respectively, is given by

$$\begin{aligned} q_1 &= -q_c + fq \\ q_2 &= q_c + (1 - f)q \end{aligned} \tag{3.3}$$

where f is the heat partition factor indicating the fraction of heat dissipated into one of the contacting bodies (sphere). Simulations were performed for f = 0.5, i.e., evenly distributed heat between the sphere and the layered medium. This is a reasonable assumption for relatively low Peclet number (e.g., Pe $\leq$ 1) and thermophysical properties of the sphere identical to those of the first layer. In view of the heat flux due to conduction across the contact interface, q_c, the heat partition factor in this study differs from the traditional heat partition factor.

3.2.4 Finite Element Simulations

Quasi-static contact simulations comprising three sequential steps of loading, sliding, and unloading of a sphere on a layered patterned medium were performed in an incremental fashion. Normal contact (indentation) was simulated by advancing the sphere toward the elastic-plastic medium up to a specified indentation depth, d (or normal load). Subsequently, the sphere was displaced laterally to a maximum distance, S, about ten times the contact radius, while maintaining constant indentation depth d and coefficient of friction, m, and then unloaded following the same steps as for the loading. All simulations were performed with the multipurpose finite element code ABAQUS. To study the effect of friction on the stress/strain fields produced in the layered medium, friction coefficients equal to 0.1 and 0.5 were used in this study. In addition, repetitive sliding of the sphere was modeled in order to investigate the dependence of stress and plastic strain on sliding cycles. This is analogous to multiple-asperity sliding contacts encountered with real surfaces. The thermomechanical simulations were performed for m = 0.5 and Peclet number equal to 0.09 and 0.9 (Pe = $2ur/a$, where r is the contact radius after indentation, and a is the thermal diffusivity of the sphere).

3.3 Results and Discussion

Finite element solutions for the stresses and strains in an elastic-plastic layered medium due to indentation and sliding of a rigid sphere are presented first in order to elucidate the significance of surface microgeometry (patterning) on contact deformation and to establish a reference for comparison with the results of the thermomechanical analysis presented later. The effects of friction coefficient, sphere radius, and sliding cycles are discussed next in terms of results for the contact pressure, contact area, subsurface stresses, and maximum plastic strain. Lastly, simulation results from a fully coupled thermomechanical contact analysis of an elastic-plastic sphere in normal and sliding contact with an elastic-plastic layered patterned medium are presented to illustrate the effect of frictional heating on the surface temperature rise and subsurface deformation.

3.3.1 Mechanical Contact Analysis

Figure 3.2 shows the contact pressure distribution (in the plane of symmetry y = 0) at a single pad indented by a rigid sphere versus normalized indentation depth, d/R. Initial contact occurred at the center of the pad (x/b = 0). For shallow indentations (d/R = 0.0025), the contact pressure distribution is similar to the profile predicted by the Hertz theory. However, increasing the indentation depth (d/R = 0.005 and 0.0075) causes the maximum contact pressure to shift toward the edge of the contact area (Fig. 3.2(a)). Further increase of the indentation depth ($d/R \geq 0.01$) produces pressure spikes at the edges of the contact area (Fig. 3.2(b)), consistent with the contact pressure profile obtained for a layered medium with a meandered surface pattern (Gong and

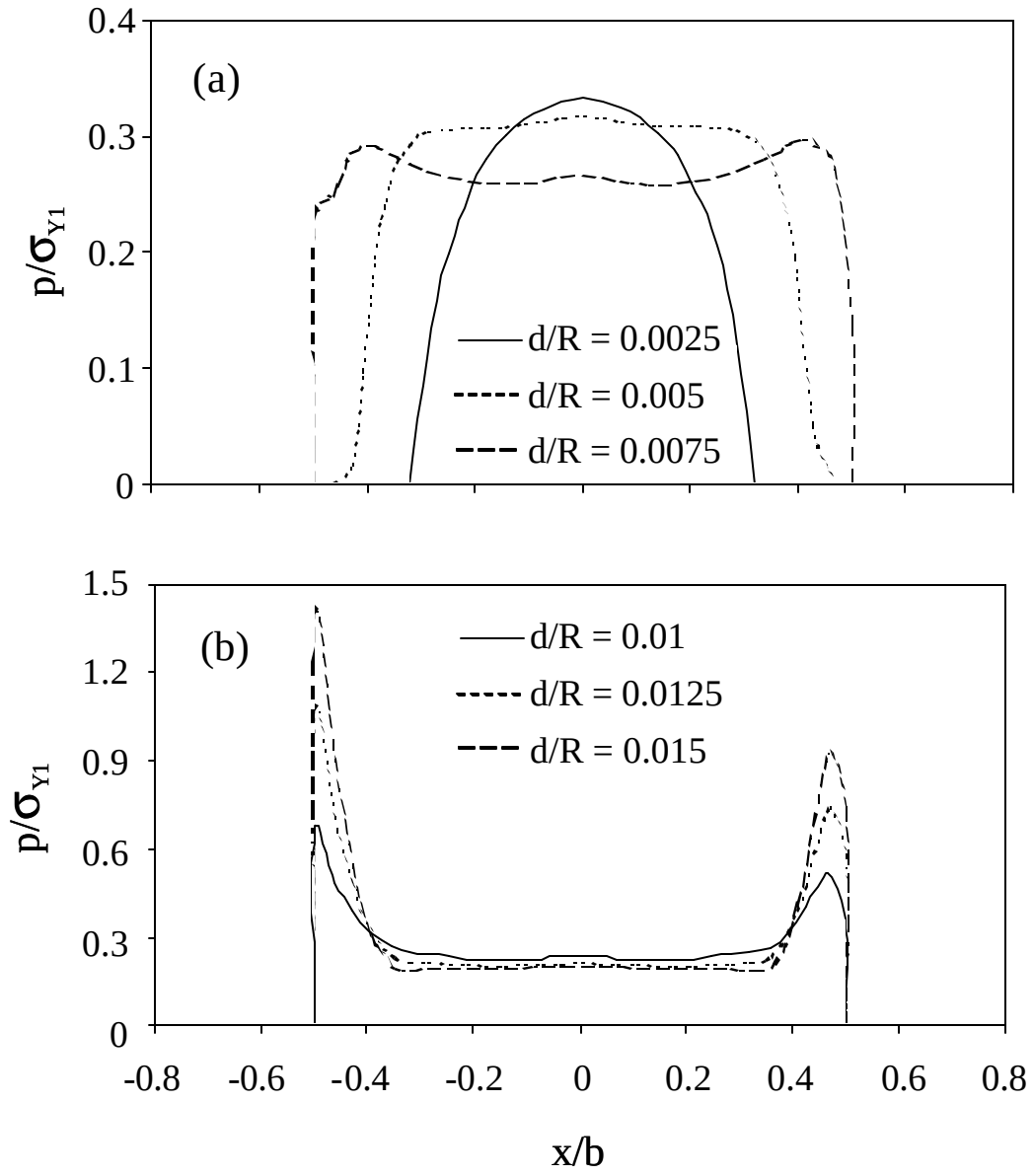

Fig. 3.2 Contact pressure distribution at a single pad in the symmetry plane (y =0) for different indentation depths. (Initial contact of the indenting rigid sphere occurs at the center of the pad surface (x/b = 0).)

Komvopoulos, 2003). This change of the contact pressure is attributed to the development of a plastic zone in the second soft layer (discussed below) and the stress concentration at the pad corners that is further enhanced by the relatively higher rigidity of the pad sides. The asymmetry of the contact pressure profiles at large indentation depths (i.e., d/R = 0.0125 and 0.015) is due to the constraint of the nodes on plane x/H = 0 against displacement in the x-direction. However, this effect is negligible in the results presented below due to the much smaller indentation depth used in these simulations.

The normalized maximum von Mises equivalent stress in the first layer, $\sigma_M^{\max} / \sigma_{Y1}$, and normalized real contact area, A_r / A_p, are plotted in Figs. 3.3(a) and 3.3(b), respectively, as functions of normalized indentation depth, d/R, where σ_{Y1} is the yield strength of the first layer and A_p is the pad surface area. For relatively shallow indentations (i.e., partial contact between the sphere and the pad surface), both maximum Mises stress and contact area increase monotonically with indentation depth. For d/R > 0.008, the maximum Mises stress reaches the yield strength of the layer material and a small plastic zone develops adjacent to the contact region. Full contact of the pad with the sphere occurs when $d/R \geq 0.1$. Thus, elastic and elastic-plastic deformation of the pad is associated with partial and full contact with the sphere, respectively.

The variation of the maximum contact pressure, $p_{\max}$, and maximum equivalent plastic strain, $\bar{\varepsilon}_p^{\max}$, in the second layer with normalized sliding distance, S/R, is shown in Figs. 3.4(a) and 3.4(b), respectively, for m = 0.1 and 0.5. The periodic fluctuation of $p_{\max}$ is due to the pattern geometry. The fact that the two peak values of $p_{\max}$ are fairly close suggests that interaction between neighboring pads is secondary. The $\bar{\varepsilon}_p^{\max}$ strain in the

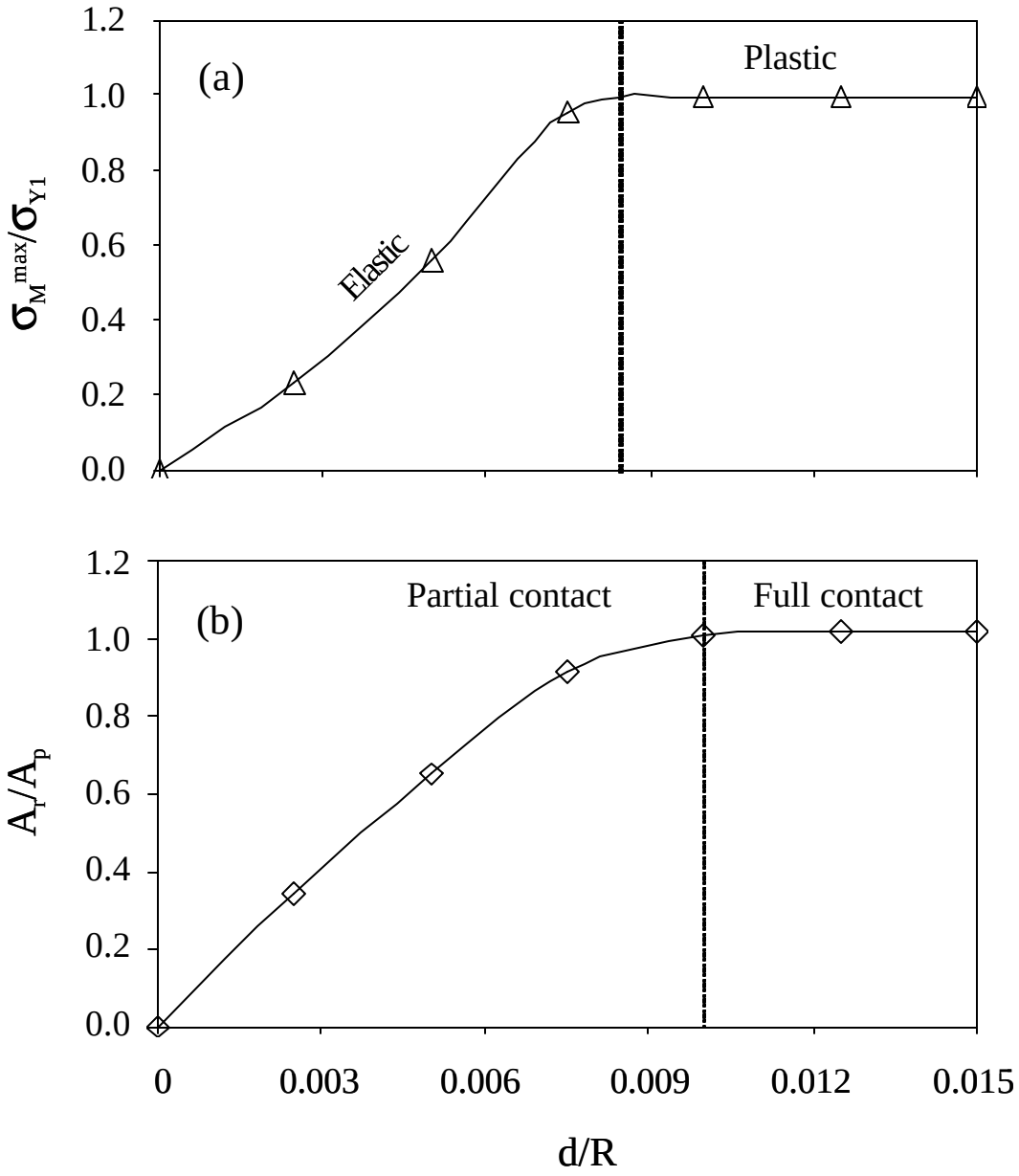

Fig. 3.3 (a) Maximum von Mises equivalent stress in the first (hard) layer and (b) real contact area versus indentation depth.

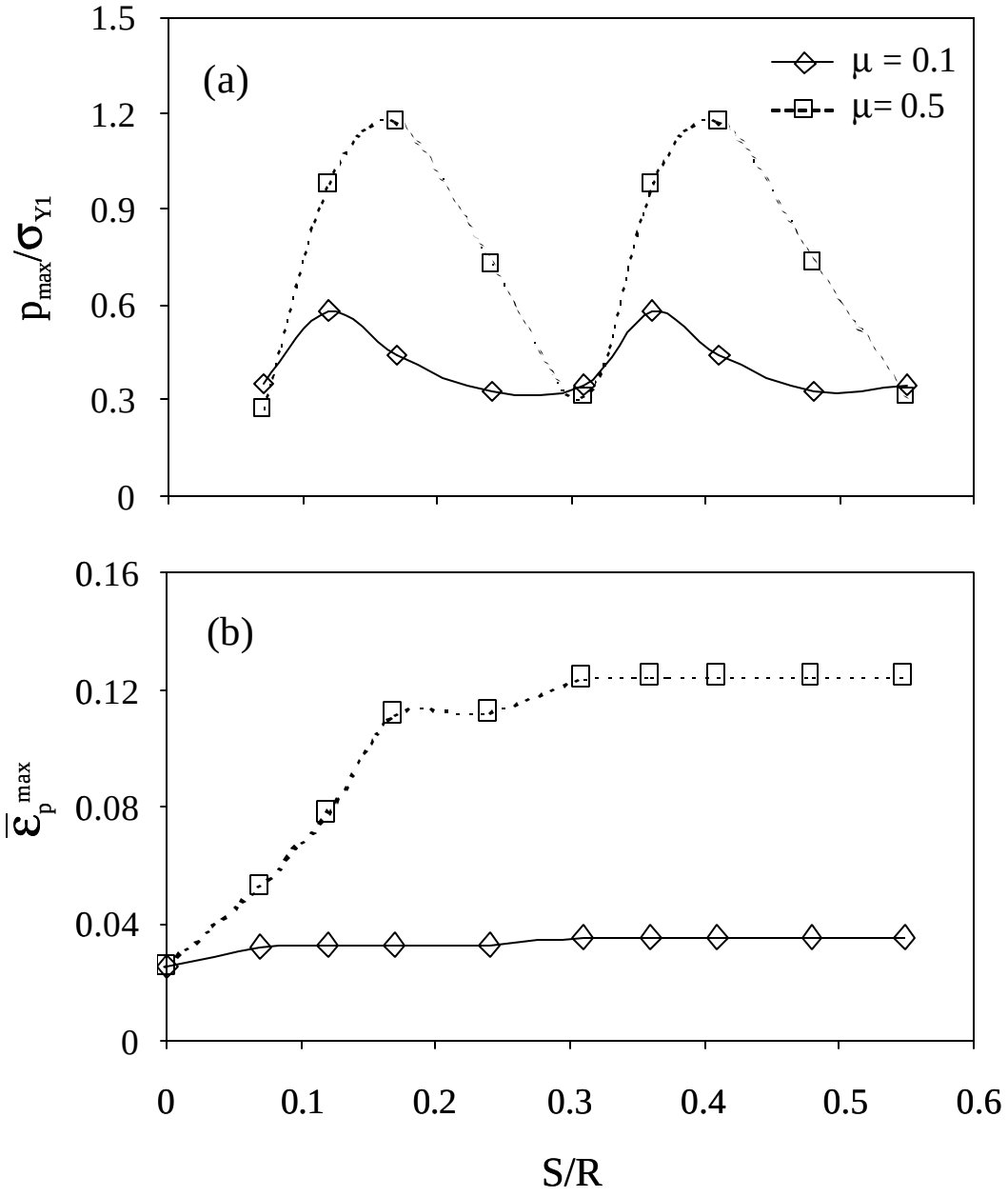

Fig. 3.4 (a) Maximum contact pressure and (b) maximum equivalent plastic strain in the second (soft) layer versus sliding distance for m = 0.1 and 0.5 and d/R = 0.005.

second layer increases significantly at the beginning of sliding and reaches a steady state at a distance of about two times the pad spatial periodicity (S/R = 0.48). However, a longer sliding distance is required for the plastic strain to reach a steady state in the case of a layered medium with a smooth (flat) surface (Gong and Komvopoulos, 2003). This difference between patterned and smooth layered media is due to the reduced plastic deformation in the patterned medium. As shown in Figs. 3.4(a) and 3.4(b), the coefficient of friction influences profoundly both $p_{\max}$ and $\bar{e}_p^{\max}$ in the second layer. Although the pressure and strain results for m = 0.1 and 0.5 exhibit similar trends, much higher peak values of $p_{\max}$ and $\bar{e}_p^{\max}$ are produced with the higher coefficient of friction.

Figure 3.5 shows the evolution of the equivalent plastic strain in the layered medium with sliding distance for m = 0.5 and d/R = 0.005. For pure normal contact (S/R = 0, Fig. 3.5(a)), the maximum plastic strain occurs below the contact interface and the plastic zone is confined within the second layer. Sliding of the sphere over the pad edge (S/R = 0.07, Fig. 3.5(b)) causes the formation of two small plastic zones in the second layer at the lower right corner of the pad due to the stress concentration effect. When the sphere slides over the next pad (S/R = 0.12, Fig. 3.5(c)), stress concentration produces a small plastic zone in the first layer at the upper left corner of this pad, and the maximum plastic strain occurs at the interface of the two layers, similar to smooth layered media (Kral and Komvopoulos, 1997). Figures 3.5(d)-3.5(f) show that the maximum equivalent plastic strain occurs always at the interface of the first and second layers. The close similarity of the plastic zones in each pad confirms that interaction of the stress fields of neighboring pads is negligible and that deformation depends only on the pad geometry and mechanical properties of each layer material.

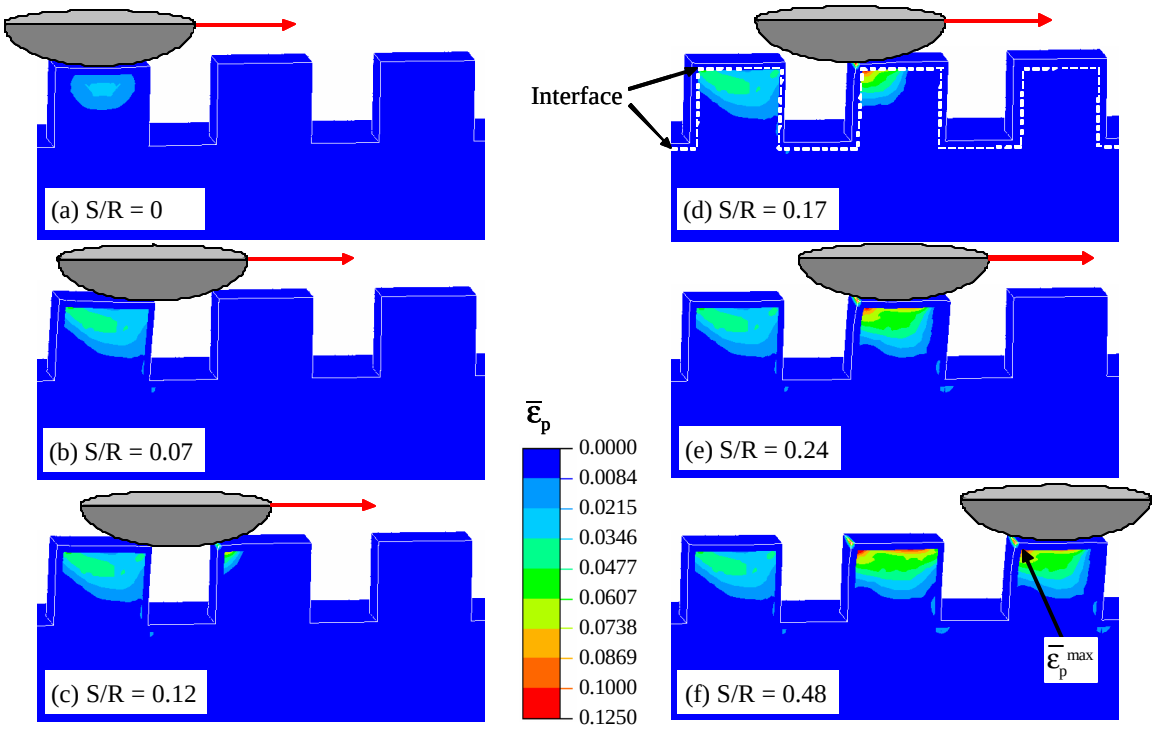

Fig. 3.5 Contours of equivalent plastic strain in the layered medium for m = 0.5, d/R = 0.005, and S/R equal to (a) 0, (b) 0.07, (c) 0.12, (d) 0.17, (e) 0.24, and (f) 0.48. (The arrow indicates the direction of the sliding rigid sphere.)

The dependence of the s_M^{max} in the first layer and $\bar{e}_p^{max}$ in the second layer on the distance and cycles of sliding is shown in Fig. 3.6 for m = 0.1 and d/R = 0.005. The close agreement between the results of the second and third sliding cycle suggests that, for the simulated friction coefficient and indentation depth, a steady-state stress/strain field is reached after only two sliding cycles. The change of s_M^{max} after the first sliding cycle (Fig. 3.6(a)) is a consequence of the residual stress due to permanent distortion of the pads encountered during the first sliding cycle. The peak value of $\bar{e}_p^{max}$ is reached during the first sliding cycle and does not change with additional sliding cycles (Fig. 3.6(b)).

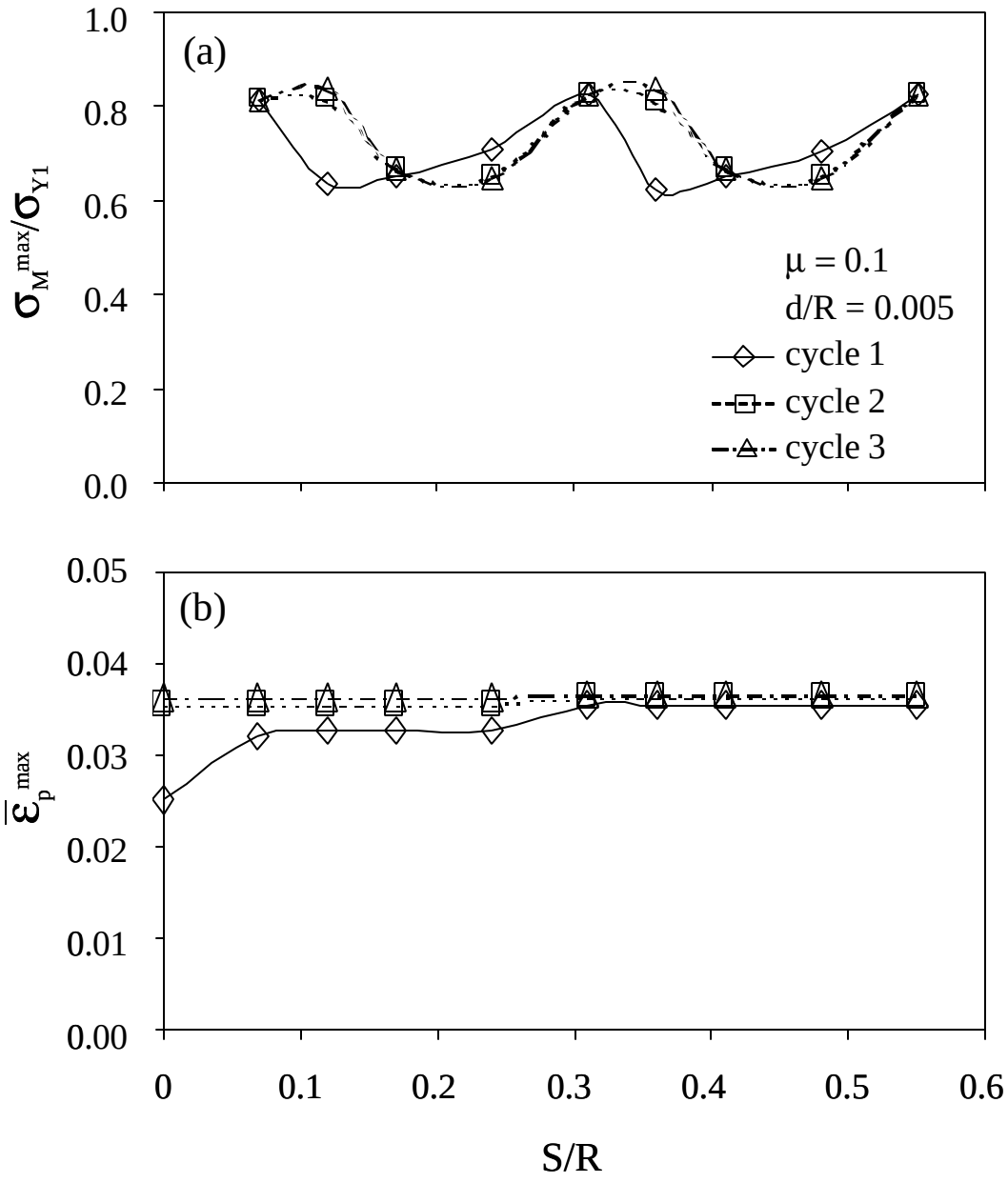

Fig. 3.6 (a) Maximum von Mises equivalent stress in the first (hard) layer and (b) maximum equivalent plastic strain in the second (soft) layer versus sliding distance for three sequential sliding cycles, m = 0.1, and d/R = 0.005.

The effect of the sharpness of the rigid spherical indenter on the normalized $s_M^{\max}$ in the first layer and $\bar{e}_p^{\max}$ in the second layer can be analyzed by comparing the results for d/R = 0.005 and 0.01 shown in Fig. 3.7. The sliding distance S is normalized by the pad spatial periodicity, $b + l$. As mentioned in the discussion of Fig. 3.6(a), the periodic fluctuation of $s_M^{\max}$ with sliding distance (Fig. 3.7(a)) is due to the pattern geometry. Significantly larger values of $s_M^{\max}$ in the first (hard) layer (Fig. 3.7(a)) and $\bar{e}_p^{\max}$ in the second (soft) layer (Fig. 3.7(b)) are produced with the relatively sharp sphere (d/R = 0.01). The Mises yield condition in the hard layer ($s_M^{\max}/s_{Y1}$ = 1.0) is satisfied only in the case of the sharp sphere. A steady-state $\bar{e}_p^{\max}$ is obtained in the soft layer after the sphere slides a distance of about two times the pad spatial periodicity, for both d/R = 0.005 and 0.01. The results shown in Fig. 3.7 illustrate the dependence of plasticity in hard overcoats on the indenter sharpness. Thus, small plastic zones may be produced even in ultrathin surface layers under relatively low contact loads, depending on the range of small wavelengths comprising the surface profile.

3.3.2 Thermomechanical Contact Analysis

Finite element results from a fully-coupled thermomechanical contact analysis of an elastic-perfectly plastic sphere (with thermomechanical properties identical to those of the fist layer) sliding over the patterned medium are presented in Figs. 3.8-3.10 to illustrate the effect of frictional heating on the surface temperature rise and plastic flow in the soft layer. Temperature and plastic strain results are interpreted in terms of sliding distance and Peclet number. To examine the effect of Peclet number on the temperature

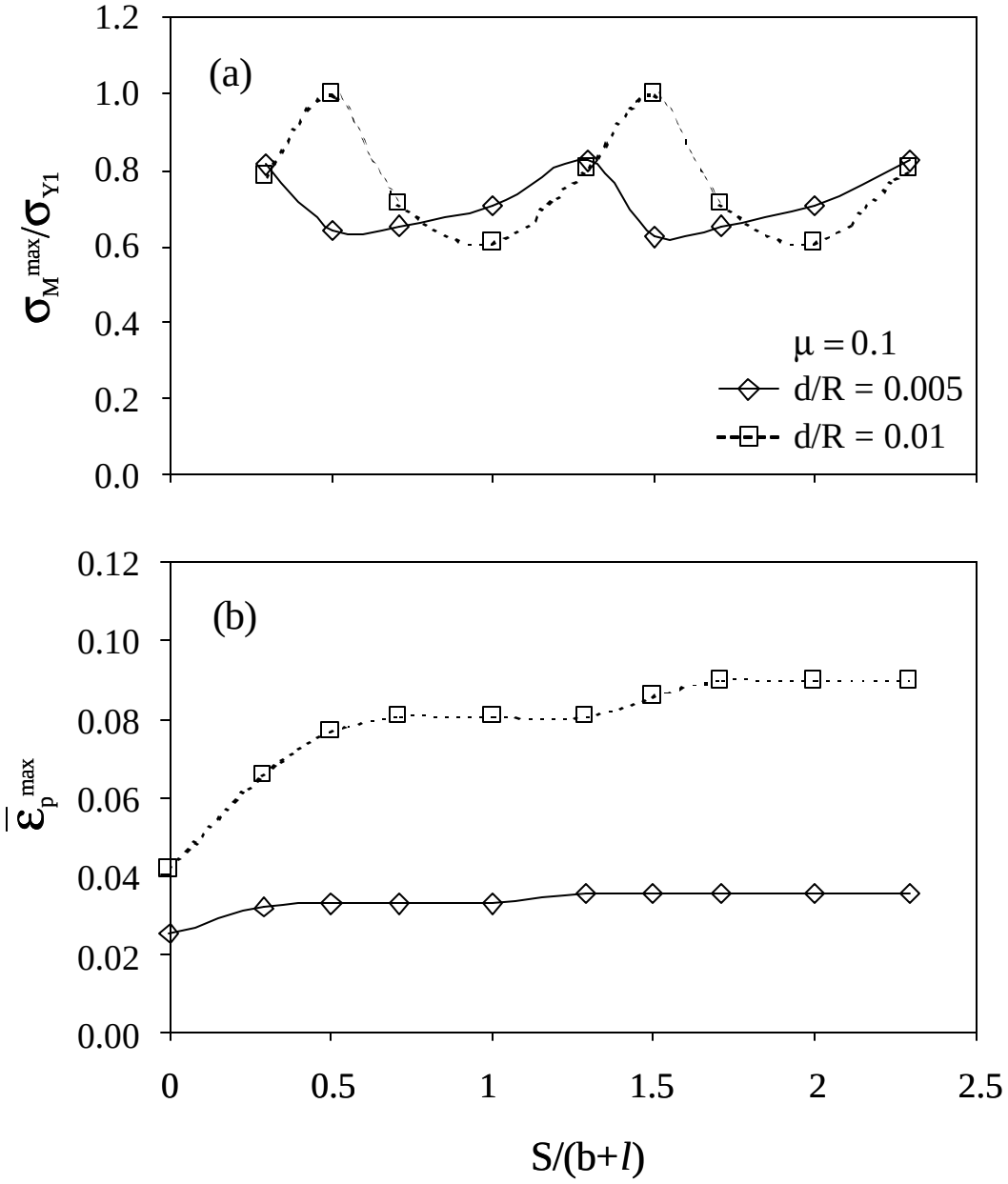

Fig. 3.7 (a) Maximum von Mises equivalent stress in the first (hard) layer and (b) maximum equivalent plastic strain in the second (soft) layer versus sliding distance for m = 0.1 and d/R = 0.005 and 0.01.

field and deformation behavior of the layered medium, simulation results are presented for m = 0.5 and Pe = 0.09 and 0.9.

Figure 3.8 shows the evolution of the surface temperature distribution on three neighboring pads at the plane of symmetry (y = 0) for Pe = 0.09 and d/R = 0.01. The results are presented as a temperature increase from the room temperature, ΔT, normalized by $2\bar{q}a/pku$, where $\bar{q}$ is the average heat flux rate at the contact region (i.e., total heat flux divided by the contact area, πr^2), and k is the thermal conductivity of the sphere, while the x coordinate is normalized by the contact radius, r. As expected, the

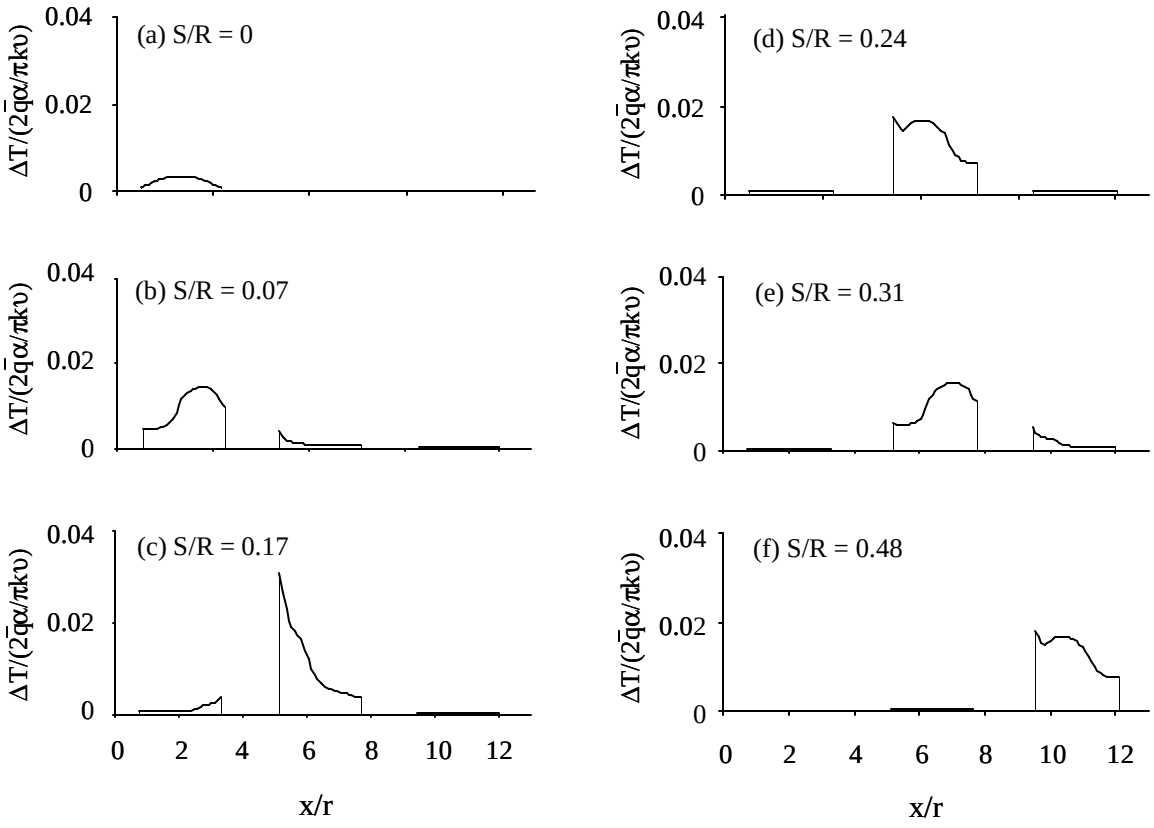

Fig. 3.8 Surface temperature rise at individual neighboring pads at the plane of symmetry (y = 0) for m = 0.5, d/R = 0.01, Pe = 0.09, and S/R equal to (a) 0, (b) 0.07, (c) 0.17, (d) 0.24, (e) 0.31, and (f) 0.48.

temperature distribution due to normal contact (indentation) of a single pad is symmetric and its effect on neighboring pads is negligible (Fig. 3.8(a)). The small temperature rise during indentation is due to the very small slip at the contact interface. When the sphere slides over the edge of the left pad (Fig. 3.8(b)), the maximum temperature increases significantly and shifts toward the trailing edge of the contact region (Fig. 3.8(b)), demonstrating a pronounced effect of frictional heating during sliding. The maximum temperature rise at the trailing edge produces a maximum tensile thermal stress slightly below this contact edge, which is considered to be responsible for thermal cracking in the wake of sliding microcontacts. In addition, a noticeable temperature rise occurs at the front contact edge as soon as the sphere establishes contact with the middle pad. This temperature rise intensifies noticeably when the sphere slides over the left corner of the middle pad (Fig. 3.8(c)), evidently due to the high-pressure peak (stress concentration effect) at the sharp corner of the pad edge. A similar temperature evolution is observed as the sphere slides over the middle and right pads (Figs. 3.8(d)-3.8(f)). The close similarity of the temperature distributions produced when the sphere is over the center of the middle and right pads (Figs. 3.8(d) and 3.8(f)) suggests that frictional heating at each pad is not affected by the heat flux at neighboring pads. A comparison of the results shown in Fig. 3.8 with those of a smooth layered medium (Ye and Komvopoulos, 2003) shows that in addition to the discontinuous surface temperature distribution, less heat accumulation is encountered in the case of the patterned layered medium.

Figures 3.9(a) and 3.9(b) show the normalized maximum temperature, $T_{\max}$, in the first and second layers, respectively, as functions of normalized sliding distance and

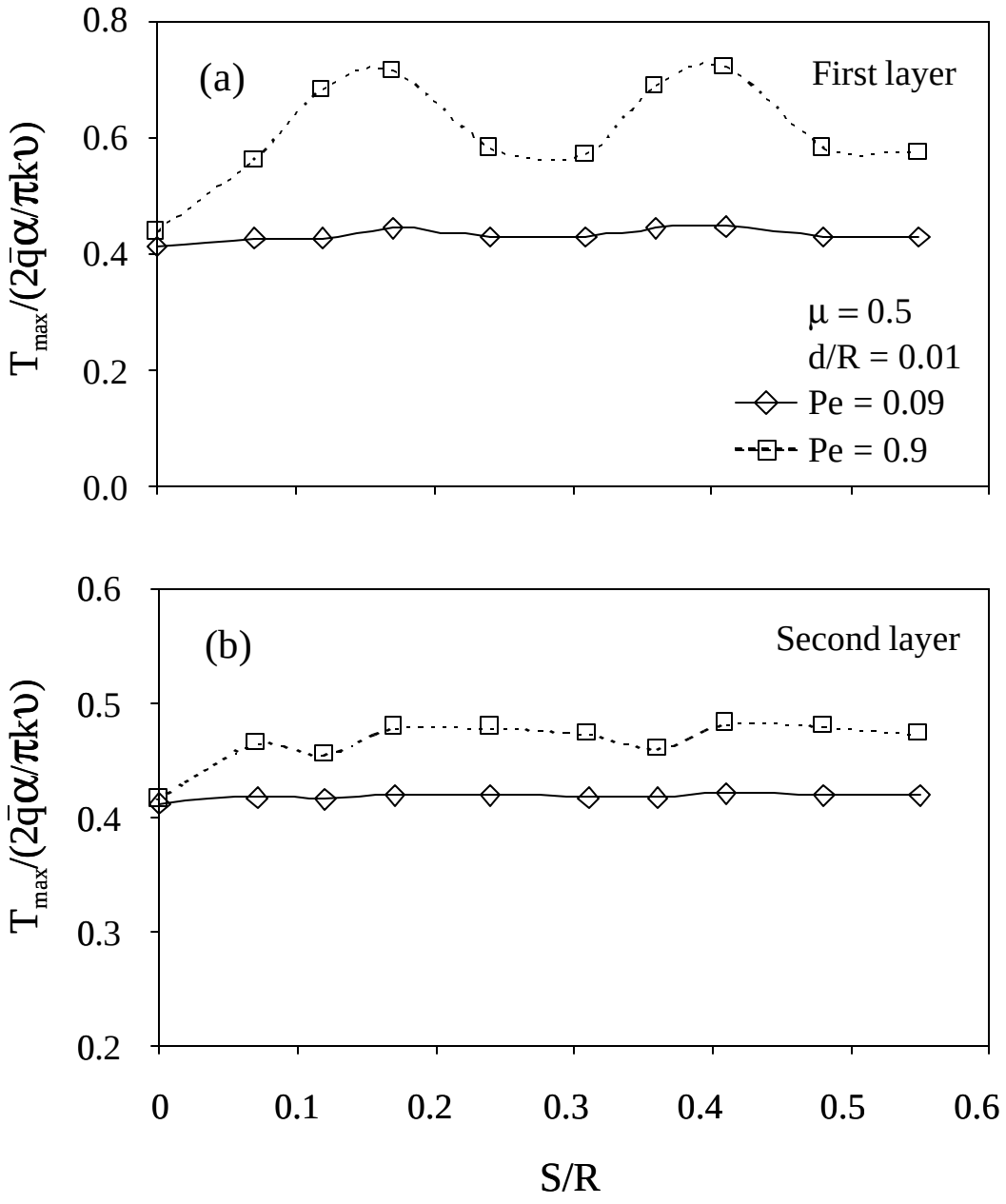

Fig. 3.9 Maximum temperature in (a) first (hard) layer and (b) second (soft) layer versus sliding distance and Peclet number for m = 0.5 and d/R = 0.01.

Peclet number. The maximum temperature in the first layer occurs at the surface and in the second layer at the interface with the first layer. The periodic fluctuation of T_{max} with sliding distance observed only for Pe = 0.9 suggests that the pattern effect on T_{max} in each layer is pronounced only for the relatively high Peclet number. The marked increase of T_{max} in both layers obtained for Pe = 0.9, especially at the surface of the first layer (Fig. 3.9(a)), demonstrates that the temperature field in the layered medium is strongly dependent on the Peclet number. The similar peak values of T_{max} in Fig. 3.9(a) provide additional evidence that interaction of temperature fields of neighboring pads is negligible. Furthermore, comparison of the results shown in Figs. 3.9(a) and 3.9(b) for Pe = 0.9 shows that T_{max} in the first layer is much higher than that in the second layer. In the sliding simulations for m = 0.5 and Pe = 0.9, the highest temperature change in the first and second layers was found to be equal to ~220 ^{o}C and ~50 ^{o}C, respectively. These T_{max} values are close to those obtained for a smooth layered medium (Ye and Komvopoulos, 2003), except at the pad corners where T_{max} is about two times higher due to the pressure peaks occurring at these locations. Such high surface temperatures may induce thermal cracking and degrade the mechanical properties of the surface layer.

Figure 3.10 shows the variation of the maximum equivalent plastic strain in the second (soft) layer with normalized sliding distance and Peclet number for m = 0.5 and d/R = 0.01. A rapid increase of $\bar{e}_p^{max}$ at the beginning of sliding and a steady state at a sliding distance S/R = 0.17 is shown for both Peclet numbers. However, a longer sliding distance for $\bar{e}_p^{max}$ to reach a steady state was found for the smooth layered medium subjected to thermomechanical loading (Ye and Komvopoulos, 2003). While the effect of the Peclet number on $\bar{e}_p^{max}$ is negligible during the initial stage of sliding, larger values of

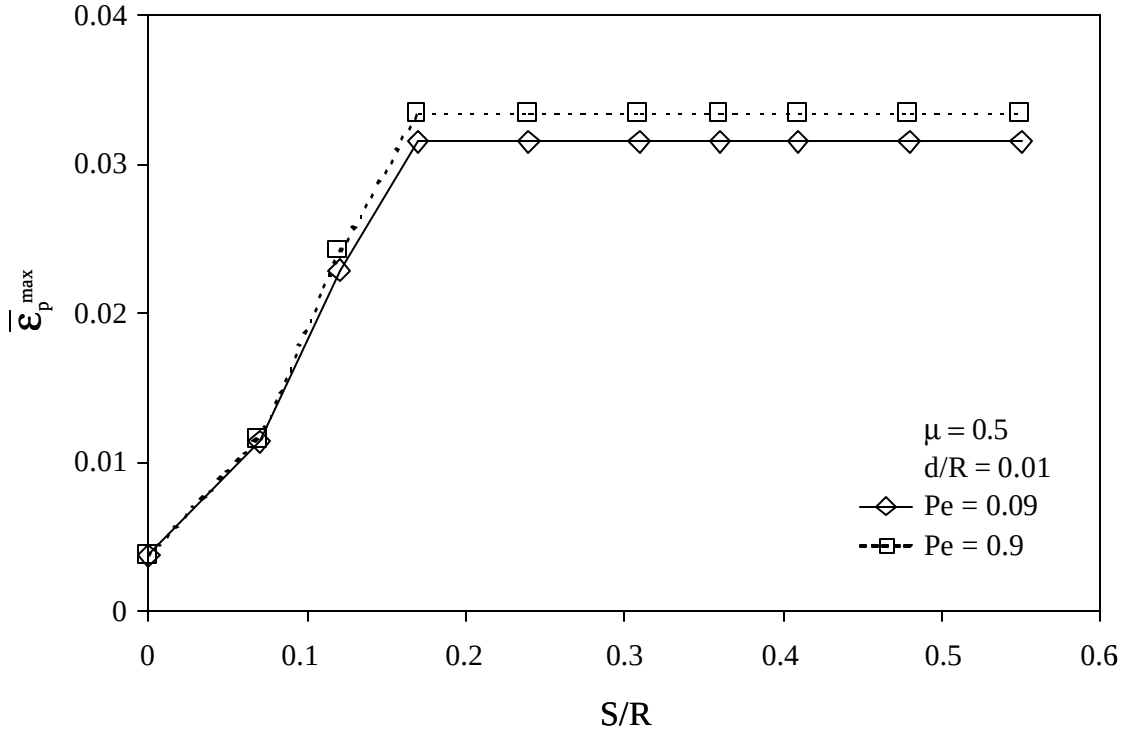

Fig. 3.10 Maximum equivalent plastic strain in the second (soft) layer versus sliding distance and Peclet number for $m = 0.5$ and $d/R = 0.01$.

$\bar{e}_p^{max}$ (~5.7%) were produced with the higher Peclet number at distances $S/R > 0.17$. This is attributed to the fact that the surface temperature rise and difference between maximum surface temperatures for Pe = 0.09 and 0.9 increase with sliding distance until $S/R > 0.17$ (Fig. 3.9(a)). The combined effects of thermal expansion coefficient mismatch and temperature gradients at the interface (which intensify with increasing Peclet number) are responsible for the produced thermal stress that enhances plasticity in the second layer. Thus, a higher Peclet number results in higher temperature rises at the surface of the hard layer and larger plastic strains in the soft underlayer of the medium.

3.4 Conclusions

An elastic-plastic finite element analysis of normal contact (indentation) and sliding of a spherical indenter on a layered medium with a patterned surface was performed in order to study the effects of coefficient of friction, sphere radius, and repetitive sliding on the contact stress and deformation fields. In addition, a fully coupled thermomechanical finite element analysis was carried out to obtain solutions for the surface temperature distribution and to elucidate the effect of Peclet number on the maximum temperature rise and subsurface plasticity. Based on the presented results and discussion, the following main conclusions can be drawn.

(1) The maximum contact pressure shifts from the center toward the edge of the contact region at a critical indentation depth (d/R > 0.005). Pressure spikes occur at the contact edges in the case of relatively deep indentations (d/R > 0.01). For shallow indentations (d/R < 0.01), both the maximum von Mises equivalent stress in the first layer and the contact area increase monotonically with indentation depth. Yielding in the first (hard) layer adjacent to the surface commences when d/R > 0.008, and full contact of a pad with the sphere occurs at d/R > 0.01 when the sphere center is over the center of the pad surface.

(2) The contact pressure and subsurface stresses and plastic strains exhibit periodic fluctuations due to the pattern geometry. The similarity of the stress/strain results at neighboring pads suggests that interaction effects are negligible for the modeled pattern geometry. High-friction sliding (i.e., m = 0.5) increases significantly the maximum equivalent plastic strain in the second (soft) layer during the beginning of sliding, leading to a steady state after a sliding distance about two times the pad

spatial periodicity. The reduced plasticity in the soft layer of patterned layered media compared to that of smooth layered media demonstrates the beneficial effect of surface patterning in sliding contact.

(3) The steady-state stress/strain fields produced after the first sliding cycle suggest that deformation in the layered medium is insensitive to subsequent similar sliding cycles. In low-friction sliding, a relatively sharp spherical indenter promotes formation of small plastic zones in the first hard layer at the sharp corners of the pad edges.

(4) Normal contact (indentation) of the sphere with a pad yields a symmetric temperature distribution and negligible temperature rise at neighboring pads. Sliding intensifies the temperature field, causing the maximum temperature to shift from the center toward the trailing edge of the contact region. The resulting temperature gradients lead to the development of a high thermal tensile stress slightly below the trailing edge of the contact region, which is considered to be responsible for thermal cracking in the wake of sliding microcontacts.

(5) The periodic variation of the maximum temperature rise in both the first and the second layer with sliding distance is due to the pattern geometry. The temperature field in the layered medium is a strong function of the Peclet number. The similar peak values of the maximum temperature in each layer illustrate that thermal interaction between neighboring pads is negligible. Increasing the Peclet number enhances the temperature rise at the surface and the development of thermal stresses in the first (hard) layer. Moreover, it produces larger plastic strains in the second (soft) layer and in small regions of the first layer, in the vicinity of the sharp pad edges.

CHAPTER 4

CONTACT STRESS ANALYSIS OF LAYERED ELASTIC SOLID IN CONTACT WITH A ROUGH SURFACE

4.1 Introduction

Surface layers (overcoats) are often used to protect components subjected to contact stresses and to enhance the tribological performance and functionality of interacting surfaces. Applications include cutting tools, piston rings, bearings, and magnetic data storage. A detailed knowledge of the contact stress state generated when two coated surfaces come into contact is critical to the analysis of friction and wear mechanisms.

The problem of a layered elastic solid subjected to indentation and sliding contact by a single asperity has been analyzed by many researchers. The elasticity theory to obtain the stress field in a layered half-space under a prescribed axisymmetric contact pressure profile was initially developed by Burmister (1945), and was later extended by Chen (1971) to a non-axisymmetric contact pressure profile. Chen and Engel (1972) analyzed a layered half-space under normal loading using a least squares approach and obtained the contact pressure profile for indenters of different geometries. Using Fourier transforms of the Airy stress function, Gupta et al. (1973) developed an analytical procedure for computing stress distributions in the layer and the substrate of layered elastic solids subjected to arbitrary normal and shear contact stresses. Gupta and Walowit (1974) investigated the plane-strain normal contact problem of a layered half-space using an integral equation approach and studied the effects of relative stiffness of the indenter,

layer, and half-space on the contact pressure distribution under a cylindrical indenter. King and O'Sullivan (1987) investigated the plane-strain problem of a rigid cylinder sliding over an elastic layered half-space in both in-plane and anti-plane (along the cylinder axis) directions and obtained the contact pressure profile and stress fields in both the layer and the half-space. This work was extended by O'Sullivan and King (1988) to three-dimensional contact stress analysis of a spherical indenter sliding over a layered elastic medium.

The aforementioned analytical and numerical studies assumed that the contacting surfaces are ideally smooth. However, real surfaces are rough in the microscopic scale and contact is generally restricted to a number of microscopic contact regions located near the peaks of the rough surface. Theoretical treatment of contacting rough surfaces is difficult due to the randomness of the surface topography. One of the earliest statistical models incorporating roughness effects is that of Greenwood and Williamson (1966), who analyzed elastic contact of two rough surfaces by considering a flat surface in normal contact with an equivalent rough surface comprising spherical asperities of constant radius, equal to the average radius of curvature of the original asperities. Bush et al. (1975, 1979), Gibson (1982), and McCool (1986) developed an elastic contact model that treated asperities as elliptical paraboloids with randomly oriented elliptical contact areas. Although these statistical models produced simple relationships between the total load, thermal and electrical contact conductance, and total contact area, they do not account for the essentially multiscale nature of the surface roughness (Greenwood, 1992) and ignore the interaction between neighboring asperity contacts (Berthe and Vergne, 1987; Goryacheva and Dobychin, 1991; Komvopoulos and Choi, 1992). Because of the

multiscale roughness of surfaces, surface parameters depend strongly on the sample size, instrument resolution, and experimental filter used to acquire the topography data. For this reason, fractal geometry (Majumdar and Tien, 1990; Borodich and Onishchenko, 1999) has been used to characterize engineering surfaces so that to overcome the limitation of scale-dependent statistical surface parameters. Many contact theories using a fractal description for the surface topography have been developed to provide the real contact area, contact load, and interfacial temperature rise due to frictional heating for both homogenous half-space (Majumdar and Bhushan, 1991; Bhushan and Majumdar, 1992; Wang and Komvopoulos, 1994a, 1994b; Yan and Komvopoulos, 1998; Ciavarella et al. 2000) as well as layered media (Komvopoulos and Ye, 2001). The focus in these studies has been on global parameters (i.e., total contact load, real contact area, etc.) based on the assumption that the number and size of truncated asperities follow a power-law relationship (Mandelbrot, 1983). However, the local stress field (asperity length scale) is essential to the prediction of yielding and potential surface crack initiation.

The finite element method is the most commonly used technique to obtain solutions for the stresses and strains due to various contact loads. Komvopoulos and Ye (2002) introduced an elastic-plastic finite element model that accounts for the actual topographies of magnetic recording head and rigid disk media, characterized by fractal geometry. However, the necessity for a large number of finite elements in the case of rough surface contact makes the finite element approach impractical.

Therefore, the main objectives of this study are to introduce a comprehensive contact stress analysis of a layered elastic solid in contact with a rough surface characterized by fractal geometry. To accomplish this objective, a finite element model

was developed in order to obtain the mean contact pressure and the ratio of truncated-to-real contact area for a single cylindrical asperity indenting an elastic layered medium in terms of the asperity radius, half-contact width, layer thickness, and mechanical properties of the layered medium. The obtained relationships were incorporated into a numerical algorithm to determine the contact pressure profiles and stress field using the distribution of real asperity contacts.

4.2 Surface Characterization

Surface topography parameters derived from traditional statistical theories exhibit dependencies on the sample length and the instrument resolution limit. Characterization of the surface topography by fractal geometry (Mandelbrot, 1983) provides a means for overcoming such shortcomings. The surface topography can be represented by a Weierstrass-Mandelbrot function (Berry and Lewis, 1980) that exhibits continuity, non-differentiability, and self-affinity over a wide range of length scales and can be written as (Wang and Komvopoulos, 1994a)

$$z(x) = L\left(\frac{G}{L}\right)^{(D-1)} \sum_{n=0}^{n_{\max}} \frac{\cos(2\pi\gamma^n x / L)}{\gamma^{(2-D)n}}, \tag{4.1}$$

where L is the fractal sample length in the x direction, G is the fractal roughness parameter that is independent of frequency, D ($1 < D < 2$) is the fractal dimension that determines the contribution of high and low frequency components in the surface function (i.e., high D values correspond to smooth surfaces), g ($\gamma > 1$) is a scaling parameter (typically, $g = 1.5$ (Komvopoulos and Yan, 1997)), and n is a frequency index with $n_{\max} = \text{int}[\log(L / L_s) / \log\gamma]$ representing the upper limit of n, where int[…] denotes the integer part of the number in the brackets and L_s is the cut-off length. The scale-

independent fractal parameters G and D can be determined experimentally from a log-log plot of the structure function of the surface profile $z(x)$ versus wavelength (Komvopoulos, 2000).

4.3 Contact Analysis

The two-dimensional plane strain problem of a rigid rough (fractal) surface in sliding contact with an elastic layered medium is shown schematically in Fig. 4.1. Coulomb friction (with friction coefficient m) is assumed between the rough surface and the surface of the layered medium. Therefore, the layered medium is subjected to distributed normal and tangential tractions producing a total normal load P and a total tangential force $F = mP$.

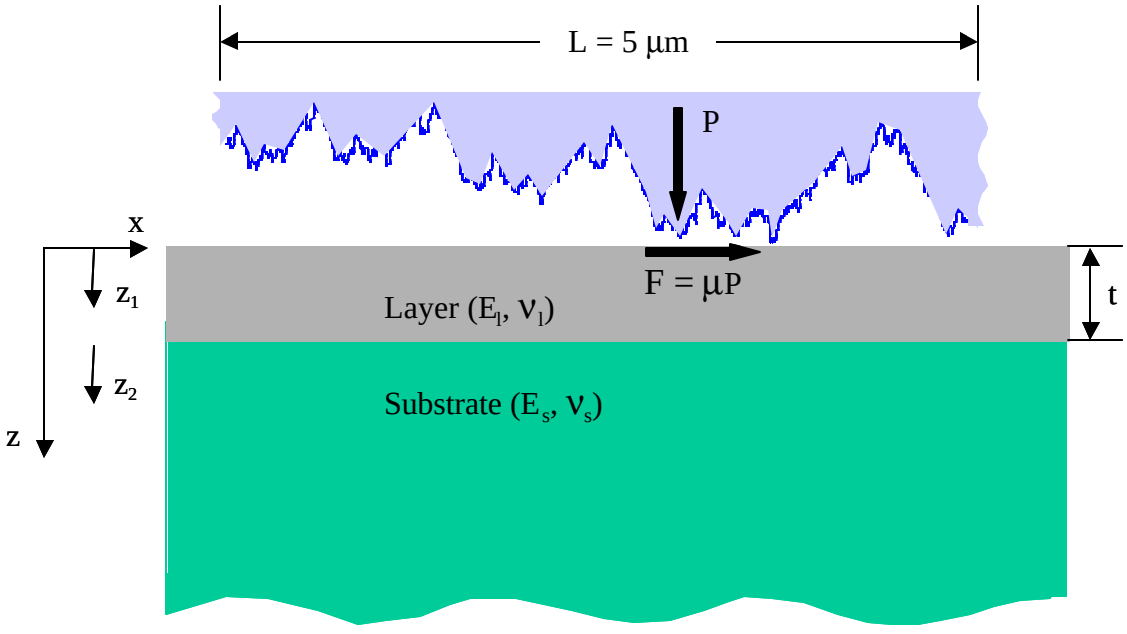

Fig. 4.1 Schematic representation of an elastic layered medium in contact with a rigid rough surface.

4.3.1 Constitutive Relationships

In order to accurately determine the contact forces at asperity contacts between the layered medium and the rough surface, it is necessary to obtain a stress-strain constitutive relationship and an expression for the ratio of truncated-to-real contact area for the layered elastic medium. To accomplish this objective, a finite element model of a rigid cylindrical asperity in normal contact with a layered elastic medium was developed. The mesh consists of 6,417, eight-node, isoparametric, quadrilateral elements comprising a total of 19,232 nodes. The horizontal and vertical dimensions of the mesh are equal to $2.4R$ and $3.1R$, respectively, where R is the radius of the rigid asperity. A 3×3 integration scheme was used for the eight-node elements. The multi-purpose code ABAQUS was used to perform the finite element simulations. The substrate material has an elastic modulus of 114 GPa and Poisson ratio of 0.3. In order to examine the layer stiffness effect on the mean contact pressure and the real contact area, seven different elastic modulus values were chosen for the layer material (i.e., E_l/E_s = 8, 4, 2, 1, 0.5, 0.25, 0.125, where E_l and E_s are the elastic moduli for the layer and the substrate, respectively). Figure 4.2 shows the normalized mean contact pressure, p_m/E_s, versus the representative strain, $E_e^* r/E_s R$, where r is the half-contact width and E_e^* is the equivalent (effective) elastic modulus of the layered medium given by (King, 1987)

$$E_e^* = [(1-e^{-\alpha t/r\sqrt{\pi}})\frac{1-\nu_l^2}{E_l} + e^{-\alpha t/r\sqrt{\pi}}\frac{1-\nu_s^2}{E_s} + \frac{1-\nu_i^2}{E_i}]^{-1}, \tag{4.2}$$

where a is a geometric factor that depends on the indenter shape and can be determined numerically, t is the layer thickness, n is the Poisson ratio, and subscript i denotes the

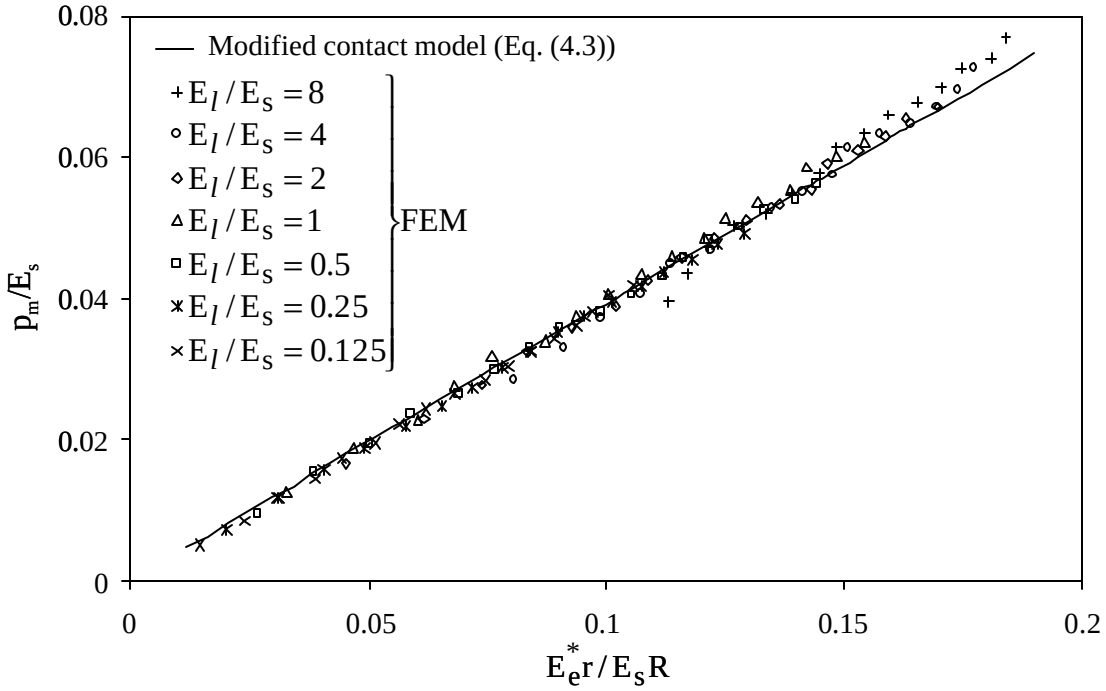

Fig. 4.2 Normalized mean contact pressure versus representative strain for an elastic layered medium with different elastic modulus ratio between the layer and the substrate.

indenter material. Based on the least-square fit to the data shown in Fig. 4.2, the mean contact pressure, p_m, can be related to the representative strain by

$$\frac{p_m}{E_s} = \frac{\pi}{8}\left(\frac{E_e^* r}{E_s R}\right). \tag{4.3}$$

Figure 4.3 shows the truncated-to-real contact area ratio, $a¢/a$, as a function of the elastic modulus ratio between the layer and the substrate, E_l/E_s, and $r¢/R$, where $r¢$ is the truncated half-contact width. When the layer is stiffer than the substrate ($E_l/E_s > 1$), $a¢/a$ depends on $r¢/R$, especially at shallow indention depths (i.e., small $r¢/R$). However, when the layer is more compliant than the substrate ($E_l/E_s < 1$), the effect of $r¢/R$ on $a¢/a$ is negligible. Least-square curve fitting of the results shown in Fig. 4.3 yields

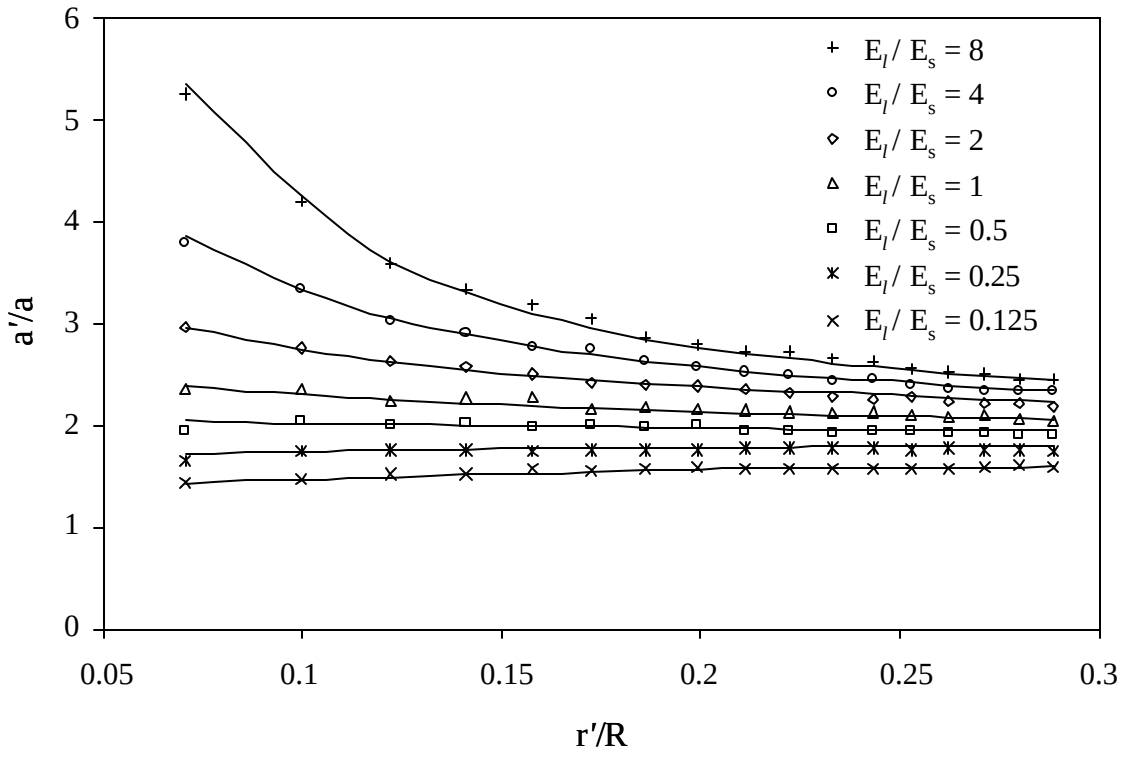

Fig. 4.3 Truncated-to-real contact area ratio versus truncated half-contact width-to-asperity radius ratio for an elastic layered medium with different elastic modulus ratio between the layer and the substrate materials. (Symbols represent finite element results and the solid lines solutions obtained from Eq. (4.4).)

$$\frac{a'}{a} = \begin{cases} a_1 \left(\frac{E_e^*}{E_s}\right)^{\beta_1} \left(\frac{r'}{R}\right)^{\gamma_1}, & \frac{E_l}{E_s} > 1 \\ a_2 \left(\frac{E_e^*}{E_s}\right)^{\beta_2} \left(\frac{r'}{R}\right)^{\gamma_2}, & \frac{E_l}{E_s} \le 1 \end{cases} \tag{4.4}$$

where a_1 = 1.8237, b_1 = 0.4353, h_1 = −0.0766, a_2 = 1.7314, b_2 = 0.3939, and h_2 = −0.1072. The results obtained from Eq. (4.4) are in good agreement with finite element results obtained for different values of E_l/E_s. The correlation factor for $E_l/E_s > 1$ and $E_l/E_s < 1$ is equal to 0.998 and 0.992, respectively.

4.3.2 Stress Analysis

As the rough surface approaches the layered medium, asperity contacts are established over the simulated apparent contact area. The basic approach for determining the total deformation force at the contact interface involves the calculation of the forces produced at individual asperity contacts and the summation of asperity contact forces over the entire surface based on the truncation of the real rough surface. For a truncated asperity of half width r', the longest wavelength in the asperity waveform is equal to $2r'$. It is assumed that the asperity contact force is primarily due to deformation of an asperity represented by the base wavelength, with the corresponding frequency index,

$$n_0 = \frac{\ln(L/2r')}{\ln g}, \tag{4.5}$$

and function,

$$z_0(x) = G^{(D-1)}(2r')^{(2-D)}\cos(\frac{px}{r'}). \tag{4.6}$$

The asperity interference, d, is equal to the peak-to-valley amplitude of the cosine function. Hence,

$$d = 2G^{(D-1)}(2r')^{(2-D)}. \tag{4.7}$$

Since the contact interface is modeled by a deformable plane compressed by rigid cylindrical asperities, the radius of a contact spot is given by

$$R = \frac{(r')^2}{2d}, \tag{4.8}$$

which is based on the fact that the asperity radius is typically orders of magnitude greater than the asperity height and the cosine-shaped asperity is approximated by a circular profile. Substituting Eq. (4.7) into Eq. (4.8) yields

$$R = \frac{(a')^D}{16G^{(D-1)}}, \tag{4.9}$$

where $a' = 2r'$ is the truncated area of the contact spot. Substituting Eq. (4.9) into Eq. (4.4) yields a relationship between the truncated area, a¢, and the real contact area, a,

$$a' = \left[\alpha_k \left(\frac{E_e^*}{E_s}\right)^{\beta_k} (8G^{D-1})^{\gamma_k} a \right]^{\frac{1}{1-(1-D)\gamma_k}}, \tag{4.10}$$

where subscript k is equal to 1 for stiff layer ($E_l/E_s > 1$) and 2 for compliant layer ($E_l/E_s < 1$). According to Eq. (4.3), the elastic force at a contact spot is given by

$$\Delta F_{df} = \frac{\pi G^{(D-1)} E_e^* a^2}{(a')^D}. \tag{4.11}$$

Substituting Eq. (4.10) into Eq. (4.11) yields the elastic force at a contact spot,

$$\Delta F_{df} = \pi G^{(D-1)} E_e^* a^{2-D/(1-\gamma_k - D\gamma_k)} \left[\alpha_k \left(\frac{E_e^*}{E_s}\right)^{\beta_k} (8G^{D-1})^{\gamma_k} \right]^{-\frac{D}{1-(1-D)\gamma_k}}. \tag{4.12}$$

Because the equivalent elastic modulus is a function of the real contact width, which is not known *a priori*, an iteration procedure was used to determine the equivalent elastic modulus and the real contact area in order to satisfy Eqs. (4.2) and (4.4). The initial value of the real contact area was assumed to be equal to the truncated area. Using this iteration scheme, the distribution of the real contact area and corresponding equivalent elastic modulus were obtained at each contact spot. Hence, the elastic force at each contact spot was determined from Eq. (4.12). It is assumed that the contact spots at the interface are sufficiently apart from each other such that interactions can be neglected. Consequently, the total contact force can be obtained as

$$F_{df} = \sum_{i=1}^{N} \Delta F_{df}^i, \tag{4.13}$$

where ΔF_{df}^{i} is the deformation force of the ith asperity contact, and N is the number of asperity contacts at the interface.

Contact pressure distributions were obtained based on the assumption that the local contact pressure is proportional to the square root of the local interference. A piecewise-linear distribution of contact pressure was obtained by superposition of overlapping triangular pressure elements (Johnson, 1985). The peak value of the jth triangular pressure element, p_i^j, at the ith asperity microcontact is expressed as

$$p_i^j = \frac{\sqrt{d_i^j}}{\sum_{j=1}^{M_i-1}\sqrt{d_i^j}} \frac{\Delta F_{df}^i}{c}, \tag{4.14}$$

where δ_i^j is the local interference at the jth point, M_i is the total number of grids at ith asperity contact, and c is the grid size. The advantage of the piecewise-linear distribution of the contact pressure is that it produces continuous surface displacements. For fully-developed sliding contact, the contact pressure profile is assumed to be unaffected by the shear traction. This assumption is reasonable for low-friction sliding. The shear traction is $q(x) = mp(x)$, where m is the coefficient of friction at the interface.

The stress field in the layered medium was calculated by superposition of the stress fields generated by triangular distributions of normal and tangential tractions at each contact spot and the stress fields of all the contact spots established at the interface. The approach presented by Gupta el al. (1973) was used to calculate the stresses in the layered medium due to the triangular distributions of normal and tangential tractions. With reference to the coordinate system shown in Fig. 4.4, the stresses and displacements in the layer are functions of x and z_1 and in the substrate are functions of x and z_2. The

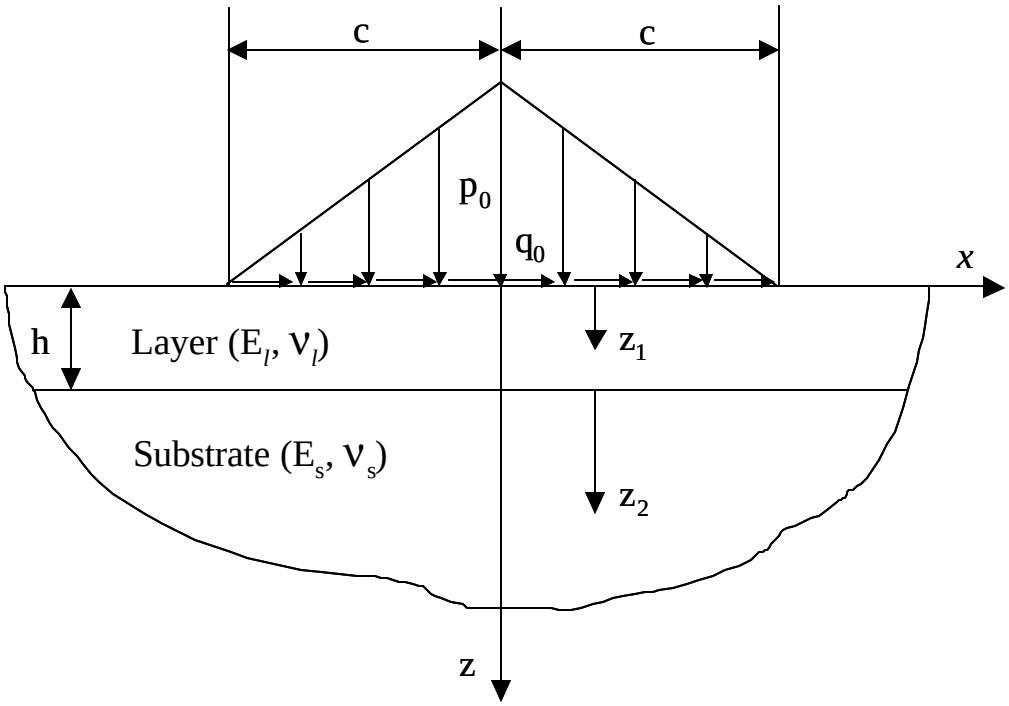

Fig. 4.4 Description of coordinates for a layered medium subjected to triangular distributions of normal and tangential tractions.

stresses are most conveniently expressed in terms of an Airy stress function, F, which must satisfy the biharmonic equation $\nabla^4 F = 0$, and can be differentiated to obtain the stresses according to

$$s_{zz} = \frac{\partial^2 F}{\partial x^2} \qquad s_{xx} = \frac{\partial^2 F}{\partial z^2} \qquad s_{zx} = -\frac{\partial^2 F}{\partial z \partial x}. \tag{4.15}$$

The traction boundary conditions at the layer surface and the interface condition that displacements and tractions must be continuous are expressed as

$$\begin{aligned}
&s_{zz}^{(1)}(x,0) = -p_0(1-|x|/c), \quad |x| \le c \qquad s_{zz}^{(1)}(x,0) = 0, \quad |x| > c \\
&s_{xz}^{(1)}(x,0) = -q_0(1-|x|/c), \quad |x| \le c \qquad s_{xz}^{(1)}(x,0) = 0, \quad |x| > c \\
&s_{xz}^{(1)}(x,h) = s_{xz}^{(2)}(x,0) \qquad u^{(1)}(x,h) = u^{(2)}(x,0) \\
&s_{zz}^{(1)}(x,h) = s_{zz}^{(2)}(x,0) \qquad w^{(1)}(x,h) = w^{(2)}(x,0)
\end{aligned}, \tag{4.16}$$

where superscripts 1 and 2 refer to the layer and the substrate, respectively, and u and w denote displacements in the x and z directions, respectively. The solution is obtained by taking the Fourier transform of F with respect to x using the definition

$$\overline{F} = \int_{-\infty}^{+\infty} F(x,z) e^{iwx} dx . \tag{4.17}$$

For F to satisfy the biharmonic equation and to generate finite stresses at infinity, $\overline{F}$ must be of the form:

$$\begin{aligned} \overline{F}^{(1)} &= (A_1 + B_1 z_1) e^{-|w| z_1} + (C_1 + D_1 z_1) e^{|w| z_1} \\ \overline{F}^{(2)} &= (A_2 + B_2 z_2) e^{-|w| z_2} \end{aligned} , \tag{4.18}$$

where $\overline{F}^{(1)}$ and $\overline{F}^{(2)}$ are solutions of $\overline{F}$ in the layer and the substrate, respectively. The two boundary and four interface conditions provide a set of six coupled equations including the coefficients in Eq. (4.18) and the Fourier transforms of the surface traction distributions, $p(x, z)$ and $q(x, z)$. When $\overline{F}$ is obtained, the stresses can be calculated from Eq. (4.15) by applying an inverse transformation of $\overline{F}$.

Therefore, the stress at a point $A(x, z)$ in the layered medium can be written as

$$s(x,z) = \sum_{i=1}^{N} \sum_{j=1}^{M_i - 1} s\Big|_i^j (x,z) , \tag{4.19}$$

where s denotes stress and $\sigma\Big|_i^j$ represents the stress due to the jth triangular distributions of contact pressure and tangential (friction) tractions at the ith contact spot.

4.4 Results and Discussion

4.4.1 Validation of the Contact Algorithm

To validate the analytical model of the layered elastic medium, numerical results for a homogenous elastic half-space in normal and sliding contact with a rigid cylinder

are contrasted with theoretical results (Johnson, 1985). The half-space has an elastic modulus of 114 GPa and Poisson ratio of 0.3. Figure 4.5(a) shows the normalized contact pressure distribution on the indented homogenous half-space. The x coordinate was normalized by the half-contact width, r_0, and the contact pressure, p, by the maximum contact pressure, p_0. The good agreement between analytical and theoretical results confirms the validity of the model and suggests that the assumption that the local contact pressure is proportional to the square root of the associated interference is reasonable. Figure 4.5(b) shows the effect of the elastic modulus ratio on the pressure profile due to indentation of a layered medium by a rigid cylinder. The maximum contact pressure obtained with the homogenous half-space ($E_l/E_s = 1$), p_0, and corresponding half-contact width, r_0, were used to normalize the pressure and the x coordinate, respectively. As expected, higher contact pressure and smaller contact area were obtained with stiff layers ($E_l/E_s > 1$) and the opposite with compliant layers ($E_l/E_s < 1$). The contact area and pressure are quite different from those of the Hertzian profile, especially when the difference between E_l and E_S is large. The contact pressure profiles shown in Fig. 4.5(b) are also in good agreement with similar results by King and O'Sulllivan (1987).

The normalized subsurface stresses, s_{xx}, s_{zz}, and t_1 (principal shear stress), along the axis of symmetry of the homogenous half-space due to indentation ($m = 0$) and normalized surface stresses, s_{xx}, s_{zz}, and t_{xz} due to sliding ($m = 0.5$) of a rigid cylinder are shown in Figs 4.6(a) and 4.6(b), respectively. The symbols represent numerical results and the curves theoretical solutions (Johnson, 1985). The good agreement between numerical and theoretical stress results demonstrates the accuracy of the algorithm and

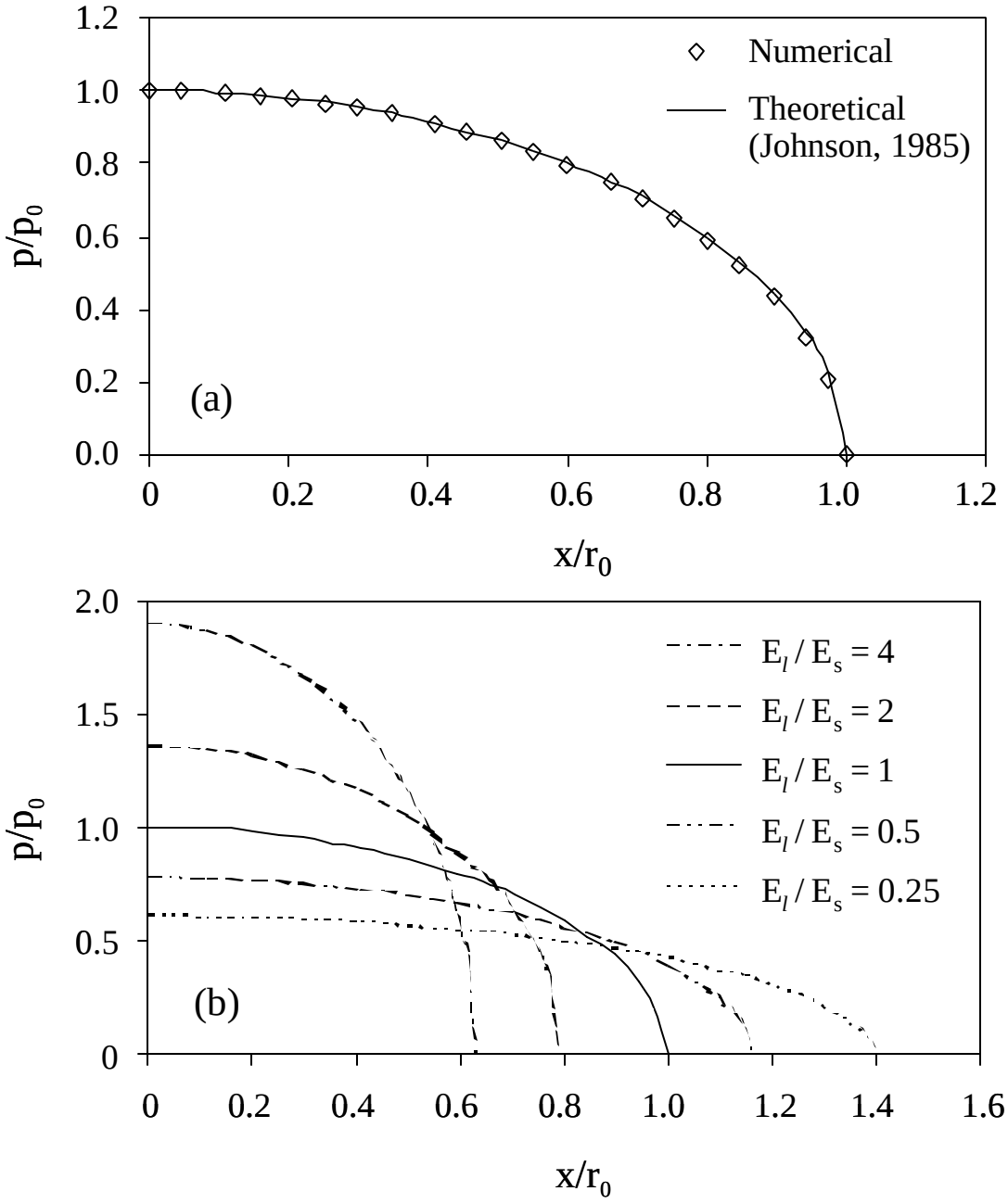

Fig. 4.5 Normalized contact pressure distributions for (a) homogenous and (b) layered media with different elastic modulus ratios of the layer and the substrate materials indented by a rigid cylinder.

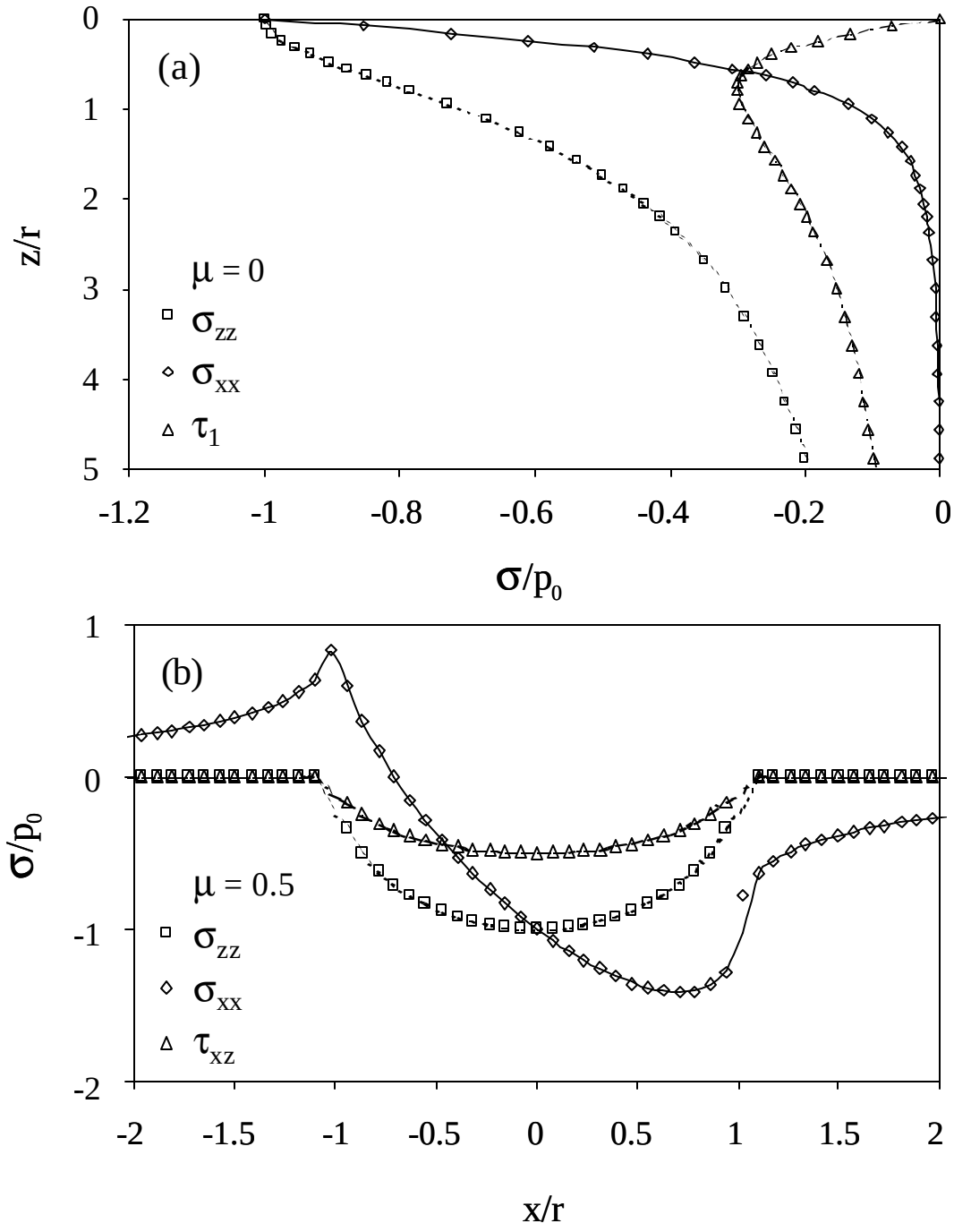

Fig. 4.6 (a) Normalized subsurface stresses along the axis of symmetry and (b) normalized surface stresses distributions of a layered medium in contact with a rigid cylinder. (Symbols represent numerical results and lines theoretical solutions (Johnson, 1985).)

the efficiency of the piecewise-linear contact pressure distributions. Figure 4.6(b) reveals the occurrence of a maximum surface tensile stress at the trailing edge of the contact region, which is accurately predicted by the algorithm. The results shown in Figs. 4.5 and 4.6 verify the appropriateness of the present analysis for obtaining solutions for the surface and subsurface stress due to normal and tangential surface tractions.

4.4.2 Contact Load and Contact Area

The total contact load and contact area of a rigid rough surface in contact with a layered elastic half-space are presented first in order to elucidate the significance of material properties, layer thickness, and surface topography on the global parameters of this contact system. The effects of the coefficient of friction, layer thickness, and material properties on the pressure profile, surface stress, interface stress, von Mises stress, and maximum principal stress are discussed next. The substrate has an elastic modulus of 114 GPa and Poisson ratio of 0.3. In all simulations, the sample length L = 5 μm and G = 9.46×10^{-4} nm.

The significance of the fractal dimension D on the contact load and real contact area can be interpreted in light of the results shown in Fig. 4.7 for E_l/E_s = 2 and t = 5 nm. Both the total contact load and the real contact area increase with the maximum surface interference. Figure 4.7(a) shows that increasing the fractal dimension D increases the contact load at larger surface interferences while the opposite is true at smaller surface interferences. This is because only one or two asperity contacts are established at smaller interferences and the rough surface with a smaller D value yields sharper asperities in contact, which generate a larger contact load. With the increase of the surface

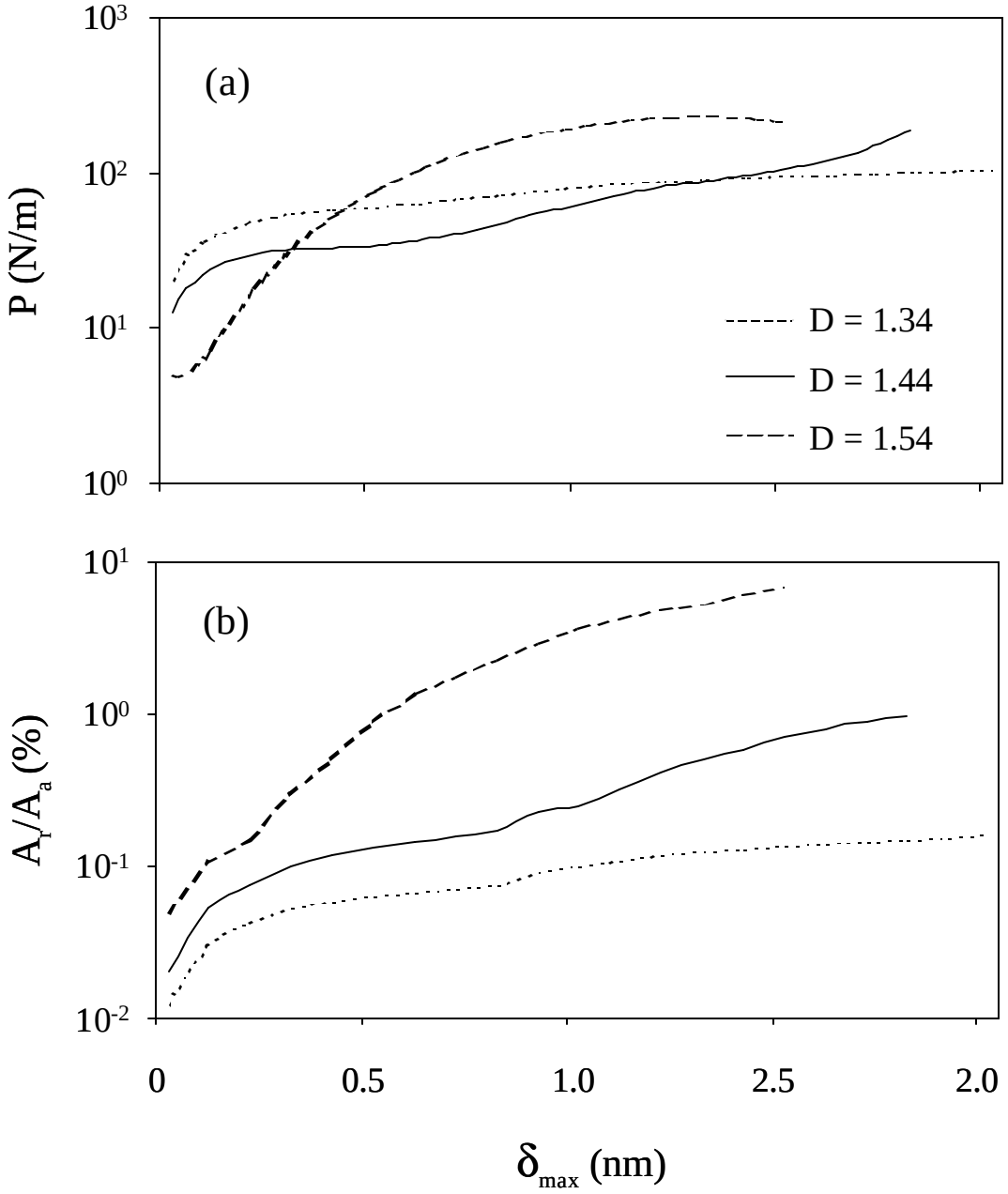

Fig. 4.7 Effect of fractal dimension on (a) contact load and (b) real-to-apparent contact area ratio versus maximum surface interference for an elastic layered medium (E_l/E_s = 2 and t = 5 nm) indented by a rough surface ($G = 9.46 \times 10^{-4}$ nm).

interference, the rough surface with the higher D value produces more asperity contacts, thus resulting in a higher contact load with increasing total real contact area. Figure 4.7(b) shows that, for fixed fractal roughness and maximum surface interference, increasing the fractal dimension increases the real contact area significantly. This is due to the fact that higher D values are associated with smoother surface profiles.

Figures 4.8(a) and 4.8(b) show the variations of the total contact load, P, and real-to-apparent contact area ratio, A_r/A_a, with the maximum surface interference distance, $d_{\max}$, and the elastic modulus ratio, E_l/E_s, for D = 1.44 and t = 5 nm. As expected, both the total contact load and the real contact area increase with the increase of the maximum surface interference. For fixed $d_{\max}$, the total load increases and the contact area decreases with the increase of E_l/E_s.

To illustrate the effect of the layer thickness on the contact load and real contact area, results for a layered medium with layer thickness t = 5, 10, 20, and 100 nm are contrasted in Fig. 4.9 for E_l/E_s = 4 and D = 1.44. It can be seen that the effect of the layer thickness is negligible at small surface interfaces (or light contact loads). For stiff layer (E_l/E_s >1) and large surface interference, the contact load increases while the contact area decreases with the increase of the film thickness. This is because the effect of the stiff layer on the contact load and contact area is stronger than that of the substrate at a larger surface interference and greater film thickness. For the specific case of D = 1.44, G = 9.46×10^{-4} nm, and E_l/E_s = 4, there is no difference between the media with t = 20 and 100 nm when $d_{\max}$ < 1.5 nm.

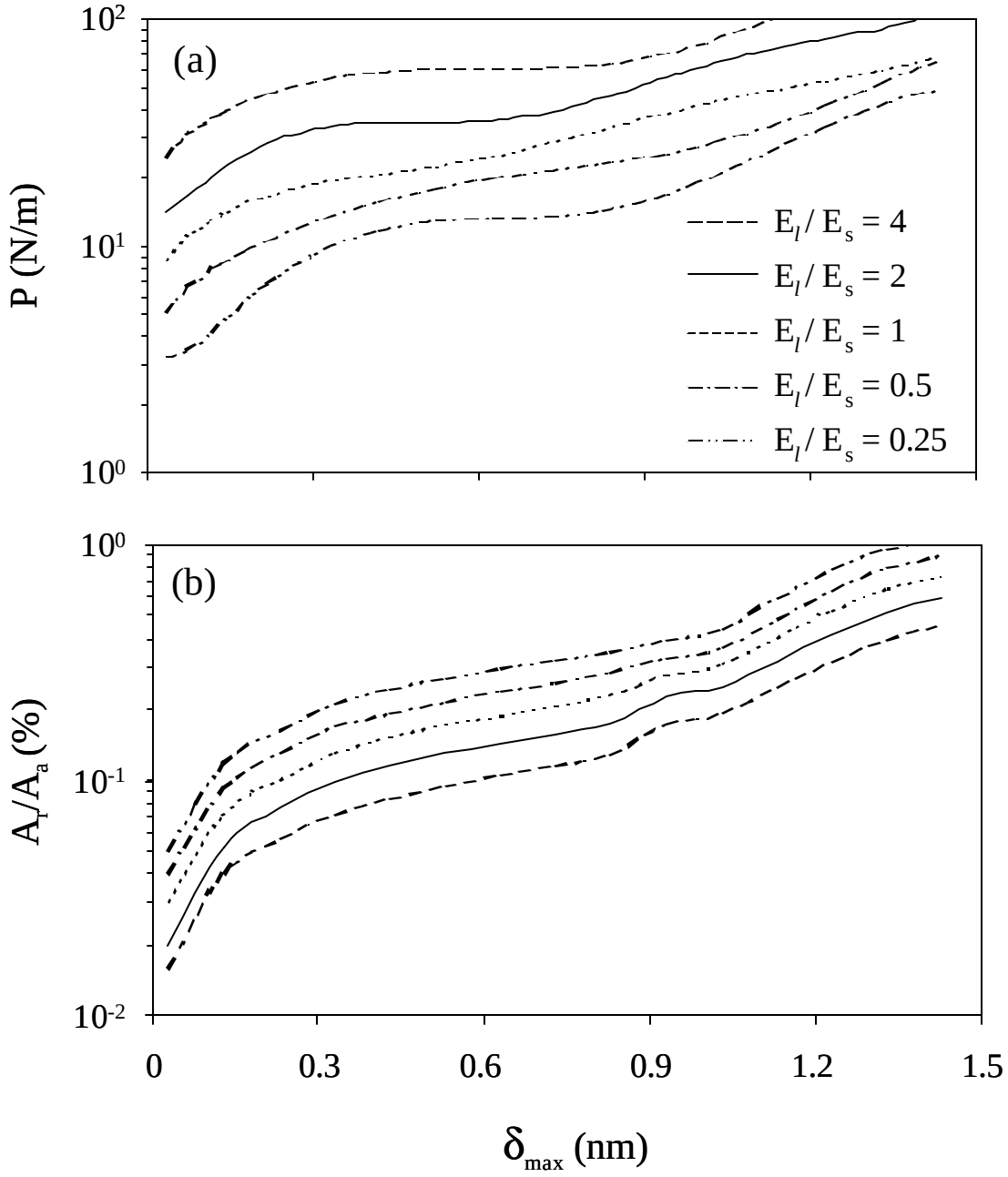

Fig. 4.8 Effect of elastic modulus ratio on (a) contact load and (b) real-to-apparent contact area ratio versus maximum surface interference for an elastic layered medium (t = 5 nm) indented by a rough surface (D = 1.44 and $G = 9.46 \times 10^{-4}$ nm).

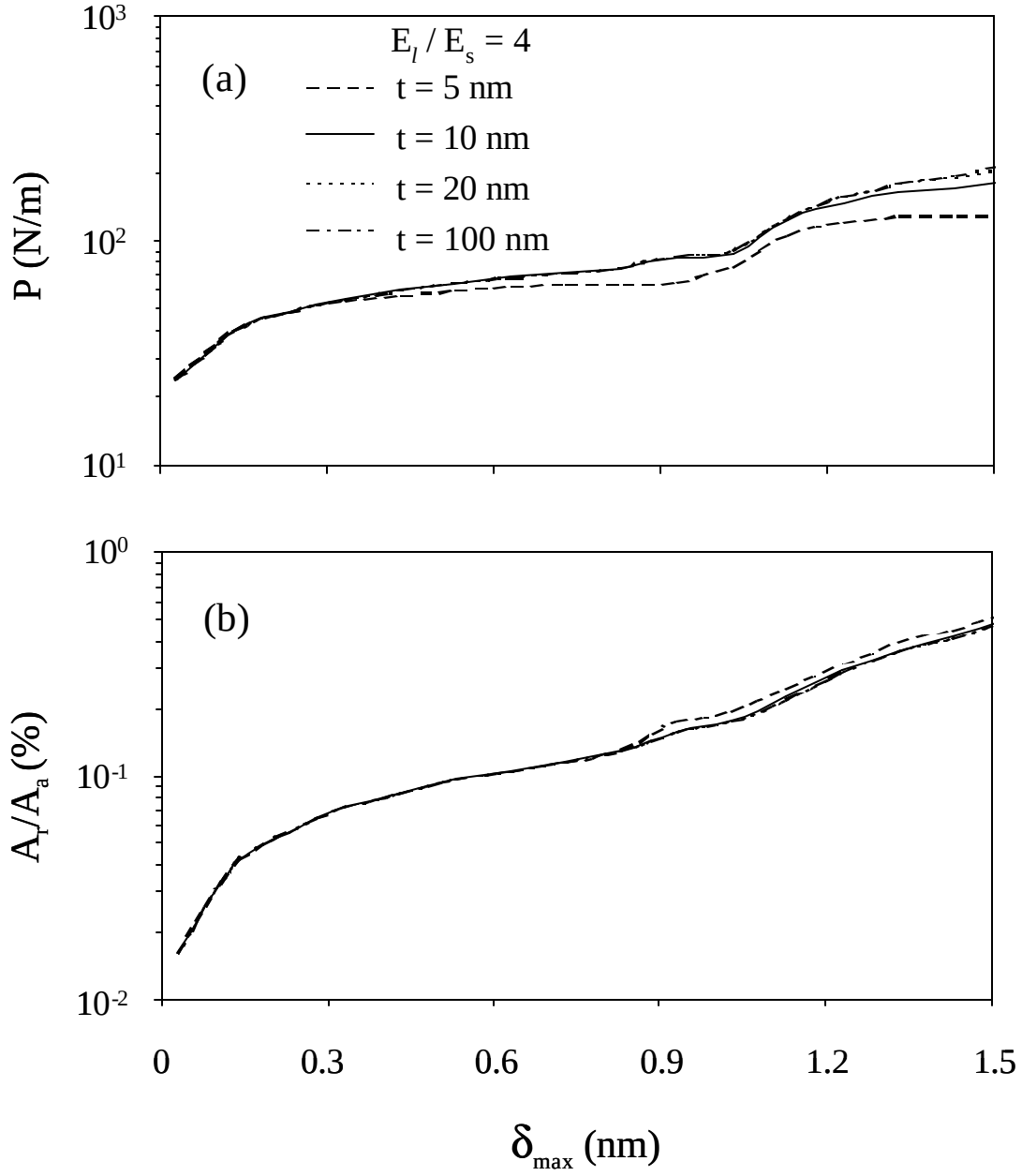

Fig. 4.9 Effect of layer thickness on (a) contact load and (b) real-to-apparent contact area ratio versus maximum surface interference for an elastic layered medium (E_l/E_s = 4) indented by a rough surface (D = 1.44 and $G = 9.46 \times 10^{-4}$ nm).

4.4.3 Contact Stresses

A detailed knowledge of the contact stress field is essential to the analysis of the mechanisms controlling fracture, fatigue, and wear. The effects of material properties and layer thickness on the contact stresses due to normal loading are presented first, followed by stress results for simultaneous normal and tangential contact loadings.

The evolution of contact stresses during indentation can be interpreted in terms of the maximum von Mises equivalent stresses, σ_M^{max}, in the layer and the substrate, shown in Figs. 4.10(a) and 4.10(b), respectively, as a function of the maximum surface interference, δ_{max}, and the elastic modulus ratio, E_l/E_s. In both layer and substrate, σ_M^{max} increases with δ_{max} and E_l/E_s. This is expected because higher δ_{max} and E_l/E_s yield larger contact loads, as shown in Fig. 4.8(a). For fixed δ_{max}, it is more likely to initiate yielding in the substrate for a stiff layer than a compliant layer. This is because the compliant layer can store more elastic energy and, consequently, reduce the stress intensity in the substrate and also due to the significant stress concentration at the interface in the case of the stiff layer resulting from the larger elastic modulus mismatch. Another important feature shown in Figs. 4.10(a) and 4.10(b) is that for shallow indentation (δ_{max} < 1 nm), σ_M^{max} varies very insignificantly because the effect of the substrate compliance is secondary. Results (not shown here for brevity) showed that, for the stiffer layer (E_l/E_s = 4), σ_M^{max} is more likely to occur at or near the surface, while for the softer layer (E_l/E_s = 0.25), σ_M^{max} is more likely to occur below the surface in the layer and at the interface. It was also found that the position of σ_M^{max} shifts from the surface to the interface with the

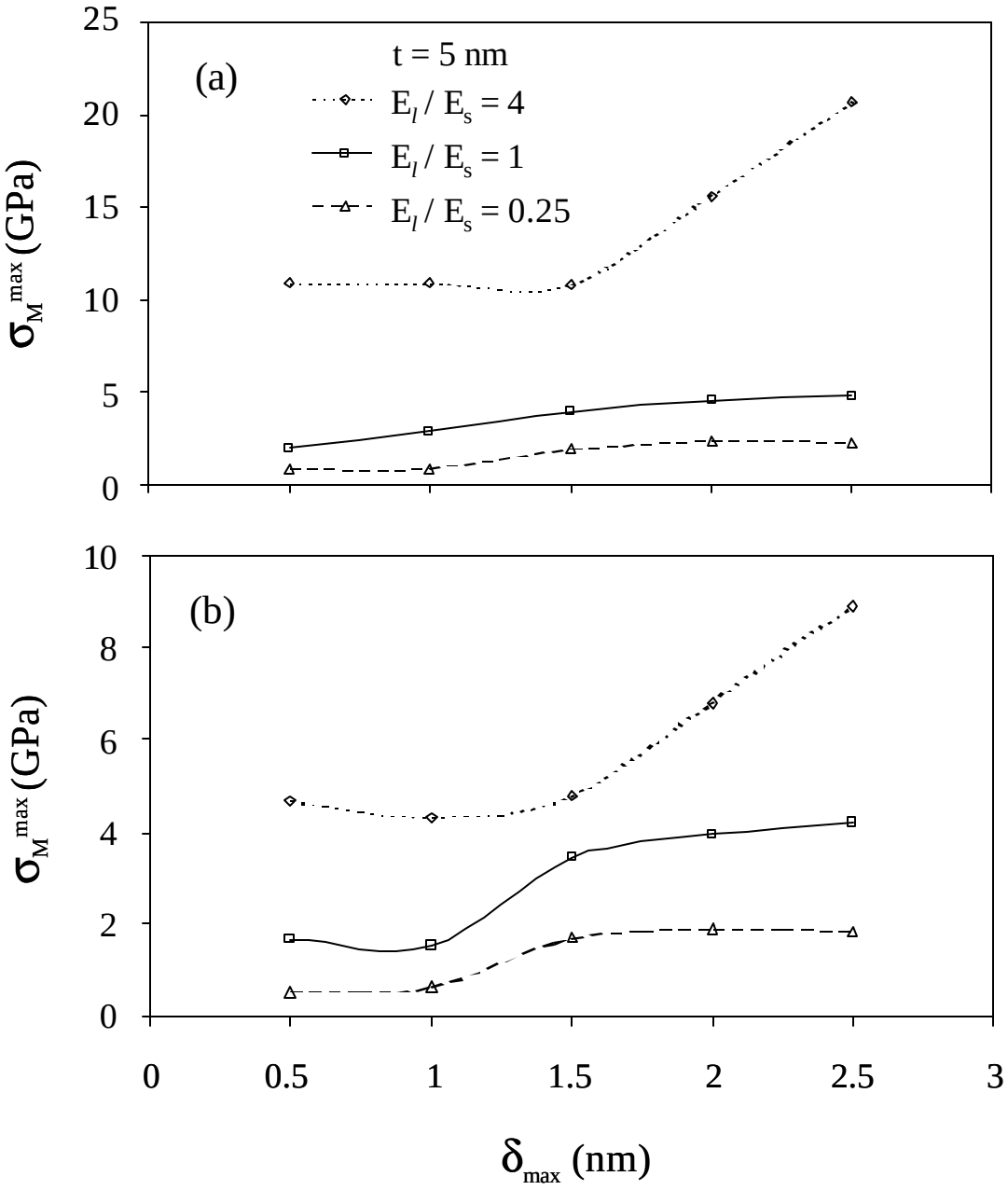

Fig. 4.10 Maximum von Mises equivalent stresses in (a) the layer and (b) the substrate versus maximum surface interference for an elastic layered medium indented by a rough surface (D = 1.44 and $G = 9.46 \times 10^{-4}$ nm).

increase of $d_{\max}$, i.e., light contact loads promote surface yielding, while high contact loads enhance in yielding at the interface.

Figure 4.11 shows $s_M^{\max}$ in the layer and the substrate as a function of $d_{\max}$ for different values of the layer thickness and $E_l/E_s = 4$. As expected, $s_M^{\max}$ increases with the increases of $d_{\max}$. The insignificant differences in $s_M^{\max}$ in the layer for t = 10 and 20 nm are due to the insignificant differences in the contact load and contact area, as shown in Fig. 4.9. However, Fig. 4.11(b) shows that $s_M^{\max}$ in the substrate depends strongly on the layer thickness for small interference, i.e., $d_{\max} < 1.5$ nm. The increase of $s_M^{\max}$ in the substrate with the decease of the layer thickness is attributed to the intensification of the stresses extending into the substrate. A comparison of Figs. 4.10 and 4.11 shows an overall stronger effect of E_l/E_s on $s_M^{\max}$, while the effect of the layer thickness is less pronounced.

Figure 4.12(a) shows $s_M^{\max}$ in the layer and the substrate as a function of E_l/E_s for t = 5 nm and $d_{\max}/s$ = 0.25, where s is the root-mean-square surface roughness. Stiffening of the layer intensifies greatly $s_M^{\max}$ in the layer; however, the effect on $s_M^{\max}$ in the substrate is less pronounced. A steady state $s_M^{\max}$ occurs when $E_l / E_s \geq 3$. Figure 4.12(b) shows $s_M^{\max}$ in the layer and the substrate as a function of layer thickness for $d_{\max}/s$ = 0.25. In the substrate, $s_M^{\max}$ decreases to a steady state with the increase of the layer thickness. Hence, layer thickness effect on $s_M^{\max}$ in the substrate is negligible for relatively thick layers (t > 10 nm). The results for $s_M^{\max}$ in the substrate shown in Figs.

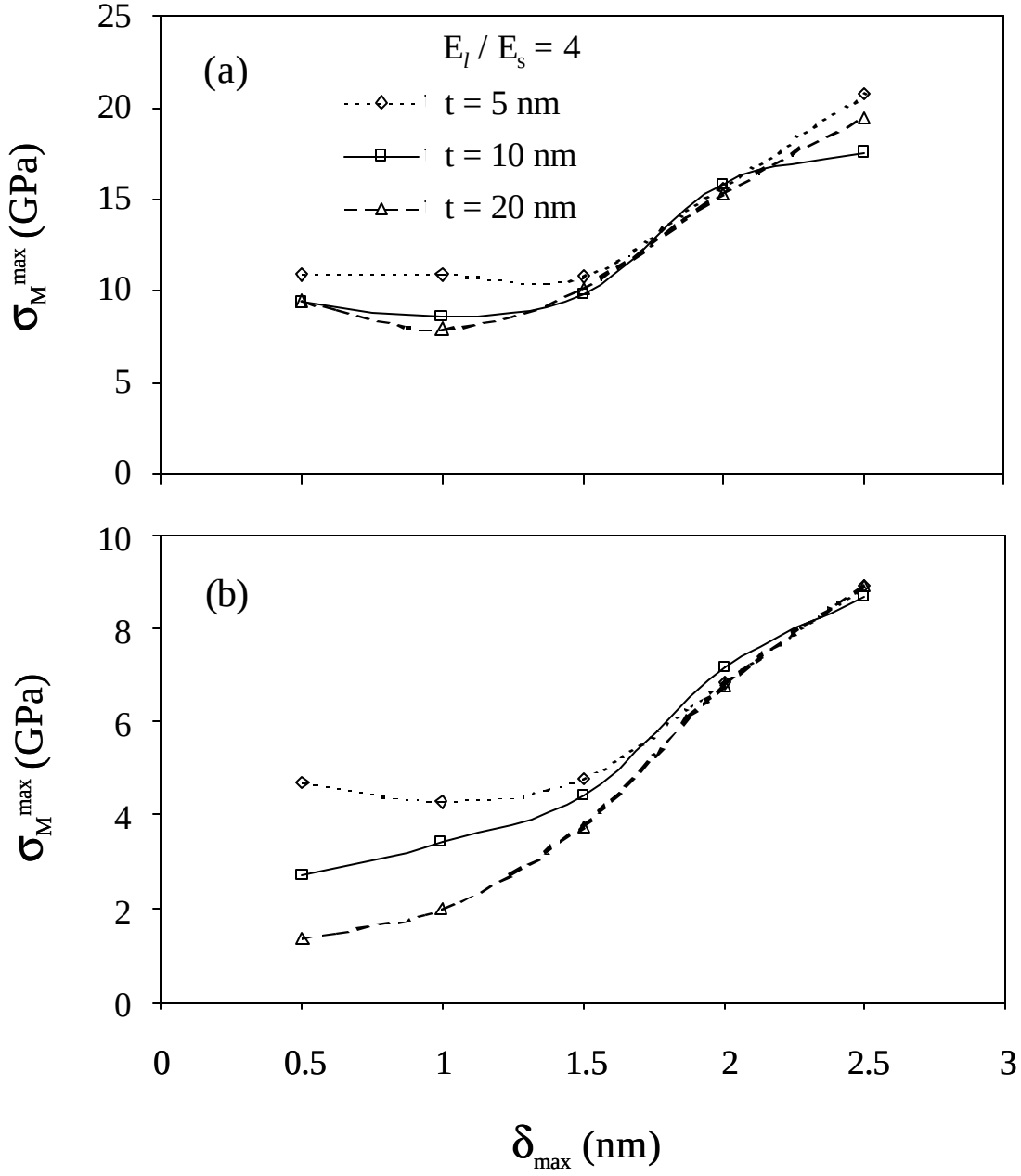

Fig. 4.11 Maximum von Mises equivalent stress in (a) the layer and (b) the substrate versus maximum surface interference for an elastic layered medium (E_l/E_s = 4) with different layer thickness (t = 5, 10, 20 nm) indented by a rough surface (D = 1.44 and G = 9.46×10^{-4} nm).

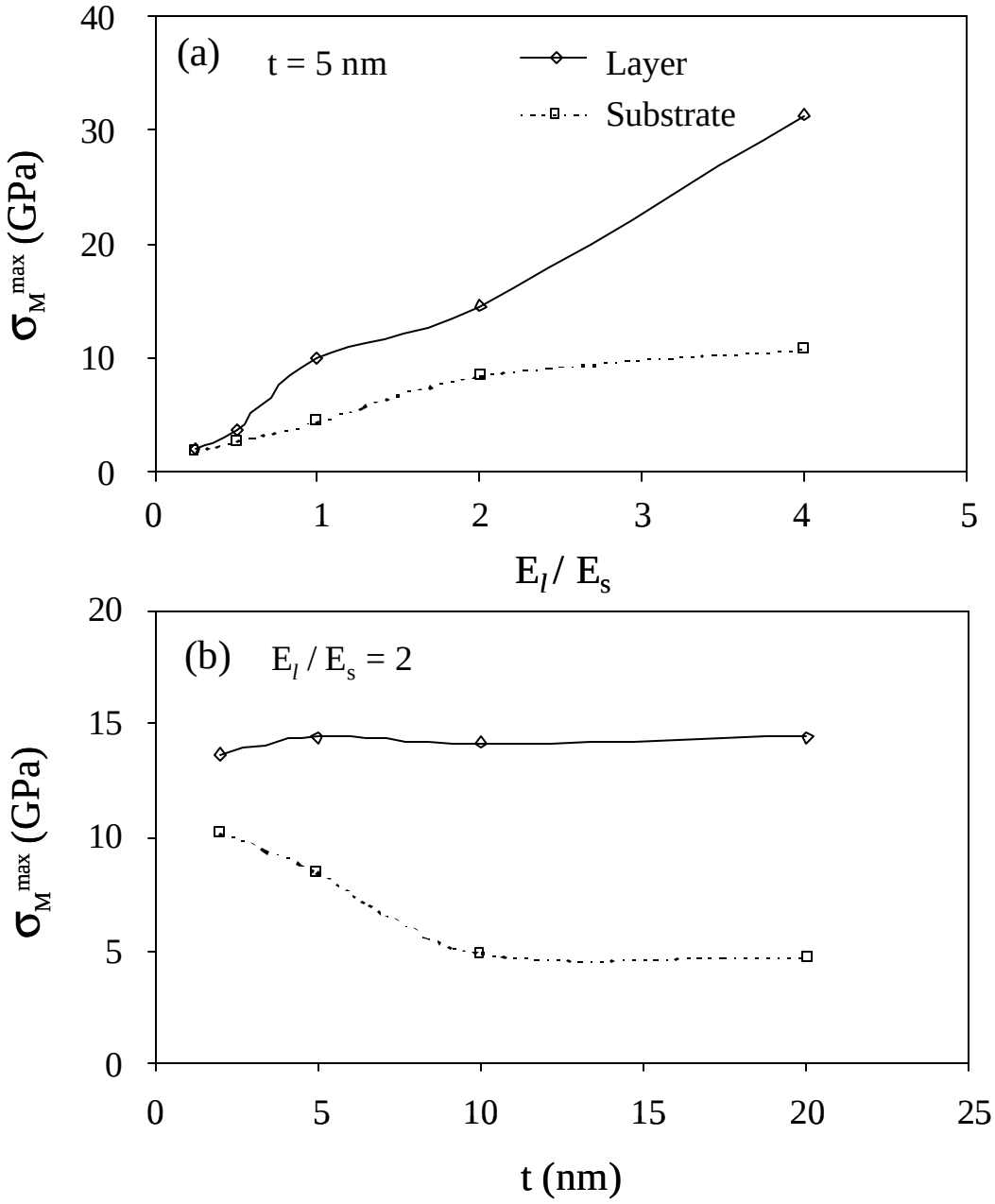

Fig. 4.12 Effects of (a) elastic modulus ratio and (b) layer thickness on the maximum von Mises equivalent stresses in the layer and the substrate of a layered medium indented by a rough surface (d_{max}/s = 0.25, D = 1.34, and $G = 9.46 \times 10^{-4}$ nm).

4.12(a) and 4.12(b) suggest the existence of critical values of E_l and t, above which, the layer is effective in suppressing the stresses.

Figure 4.13 shows pressure distributions at asperity contacts and associated von Mises equivalent stress contours for E_l/E_s = 4, 1, and 0.25, D = 1.34, $G = 9.46 \times 10^{-4}$ nm, and d_{max}/s = 0.25. The corresponding segments of the rough surface are also shown at the top of Fig. 4.13 for reference. A comparison of the contact pressure profiles shown in Figs. 4.13(a)-4.13(c) shows a strong effect of E_l/E_s on the contact pressure distribution. Higher pressure peaks and smaller asperity contact areas are produced with the increase of E_l/E_s. This is expected because, at a given d_{max} value, the contact load increases with E_l/E_s, as shown in Fig. 4.8. For the stiffer layer (E_l/E_s = 4), the contact interface consists of four distinct contact spots, while for the compliant layer (E_l/E_s = 0.25) there are five contact spots. The von Mises stress contours show that the subsurface stress field depends strongly on the elastic modulus ratio E_l/E_s. The von Mises stress contours for E_l/E_s = 4 are confined within the stiff layer and exhibit significant discontinuities at the interface. The increase of s_M with E_l/E_s is due to the increase of the contact pressure. It is noted that p^{max} and s_M^{max} always occur at the sharper asperity contact. For E_l/E_s = 0.25, the position of s_M^{max} shifts from the surface to the interface due to the increase of the asperity contact area.

To evaluate the effect of friction on the propensity for surface cracking, the maximum tensile stress, s_{xx}^{max}, at the layer surface as a function of E_l/E_s is shown in Fig. 4.14 for m = 0.1 and 0.5. For m = 0.1, s_{xx}^{max} is insensitive to the variation of E_l/E_s.

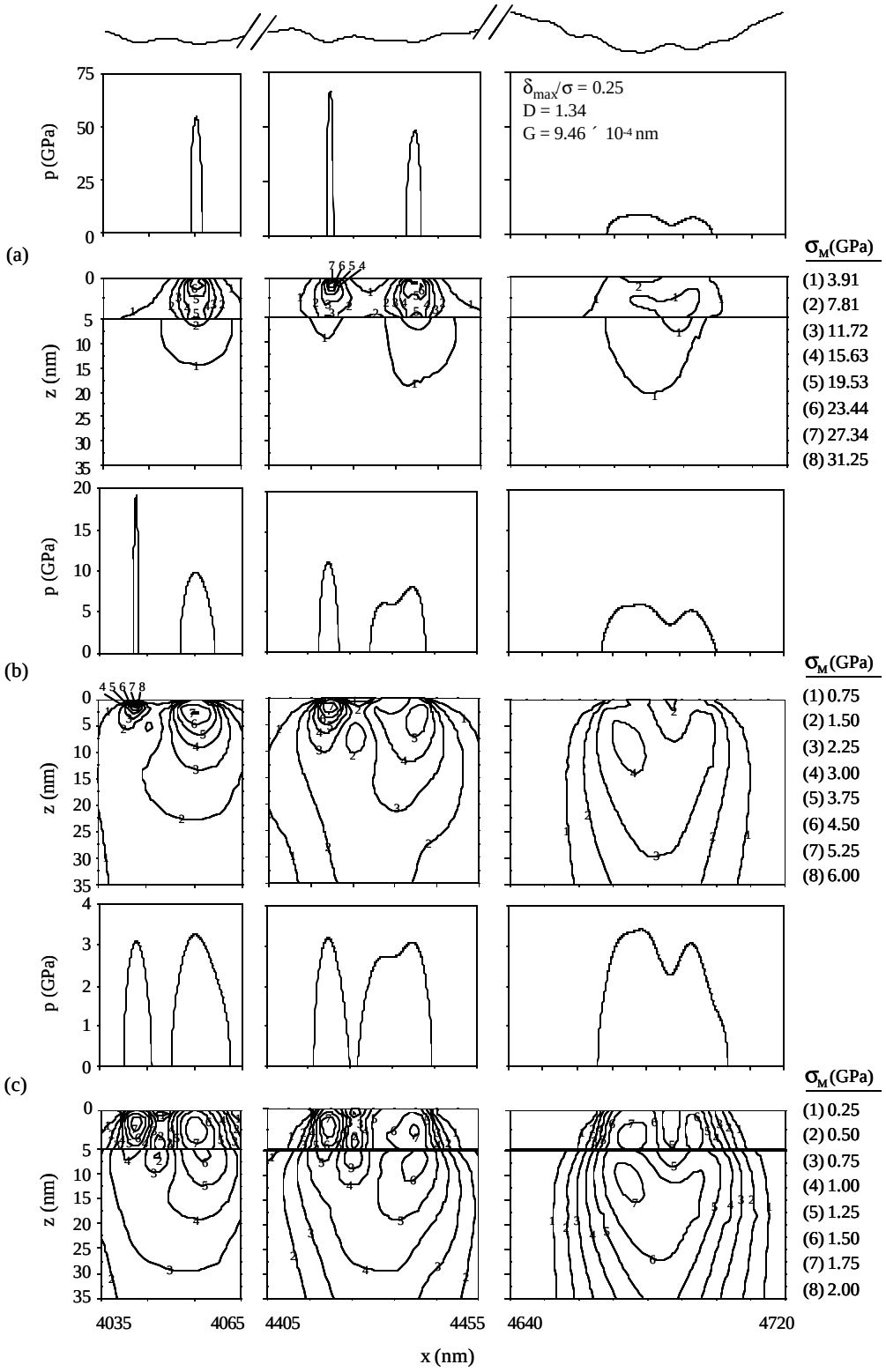

Fig. 4.13 Pressure distributions at asperity contacts and corresponding contours of von Mises equivalent stress in an elastic layered medium due to indentation by a rough surface ($d_{\max}/s$ = 0.25, D = 1.34, and G = 9.46 × 10^{-4} nm): (a) E_l/E_s = 4, (b) E_l/E_s = 1, and (c) E_l/E_s = 0.25.

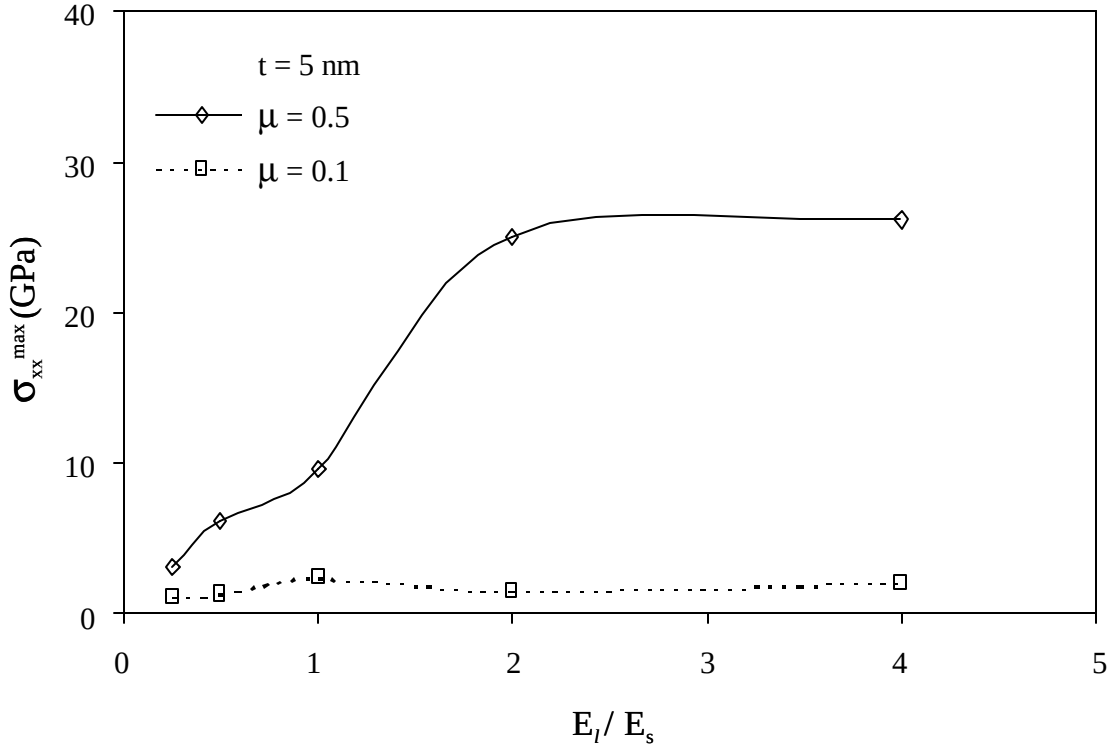

Fig. 4.14 Maximum surface tensile stress at the surface of a layered medium in sliding contact with a rough surface (d_{max}/s = 0.25, D = 1.34, and G = 9.46 × 10^{-4} nm) versus elastic modulus ratio E_l/E_s for m = 0.5 and 0.1.

However, s_{xx}^{max} increases significantly with the increase of E_l/E_s when m = 0.5. The high value of s_{xx}^{max} obtained for E_l/E_s = 4 and m = 0.5 indicates a greater likelihood for surface cracking. It is well established that s_{xx}^{max} at the surface and s_1^{max} in the subsurface control crack initiation. Figure 4.15 shows distributions of s_{xx} at the surface and s_1 in the subsurface for E_l/E_s = 4, 1, and 0.25 due to sliding of a rough surface (D = 1.34 and G = 9.46×10^{-4} nm) for m = 0.5, d_{max}/s = 0.25, and t = 5 nm. Corresponding segments of the rough surface are also provided for reference. The simulation results reveal a similar

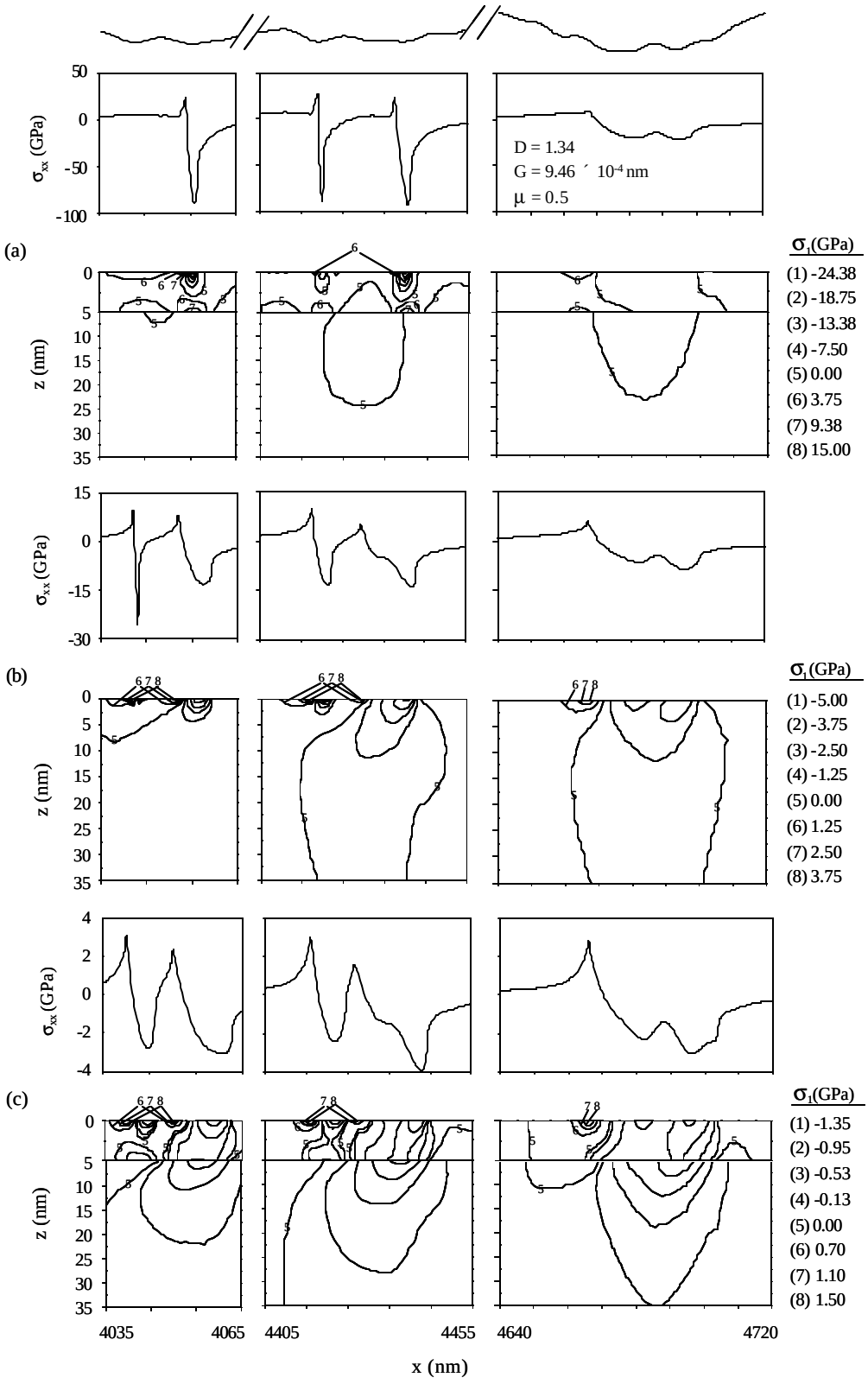

Fig. 4.15 Surface stress distributions and contours of maximum principal stress in an elastic layered medium in sliding contact with a rough surface (d_{max}/s = 0.25, D = 1.34, and $G = 9.46 \times 10^{-4}$ nm): (a) E_l/E_s = 4, (b) E_l/E_s = 1, and (c) E_l/E_s = 0.25.

trend for different E_l/E_s values, i.e., σ_{xx}^{max} at the trailing edges of asperity contacts. However, the magnitudes of σ_{xx}^{max} for E_l/E_s = 4 are significantly higher than those obtained for E_l/E_s = 0.25. The contours of σ_1, which is the surface tensile stress σ_{xx} in the wake of sliding, show that the stiffer layer is subjected to significantly higher tensile stresses than the compliant layer, consistent with the conclusion of a previous study (Kral and Komvopoulos, 1996). Since σ_1^{max} occurs always at the surface, surface cracking is predominant under sliding conditions conducive to high friction coefficients. This phenomenon was confirmed by an earlier fracture analysis (Bower and Fleck, 1994). It was shown that crack initiation at the surface commences immediately behind the contact region of a sliding indenter, where the tensile stress reaches a maximum. Moreover, in the case of E_l/E_s = 4, there are three small regions at the interface where a high tensile stress is produced. Consequently, for relatively stiff layers, crack initiation is likely to occur either at the surface or the interface, while for compliant layers crack initiation is favored at the surface.

Layer debonding (delamination) depends on the magnitude of the shear stress, τ_{xz}, at the interface. Figure 4.16 shows the distribution of τ_{xz} at the interface of the layered medium in sliding contact with a rough surface (D = 1.34 and G = 9.46×10^{-4} nm) for E_l/E_s = 4, 1, and 0.25 and m = 0.5. The magnitude of τ_{xz} depends strongly on E_l/E_s. A comparison of the shear stress results for different values of E_l/E_s shows an increased propensity for delamination across the interface of the stiffer layer. The existence of several interfacial locations of high τ_{xz} suggests that delamination may occur at several

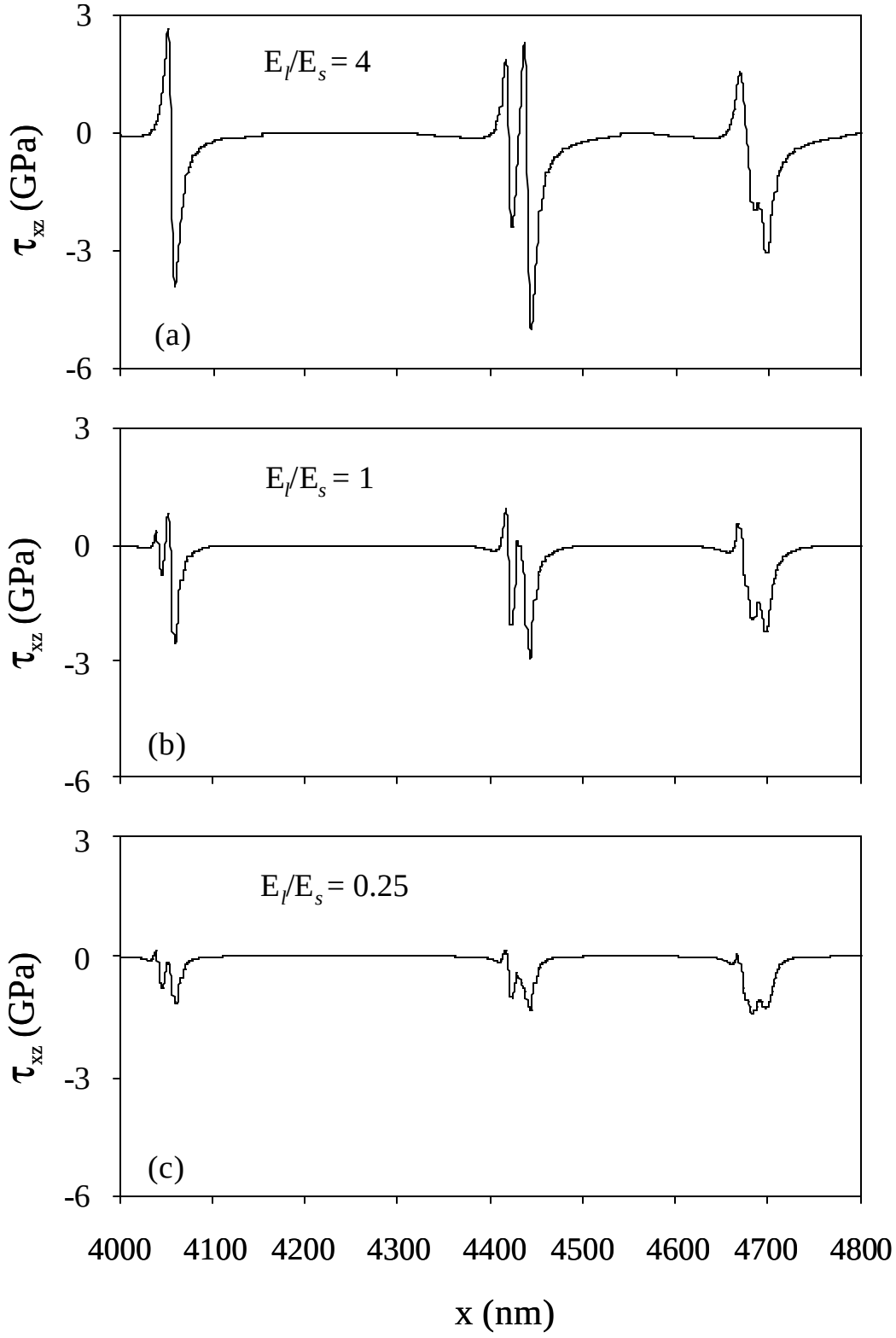

Fig. 4.16 Shear stress distributions at the interface of an elastic layered medium in sliding contact with a rough surface (d_{max}/s = 0.25, D = 1.34, and G = 9.46 × 10^{-4} nm) for m = 0.5: (a) E_l/E_s = 4, (b) E_l/E_s = 1, and (c) E_l/E_s = 0.25.

locations along the interface. Figure 4.17(a) shows the maximum shear stress, t_{xz}^{max}, at the interface as a function of E_l/E_s for m = 0.1 and 0.5. The t_{xz}^{max} stress increases significantly with the increase of E_l/E_s when $E_l/E_s < 2$, and reaches a steady state when $E_l/E_s > 2$. The effect of friction on t_{xz}^{max} is secondary compared to that of E_l/E_s, conversely to the s_{xx}^{max} (Fig. 4.14). The significance of the layer thickness on the maximum interfacial shear stress can be interpreted in terms of the results shown in Fig. 4.17(b). The magnitude of τ_{xz}^{max} decreases by a factor of 2 to 3, depending on the value of m, with the increase of the layer thickness, reaching a constant value when $t > 10$ nm. This behavior is expected because the substrate effect on the stress field diminishes with the increases of the layer thickness. A comparison of the shear stress curves for m = 0.1 and 0.5 shows that the effect of m on t_{xz}^{max} is secondary compared to the effects of E_l/E_s and t.

4.5 Conclusions

A plane-strain analytical model was developed for an elastic layered medium in sliding contact with a rough (fractal) surface. The significance of the material properties, layer thickness, and surface topography on global parameters was examined in the context of results for the normal load and contact area. The contact pressure and local stress fields were interpreted in terms of the effects of the coefficient of friction, layer thickness, and material properties on the pressure profile, surface and interface stresses, maximum principal stress, and von Mises equivalent stress. Based on the obtained results and discussion, the following main conclusions can be drawn.

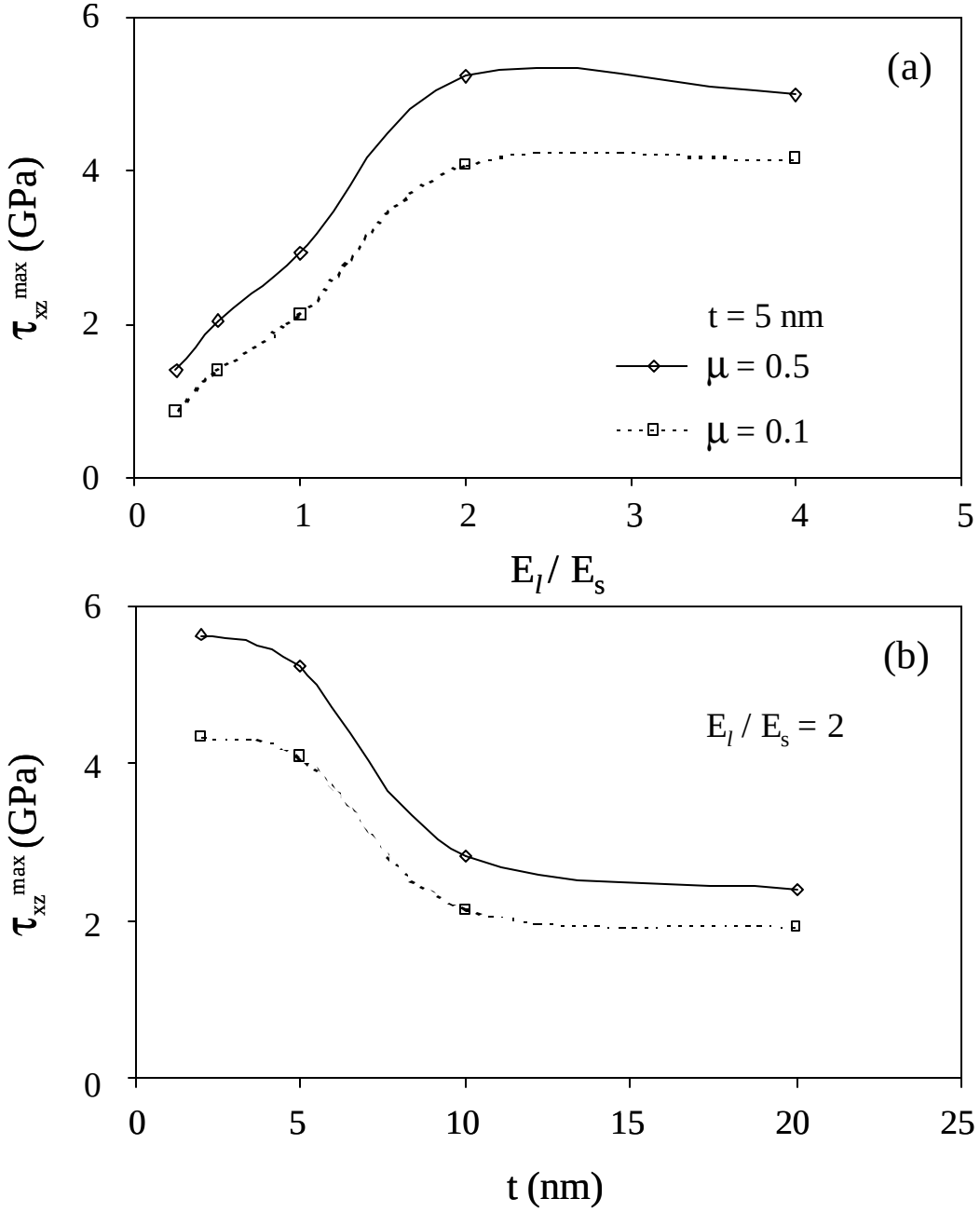

Fig. 4.17 Variation of maximum shear stress at the interface of an elastic layered medium in sliding contact with a rough surface (d_{max}/s = 0.25, D = 1.34, and $G = 9.46 \times 10^{-4}$ nm) for m = 0.1 and 0.5 and different values of (a) E_l/E_s and (b) t.

(1) A constitutive relationship between the mean contact pressure and a representative strain parameter was derived for an indented elastic layered medium. The real contact area of an asperity contact spot was obtained as a function of mechanical properties of the layered medium, layer thickness, truncated half-contact width, and asperity radius.

(2) Contact pressure profiles and the stress field were determined for the distribution of the asperity contacts.

(3) Both the contact load and real contact area increase monotonically with the maximum surface interference. The effects of the fractal parameter and elastic modulus of the layer on the contact load and real contact area are dominant, while the effect of the layer thickness is relatively small. The contact load increases and the contact area decreases with the increase of the elastic modulus of the layer. The effect of the layer thickness is negligible for small interference (or light contact loads) and secondary for relatively large interferences.

(4) The maximum von Mises equivalent stress in both the layer and the substrate increases with the maximum interference and the elastic modulus of the layer. The maximum von Mises stress occurs always at the sharper asperity contacts. For a stiff layer, the maximum von Mises is more likely to occur at or near the surface, while for a compliant layer it is favored to arise under the surface or at the interface. The maximum von Mises stress in the substrate depends strongly on the layer thickness at small interference.

(5) The maximum tensile stress at the surface arises at the trailing edges of asperity contacts and intensifies with the increase of the elastic modulus of the layer and the coefficient of friction. The stiffer layer is subjected to significantly higher tensile

stresses than the compliant layer. The peak value of the maximum principal stress occurs always at the surface, which indicates that crack initiation at the layer surface is favored. However, for stiff layers, crack initiation at the interface is also possible.

(6) The shear stress at the interface depends strongly on the elastic modulus and the thickness of the layer. A stiff layer enhances the likelihood for interface cracking and delamination much more than a compliant layer. The effect of the coefficient of friction on the interfacial shear stress is secondary compared to the effects of the elastic modulus and thickness of the layer.

CHAPTER 5

THERMOMECHANICAL ANALYSIS OF SEMI-INFINITE SOLID IN SLIDING CONTACT WITH A FRACTAL SURFACE

5.1 Introduction

Frictional heating and associated temperature rise may significantly affect the mechanical response of interacting surfaces. Knowledge of thermoelastic stresses in sliding solid bodies is essential for accurate failure analysis of mechanical systems. The determination of the thermal and thermoelastic fields in semi-infinite homogeneous media due to different surface heat sources has been the objective of several past studies. One of the pioneering early analyses is attributed to Blok (1937) who examined the flash temperature and maximum temperature rise at the surface of a semi-infinite elastic body due to a uniform square heat source moving at speeds corresponding to high and low Peclet numbers. Later, Jaeger (1942) extended the previous analysis to the intermediate regime of Peclet number.

The previous studies established the foundation of both analytical and numerical thermomechanical studies. Based on a Green's function method, Tian and Kennedy (1994) determined the temperature rise at the surface of a semi-infinite body due to different moving heat sources. Ju and Huang (1982) performed a thermomechanical analysis of homogeneous half-spaces exposed to a fast moving heat source and found predominantly compressive stresses at the surface. Huang and Ju (1985) and Ju and Liu (1988) observed that the maximum tensile thermal stress occurs slightly below the

trailing edge of the contact region at a depth controlled by the Peclet number. Leroy et al. (1989) conducted a two-dimensional analysis of a heat source moving over a layered medium and reported high stresses in the surface layer when the mismatch between the layer and substrate thermomechanical properties was large. Bryant (1988) used a Fourier transformation method to derive thermal and thermoelastic solutions for a moving line heat source, and Ju and Farris (1997) obtained thermal and thermoelastic solutions in the frequency domain for an arbitrary heat source moving over an elastic half-space. More recently, Liu and Wang (2003) investigated the transient thermoelastic stress fields generated in a half-space due to parabolic or irregularly distributed heat source moving at constant velocity.

In the previous studies, the *a priori* assumed distribution of the heat sources was decoupled from the mechanical response of the deformed medium. To consider the effect of frictional heating on contact deformation, it is necessary to account for the concomitant effects of mechanical and thermal stresses. In view of the complex analytical relationships in fully coupled thermomechanical contact problems, the majority of earlier analyses were based on the finite element method. Gupta et al. (1993) used a two-dimensional finite element model to study rolling and sliding contact on a semi-infinite medium under the assumption of invariant contact pressure. Cho and Komvopoulos (1997) presented a thermoelastic finite element analysis of subsurface crack propagation. Ye and Komvopoulos (2003) developed a finite element model to examine the simultaneous effects of mechanical and thermal surface traction on the deformation of elastic-plastic layered media. Gong and Komvopoulos (2004a) conducted a fully coupled finite element analysis of an elastic-plastic layered medium with a patterned surface in

contact with an elastic-plastic sphere. Despite the mathematical complexity of analytical approaches dealing with thermomechanical contact problems, some analytical solutions have also been obtained for thermoelastic contacts. Azarkhin and Barber (1986) derived solutions for the transient thermoelastic Hertz problem using Green's function and Fourier transformation techniques, and Lee and Barber (1993) examined the stability of a brake disk sliding between two friction pads and found that the mode with the lowest critical speed was always antisymmetric about the layer mid-plane. Wang and Liu (1999) and Liu and Wang (2000) introduced a two-dimensional thermoelastic contact model of two infinitely large rough surfaces that accounts for the thermal effect on the mechanical response, and later extended the previous analysis to a three-dimensional thermomechanical model of non-conforming contacts (Liu and Wang, 2001).

Although the previous studies have provided useful insight into the temperature and thermoelastic stress fields in solids due to moving heat sources or sliding rough surfaces, analytical thermomechanical studies of rough surfaces elucidating the dependence of temperature and stress fields on surface topography parameters and Peclet number have not been reported yet. Therefore, the objective of this study was to develop a thermomechanical analysis of sliding contact between a semi-infinite elastic medium and a rough (fractal) surface, accounting for the simultaneous effects of thermal and mechanical deformation. Results are presented for the contact pressure distribution and surface and subsurface temperature and stress fields in terms of Peclet number and surface topography (fractal) parameters. The significance of mechanical surface traction and frictional heating on the propensity for yielding and cracking at the sliding surface are interpreted in light of numerical results.

5.2 Thermomechanical Contact Analysis

Sliding friction leads to energy dissipation in the form of heat within the vicinity of the real contact area. The frictional heat dissipated in the medium is responsible for the temperature rise, resulting in the development of thermal stresses and variations in the real contact area and contact pressure distribution due to thermal expansion. Because such changes affect heat generation rate and heat conduction across the contact interface, the thermal and mechanical stress and strain fields are fully coupled and, therefore, must be determined simultaneously.

5.2.1 Surface Deformation and Temperature Field

Figure 5.1 shows a schematic of a rough, rigid, and adiabatic surface in sliding

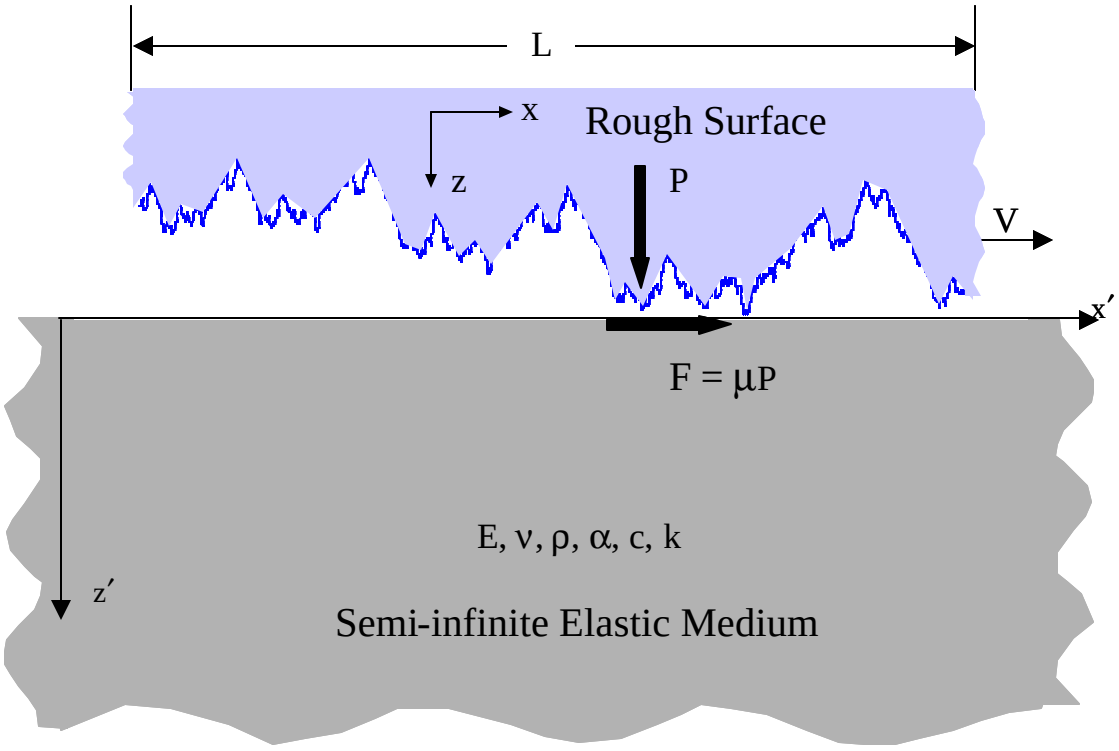

Fig. 5.1 Schematic representation of a rough (fractal) surface sliding over an elastic semi-infinite solid and pertinent nomenclature.

contact with a deformable semi-infinite solid possessing a smooth surface. Coulomb friction is assumed at the sliding contact interface. The elastic medium is subjected to normal and tangential (friction) surface tractions, producing a total normal load, P, in the z direction and a total tangential load, $F = mP$, in the x direction, where m is the coefficient of friction. Frictional heat generated at each asperity microcontact is conducted into the elastic medium. Similar to the treatment of Carslaw and Jaeger (1959), a coordinate system (x, y, z) on the moving rough surface and a coordinate system (x', y', z') on the stationary elastic medium are used in the analysis. The two coordinate systems are related by

$$x = x' - Vt \qquad z = z', \tag{5.1}$$

where t is the time, and V is the moving (sliding) velocity. The heat flux density due to frictional heat, Q, is given by

$$Q = y\, mpV, \tag{5.2}$$

where y is the fraction of mechanical work dissipated as heat, and p is the contact pressure. It is assumed that y = 1.0, i.e., all the energy dissipated in a frictional contact is converted to heat, consistent with the conclusion of Uetz and Föhl (1978). Since the rough surface is assumed to be adiabatic, heat conduction occurs only into the elastic medium.

The normal displacement is due to the effects of contact pressure, shear traction, and thermoelastic distortion induced by frictional heating. Hence, the normal displacement at the surface, u_z, can be expressed as,

$$u_z = u_z^N + u_z^S + u_z^T, \tag{5.3}$$

where u_z^N, u_z^S, and u_z^T are the normal displacements due to the contact pressure, shear traction, and frictional heating, respectively. Each microcontact area is divided into a number of small segments of equal width, b. A piecewise-linear distribution of the contact pressure is obtained by superposition of overlapping triangular pressure elements (Johnson, 1985).

The u_z^N displacement due to the triangular pressure distribution shown in Fig. 5.2(a) is given by (Johnson, 1985)

$$u_z^N = -\frac{(1-\nu^2)}{2\pi E}\frac{p_0}{b}\left\{(x+b)^2\ln\left(\frac{x+b}{b}\right)^2 + (x-b)^2\ln\left(\frac{x-b}{b}\right)^2 - 2x^2\ln\left(\frac{x}{b}\right)^2\right\} + C, \qquad (5.4)$$

where p_0 is the maximum contact pressure, E and ν are the elastic modulus and Poisson ratio of the semi-infinite solid, and C is a constant determined from a reference point chosen on the z axis at distance d below the surface. The u_z^S displacement due to the triangular shear traction distribution shown in Fig. 5.2(a) is obtained as (Johnson, 1985)

$$u_z^S = \begin{cases} \dfrac{(1-2n)(1+n)}{E}\dfrac{q_0}{b}x\left(b-\dfrac{1}{2}|x|\right) & |x| \le b \\ \dfrac{(1-2n)(1+n)}{E}\dfrac{q_0 b}{2} & x > b \\ -\dfrac{(1-2n)(1+n)}{E}\dfrac{q_0 b}{2} & x < -b \end{cases} \qquad (5.5)$$

where q_0 is the peak value of the shear traction. A triangular distribution of a heat source moving from left to right at velocity V is shown in Fig. 5.2(b). For convenience, the following non-dimensional parameters are introduced in the analysis,

$$x = \frac{x}{b}, \quad z = \frac{z}{b}, \quad h = \frac{x'}{b}. \qquad (5.6)$$

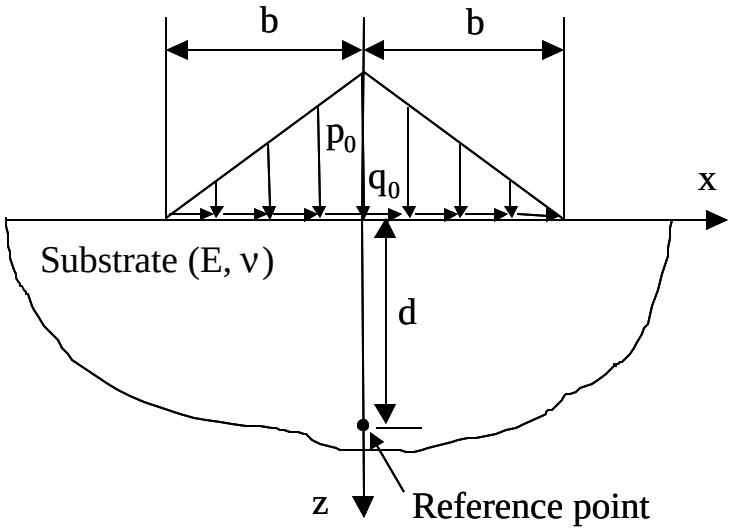

(a)

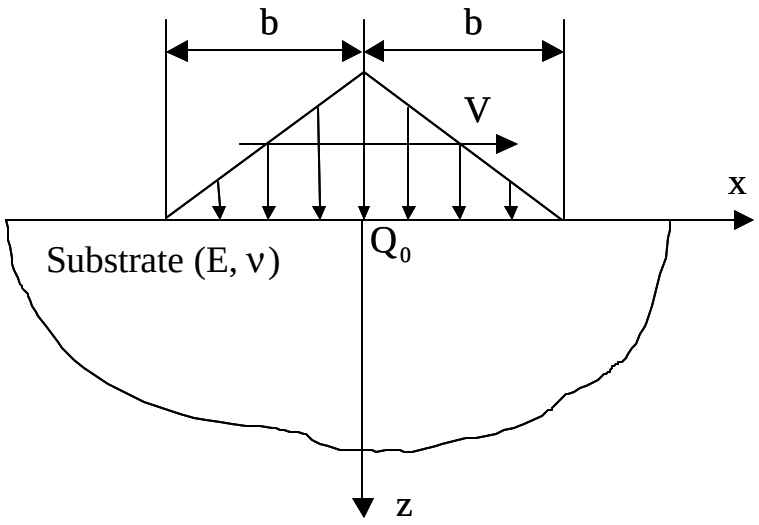

(b)

Fig. 5.2 Triangular distributions of (a) normal and tangential tractions and (b) heat source.

The thermoelastic distortion at the surface due to a moving heat source of triangular distribution can be obtained by superposition of the moving line heat source solutions by Barber (1984). Hence, the u_z^T displacement can be expressed as

$$u_z^T = \begin{cases} l & x \le -1 \\ l\int_{-1}^{1}(1-|h|)e^{-Pe(x-h)}I_0[Pe(x-h)]dh & x \ge 1 \\ l\left\{\int_{-1}^{x}(1-|h|)e^{-Pe(x-h)}I_0[Pe(x-h)]dh + \frac{1}{2} - x + \frac{1}{2}x^2\,\mathrm{sgn}(x)\right\} & -1 \le x \le 1 \end{cases} \tag{5.7}$$

where I_0 is the modified zero-order Bessel function of the first kind, sgn(x) is a sign function of x, and l is defined as

$$l = -\frac{aQ_0(1+n)b^2}{rckPe}, \tag{5.8}$$

where Q_0 is the peak value of the heat flux, Pe is the Peclet number (Pe = $Vb/2k$), and a, r, c, and k are the thermal expansion, mass density, specific heat, and thermal diffusivity of the semi-infinite solid, respectively.

Therefore, the total surface displacement u_z can be obtained by summing the displacement components given by Eqs. (5.4), (5.5), and (5.7) at each triangular element and then integrating over all the asperity microcontacts comprising the real contact area,

$$u_z(x) = \sum_{i=1}^{N}\sum_{j=1}^{M_i-1}[u_z^N\big|_i^j(x) + u_z^S\big|_i^j(x) + u_z^T\big|_i^j(x)], \tag{5.9}$$

where N is the total number of asperity microcontacts, M_i is the total number of segments in the ith asperity microcontact, and $u_z^N\big|_i^j$, $u_z^S\big|_i^j$, and $u_z^T\big|_i^j$ are the normal surface

displacements due to the *j*th triangular distributions of contact pressure, shear traction, and frictional heat, respectively, at the *i*th asperity microcontact.

Since Q_0 and q_0 can be expressed as functions of p_0, i.e.,

$$Q_0 = \psi \pi p_0 V, \qquad q_0 = \mu\, p_0, \tag{5.10}$$

it follows that Eq. (5.9) represents a set of $\sum_{i=1}^{N} M_i$ simultaneous equations that can be expressed in matrix form,

$$\{U_Z\} = \{C\}\{P\}, \tag{5.11}$$

where $\{U_Z\}$ is the matrix of normal surface displacements, $\{P\}$ is the contact pressure matrix, and $\{C\}$ is a square and symmetric matrix termed the influence coefficient matrix. A procedure based on the matrix inversion method, which is similar to that used by Bailey and Sayles (1991) to determine the subsurface stresses in rough surfaces due to both normal and tangential forces, was used to solve Eq. (5.11). Since both the contact pressure and the real contact area are unknown, the following iteration method was used to solve Eq. (5.11). First, the initial surface displacement matrix $\{U_z\}$ was determined by truncating the rough surface by a plane to a maximum surface interference, $d_{\max}$, and the corresponding contact pressure was calculated from $\{P\} = \{C^{-1}\}\{U_z\}$. Any triangular pressure elements exhibiting negative pressure violate the requirement $p > 0$ and were removed from the contact region. Then, the surface displacement was recalculated using Eq. (5.11) and any overlapping points were added to the assumed contact region. With the new set of contact points, Eq. (5.11) was solved again to obtain the contact pressure $\{P\}$. This iteration procedure was repeated until conditions of positive contact pressure, no surface penetration, and contact only within the current contact region were satisfied.

Following an approach similar to that for a uniform band heat source (Carslaw and Jaeger, 1959), the temperature rise, ΔT, due to a heat source of triangular distribution was found to be

$$\Delta T = \frac{Q_0 b}{pk}\int_{-1}^{1}(1-|h|)e^{-Pe(x+h)}K_0\{Pe[(x+h)^2+z^2]^{1/2}\}dh\,, \tag{5.12}$$

where k is the thermal conductivity of the semi-infinite solid, and K_0 is the modified zero-order Bessel function of the second kind. Therefore, the temperature rise at a point (x, z), obtained by superimposition, is given by

$$\Delta T(x,z) = \sum_{i=1}^{N}\sum_{j=1}^{M_i-1}\Delta T\Big|_i^j(x,z)\,, \tag{5.13}$$

where $\Delta T\Big|_i^j(x,z)$ is the temperature rise due to the jth triangular distribution of heat flux at the ith asperity microcontact.

5.2.2 Stress Field

The stress field in the elastic semi-infinite solid due to contact with the rough surface can be obtained by superposition of the stress fields generated by the triangular distributions of contact pressure, shear traction, and heat flux at each microcontact. The stresses in the elastic solid due to a moving heat source with triangular distribution shown in Fig. 5.2(b) were obtained in the frequency domain using spatial Fourier transformation, following an analytical approach similar to that of Ju and Farris (1997),

$$\hat{s}_{xx}^{T} = \frac{Ea\hat{T}_0}{(1-n)b}\{[2(b_2+b_1 i)\,\mathrm{sgn}(w) - wi - wz(b_2+b_1 i-|w|i)]e^{-|w|z} - (b+wi)e^{(b_2 i-b_1)z}\} \tag{5.14}$$

$$\hat{s}_{zz}^{T} = \frac{Ea\hat{T}_0}{(1-n)b}\{[-wi+wz(b_2+b_1 i-|w|i)]e^{-|w|z} + wie^{(b_2 i-b_1)z}\} \tag{5.15}$$

$$\hat{s}_{xz}^{T} = \frac{Ea\hat{T}_0}{(1-n)b}\{[b_2 i-b_1-|w|z(b_2 i-b_1+|w|)]e^{-|w|z} + (b_1-ai)e^{(b_2 i-b_1)z}\} \tag{5.16}$$

where $i = \sqrt{-1}$, and parameters b, b_1, b_2, and $\hat{T}_0$ are defined as

$$b = V / k \tag{5.17}$$

$$b_1 = \sqrt{\frac{w^2 + \sqrt{w^4 + w^2 b^2}}{2}} \tag{5.18}$$

$$b_2 = \frac{bw}{2b_1} \tag{5.19}$$

$$\hat{T}_0 = \frac{2[1-\cos(b_2 w)]}{b_2 w^2 k(b_1 - b_2 i)}. \tag{5.20}$$

The spatial stress field due to frictional heating was obtained by applying inverse Fourier transformation to the numerical solution derived in the frequency domain, i.e.,

$$s^T(x,z) = \int_{-\infty}^{+\infty} \hat{s}^T(w,z) e^{iwx} dw, \tag{5.21}$$

where s^T and $\hat{s}^T$ denote thermal stress components in spatial and frequency domains, respectively.

The above method was validated by comparing numerical results for a moving line heat source with analytical solutions from previous studies. Surface and subsurface stresses along x = 0 are shown in Figs. 5.3(a) and 5.3(b), respectively, for a moving line heat source of energy per unit length per unit time Q located at x = 0. Stresses are normalized by $E'aQ/k$, where E' = $E/(1-n)$, and x and z coordinates are normalized by $1/b$. Solid lines represent analytical results for surface and subsurface stresses obtained from the studies of Barber (1984) and Bryant (1988), respectively, and symbols denote numerical solutions obtained from the present analysis. The good agreement between numerical and analytical results for the thermoelastic stresses demonstrates the accuracy of the present analysis and validates the adopted numerical scheme.

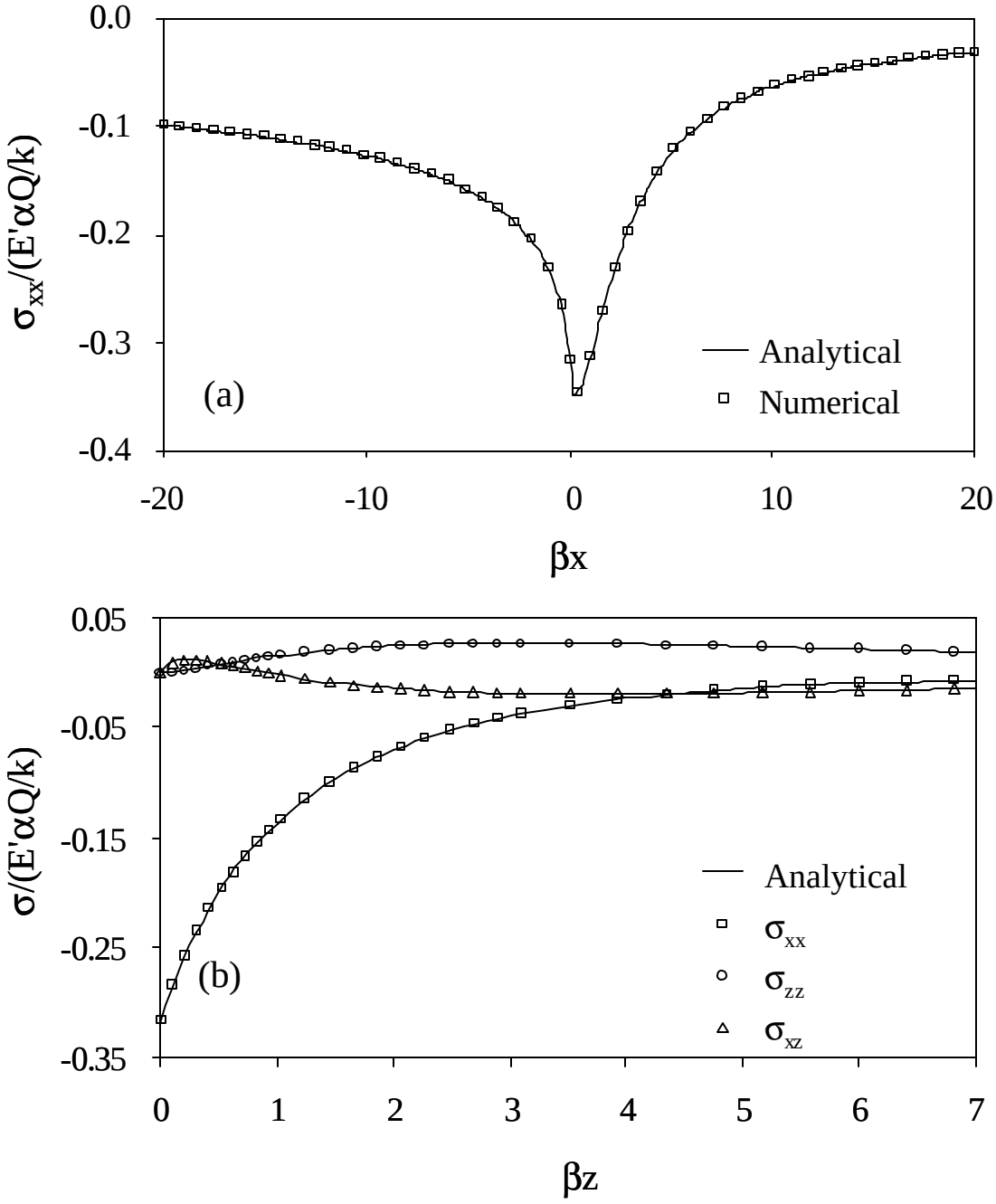

Fig. 5.3 (a) Surface stress and (b) subsurface stresses along $x = 0$ for a moving line heat source located at $x = 0$.

Closed-form solutions for the stresses due to normal and shear tractions possessing triangular distributions have been obtained by Johnson (1985). Consequently, the stress at any point *(x, z)* in the solid can be expressed as

$$s(x,z) = \sum_{i=1}^{N} \sum_{j=1}^{M_i - 1} [s^{N}\Big|_{i}^{j}(x,z) + s^{S}\Big|_{i}^{j}(x,z) + s^{T}\Big|_{i}^{j}(x,z)], \tag{5.22}$$

where $s^{N}\Big|_{i}^{j}$, $\sigma^{S}\Big|_{i}^{j}$, and $s^{T}\Big|_{i}^{j}$ are the stresses due to the *j*th triangular distributions of contact pressure, shear traction, and heat flux at the *i*th asperity microcontact, respectively.

5.3 Results and Discussion

Numerical results are presented in this section for a semi-infinite solid with thermomechanical properties given in Table 5.1 (Gong and Komvopoulos, 2004a). Numerical solutions for a single asperity sliding over the semi-infinite solid are presented

Table 5.1. Thermomechanical properties of semi-infinite solid

Property	Magnitude
Elastic modulus, *E* (GPa)	92
Poisson's ratio, *n*	0.3
Thermal expansion, *a* (K^{-1})	3.1×10^{-6}
Specific heat, *c* (J/g·K)	0.5
Conductivity, *k* (W/m·K)	0.052, 0.52, 5.2
Density, *r* (kg/m^3)	2.15×10^{3}
Diffusivity, *k* (m^2/s)	$4.84 \times (10^{-8}, 10^{-7}, 10^{-6})$

first to validate the algorithm and to establish a reference for comparison with results obtained with the rough (fractal) surface, illustrating the effects of surface topography and interaction between neighboring asperities on the temperature and stress fields in the elastic medium. In the simulation results presented below, the total real contact area was used to determine the Peclet number, and the segment width in the discretization of the contact region was fixed at 0.1 nm.

5.3.1 Single Asperity Sliding

Numerical results for a rigid cylindrical asperity are contrasted with analytical solutions in order to demonstrate the accuracy of the algorithm derived from the present analysis. Figure 5.4(a) shows the deformed surface of the elastic medium for different loading conditions and $d_{\max}/R$ = 0.0075, where R is the asperity radius. The x and z coordinates were normalized by the half-contact width due to indentation, r_i. Normal contact yields a symmetric profile of the deformed surface, while normal and tangential traction (m = 0.5) produce pile-up and sink-in at the rear and front of the contact region, respectively. Thermoelastic deformation enhances pile-up at the rear of the contact region due to the effect of frictional heating (Pe = 0.05). The good match between the deformed surface and the asperity profile over the contact region illustrates the accuracy of the thermomechanical contact algorithm. Figure 5.4(b) shows the contact pressure distribution for $d_{\max}/R$ = 0.0075. The contact pressure was normalized by the maximum contact pressure due to indentation, p_{oi}. The curves represent numerical solutions and the symbols theoretical results (Johnson, 1985). Shear traction produced an asymmetric contact pressure profile. The peak contact pressure predicted by the theoretical solution

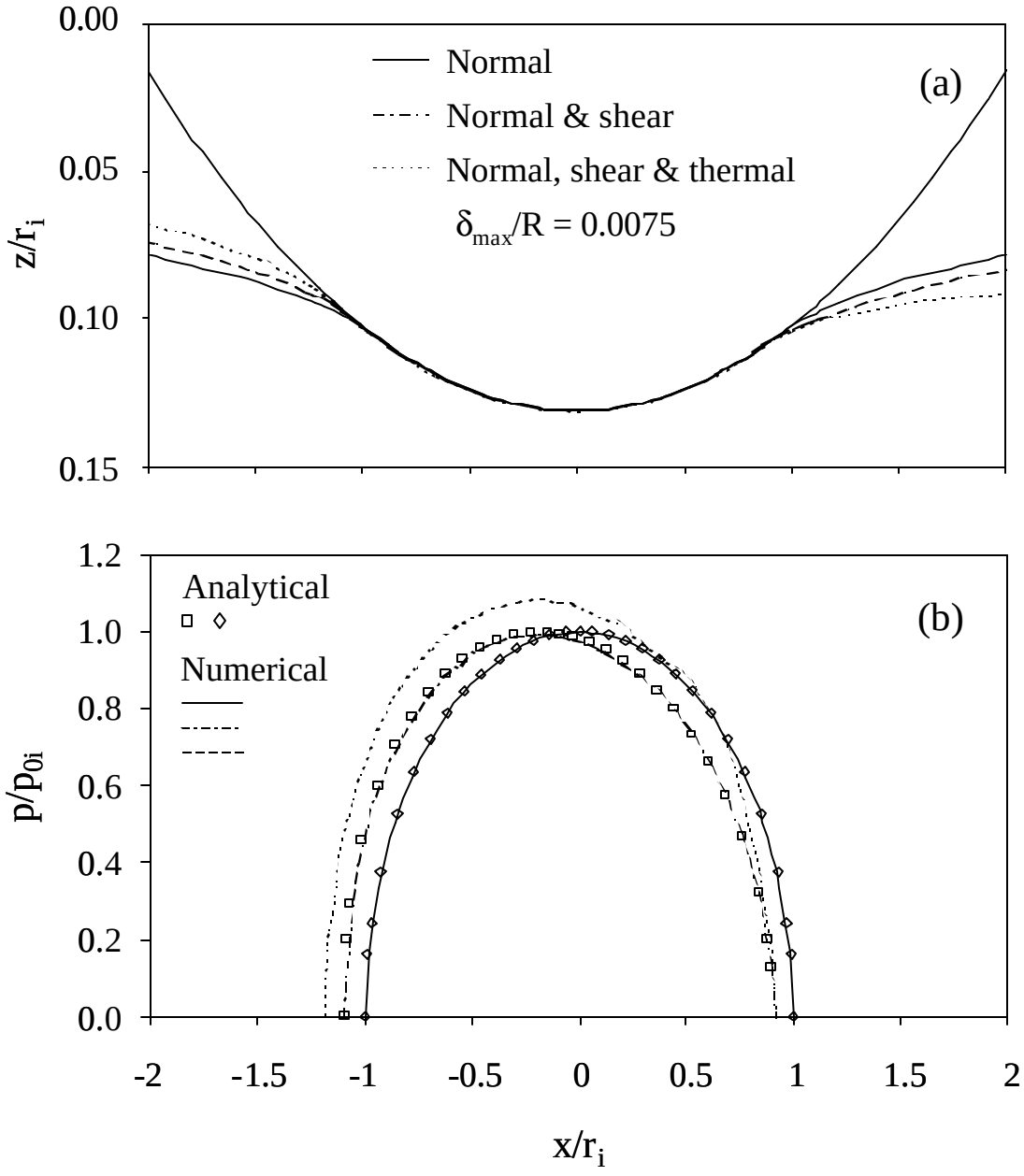

Fig. 5.4 Dimensionless (a) surface displacement z/r_i and (b) contact pressure p/p_{0i} distribution due to different loadings for elastic semi-infinite solid in contact with a rigid asperity (d_{max}/R = 0.0075 and Pe = 0.05).

and the present analysis occurs at x/r_i = 0.092 and 0.088, respectively. The good agreement between numerical and theoretical results for the contact pressure distribution illustrates the accuracy of the piecewise-linear distribution of the contact pressure profile obtained by superposition of overlapping triangular pressure elements. For fixed surface interference, frictional heating increases both the contact area and the contact pressure. This is expected because frictional heating causes thermal expansion due to the development of temperature gradients, which increases both the contact area and the contact pressure.

Figure 5.5 shows the variation of the surface temperature distribution with Peclet

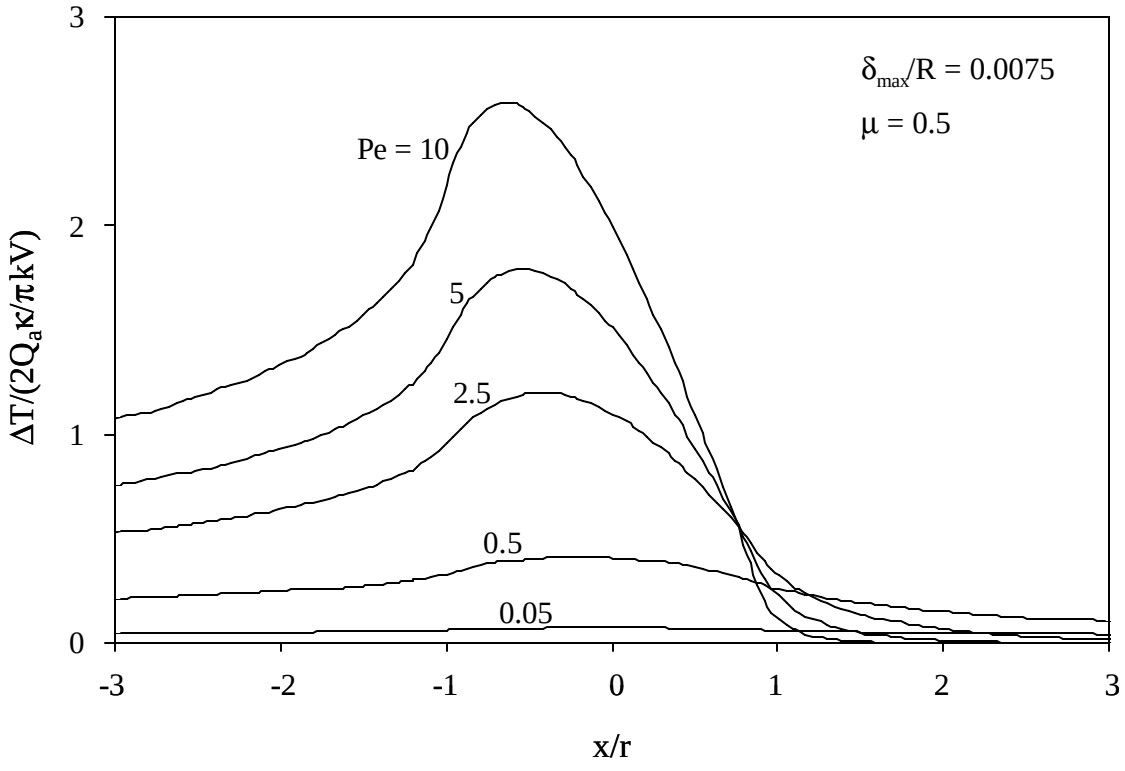

Fig. 5.5 Dimensionless temperature rise $\Delta T/(2Q_a k/pkV)$ at the surface of elastic semi-infinite solid due to sliding contact with a rigid asperity versus Peclet number (m = 0.5 and $d_{\max}/R$ = 0.0075).

number for m = 0.5 and $d_{\max}/R$ = 0.0075. In this figure, as well as in subsequent figures, temperature results are presented in the form of temperature rise above room temperature, ΔT, normalized by $2Q_a k/pkV$, where Q_a is the average heat flux rate at the contact region (i.e., total heat flux divided by contact area), and x coordinate is normalized by the half-contact width, r. The surface temperature increases significantly with the increase of the Peclet number. For Pe < 0.5, the surface temperature distribution is symmetric, while for Pe > 0.5 the maximum surface temperature shifts from the center toward the trailing edge of the contact region, in agreement with the result of Carslaw and Jaeger (1959) for a moving heat source and the three-dimensional numerical result of Gong and Komvopoulos (2004a) for a spherical indenter sliding on a half-space. Following an approach similar to that for a uniform heat band source (Carslaw and Jaeger, 1959), the temperature rise due to a moving heat band elliptically distributed over region $-l \le x \le l$ was obtained as

$$\Delta T = \frac{Q_0 l}{pk}\int_{-1}^{1}\sqrt{1-h^2}\,e^{-Pe(x+h)}K_0\{Pe[(x+h)^2+z^2]^{1/2}\}dh\,. \tag{5.23}$$

As shown in Fig. 5.5, the normalized maximum temperature rise for Pe = 10 is equal to 2.59, which differs only by 0.4% from the theoretical solution obtained from Eq. (5.23). This provides additional confirmation about the accuracy of the present algorithm. To examine the dependence of the subsurface temperature field on the Peclet number, temperature contours for Pe = 0.05 and 5, m = 0.5, and $d_{\max}/R$ = 0.0075 are contrasted in Fig. 5.6. For relatively low Peclet number (Pe = 0.05), the temperature field is almost symmetric with respect to the contact region (Fig. 5.6(a)). However, for relatively high

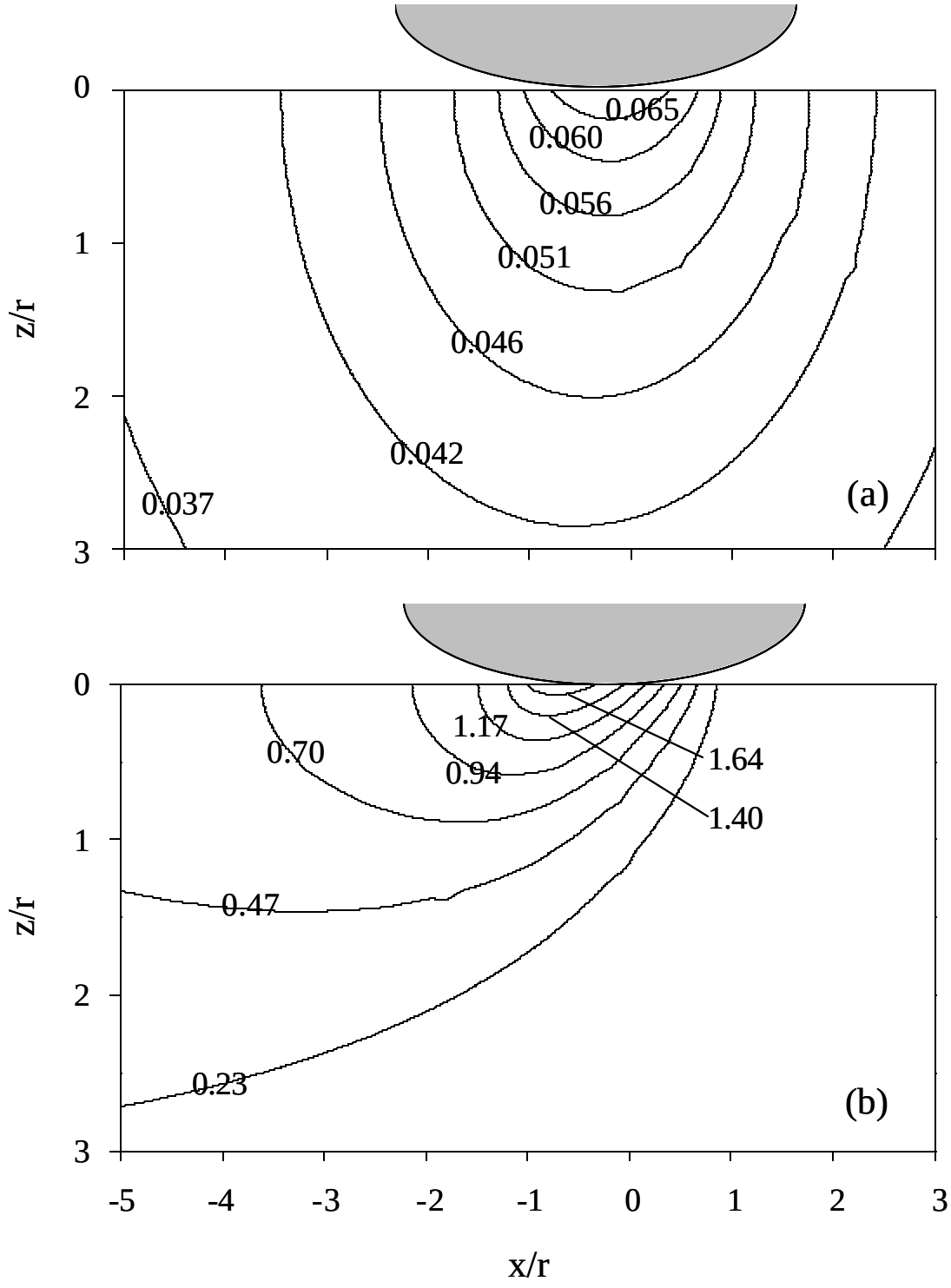

Fig. 5.6 Contours of dimensionless temperature rise $\Delta T/(2Q_a k/pkV)$ in the subsurface of elastic semi-infinite solid due to sliding contact with a rigid asperity (m = 0.5 and $d_{\max}/R$ = 0.0075): (a) Pe = 0.05 and (b) Pe = 5.

Peclet number (Pe = 5), the temperature field is greatly distorted and the maximum temperature arises at the trailing edge of the contact region (Fig. 5.6(b)). In addition, the temperature field intensifies significantly with the increase of the Peclet number.

The effect of frictional heating on the surface stress s_{xx} is illustrated in Fig. 5.7 for m = 0.5 and $d_{\max}/R$ = 0.0075. The surface stress s_{xx} was normalized by the maximum contact pressure, p_0, and x coordinate by the half-contact width in the elastic analysis, r_0. Frictional heating yields a profound decrease of the surface tensile stress at the trailing edge of the contact region (Pe = 49). Such high Peclet number produces a compressive s_{xx} stress in the wake of the contact region, where, in the absence of frictional heating, the stress is tensile (elastic case). Therefore, surface originating cracks are less likely to

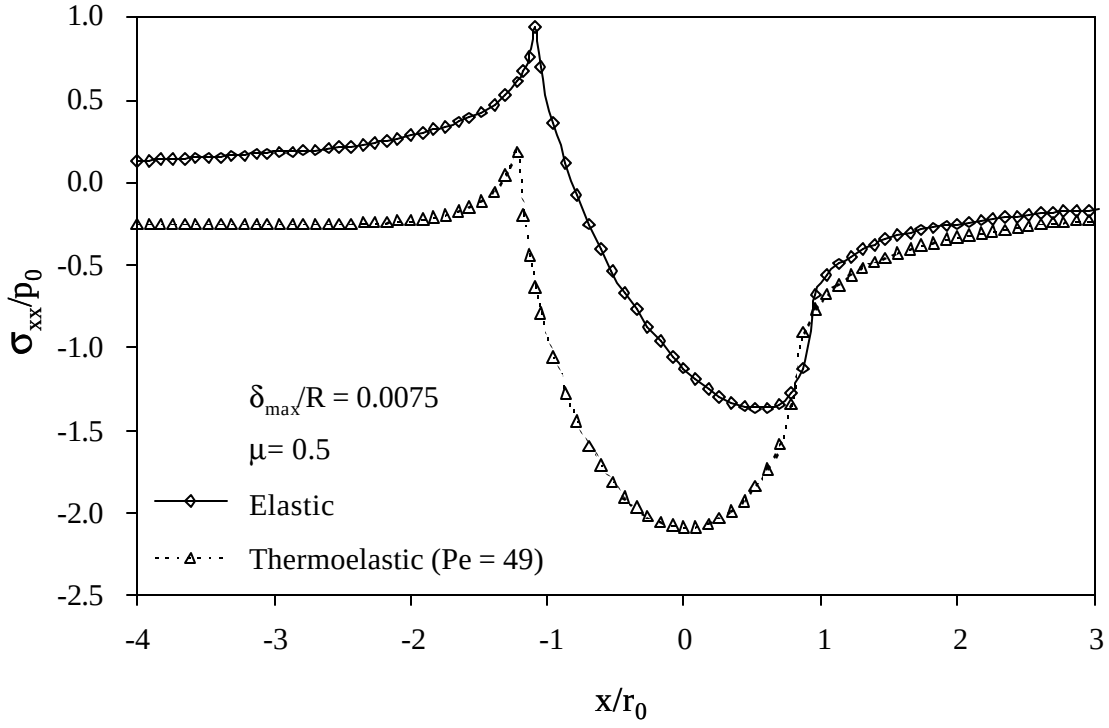

Fig. 5.7 Dimensionless s_{xx}/p_0 stress at the surface of elastic semi-infinite solid due to sliding contact with a rigid asperity (m = 0.5 and $d_{\max}/R$ = 0.0075). Solid and discontinuous curves represent elastic and thermoelastic (Pe = 49) results, respectively.

occur under conditions promoting significant frictional heating (e.g., high Peclet number).

Figure 5.8 shows the effect of frictional heating on the subsurface von Mises equivalent stress, s_M, for $m = 0.5$ and $d_{\max}/R = 0.0075$. (The same stress levels were used for comparison purposes.) The Mises stress was normalized by the maximum contact pressure, p_0, and x and z coordinates by the half-contact width in the elastic analysis, r_0. Frictional heating (Pe = 49) intensifies the subsurface stress field. This is because the compressive stress field due to frictional heating enhances significantly the stresses below the contact region. The results shown in Fig. 5.8 are consistent with the finite element results of Ye and Komvopoulos (2003) that also showed an increase of the Mises stress due to frictional heating. The maximum value of s_M/p_0 in the thermoelastic analysis is equal to 1.42, which is 48% higher than the value obtained from the elastic analysis. The dimensionless maximum tensile stress, $s_{xx}^{\max}/p_0$, and maximum von Mises equivalent stress, $s_M^{\max}/p_0$, at the surface of the semi-infinite solid are plotted as functions of Peclet number in Fig. 5.9 for $m = 0.5$ and $d_{\max}/R = 0.0075$. It is noted that $s_{xx}^{\max}$ decreases while $s_M^{\max}$ increases with the increase of the Peclet number due to the significant compressive stress induced by frictional heating. Hence, in the case of metals or polymers and sliding conditions favoring high Peclet number, surface plasticity is more likely to occur than surface cracking.

5.3.2 Rough Surface Sliding

Unless otherwise stated, the numerical results for rough-surface sliding presented

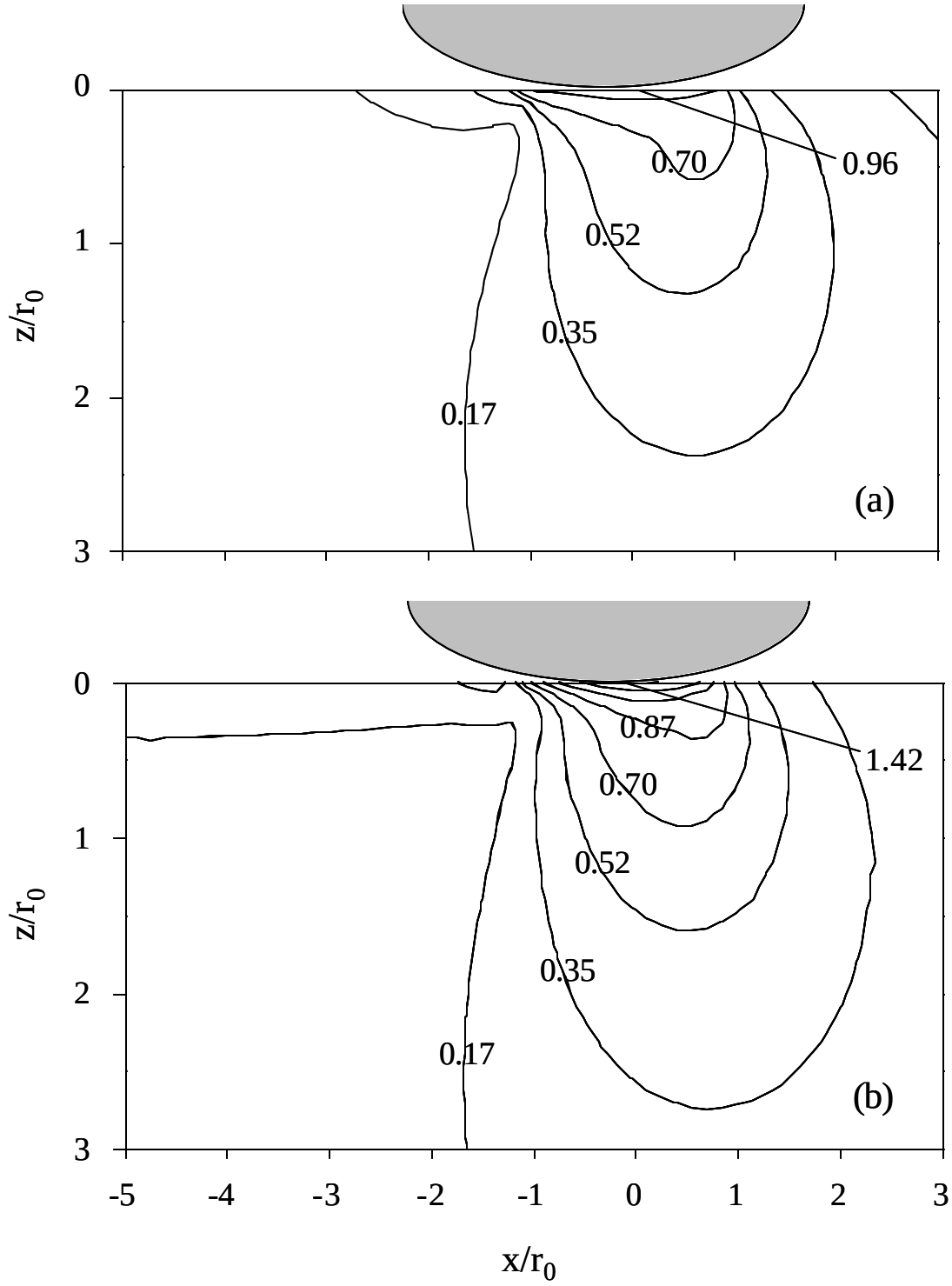

Fig. 5.8 Contours of dimensionless von Mises equivalent stress s_M/p_0 in the subsurface of elastic semi-infinite solid due to sliding contact with a rigid asperity (m = 0.5 and $d_{\max}/R$ = 0.0075): (a) Pe = 0 and (b) Pe = 49.

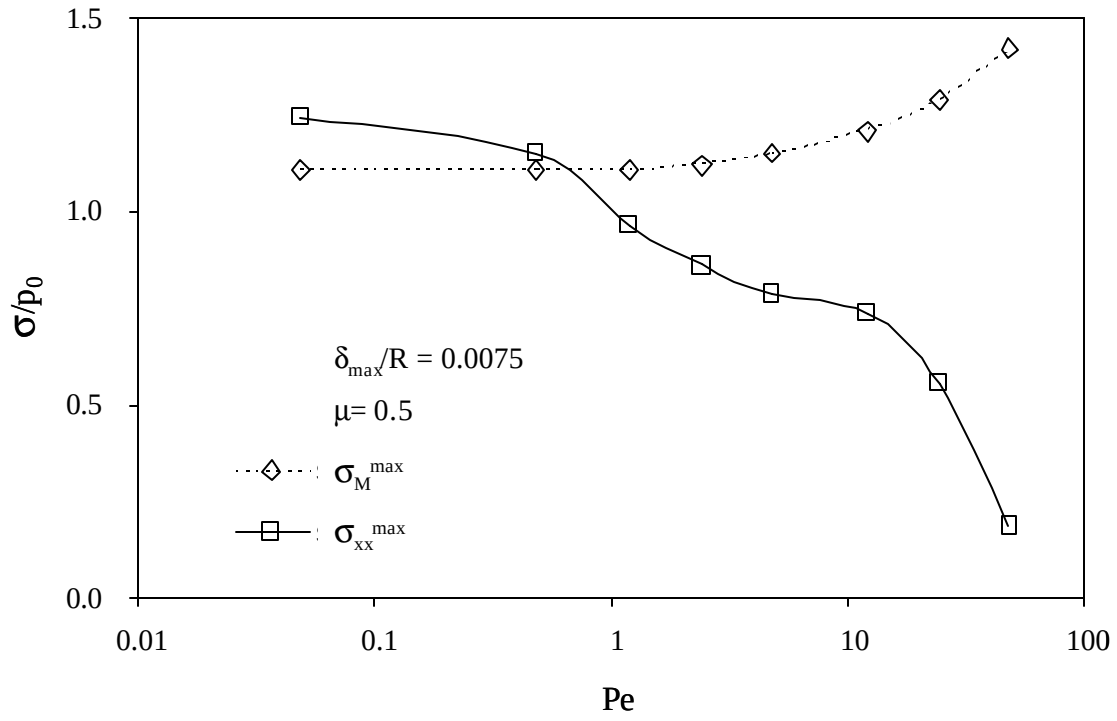

Fig. 5.9 Dimensionless maximum tensile stress $s_{xx}^{\max}/p_0$ and maximum von Mises equivalent stress $s_M^{\max}/p_0$ at the surface of elastic semi-infinite solid in sliding contact with a rigid asperity versus Peclet number (m = 0.5 and $d_{\max}/R$ = 0.0075).

in this section are for $d_{\max}$ = 1.5 nm, L = 5 μm, D = 1.44, and $G = 9.46 \times 10^{-4}$ nm. These values of the fractal parameters are typical of the surface topographies of magnetic recording heads (Komvopoulos, 2000). Based on the value of $n_{\max}$ (= int[log(L/L_s)/log$g$]), the number of terms in Eq. (4.1) used to generate the rough surface was set equal to 15. For generality, results for the temperature rise are shown in dimensionless form, $\Delta T/(2Q_a k/\pi kV)$.

Figure 5.10 shows the surface deformation of the elastic half-space due to sliding of a rough surface from left to right for different types of loading. Figure 5.10(a) shows the establishment of four asperity microcontacts in the contact region. The high

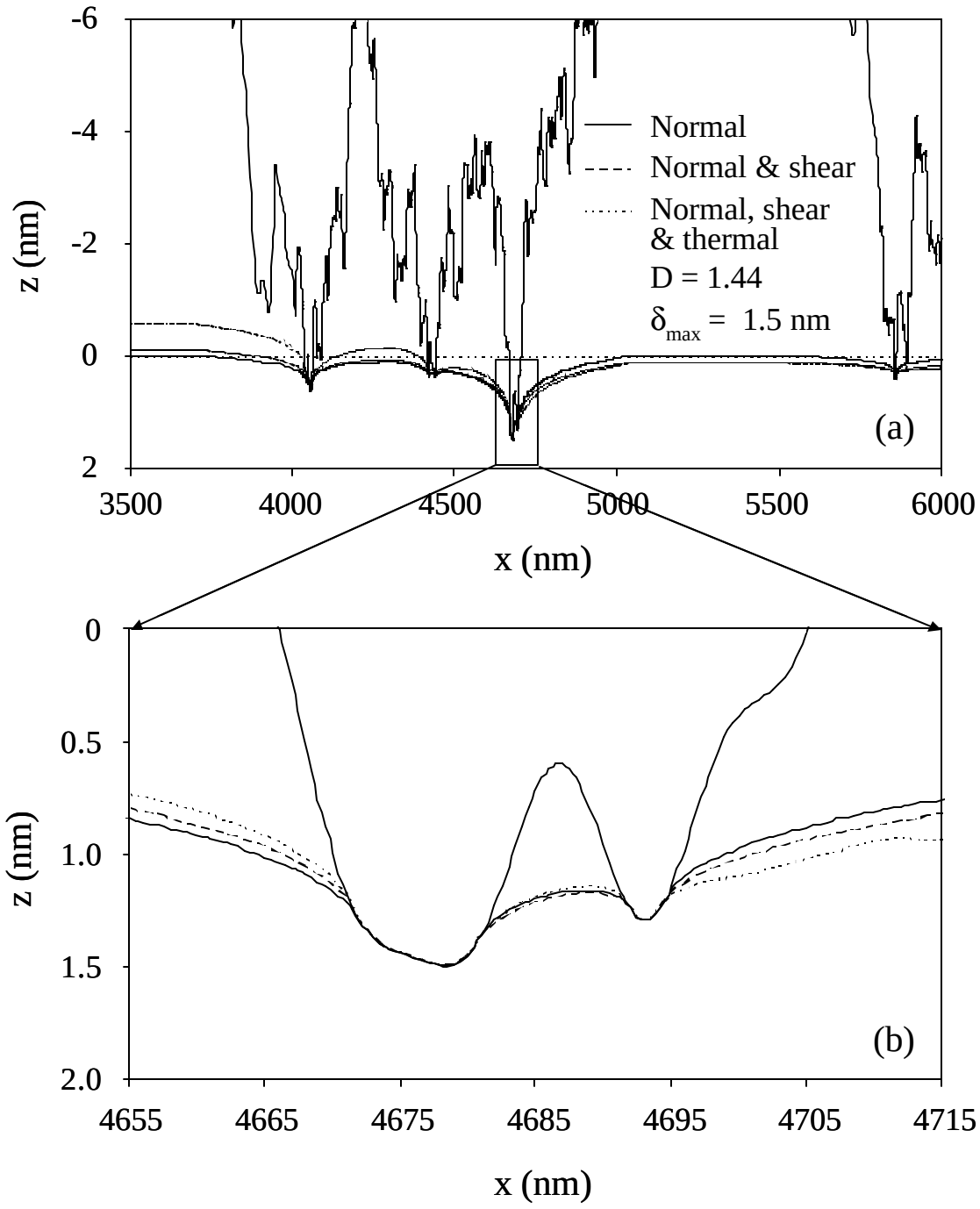

Fig. 5.10 (a) Deformed surface and (b) portion of interfacial region of elastic semi-infinite solid subjected to different loadings by a rigid rough (fractal) surface (D = 1.44, $G = 9.46 \times 10^{-4}$ nm, m = 0.5, d_{max} = 1.5 nm, and Pe = 0.06).

magnification of a region of the surface profile shown in Fig. 5.10(b) demonstrates that the deformed surface follows very closely the contour of the rough surface. The exact match between the deformed surface of the half-space and the rough surface illustrates the accuracy of the algorithm. For pure normal indentation (m = 0) the total contact width is equal to 23.6 nm, and increases to 28.8 nm with the occurrence of frictional heating (m = 0.5 and Pe = 0.06). This is a consequence of surface pile-up due to frictional heating that increases the real contact area, especially at the trailing contact region where thermoelastic distortion is more pronounced.

To illustrate the significance of frictional heating on the pressure distributions at asperity microcontacts, contact pressure profiles are shown in Fig. 5.11 for m = 0.5 and Pe = 54. The four plots in Fig. 5.11 show contact pressure distributions corresponding to the four contact regions shown in Fig. 5.10. Numerical results for thermoelastic and elastic sliding contact are indicated by solid and discontinuous curves, respectively. The contact pressures and microcontact areas predicted by the thermoelastic analysis are larger than those obtained from the elastic analysis. This is mostly pronounced at the fourth asperity microcontact (region 4) and is attributed to the greater cumulative effect of frictional heating at the trailing contact region.

Figure 5.12 shows the Peclet number effect on the distribution of dimensionless surface temperature rise due to sliding (m = 0.5). For convenience, the corresponding regions of the rigid rough surface are also shown at the top of Fig. 5.12. For low Peclet number (Pe = 0.06) the temperature at the front of the contact region is quite close to that encountered in the wake of sliding, i.e., the temperature distribution is approximately symmetric within each microcontact area (Fig. 5.12(a)). However, in the case of

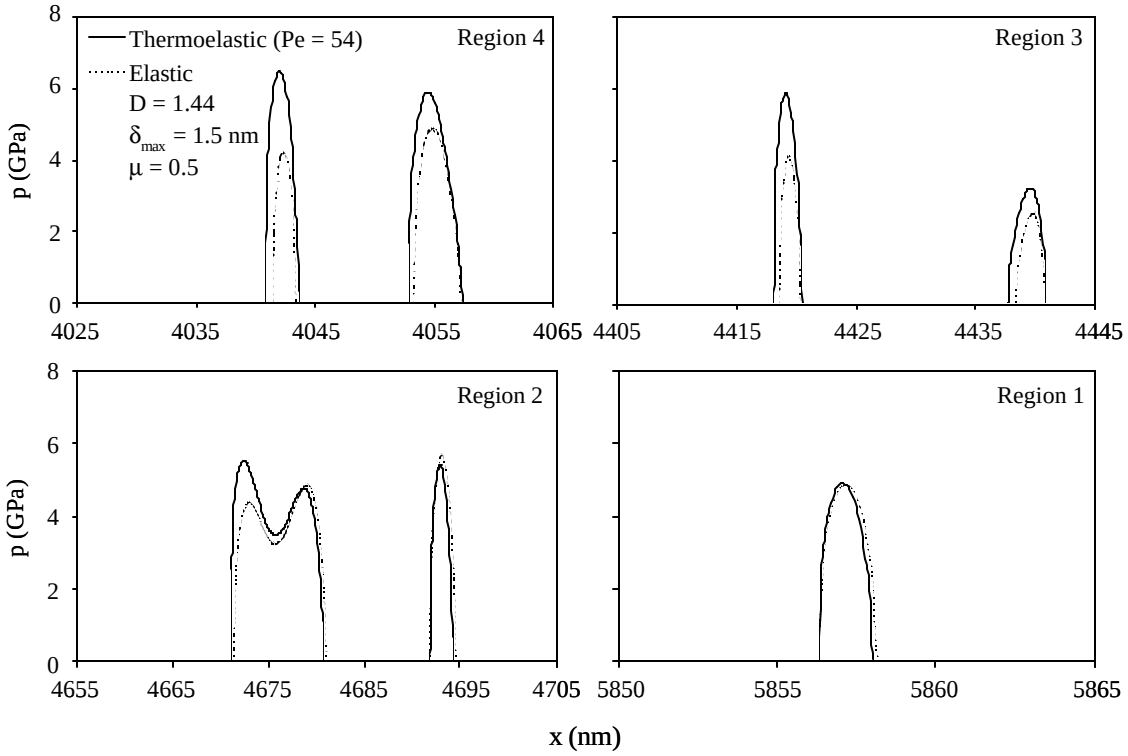

Fig. 5.11 Contact pressure profiles on elastic semi-infinite solid in normal contact with a rigid rough (fractal) surface (D = 1.44, G = 9.46 × 10^{-4} nm, m = 0.5, and d_{max} = 1.5 nm). Solid and discontinuous curves represent thermoelastic (Pe = 54) and elastic results, respectively.

relatively high Peclet number (Pe = 6), the temperature rise in the wake of sliding is significantly higher than that at the contact front (Fig. 5.12(b)), consistent with the single-asperity results (Fig. 5.5). In addition, the surface temperature for Pe = 6 is much higher than that for Pe = 0.06, evidently due to the more pronounced effect of frictional heating. For both low and high Peclet numbers, the maximum temperature rise at the surface occurs at the second microcontact (region 2) due to the correspondingly much larger contact area (Fig. 5.11). Figure 5.12(b) shows that, contrary to the first and second microcontacts (regions 1 and 2, respectively), the temperature at the front of the third and

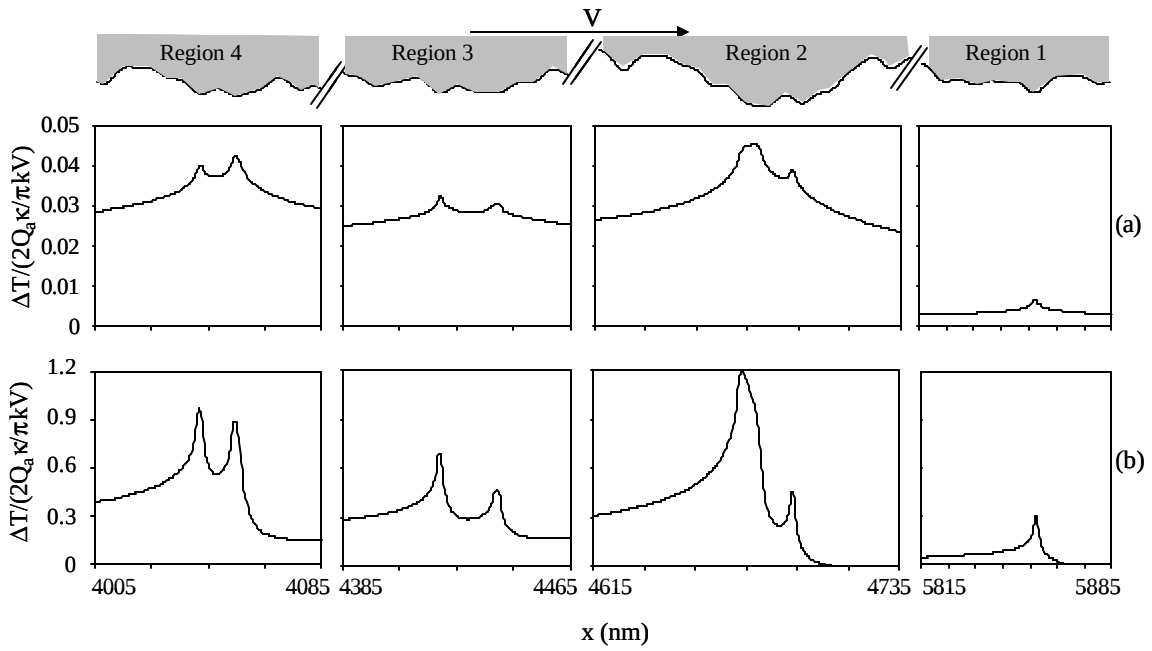

Fig. 5.12 Dimensionless temperature rise $\Delta T/(2Q_a k/pkV)$ at the surface of elastic semi-infinite solid in sliding contact with a rigid rough (fractal) surface (D = 1.44, G = 9.46 × 10^{-4} nm, m = 0.5, and $d_{\max}$ = 1.5 nm): (a) Pe = 0.06 and (b) Pe = 6.

fourth microcontacts (regions 3 and 4, respectively) does not decrease to zero due to the more pronounced cumulative thermal effect at the trailing contact region.

Contours of normalized temperature rise, $\Delta T/(2Q_a k/pkV)$, in the subsurface of the semi-infinite medium for Pe = 0.06 and 6, corresponding to the regions shown in Figs. 5.11 and 5.12, are contrasted in Fig. 5.13. For both low and high Peclet numbers, the maximum temperature rise at each microcontact occurs always at the surface. As expected, the temperature rises for Pe = 6 are much higher than those for Pe = 0.06. The appreciably higher temperature gradients produced with the higher Peclet number are responsible for the increase of the thermoelastic surface distortion and the intensification of the thermal stress. Comparison of Figs. 5.13(a) and 5.13(b) shows a profound effect of the Peclet number on the subsurface temperature distribution. The temperature contours

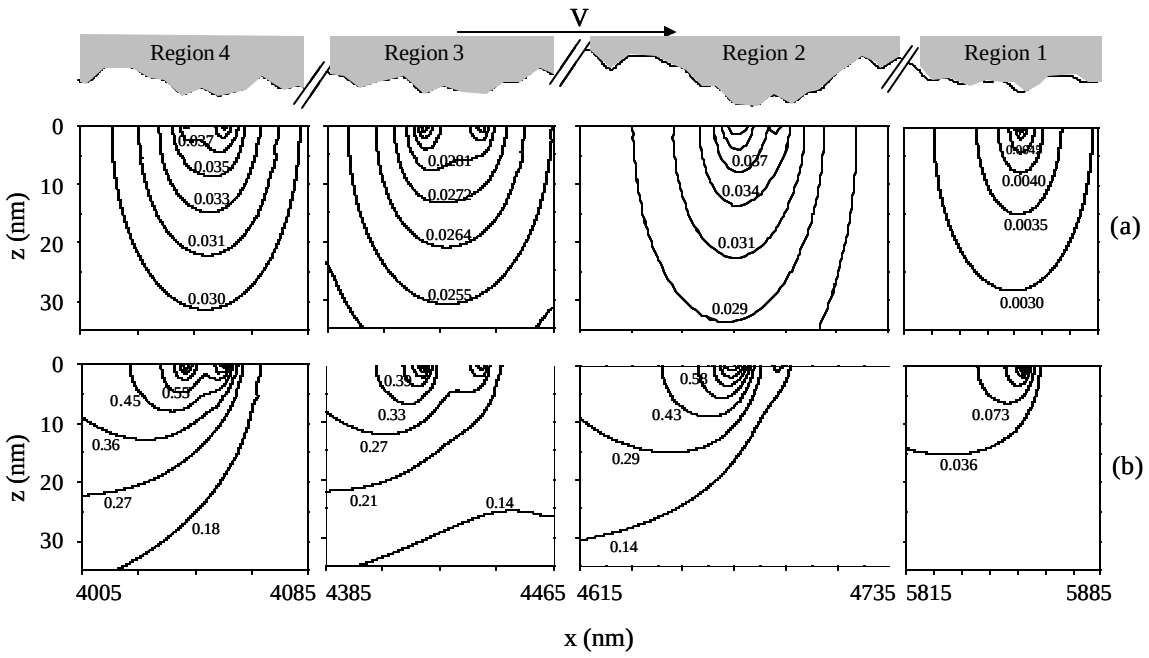

Fig. 5.13 Contours of dimensionless temperature rise $\Delta T/(2Q_a k/pkV)$ in the subsurface of elastic semi-infinite solid in sliding contact with a rigid rough (fractal) surface (D = 1.44, $G = 9.46 \times 10^{-4}$ nm, m = 0.5, and $d_{\max}$ = 1.5 nm): (a) Pe = 0.06 and (b) Pe = 6.

for Pe = 6 are significantly distorted compared to those for Pe = 0.06, which are fairly symmetric.

The significance of the surface topography on the surface temperature rise can be interpreted in light of the dimensionless maximum temperature rise, $DT_{\max}/(2Q_a k/pkV)$, shown as a function of Pe and D in Fig. 5.14. $DT_{\max}$ increases monotonically with the Peclet number due to the increase of frictional heating at the sliding interface. For given Peclet number and maximum surface interference, $DT_{\max}$ increases with the decrease of the fractal dimension. This is due to the dependence of dominant frequencies in the surface profile on the value of D. Smaller D values are associated with rougher surfaces yielding asperity microcontacts of smaller radius of curvature that produce higher mean

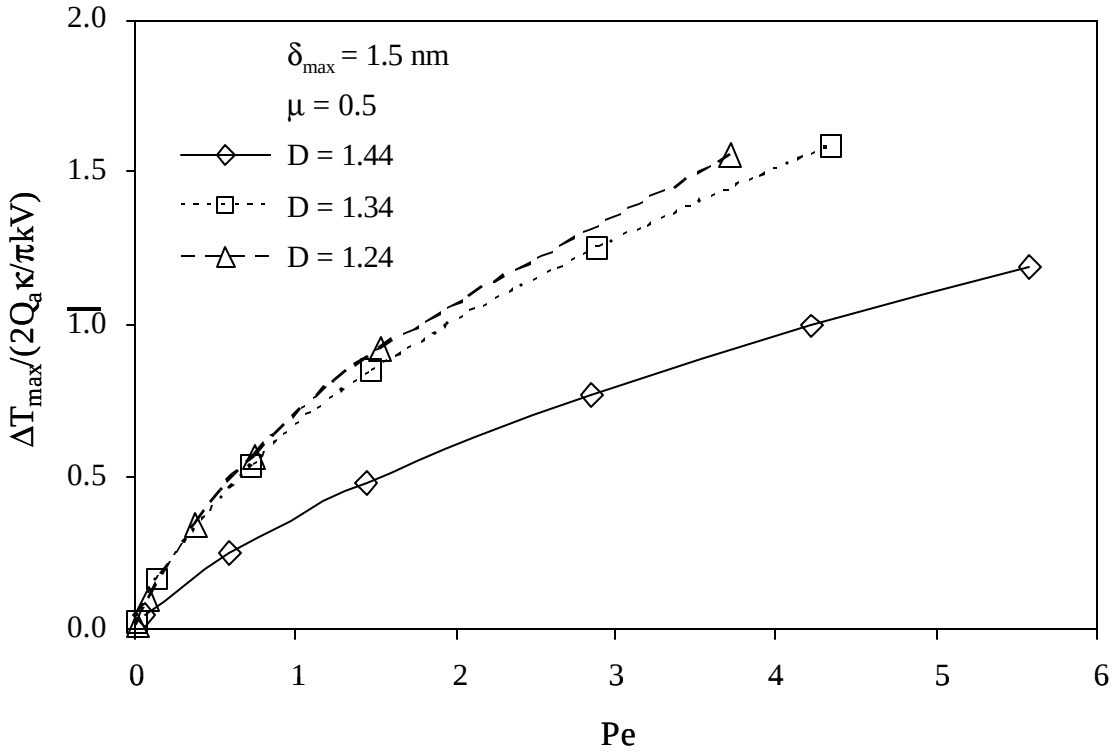

Fig. 5.14 Dimensionless maximum temperature rise $\Delta T_{\max}/(2Q_a k/pkV)$ at the surface of elastic semi-infinite solid in sliding contact with a rigid rough (fractal) surface versus Peclet number and fractal dimension ($G = 9.46 \times 10^{-4}$ nm, $m = 0.5$, and $d_{\max} = 1.5$ nm).

contact pressures and smaller contact areas. For fixed Peclet number, smaller contact areas imply higher sliding speed. Thus, the combination of higher contact pressure and higher sliding speed, obtained with small D values, enhances frictional heating, which, in turn, leads to the increase in the temperature rise at the surface.

Figure 5.15 illustrates the effect of frictional heating on the stress, s_{xx}, at the surface of the semi-infinite medium. Solid curves denote numerical results from the thermoelastic analysis (Pe = 54) and discontinuous curves results from the elastic analysis. Frictional heating decreases the tensile stress at the trailing edge of each microcontact and shifts the location of the maximum tensile stress slightly toward the

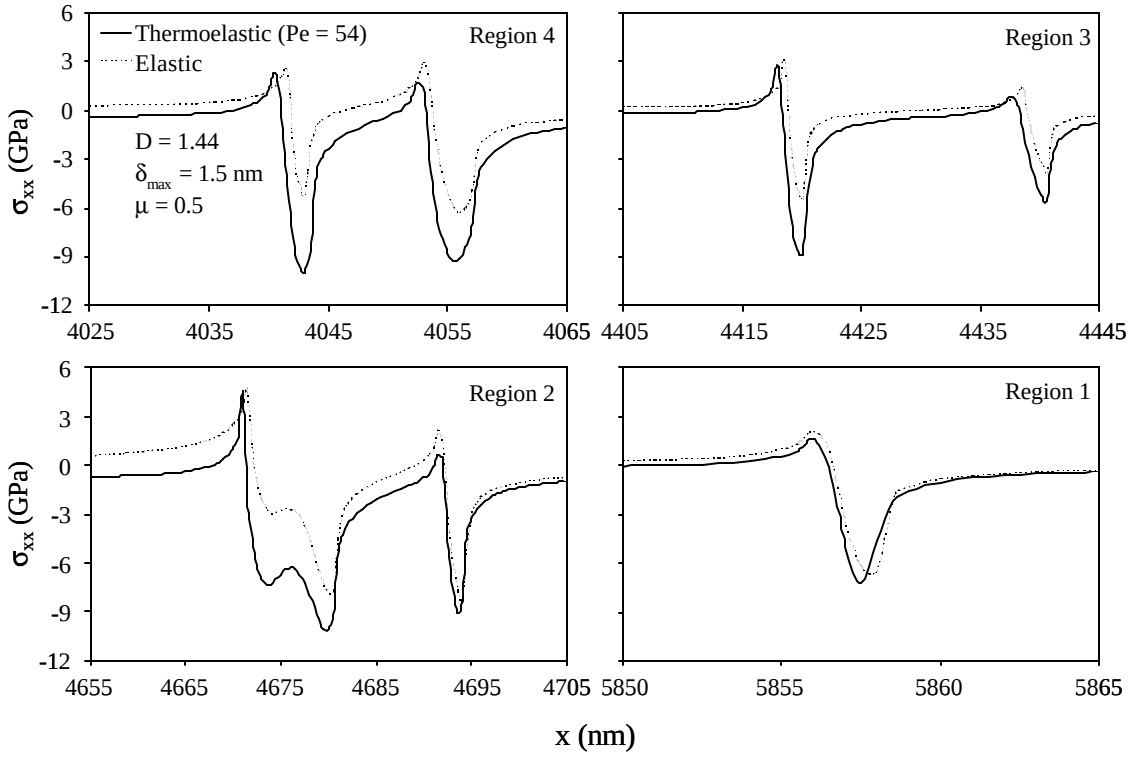

Fig. 5.15 Stress s_{xx} at the surface of elastic semi-infinite solid in sliding contact with a rigid rough (fractal) surface (D = 1.44, G = 9.46 × 10^{-4} nm, m = 0.5, and d_{max} = 1.5 nm). Solid and discontinuous curves represent thermoelastic (Pe = 54) and elastic results, respectively.

trailing contact edge. Again, the largest differences between thermomechanical and mechanical results are encountered in the region with the largest microcontact area (region 2).

Figure 5.16 shows contours of von Mises equivalent stress in the subsurface corresponding to the regions shown in Fig. 5.15. For clarity and comparison purposes, different contour levels were used for each microcontact stress field. Comparison of Figs. 5.16(a) and 5.16(b) shows that frictional heating increases the Mises stress, especially below the third and fourth microcontacts (regions 3 and 4, respectively) where the cumulative effect of frictional heating is greater. The maximum von Mises stress in the

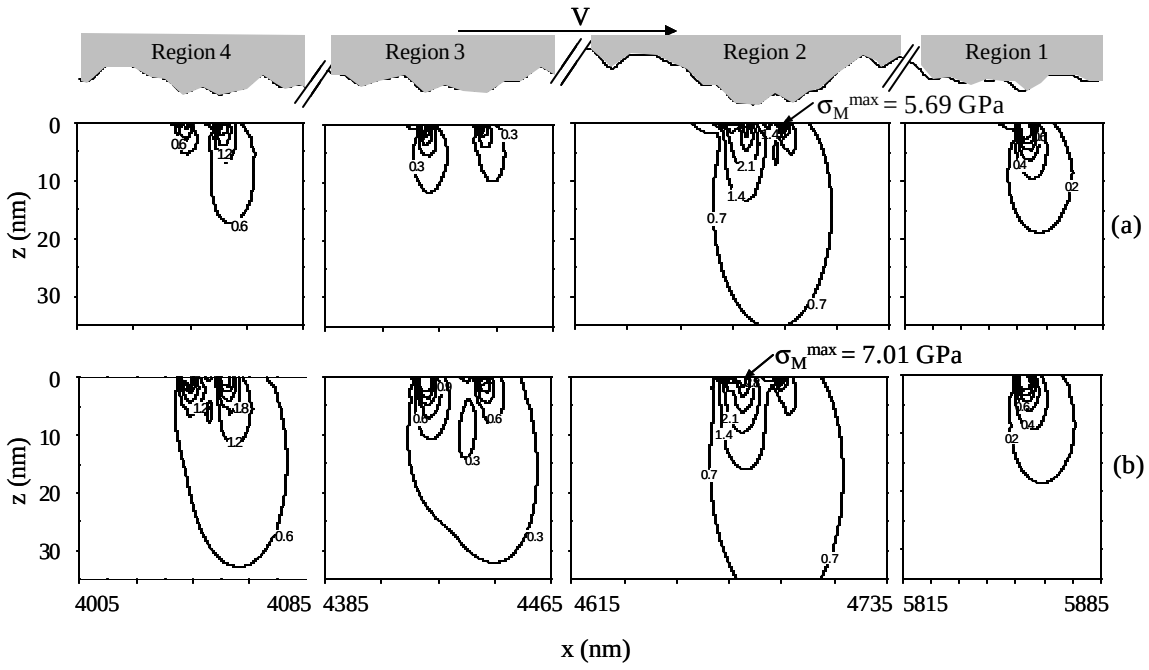

Fig. 5.16 Contours of von Mises equivalent stress, s_M, in the subsurface of elastic semi-infinite solid in sliding contact with a rigid rough (fractal) surface (D = 1.44, G = 9.46 × 10^{-4} nm, m = 0.5, and $d_{\max}$ = 1.5 nm): (a) Pe = 0 and (b) Pe = 54.

thermomechanical analysis is equal to 7.01 GPa (Fig. 5.16(b)), which is 23% higher than that in the elastic analysis (Fig. 5.16(a)). The results shown in Fig. 5.16 are consistent with finite element simulation results of Ye and Komvopoulos (2003) demonstrating that the maximum Mises stress at each microcontact occurs always at the surface for relatively high coefficient of friction (e.g., m = 0.5) and that frictional heating affects the location of the maximum Mises stress, as shown for the second microcontact in Fig. 5.16.

Figure 5.17 shows a comparison between the maximum tensile stress at the surface, $s_{xx}^{\max}$, and the maximum von Mises equivalent stress in the subsurface, $s_M^{\max}$, plotted as functions of Peclet number. The $s_{xx}^{\max}$ stress increases slightly with the increase

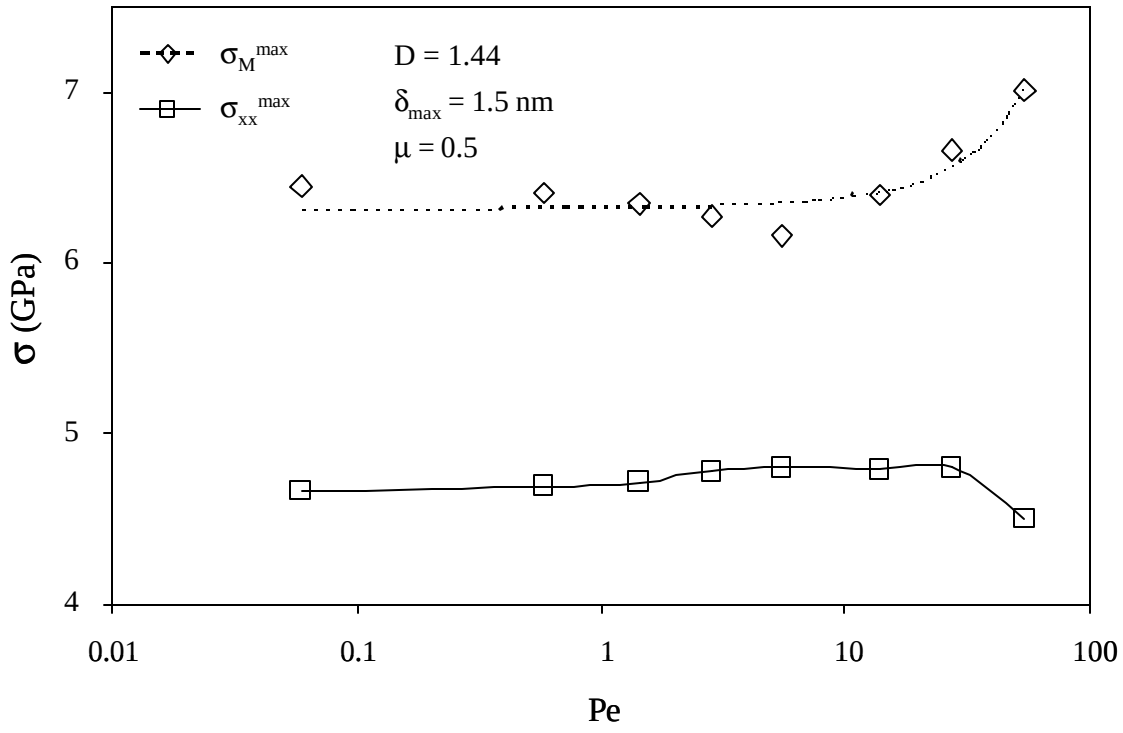

Fig. 5.17 Maximum tensile surface stress, $s_{xx}^{\max}$, and maximum subsurface von Mises equivalent stress, $s_{M}^{\max}$, for elastic semi-infinite solid in sliding contact with a rigid rough (fractal) surface versus Peclet number (D = 1.44, G = 9.46 × 10-4 nm, m = 0.5, and $d_{\max}$ = 1.5 nm).

of the Peclet number in the range of Pe < 20 due to the dominant effect of the increasing mean contact pressure. However, when Pe > 20, $s_{xx}^{\max}$ decreases due to the increase of the compressive thermal stress, which is enhanced by the interaction of neighboring microcontacts. The fact that $s_{M}^{\max}$ increases when Pe > 20 suggests that the contribution of thermal stresses is comparable with that of mechanical stresses. The small variations of $s_{xx}^{\max}$ and $s_{M}^{\max}$ when Pe < 20 suggests that at relatively low and intermediate values of Peclet number the stress field is dominated by mechanical stresses and, therefore, the

effect of thermal stresses due to frictional heating is secondary under these sliding conditions.

5.4 Conclusions

A thermomechanical analysis was presented for semi-infinite elastic solid in sliding contact with a rough surface characterized by fractal geometry. The effect of frictional heating on the contact pressure, temperature rise, and stress field was examined in terms of the Peclet number in light of simulation results for single asperity and rough surface sliding on the elastic medium. Based on the presented results and discussion, the following main conclusions can be drawn.

(1) For fixed surface interference, frictional heating increases both the contact area and the contact pressure. This effect is mostly pronounced at asperity microcontacts at the trailing edge of the contact interface, where the cumulative effect of frictional heating is most pronounced.

(2) For low Peclet numbers (e.g., Pe < 1), the surface temperature distribution at a single asperity contact is fairly symmetric. However, for relatively high Peclet numbers (e.g., Pe > 2.5), the peak temperature shifts toward the trailing edge of the contact region.

(3) The maximum temperature at each microcontact occurs always at the surface and increases with the Peclet number. Intensification of the temperature gradients with the increase of the Peclet number is responsible for the enhancement of thermoelastic distortion of the surface and the development of high thermal stresses. The increase of the Peclet number changes significantly the fairly symmetric temperature field below

each microcontact obtained with low Peclet numbers (e.g., Pe = 0.06). The maximum temperature rise at the surface increases with the decrease of the fractal dimension.

(4) For low Peclet numbers (Pe < 1), the stress field is dominated by the effect of mechanical stresses. Frictional heating decreases the maximum tensile stresses at the trailing edges of asperity microcontacts and shifts slightly their locations towards the trailing contact edge.

(5) The von Mises equivalent stress is strongly affected by frictional heating, especially at microcontact regions close to the trailing contact edge where the highest thermal stresses are produced due to the cumulative heating effect. High friction (m = 0.5) increases the maximum Mises stress at each microcontact and shifts its location to the surface. The increase of the Peclet number promotes surface plastic deformation and reduces the likelihood for surface cracking.

CHAPTER 6

SURFACE CRACKING IN ELASTIC-PLASTIC MULTI-LAYERED MEDIA DUE TO REPEATED SLIDING CONTACT

6.1 Introduction

Coatings are often used to enhance the tribological performance and endurance of various components with contact interfaces. The wear resistance of hard protective coatings, such as ceramics, cemented carbides, and diamond-like carbon, greatly affects the reliability of many mechanical systems. However, the inherent high hardness of these materials is obtained at the expense of low fracture toughness. Consequently, contact fatigue and/or fracture of hard overcoats are dominant failure mechanisms in many mechanical systems subjected to continuous sliding contact, such as gear flanks, bearing surfaces, and hard disk drives.

Contact analysis of layered media subjected to normal and tangential (friction) surface tractions has been the objective of numerous past studies. King and O'Sulllivan (1987) investigated the plane-strain problem of a rigid cylinder sliding over an elastic layered half-space in both in-plane and anti-plane (i.e., along the cylinder axis) directions and found a high tensile stress at the trailing edge of the contact region. Kral and Komvopoulos (1996) performed three-dimensional finite element simulations of a rigid spherical indenter sliding against an elastic-plastic layered medium and discussed the likelihood of transverse (ring) crack formation at the surface in the wake of the indenter. Ring crack formation has been observed on glass along the wake of a sliding conical

indenter (Lawn, 1992) and on the surface of carbon-coated magnetic rigid disks subjected to microscratching (Wu, 1991). Gong and Komvopoulos (2003) used the finite element method to analyze normal and sliding contact of a rigid cylindrical asperity on a patterned elastic-plastic layered medium. The high surface tensile stress at the trailing edge of the contact region indicated a greater probability of surface cracking in patterned layered media compared to smooth-surface media. In a three-dimensional thermomechanical analysis of Gong and Komvopoulos (2004a), a high thermal tensile stress was predicted slightly below the trailing edge of the contact region, which is considered to be responsible for the initiation of thermal cracking in the wake of sliding microcontacts.

Although the contact stress/strain field in layered media has been extensively investigated, fracture mechanics studies are relatively sparse and limited to homogenous and brittle (elastic) half-spaces. Several fracture analyses of homogenous media (Keer and Worden, 1990; Keer and Kuo, 1992; Chen et al., 1991; Bower and Fleck, 1994) have shown that crack initiation is favored at the trailing edge of the contact region, where the maximum tensile stress arises during sliding. Beuth and Klingbeil (1996) performed a plane-strain fracture analysis of an elastic thin film bonded to an elastic-plastic substrate and observed that substrate yielding increased the likelihood of film cracking due to the increase of the energy for crack growth in the film. Oliveira and Bower (1996) studied fracture and delamination of thin coatings due to contact loading and reported a greater probability for fracture originating from flaws in the coating than the substrate or the interface. It was also found that the fracture load and crack pattern were strongly affected by the elastic property mismatch between the layer and the substrate materials.

Surface crack growth due to repeated sliding contact resembles a fatigue process in which the crack propagation rate is proportional to a power of the stress intensity factor (SIF) range, ΔK. Experiments by Mageed and Pandey (1992) have shown that the crack propagation direction due to mixed mode cyclic loading can be determined from the maximum tensile stress criterion, which depends on ΔK_I and ΔK_{II}. Alfredsson and Olsson (2000) performed experimental and numerical studies of normal contact fatigue caused by the formation of ring/cone and lateral cracks and discovered that surface crack growth occurred in the direction where the shear SIF was close to zero and that the propagation rate was dominated by ΔK_I. Lin and Smith (1999a, 1999b) conducted a finite element fatigue analysis of surface cracked plates and obtained results for the SIF and fatigue life. Ko et al. (2001) studied both experimentally and analytically crack growth and wear particle formation on sliding steel surfaces and reported that the analytical predictions for the wear particle size and wear volume were in fair agreement with experimental results.

Despite valuable insight into surface cracking in thin coatings obtained from earlier studies, very little is known about the effect of plastic deformation in the underlying material (layer or substrate) on the growth direction of surface cracks. In addition, the effects of friction, initial crack length, and crack growth on the accumulation of plasticity in the underlying medium have not been considered in previous fracture mechanics analyses. Therefore, the objective of this investigation was to analyze surface cracking in a multi-layered medium due to repetitive sliding of a rigid asperity using the finite element method. SIF and crack propagation results are presented in terms of coefficient of friction at the contact region and crack interface and initial crack length.

Another goal of this study was to develop a fracture mechanics approach that yields estimates of contact fatigue life for elastic-plastic multi-layered media undergoing surface cracking due to repetitive sliding contact.

6.2 Modeling Procedures

6.2.1 Problem Definition and Finite Element Model

Normal and shear tractions produced between contacting rough surfaces are transmitted through asperity microcontacts with statistical distributions depending on the effective surface roughness, normal load, and material properties of the interacting surfaces. When the average asperity spacing is significantly larger than the mean microcontact size, interaction of the stress/strain fields of neighboring microcontacts is secondary (Komvopoulos and Choi, 1992) and the problem is simplified to that of a single asperity in contact with a layered medium. Figure 6.1 shows schematically an asperity sliding over a layered medium containing a crack of initial length c_i perpendicular to the free surface of the medium. The position of the asperity relative to the crack is denoted by y_P (Fig. 6.1).

Plane-strain sliding simulations were performed with a two-dimensional finite element mesh, such as that shown in Fig. 6.2(a), consisting of approximately 9,000 eight-node, isoparametric, quadrilateral elements (depending on the initial crack length and crack propagation path). The horizontal and vertical dimensions of the mesh are equal to $2.4R$ and $3.1R$, respectively, where R is the radius of the rigid asperity (assumed constant in all simulations). The nodes at the bottom boundary of the mesh were constrained against displacement in the vertical direction, while the nodes at the left boundary were constraint against displacement in the horizontal direction. The mesh was refined at the

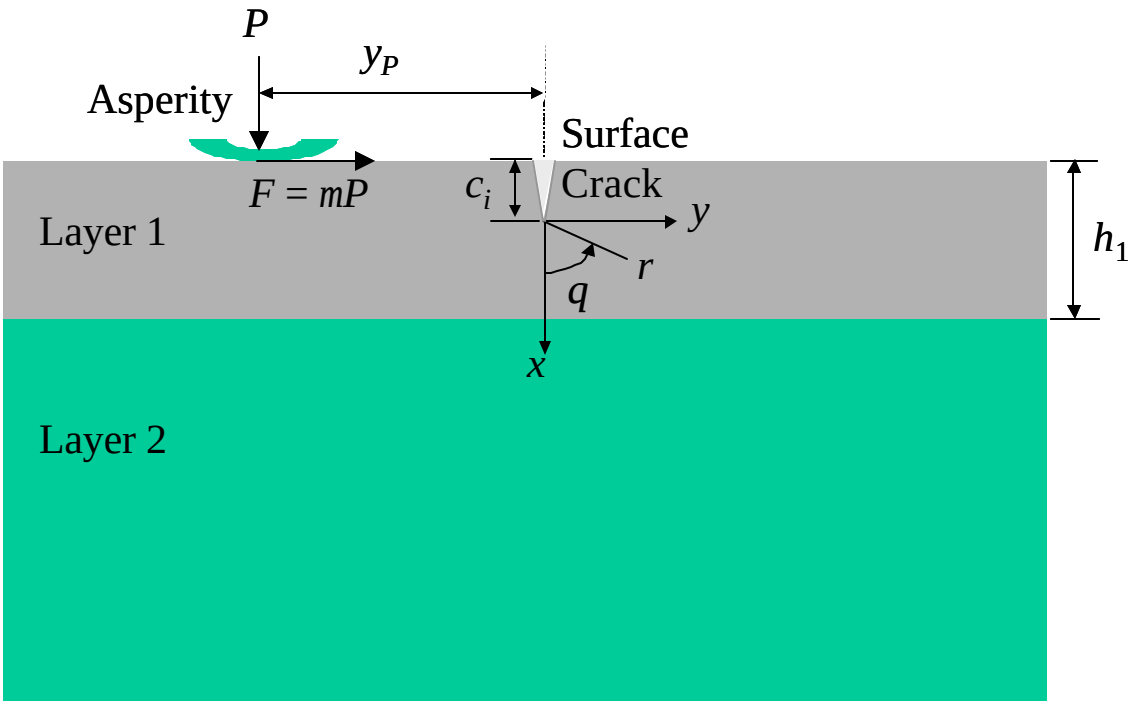

Fig. 6.1 Schematic of a cylindrical rigid asperity sliding over a layered medium with a crack perpendicular to the free surface.

surface in order to increase the accuracy in the calculation of the contact area and stress/strain field in the highly stressed surface layer. The mesh was further refined around the crack, as shown in Fig. 6.2(b) for a propagating crack. In the vicinity of the crack tip, the mesh consists of 36 eight-node, isoparametric, collapsed quadrilateral plane-strain elements with their midside nodes adjacent to the crack tip displaced to the quarter-point distance in order to simulate the square root singularity of the stress field at the crack tip (Henshell and Shaw, 1975; Barsoum, 1976). Since the analysis is based on linear fracture mechanics, the crack-tip nodes were constrained to move together in order to prevent crack-tip blunting during crack growth.

Special contact elements were used to model contact or separation between

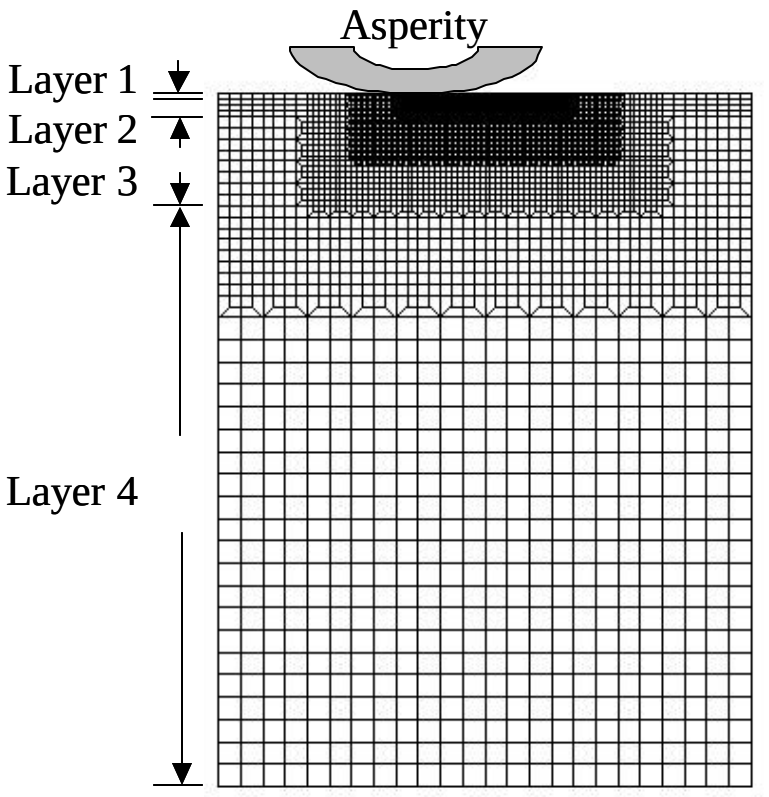

(*a*)

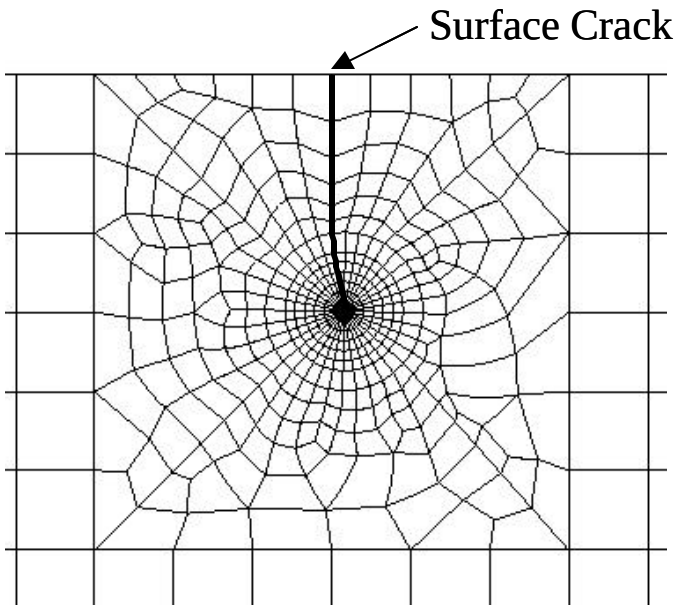

(*b*)

Fig. 6.2 (a) Finite element discretization of a multi-layered medium with a surface crack, and (b) refined mesh in the vicinity of the propagating surface crack.

surface nodal points and the surface of the rigid asperity, based on the measurement of the relative distance of the two surfaces in the normal direction. If the obtained distance was less than the specified tolerance, it was assumed that contact was established and the appropriate contact force was applied at the corresponding node. The local surface overclosure (i.e., displacement of a nodal point at the surface of the deformable medium into the rigid surface) and relative slip were obtained at each integration point of the contact elements. These kinematics were used in conjunction with appropriate Lagrange multiplier techniques to model surface interaction.

To examine the accuracy of the finite element model, especially the mesh around the crack tip, the classical problem of an edge-cracked medium subjected to far-field tension in the direction perpendicular to the crack plane was solved using the finite element mesh shown in Fig. 6.2. The entire mesh was modeled as a homogeneous elastic material. The value of the mode I SIF obtained from the finite element analysis was found to differ from the analytical solution (Hertzberg, 1996) by only 2.3 percent, indicating the suitability of the finite element model for fracture analysis.

6.2.2 Material Properties and Plasticity Models

The thickness, h, elastic modulus, E, and yield strength, s_Y, of each layer in the multi-layered medium are given in Table 6.1. These thickness and mechanical property values are typical of layers used in magnetic rigid disks consisting of carbon overcoat (layer 1), CoCrPt magnetic medium (layer 2), CrV underlayer (layer 3), and NiP (layer 4) electroplated on Al-Mg substrate. The von Mises yield criterion was used to determine whether yielding occurred at a material point. In the present model, the first layer was assumed to be elastic, while all the other layers were modeled as elastic-perfectly plastic.

Table 6.1. Thickness and material properties of each layer in the multi-layered medium

Layer	*h/R*	*E* (GPa)	s_Y (GPa)
1	0.025	260	-
2	0.078	130	2.67
3	0.4	140	2.58
4	2.6	160	2.67

6.2.3 Calculation of Stress Intensity Factors

In linear elastic fracture mechanics, the normal and shear stresses at the crack tip due to sliding contact can be expressed in terms of the tensile (mode I) and shear (mode II) SIFs, K_I and K_{II}, respectively, defined as

$$K_I = \lim_{r \to 0} \sqrt{2pr}\, s_{yy}(r, q) \tag{6.1}$$

$$K_{II} = \lim_{r \to 0} \sqrt{2pr}\, t_{xy}(r, q), \tag{6.2}$$

where r and q are cylindrical polar coordinates and x and y are Cartesian coordinates at the crack tip (Fig. 6.1). Based on the method proposed by Chan et al. (1970), the magnitudes of K_I and K_{II} were determined from linear extrapolation of least-square line fits to the s_{yy} and t_{xy} stress data calculated at ten nodes in the vicinity of the crack tip along the crack plane ($q = 0$). The accuracy of this method has been evaluated in an earlier finite element analysis of Komvopoulos and Cho (1997) dealing with subsurface crack propagation in a half-space due to a moving asperity.

6.2.4 Crack Growth Rate and Fatigue Life

The crack growth rate was assumed to follow a power-law relationship (Paris and Erdogan, 1963)

$$\frac{dc}{dN} = A(\Delta K)^m, \tag{6.3}$$

where N is the number of loading cycles (representing the number of asperity passes required for the crack to propagate by an infinitesimal distance, dc), and A and m are material constants.

Integration of Eq. (6.3) yields a fatigue life relation,

$$\int_0^{N_f} dN = \int_{c_i}^{c_f} \frac{dc}{A(\Delta K)^m}, \tag{6.4}$$

where N_f is the number of fatigue cycles required for the crack to grow from an initial length c_i to a length c_f. Since ΔK depends on the specific geometry, external loading, and crack length, it is not possible to obtain accurate estimates of fatigue life using Eq. (6.4). To circumvent this difficulty, an Euler integration algorithm was adopted in the numerical simulations,

$$N_{j+1} = N_j + \frac{\Delta c}{A\left[\Delta K(c_j)\right]^m} \qquad j = 0,1,\cdots,r \tag{6.5}$$

and

$$c_{j+1} = c_j + \Delta c \ , \tag{6.6}$$

where c_j is the crack length in the jth crack growth cycle, and Δc is the crack growth increment, which is constant in each simulation. The effect of the crack growth increment on the crack propagation path is discussed in a later section.

6.2.5 Simulation of Sliding Contact and Crack Growth

Simulations were performed with the finite element code ABAQUS (version 5.8). Each simulation consisted of three sequential steps. First, the rigid asperity was incrementally advanced into the medium to a specified depth and then displaced tangentially over the neighborhood of the surface crack by a distance approximately equal to eight times the half-contact width. Finally, the asperity was unloaded following the same incremental path as for the loading. These simulation steps were repeated in the same order for several cycles in order to model repetitive sliding. To examine the dependence of the SIFs on friction, the coefficient of friction between the surface of the multi-layered medium and the asperity, m, and the crack faces, m_c, was varied between 0 and 0.5. In order to study the effect of the initial crack length on the SIF distributions and crack propagation direction, four initial crack lengths (i.e., c_i/h_1= 0.125, 0.25, 0.5, and 0.875) were used in the finite element model. After each loading cycle, the mesh around the crack tip was modified to account for the growth of the crack by the specified increment in the direction of maximum tensile SIF range, $\Delta K_s^{\max}$, determined during the particular loading cycle.

To account for the deformation history effect on the SIF ranges, crack propagation, and evolution of plasticity in the second layer, the stress/strain state in the multi-layered medium generated after a given number of cycles was included in the subsequent loading cycle by using the following method. First, sliding of the asperity over the modified mesh was simulated with all the nodes of the kink faces locked together. Then, the nodes of the first kink were unlocked and asperity sliding over the medium was simulated again following exactly the same path. This procedure was

repeated until all the kinks were unlocked sequentially. Finally, a new crack growth increment was simulated in the next sliding cycle. In view of the excessive computational time of these crack growth simulations, only one initial crack length (c_i/h_1 = 0.25), but different crack growth increments, were modeled in this study. A simulation was terminated when the crack propagated very close to the interface of the first and second layers.

6.3 Results and Discussion

6.3.1 Crack Length Effect

To obtain generalized solutions, the SIFs were normalized by $2P/\pi a^{1/2}$, where P is the normal force applied by the moving asperity, and a is the corresponding half-contact width. In addition, the asperity distance from the crack, y_P, was normalized by the half-contact width, and the crack length by the thickness of the first layer, h_1. Figure 6.3(a) shows K_I as a function of dimensionless asperity position and crack length for $m = m_c = 0.5$. In all simulation cases, K_I assumes nonzero values only when the asperity passes over the crack ($y_P/a > 0$), apparently due to the effect of crack closure that is enhanced by the predominantly compressive stress field ahead of the sliding asperity. When the crack is just behind the trailing contact edge ($y_P/a > 1$), K_I increases rapidly to a peak value and then decreases gradually as the asperity moves further to the right of the crack. In addition, Fig. 6.3(a) reveals a strong dependence of K_I on crack length, indicating that the longer the crack, the higher the tensile stress at the crack tip. Moreover, the maximum K_I increases with an increase in crack length and the corresponding asperity position occurs further to the right of the crack.

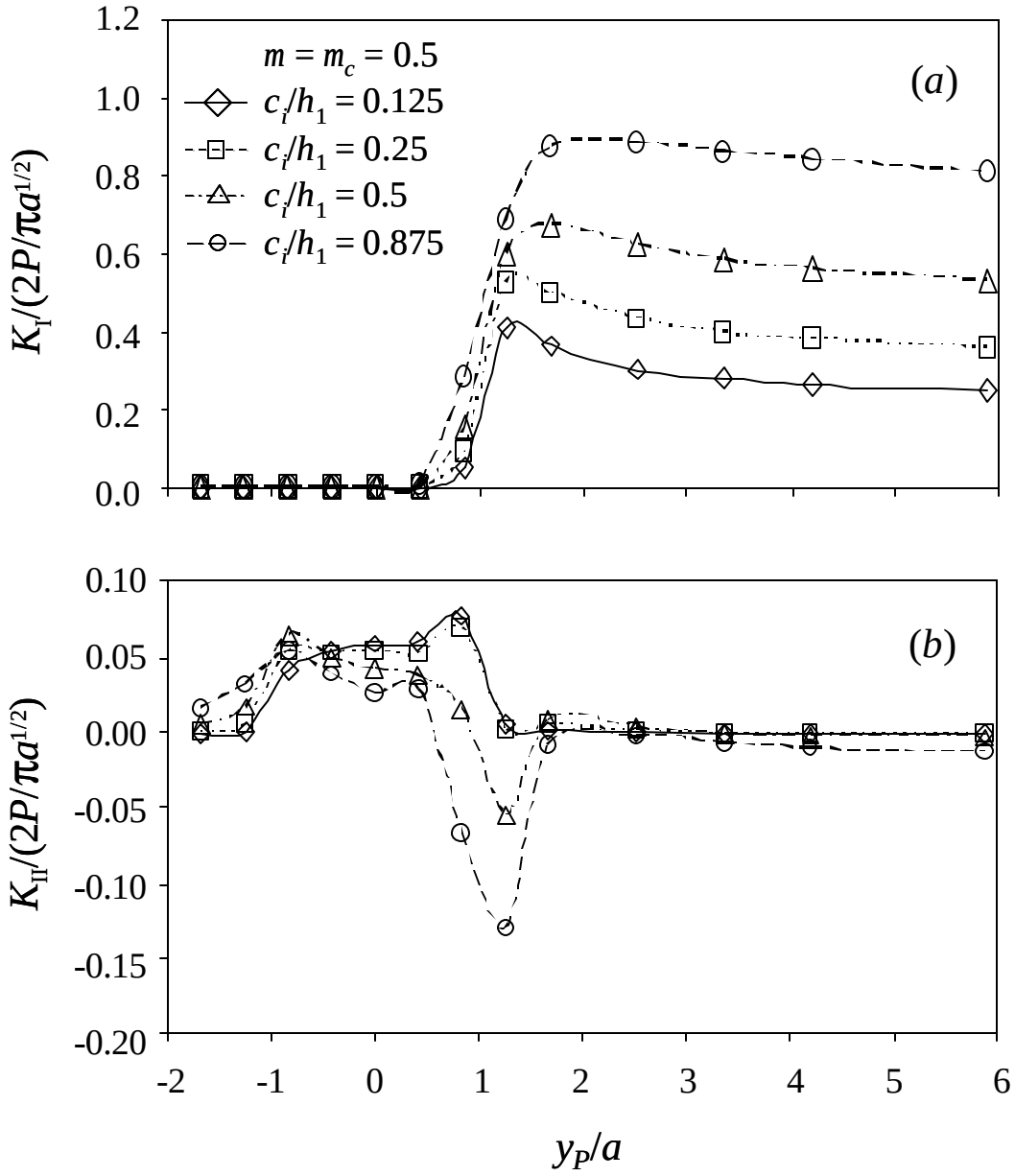

Fig. 6.3 Dimensionless tensile and shear stress intensity factors, K_I and K_{II}, respectively, versus dimensionless asperity position, y_P / a, and dimensionless crack length, c_i / h_1, for $m = m_c = 0.5$.

The variation of K_{II} with asperity position and initial crack length, shown in Fig. 6.3(b), is complex compared to that of K_I. The range of K_{II} increases with crack length; however, K_{II} decreases rapidly to zero after the asperity passes over the crack ($y_P/a >$ 1). When the asperity slides over the crack region, the predominant mode changes from shear to tensile. However, a comparison of the results shown in Figs. 6.3(a) and 6.3(b) shows that ΔK_{II} is significantly less than ΔK_I, approximately by an order of magnitude. Hence, because the crack growth rate depends on ΔK (Eq. (6.3)), it may be inferred that crack growth is predominantly affected by the tensile mode.

6.3.2 Sliding Friction Effect

The stress field in the vicinity of the crack tip is strongly affected by the magnitude of friction traction at the surface. Figure 6.4 shows the variation of K_I and K_{II} with asperity position and coefficient of friction at the contact region ($m = 0.1$, 0.25, and 0.5) for $c_i/h_1 = 0.125$ and $m_c = 0$. The increase of K_I and K_{II} with friction coefficient is a consequence of the enhancement of the shear traction at the contact region and the higher stresses produced at the crack tip. The maximum value of K_I occurs as soon as the asperity slides over the crack, while that of K_{II} occurs when the asperity is over the crack.

Figures 6.5 shows the effect of coefficient of friction between the crack faces on the variation of K_I and K_{II} for $c_i/h_1 = 0.125$ and $m = 0.5$. Figure 6.5(a) shows that K_I is not affected by the friction condition at the crack interface. This is expected because the magnitude of K_I is controlled solely by the s_{yy} stress (Eq. (6.1)), which is not

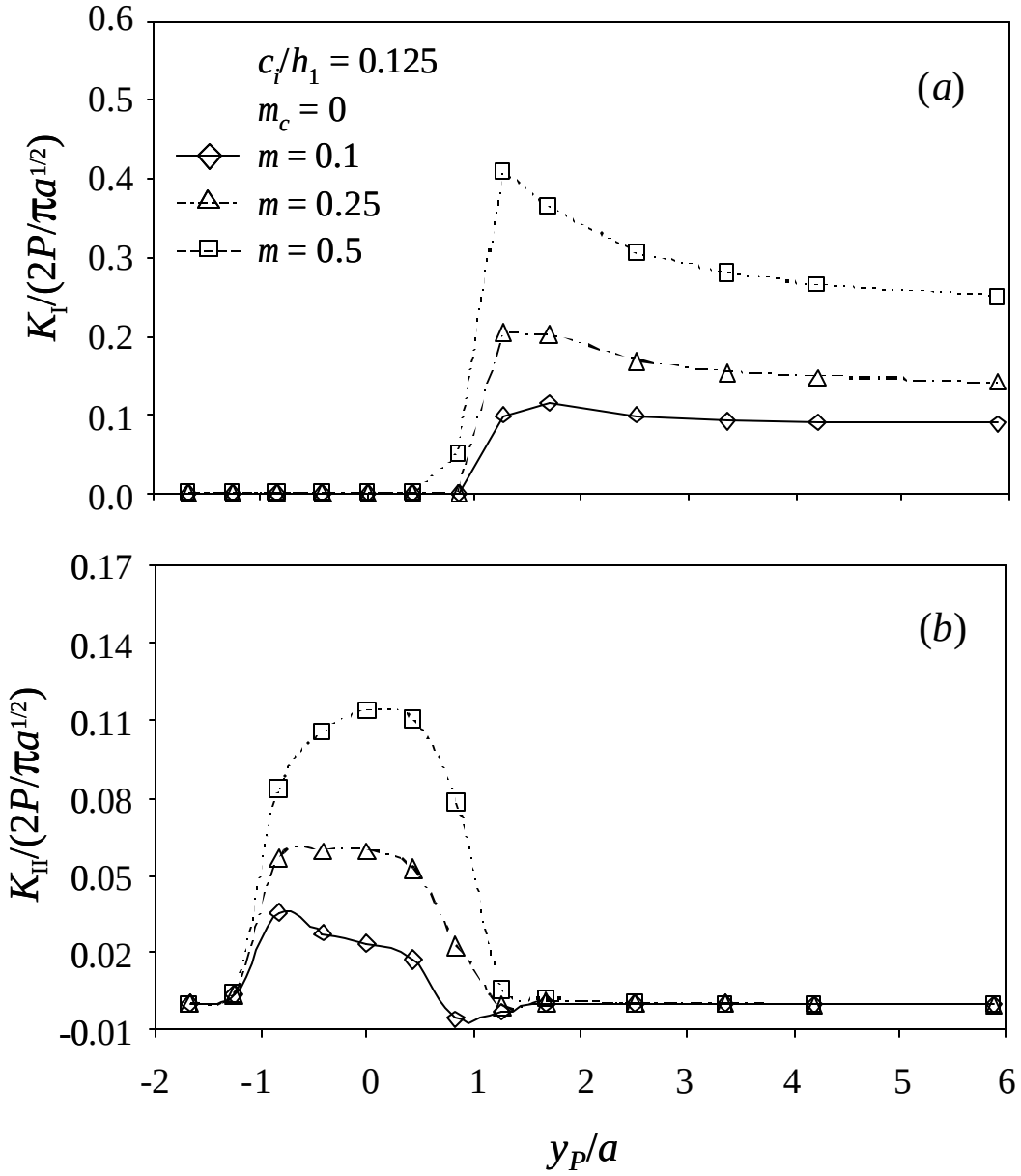

Fig. 6.4 Dimensionless tensile and shear stress intensity factors, K_I and K_{II}, respectively, versus dimensionless asperity position, y_P / a, and friction coefficient at the asperity/multi-layered medium contact region, m, for $c_i / h_1 = 0.125$ and $m_c = 0$.

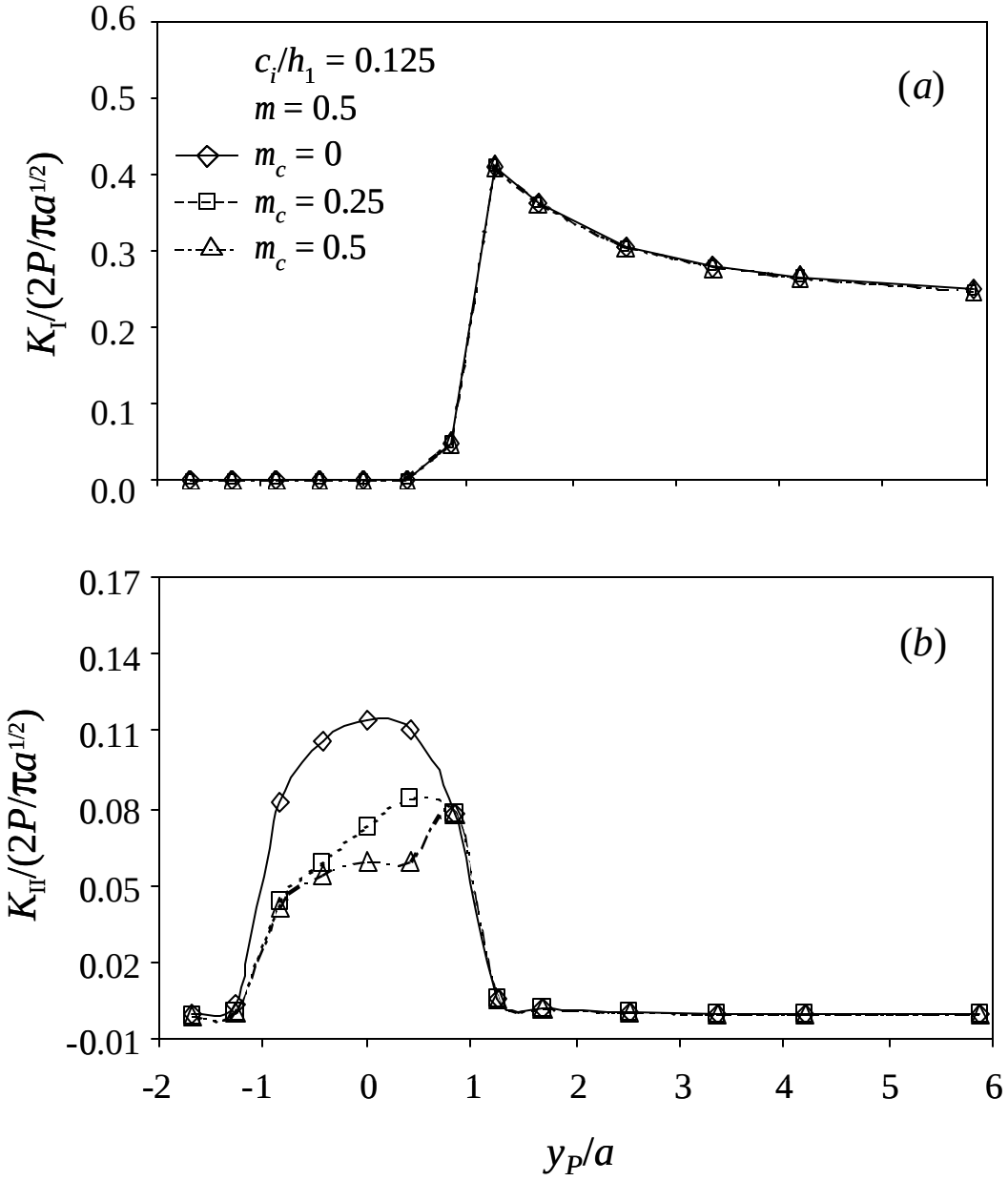

Fig. 6.5 Dimensionless tensile and shear stress intensity factors, K_I and K_{II}, respectively, versus dimensionless asperity position, y_P / a, and crack-face friction coefficient, m_c, for $c_i / h_1 = 0.125$ and $m = 0.5$.

affected by the shear traction generated between the crack faces. Although the variation of K_{II} with asperity position is qualitatively similar to that shown in Fig. 6.4(b), K_{II} deceases with the increase of crack-face friction, which is opposite from the trend obtained with the increase of coefficient of friction at the contact interface. This behavior is attributed to reduced slip between the crack faces due to the increase of the coefficient of friction at the crack interface. Thus, crack-face friction promotes shear stress relaxation, in agreement with the fracture mechanics analysis of Komvopoulos and Cho (1997) for subsurface crack growth parallel to the free surface of a homogeneous half-space. Since K_I is significantly greater than K_{II} (Figs. 6.4 and 6.5), it may be inferred that sliding friction exhibits a strong effect on the variation of the tensile and shear SIFs, whereas the effect of crack-face friction is relatively secondary.

6.3.3 Crack Growth Direction

The crack growth direction was determined based on the maximum shear or tensile SIF ranges. The dominance of the shear and tensile modes during crack growth depends on the maximum values of ΔK_s and ΔK_t, where K_s and K_t are given by (Erdogan and Sih, 1963)

$$K_\sigma(\theta, y_P/a) = \sigma_\theta \sqrt{2\pi r} = \cos\frac{\theta}{2}\left[K_I \cos^2\frac{\theta}{2} - \frac{3}{2}K_{II}\sin\theta\right] \tag{6.7}$$

$$K_\tau(\theta, y_P/a) = \sigma_{r\theta} \sqrt{2\pi r} = \cos\frac{\theta}{2}\left[K_I \sin\theta + K_{II}(3\cos\theta - 1)\right] \tag{6.8}$$

Because of the dependence of K_I and K_{II} on asperity position (Figs. 6.3-6.5), K_s and K_t are functions of y_P/a. The maximum tensile and shear SIF ranges, $\Delta K_s^{\max}$ and $\Delta K_t^{\max}$, respectively, are defined as

$$\Delta K_s^{\max} = \max[\Delta K_s(q)] = \max[K_{s,\max}\big|_{q=q^*} - K_{s,\min}\big|_{q=q^*}] \tag{6.9}$$

$$\Delta K_t^{\max} = \max[\Delta K_t(q)] = \max[K_{t,\max}\big|_{q=q^*} - K_{t,\min}\big|_{q=q^*}] \tag{6.10}$$

where subscripts max and min denote maximum and minimum values of K_s and K_t, and q^* is a given value of q, which varies between -180 and 180 deg. For fixed angle $q = q^*$, $K_{\sigma,\max}\big|_{\theta=\theta^*}$ and $K_{\sigma,\min}\big|_{\theta=\theta^*}$ were determined at different asperity positions during a sliding cycle. Then, the angle q was varied between -180 and 180 deg. to determine the maximum value of $(K_{\sigma,\max}\big|_{\theta=\theta^*} - K_{\sigma,\min}\big|_{\theta=\theta^*})$, which is used to obtain $\Delta K_\sigma^{\max}$. The same procedure was used to determine $\Delta K_t^{\max}$. Based on this approach, the crack growth direction was determined from Eqs. (6.7)-(6.10).

Figure 6.6 shows the variation of dimensionless ΔK_s and ΔK_t with angle q and crack length for $m = m_c = 0.5$. The increase of ΔK_s and ΔK_t with crack length is a consequence of the increase of K_I with crack length and the relatively small contribution of K_{II} (Fig. 6.3). The fact that the maximum values of ΔK_s are higher than those of ΔK_t indicates the dominance of the tensile mode in the crack growth process. Moreover, the maximum values of ΔK_s occur at an angle $q \approx 10$ deg. independent of crack length, suggesting that crack propagation will occur toward the sliding direction. Figure 6.7 shows the initial crack propagation direction, i.e., first deviation (kink) angle, q_1, as a function of initial crack length for $m = m_c = 0.5$. The data indicate a greater tendency for shorter cracks to propagate initially toward the sliding direction than longer cracks.

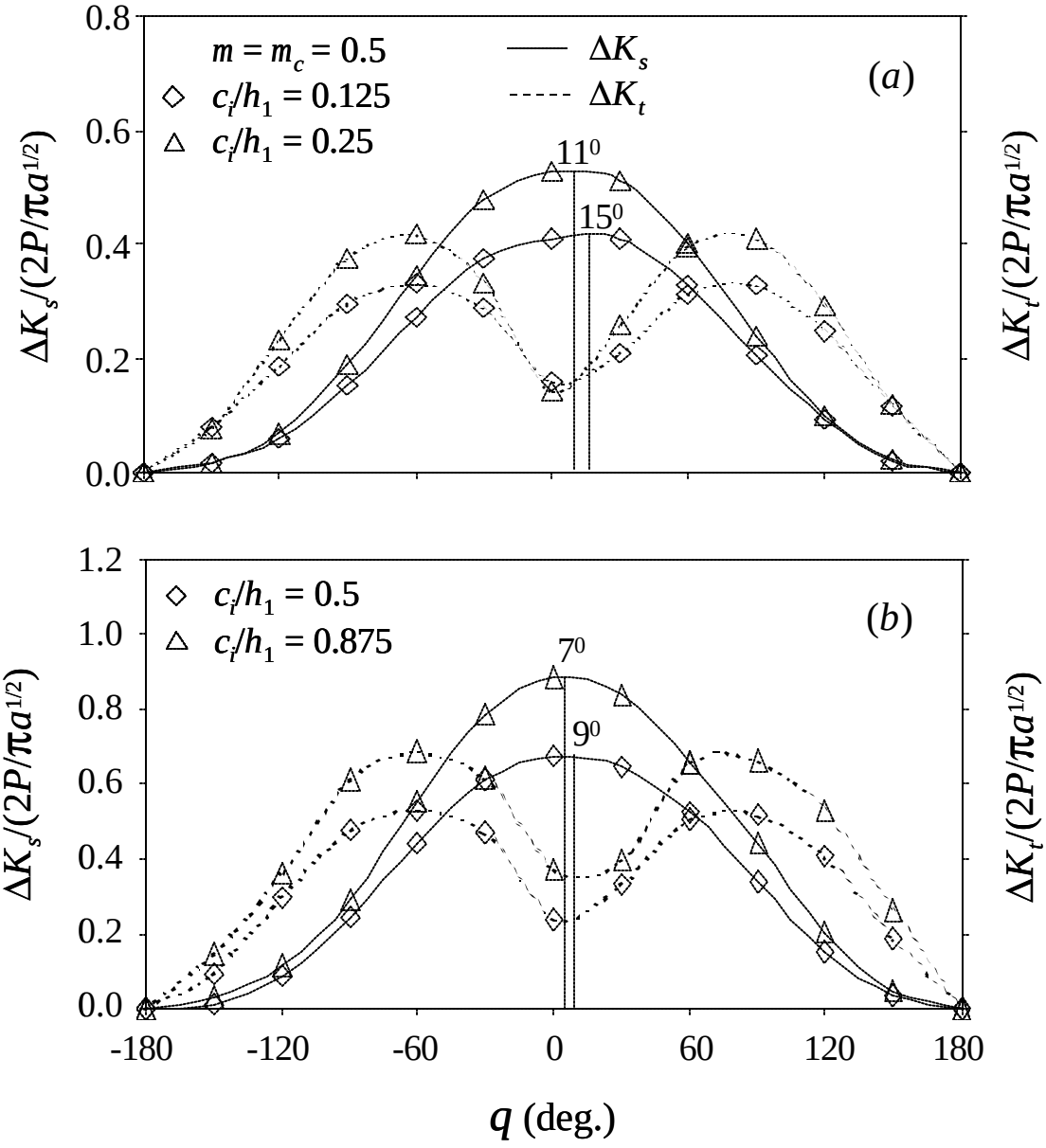

Fig. 6.6 Dimensionless tensile and shear stress intensity factor ranges ΔK_s and ΔK_t, respectively, versus angle measured from the original crack plane, q, for $m = m_c = 0.5$: (a) $c_i / h_1 = 0.125$ and 0.25, and (b) $c_i / h_1 = 0.5$ and 0.875.

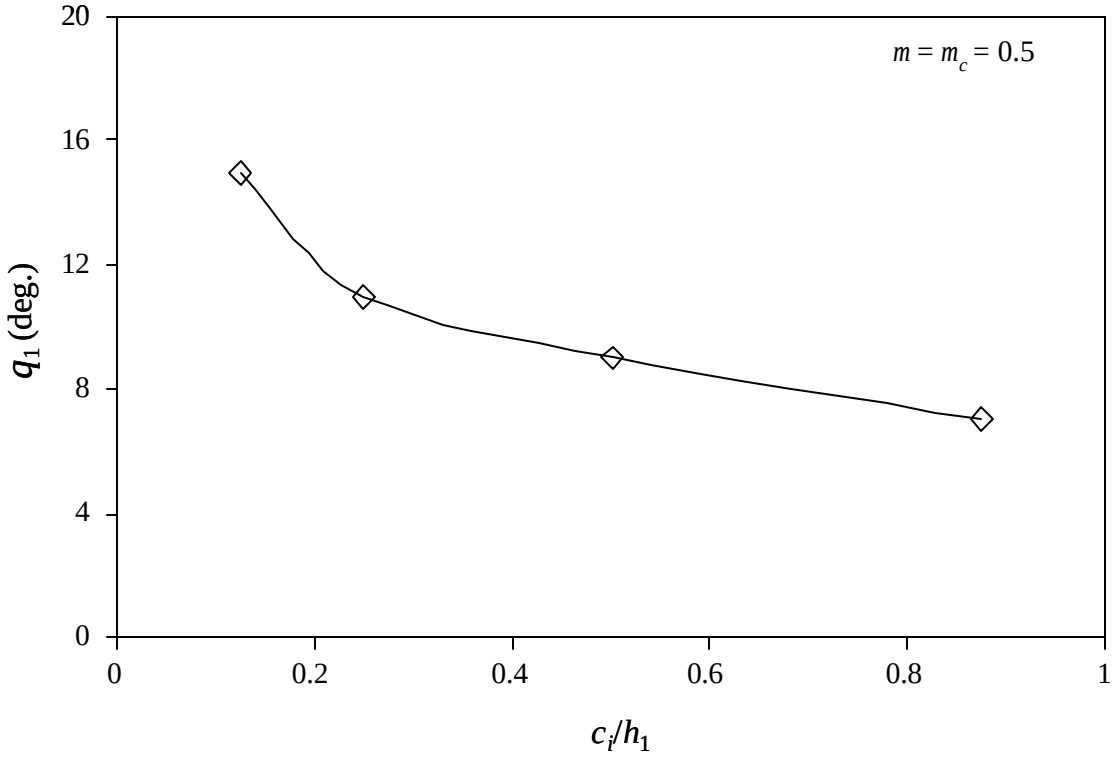

Fig. 6.7 Crack deviation angle in the first crack growth increment, q_1, versus normalized initial crack length, c_i / h_1, for $m = m_c = 0.5$.

6.3.4 Crack Propagation

To examine the evolution of crack-tip stresses, development of crack growth path, and accumulation of plastic deformation in the underlying layer, results are presented in this section for $c_i/h_1 = 0.25$ and $m = m_c = 0.5$. Crack propagation was simulated based on the crack growth direction predicted based on the maximum tensile SIF range, assuming a certain crack growth increment. As explained in section 2.5, the stress and strain fields produced in a given crack growth cycle were updated in the subsequent cycle in order to simulate continuous crack growth by taking into account the stress/strain history effect.

Figure 6.8 shows the effect of crack growth cycles on the variation of

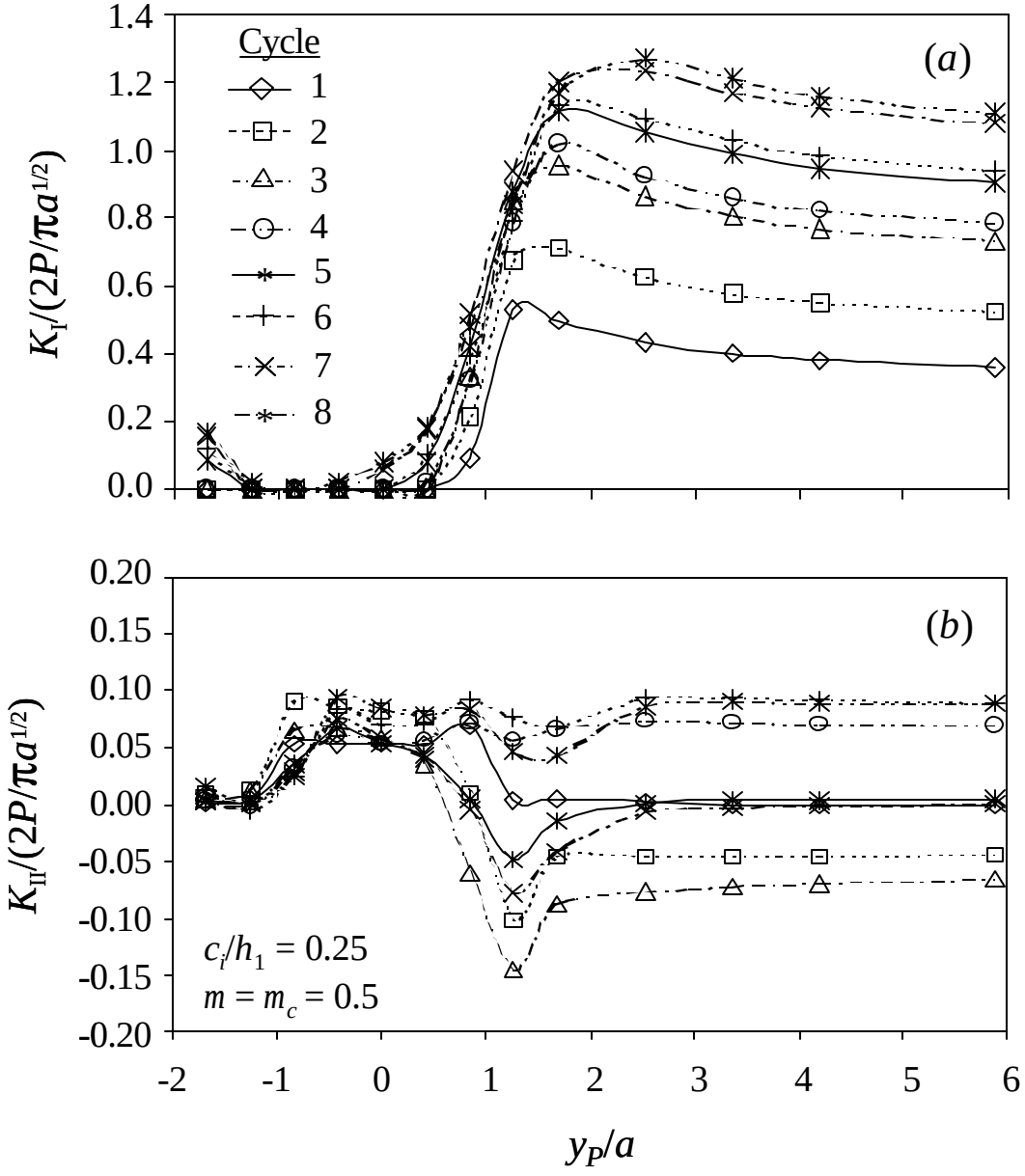

Fig. 6.8 Dimensionless tensile and shear stress intensity factors, K_I and K_{II}, respectively, versus crack growth cycle and dimensionless asperity position, y_P / a, for $c_i / h_1 = 0.25$, $\Delta c = h_1 / 8$, and $m = m_c = 0.5$.

dimensionless K_I and K_{II} with dimensionless asperity position for $\Delta c = h_1/8$. In each cycle, the crack propagated by an increment Δc in the direction of $\Delta K_s^{\max}$. Figure 6.8(a) shows that the variation of K_I with asperity position is qualitatively similar to that shown in Fig. 6.3(a). However, crack growth causes the increment of ΔK_I initially to increase and then to exhibit small fluctuations with further crack growth, which are attributed to variations in the crack growth direction as the crack propagates deeper into the first layer, discussed in detail below. In addition, crack growth produces nonzero K_I values even when the asperity is to the left of the crack and causes the maximum value of ΔK_I to occur at a greater distance of the asperity from the crack. These phenomena are attributed to the effect of crack face separation (either partial or complete) and the mixed mode crack growth. As discussed earlier, the appreciably lower values of K_{II}, by an order of magnitude, compared to those of K_I (Fig. 6.8(b)) reveal a dominant effect of the tensile mode in crack propagation. Indeed, in all crack growth cycles it was found that $\Delta K_s^{\max} > \Delta K_t^{\max}$. Table 6.2 gives normalized $\Delta K_\sigma^{\max}$ in terms of deviation angle at each crack growth cycle, Δq, total deviation angle from the initial crack direction (perpendicular to the surface), q_{total}, and corresponding crack growth cycle. $\Delta K_\sigma^{\max}$ was calculated from the results of K_I and K_{II}, shown in Fig. 6.8, using Eqs. (6.7) and (6.9). The data given in Table 6.2 confirm that crack growth leads to an increase in $\Delta K_\sigma^{\max}$ and crack propagation direction at $q \approx 57$ deg.

To examine the dependence of the crack growth direction (i.e., direction of $\Delta K_\sigma^{\max}$) on the magnitude of crack growth increment, crack paths obtained for $\Delta c = h_1/4$,

Table 6.2. Current crack deviation angle, total deviation angle, and maximum tensile stress intensity factor range versus crack growth cycle for $c_i / h_1 = 0.25$, $\Delta c = h_1 / 8$, and $\mu = \mu_c = 0.5$

Crack growth cycle	Δq (deg.)	q_{total}(deg.)	$\Delta K_{\sigma}^{\max} / (2P / \pi a^{1/2})$
1	11	11	0.5342
2	28	39	0.7462
3	18	57	0.9947
4	-8	49	1.0256
5	8	57	1.1281
6	-8	49	1.1416
7	8	57	1.2397
8	-6	51	1.2778

$h_1/8$, and $h_1/16$, c_i/h_1 = 0.25, and $m = m_c = 0.5$ are compared in Fig. 6.9. It is interesting to note that, after the first or second crack increments, the crack growth paths become almost parallel to each other, showing a common deviation angle from the direction normal to the free surface of ~57 deg. This suggests that the crack growth increment does not affect the crack propagation direction. The obtained crack growth path is consistent with experimental observations of Ko et al. (2001) according to which, crack growth commences at an angle of ~30 deg. with respect to the sliding direction, i.e., 60 deg. from the direction normal to the surface versus 57 deg. predicted in the present study. Moreover, the simulated crack propagation toward the interface is in qualitative

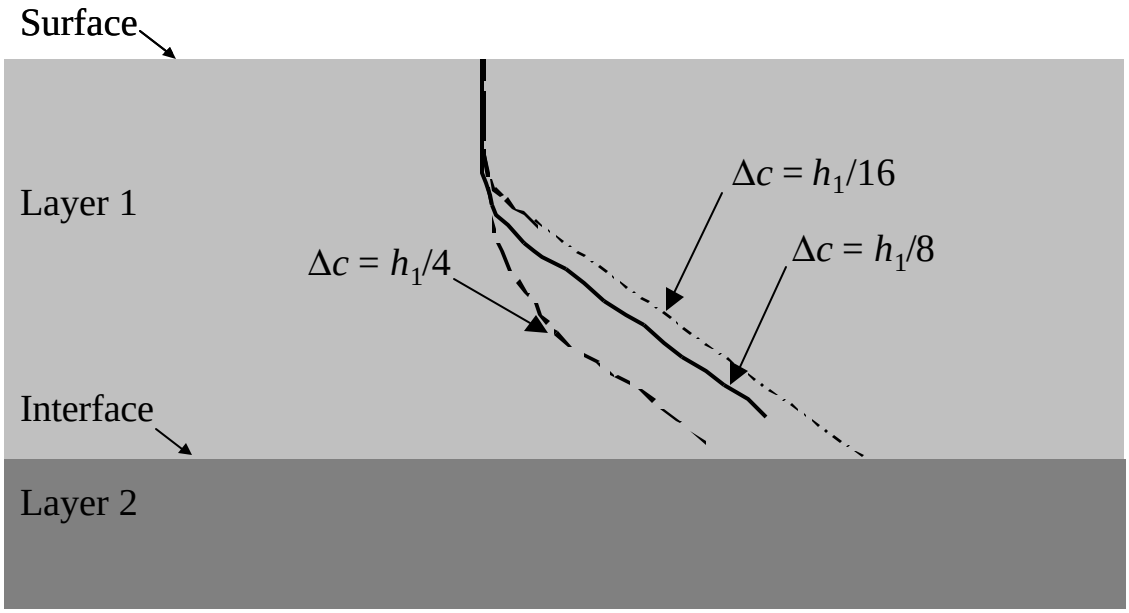

Fig. 6.9 Simulated crack paths for crack growth increment $\Delta c = h_1/4$, $h_1/8$, and $h_1/16$, $c_i / h_1 = 0.25$, and $m = m_c = 0.5$.

agreement with numerical results reported by Oliveira and Bower (1996) for fracture of thin coatings due to contact loading.

6.3.5 Fatigue Life Model

The finite element results presented above can be used in conjunction with the Euler integration algorithm discussed in section 6.2.4 to derive a contact fatigue model. While in the finite element simulations the crack grows by an increment Δc in each asperity passage, in reality crack growth commences after several asperity passes. To model this phenomenon using the simulation results, it is assumed that $\Delta K^{\max}$ (either tensile or shear, depending on which is larger) remains constant during crack propagation by Δc, and the actual number of asperity passes, i.e., fatigue cycles, is calculated from Eq. (6.5). To demonstrate this approach, a graphite substrate coated with a pyrolytic carbon layer was selected for analysis because it consists of an elastic (hard/brittle) carbon layer

and an elastic-plastic (soft/ductile) graphite substrate. The fatigue properties of pyrolytic carbon, $m = 19$ and $A = 1.86 \times 10^{-18}$ m/cycle $(\text{MPa}\sqrt{\text{m}})^{-19}$, quoted from the study of Ritchie and Dauskardt (1991), were used in the calculations. The normalized number of fatigue crack growth cycles, N^*, is given by

$$N^* \equiv \frac{A}{h_1}\left(\frac{2P}{\pi a^{1/2}}\right)^m N = \sum_{j=1}^{n} \frac{\Delta c / h_1}{D_j^m}, \tag{6.11}$$

where N is obtained from Eqs. (6.5) and (6.6), and $D_j = \Delta K_s^{\max}(c_j)/(2P/pa^{1/2})$ is the normalized SIF range. Figure 6.10 shows the variation of normalized crack length, c/h_1, with N^* for $c_i / h_1 = 0.25$ and $\Delta c = h_1 / 8$. The very steep slope of the fatigue curve

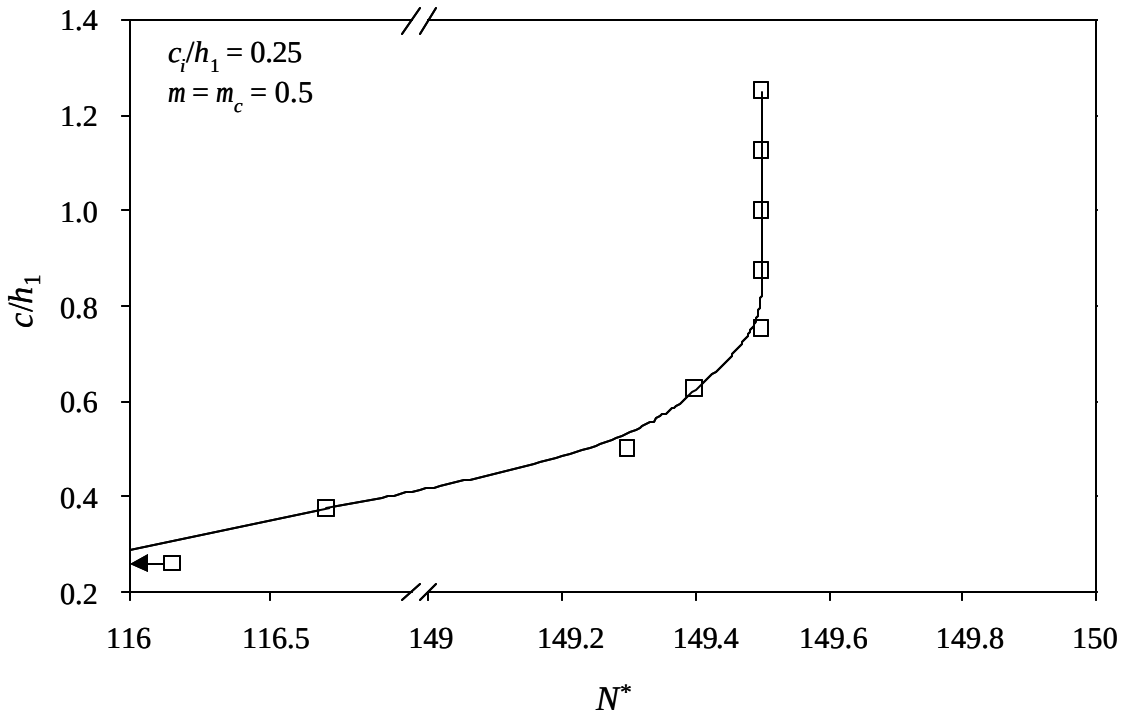

Fig. 6.10 Dimensionless crack length, c/h_1, versus dimensionless number of estimated fatigue crack growth cycles, N^*, for pyrolytic carbon-coated graphite, $c_i / h_1 = 0.25$, $\Delta c = h_1 / 8$, and $m = m_c = 0.5$.

observed after the first few crack increments is indicative of the brittle behavior of pyrolytic carbon.

6.3.6 Evolution of Crack-Tip Stresses

Results for the stress field at the crack tip, obtained at different stages of the simulated crack growth process, are presented next for $c_i / h_1 = 0.25$, $\Delta c = h_1 / 8$, and $m = m_c = 0.5$. Figure 6.11 shows contours of von Mises equivalent stress in the vicinity of the crack tip produced in the first crack growth cycle. When the crack is adjacent to the trailing edge of the contact region ($y_P / a = 1.26$), it remains fully open (Fig. 6.11(a)) and the intensified stresses at the crack tip produce the maximum value of K_I shown in Fig. 6.3(a). However, when the asperity slides further to the right ($y_P / a = 5.88$), the crack faces move closer to each other (stress relaxation) and the size of the high-stress region at the crack tip decreases (Fig. 6.11(b)). This crack behavior is attributed to the high tensile stress at the trailing edge of the contact region (sliding friction effect), which decreases rapidly with the increase of the distance from the contact edge. Since the high stresses at the crack tip occur remote from the interface during the initial stage of crack growth, the crack-tip stresses do not affect the accumulation of plastic deformation in the second layer during sliding contact.

Figure 6.12 shows contours of von Mises equivalent stress in the eighth crack growth cycle, revealing remarkable changes in the stress field at the crack tip due to the propagation of the crack close to the interface. Conversely to the initial stage of crack growth, Fig. 6.12(a) shows that the crack remains partially open when it is close to the

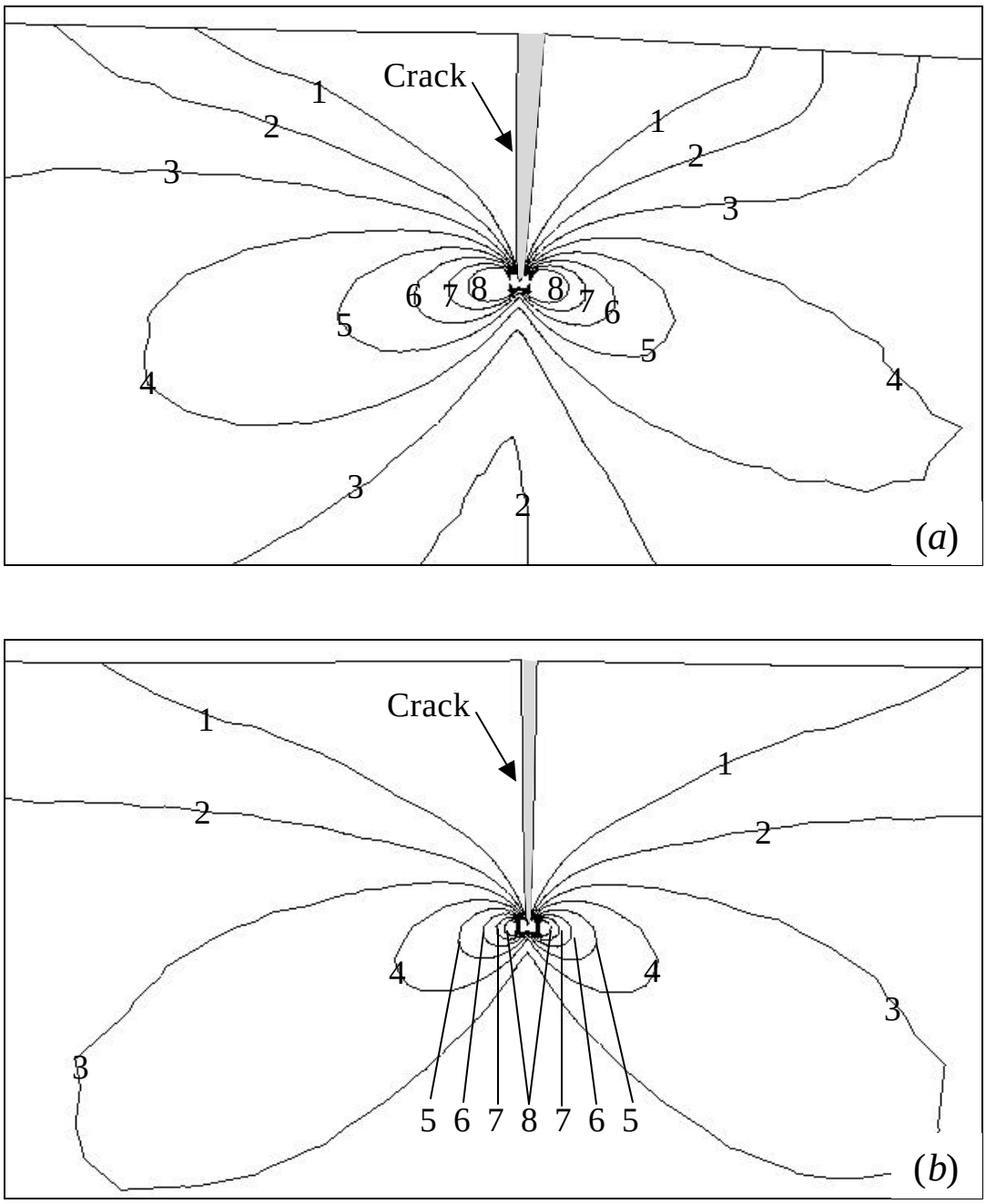

Fig. 6.11 Contours of von Mises equivalent stress, s_M, in the vicinity of the crack tip obtained in the first crack growth cycle for $c_i / h_1 = 0.25$, $\Delta c = h_1 / 8$, $m = m_c = 0.5$, and dimensionless asperity position (a) $y_P / a = 1.26$ and (b) $y_P / a = 5.88$.

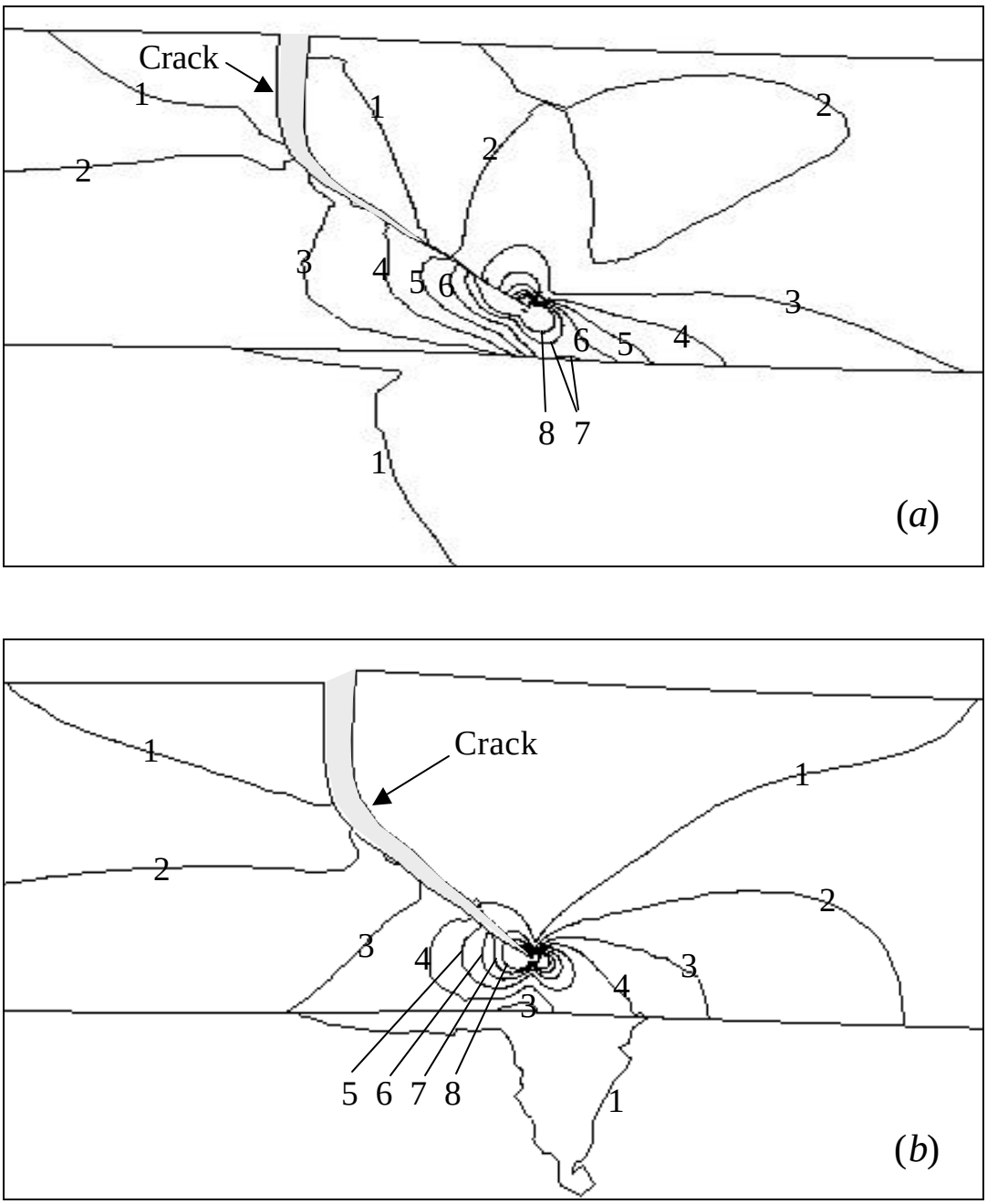

s_M (GPa)

(1) 1.88 (2) 3.75 (3) 5.63 (4) 7.50 (5) 9.38 (6) 11.3 (7) 13.1 (8) 15.0

Fig. 6.12 Contours of von Mises equivalent stress, s_M, in the vicinity of the crack tip obtained in the eighth crack growth cycle for $c_i / h_1 = 0.25$, $\Delta c = h_1 / 8$, $m = m_c = 0.5$, and dimensionless asperity position (a) $y_P / a = 1.26$ and (b) $y_P / a = 2.52$.

trailing edge of the contact region ($y_P / a = 1.26$), while Fig. 6.12(b) shows that the crack opens fully when the asperity moves further to the right ($y_P / a = 2.52$). This behavior is consistent with the fact that the maximum value of K_I in this case occurs at $y_P / a = 2.52$ (Fig. 6.8(a)) and is a consequence of the change of the crack propagation direction. In addition, the high-stress region at the crack tip is very close to the interface, affecting the stresses in the second layer. The large stress discontinuities at the interface (Fig. 6.12(b)) are due to the significant elastic modulus mismatch of the two layers. The intensification of the stress field in the second layer as the crack propagates closer to the interface affects the deformation in the second layer adjacent to the interface. This phenomenon is discussed in detail in the following section.

6.3.7 Development of Plasticity in the Second Layer

The effects of crack length, friction at the contact region and crack interface, and sliding cycles on the deformation of the elastic-plastic second layer are examined in this section. It is noted that for the loading conditions and layer material properties used in this study, the deformation in the third and fourth elastic-plastic layers is purely elastic. Thus, stress/strain results for these layers are not presented here for the sake of brevity.

Figure 6.13(a) shows the maximum equivalent plastic strain, $\bar{e}_p^{\max}$, in the second layer versus dimensionless asperity position and crack length for $m = m_c = 0.5$. In all cases, $\bar{e}_p^{\max}$ increases as the asperity slides over the multi-layered medium in a similar fashion, reaching a steady state at a distance from the crack approximately equal to five times the half-contact width. The results show that the accumulation of plasticity does not

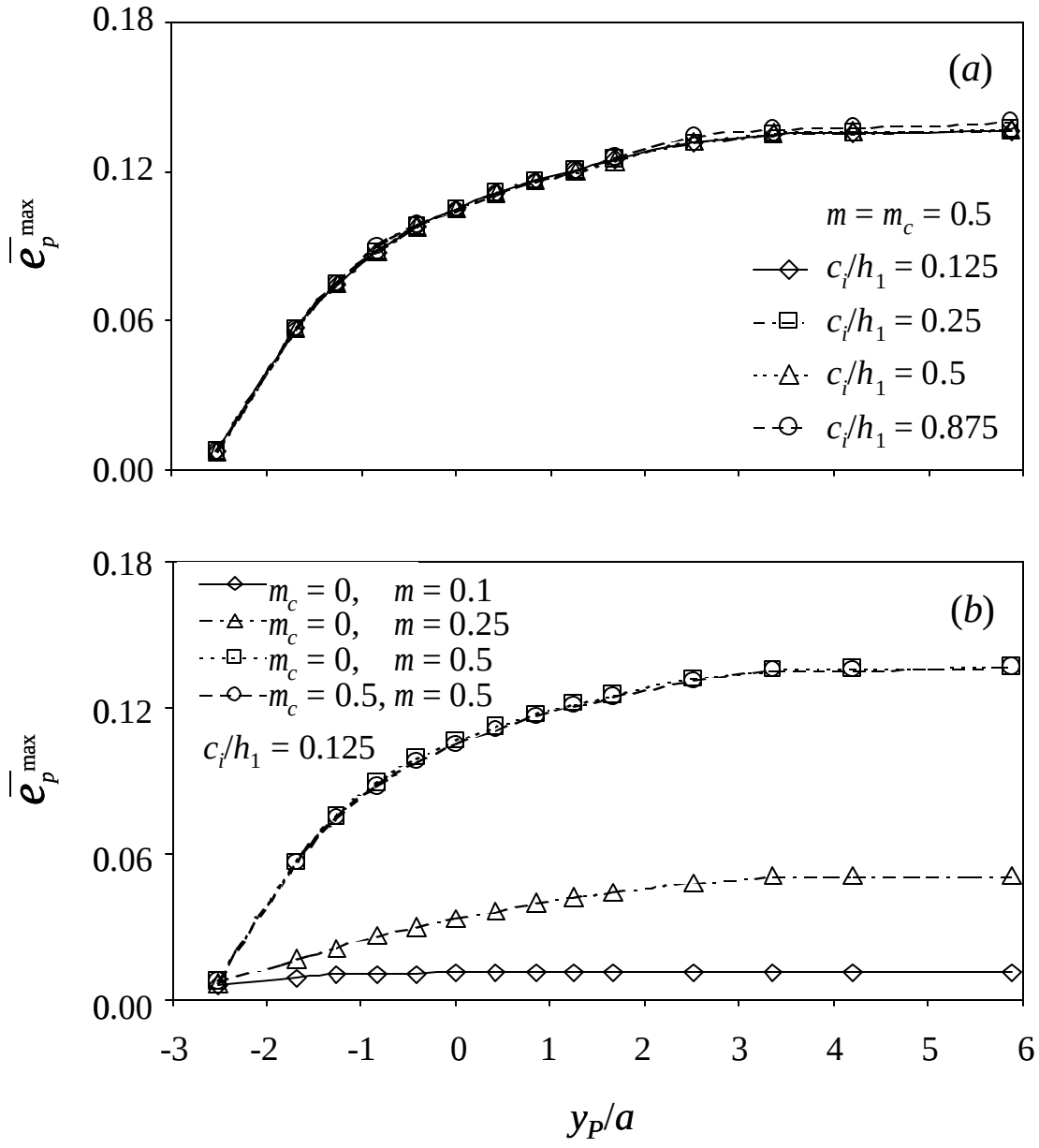

Fig. 6.13 Maximum equivalent plastic strain, $\bar{e}_p^{\max}$, in the elastic-plastic second layer versus dimensionless asperity position, y_P / a: (a) c_i/h_1 = 0.125, 0.25, 0.5, and 0.875 and $m = m_c = 0.5$, and (b) c_i/h_1 = 0.125, m = 0.1, 0.25, and 0.5, and m_c = 0 and 0.5.

depend on the (initial) crack length, evidently because the high-stress field at the crack tip is far away from the interface (when the crack is relatively short) to affect deformation in the second layer. Thus, the crack effect on the propensity for plastic flow in the second layer is negligible until the crack tip reaches a distance less than $h_1/8$ from the interface, as shown by the simulation results. The location of $\bar{e}_p^{\max}$ in the second layer is always at the interface with the first layer below the asperity and shifts along the interface as the asperity slides over the medium, in agreement with a previous finite element analysis of normal and sliding contact of a rigid cylindrical asperity on a patterned elastic-plastic layered medium (Gong and Komvopoulos, 2003).

Figure 6.13(b) shows the variation of $\bar{e}_p^{\max}$ in the second layer with dimensionless asperity position and coefficient of friction at the contact region and crack interface for $c_i / h_1 = 0.125$. As the asperity slides on the surface of the multi-layered medium, $\bar{e}_p^{\max}$ increases monotonically, exhibiting a trend similar to that shown in Fig. 6.13(a). As expected, $\bar{e}_p^{\max}$ intensifies with the increase of coefficient of friction at the contact region due to the pronounced effect of the surface shear (friction) traction on the subsurface stress field. However, the effect of crack-face friction is negligible because it only affects the stress field at the crack tip, which, in this case, is far away from the interface to affect the stress state in the second layer. Therefore, only friction at the contact region affects the accumulation of plasticity in the second layer when the crack tip is remote from the layer interface.

Figure 6.14 shows contours of $\bar{e}_p$ in the second layer obtained in the eighth crack

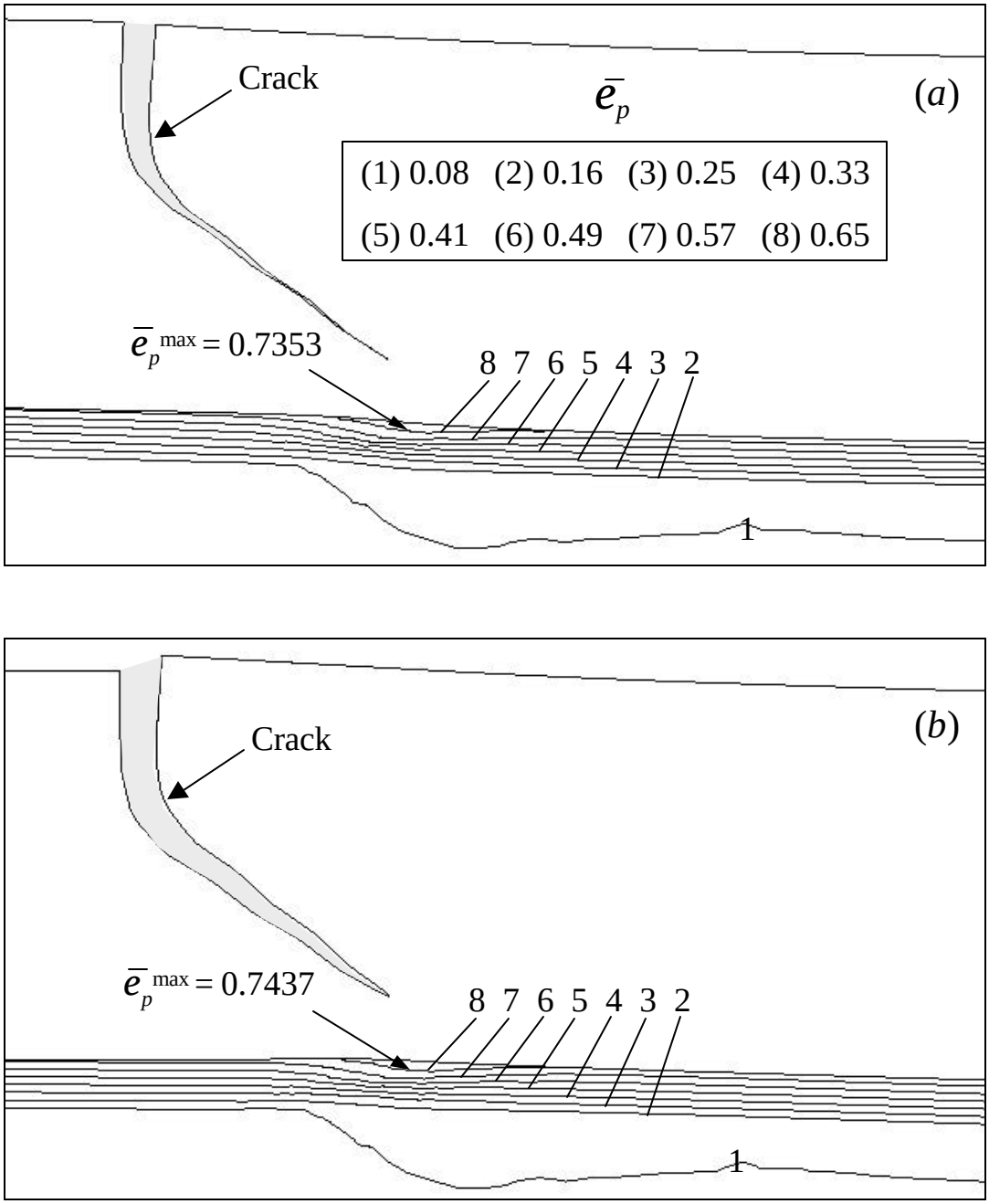

Fig. 6.14 Contours of equivalent plastic strain, $\bar{e}_p$, in the elastic-plastic second layer obtained in the eighth crack growth cycle for $c_i / h_1 = 0.25$, $\Delta c = h_1 / 8$, $m = m_c = 0.5$, and dimensionless asperity position (a) $y_P / a = 1.26$ and (b) $y_P / a = 2.52$.

growth cycle for two asperity positions, $c_i / h_1 = 0.25$, $\Delta c = h_1 / 8$, and $m = m_c = 0.5$. When the crack is just behind the trailing edge of the contact region ($y_P / a = 1.26$), the crack is partially closed and $\bar{e}_p^{\max}$ arises below the crack tip, adjacent to the interface with the first layer (Fig. 6.14(a)). However, when the asperity moves further away from the crack ($y_P / a = 2.52$), the crack opens fully, while $\bar{e}_p^{\max}$ occurs again below the crack tip close to the interface (Fig. 6.14(b)). This differs from the results of previous crack growth cycles showing that $\bar{e}_p^{\max}$ shifts along the interface under the moving asperity. This finding provides additional evidence for the effect of crack-tip stresses on the evolution of plasticity in the second layer.

In the case of multiple asperity contacts, knowledge of the accumulation of plasticity in the multi-layered medium is of particular importance. The results of the present analysis can be used to examine the evolution of plasticity in the second layer due to multi-asperity contacts with spacing larger than the average contact width. Figure 6.15(a) shows $\bar{e}_p^{\max}$ in the second layer versus dimensionless asperity position for different crack growth cycles, $c_i / h_1 = 0.25$, $\Delta c = h_1 / 8$, and $m = m_c = 0.5$. A gradual increase in $\bar{e}_p^{\max}$ occurs when the asperity slides over the medium and with the increase of crack growth cycles (i.e., crack propagation). The increments of $\bar{e}_p^{\max}$ decrease with increasing crack growth cycles because the crack tip is remote from the interface to affect the development of plasticity. However, in the eighth crack growth cycle, a sharp increase in $\bar{e}_p^{\max}$ is encountered when the asperity slides over the crack due to the small

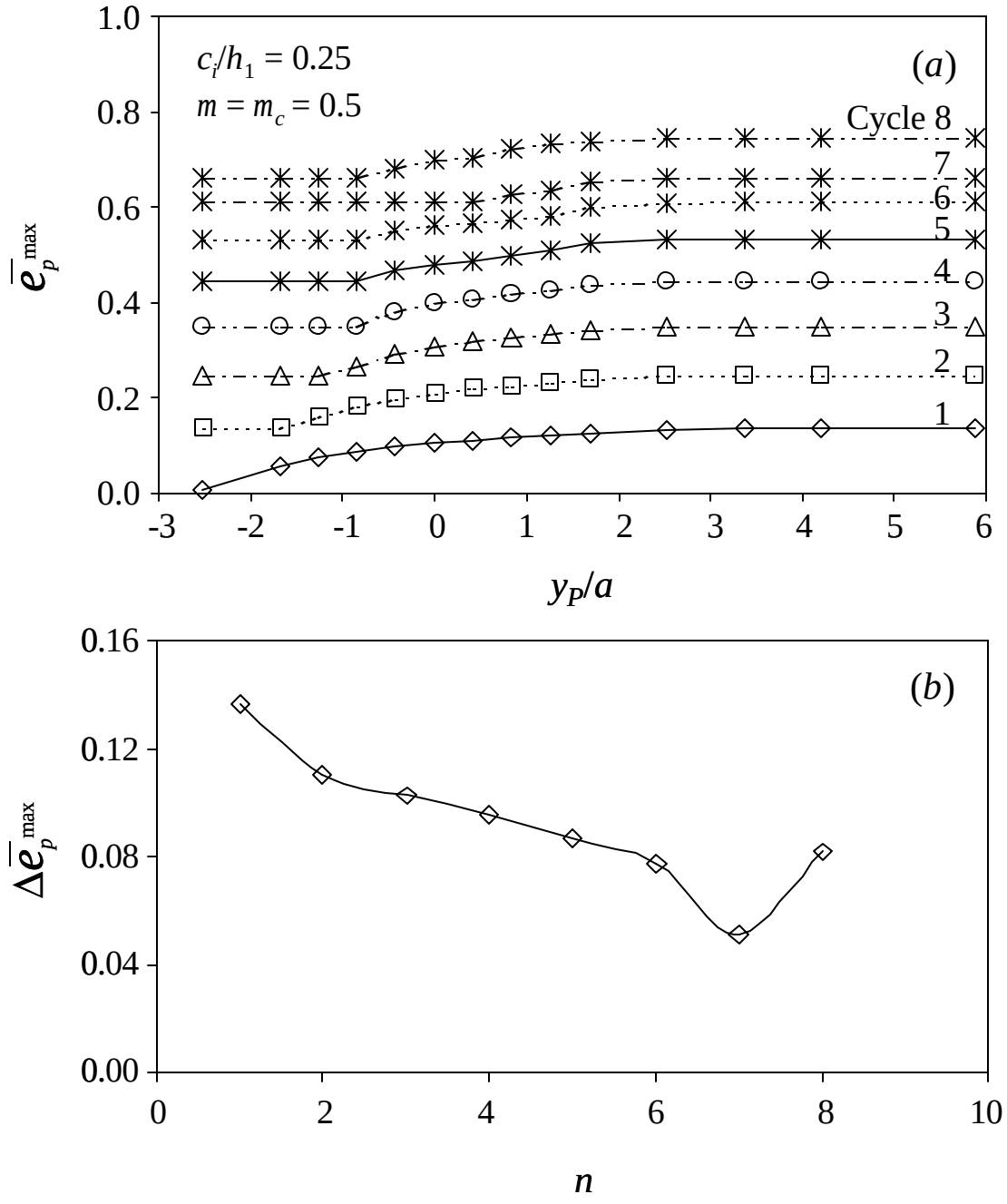

Fig. 6.15 (a) Maximum equivalent plastic strain, $\bar{e}_p^{\max}$, in the elastic-plastic second layer versus dimensionless asperity position, y_P / a, for different simulated crack growth cycles, and (b) increment of maximum equivalent plastic strain, $\Delta\bar{e}_p^{\max}$, in the elastic-plastic second layer versus number of simulated crack growth cycles, n. (The results shown in (a) and (b) are for $c_i / h_1 = 0.25$, $\Delta c = h_1 / 8$, and $m = m_c = 0.5$.)

distance of the high-stress region at the crack tip from the interface. To better illustrate the effect of crack-tip stresses on the evolution of plastic deformation in the second layer, the increment of maximum plastic strain, $\Delta\bar{e}_p^{\max}$, is plotted as a function of number of (simulated) crack growth cycles, *n*, in Fig. 6.15(b). The decrease of $\Delta\bar{e}_p^{\max}$ up to the seventh crack growth cycle reveals the dominant effect of repetitive sliding, while the sharp increase of $\Delta\bar{e}_p^{\max}$ in the eight crack growth cycle, i.e., when the crack propagates very close to the interface, illustrates the effect of the crack-tip stresses on plastic flow in the second layer, within a small region close to the interface with the first layer.

While the present analysis provides insight into surface cracking in elastic-plastic multi-layered media subjected to cyclic loading, the obtained results can be used to discuss possible failure mechanisms. For instance, when the crack propagates to the interface, failure may occur due to delamination along the weaker interface, resulting in the formation of a sheet-like wear particle. Assuming that the fatigue life is dominated by crack growth in the first layer, i.e., layer debonding occurs rapidly after the crack reaches the interface, the fracture approach presented in this study can be used to estimate the loading cycles required to form a wear particle. However, in the case of high interfacial strength, the crack may propagate into the second layer, where it may become inactive or shear eventually toward the surface to produce a wear particle, as in the case of homogeneous media (Ko et al., 2001), depending on the stress field. Crack growth in the elastic-plastic second layer can be accomplished with appropriate modification of the finite element mesh used in this analysis.

6.4 Conclusions

Surface cracking in a multi-layered medium containing a crack perpendicular to the free surface due to repetitive sliding of a rigid asperity was analyzed using linear elastic fracture mechanics and the finite element method. Based on the presented results and discussion, the following main conclusions can be drawn from this study.

(1) The significantly higher values (by an order of magnitude) of the tensile stress intensity factor, K_I, than those of the shear stress intensity factor, K_{II}, obtained in all simulation cases indicate that surface cracking in the multi-layered medium due to sliding contact is controlled by the tensile fracture mode.

(2) Longer surface cracks produce significantly higher K_I values and marginally different K_{II} values. Higher friction at the sliding contact region increases both K_I and K_{II} significantly due to the strong effect of the surface shear traction on the crack-tip stresses. The increase of friction at the crack interface promotes stress relaxation that decreases the magnitude of K_{II}; however, the effect on K_I is negligible.

(3) Based on the maximum tensile stress intensity range, ΔK_s^{max}, initial crack growth was found to occur at an angle of ~10 deg. from the original crack plane, independent of initial crack length. Although the crack length effect on the crack growth direction is negligible, the effect on the magnitudes of ΔK_σ^{max} and ΔK_τ^{max} is significant.

(4) After the first few (1-3) crack growth increments, the crack growth paths obtained with different propagation increments become almost parallel to each other,

exhibiting a common deviation angle from the original crack plane of ~57 deg., in fair agreement with experimental observations.

(5) Crack growth increases the magnitudes of K_I and ΔK_s. An approach for estimating the contact fatigue life due to surface crack growth in multi-layered media was derived from the finite element results, and its application was demonstrated by fatigue crack growth results obtained for a graphite substrate coated with a pyrolitic carbon layer.

(6) The effect of initial crack length on plastic deformation in the elastic-plastic second layer is negligible because the crack-tip stresses do not reach the layer interface. The effect becomes significant only when the crack propagates very close to the interface, a distance approximately less than one-eighth of the first layer thickness. The coefficient of friction at the contact (sliding) region exhibits a dominant effect on the plastic strain accumulating in the second layer, while the effect of crack-face friction is insignificant.

(7) The maximum plastic strain in the second layer increases rapidly as the crack tip approaches the interface due to the effect of the high-stress field at the crack tip. This causes the maximum plastic strain in the second layer to arise always below the crack tip adjacent to the interface rather than below the sliding asperity, as found for uncracked elastic-plastic layered media in earlier studies.

CHAPTER 7

CONTACT FATIGUE ANALYSIS OF AN ELASTIC-PLASTIC LAYERED MEDIUM WITH A SURFACE CRACK IN SLIDING CONTACT WITH A FRACTAL SURFACE

7.1 Introduction

Layered media are used in various engineering applications to enhance the durability and functionality of interacting surfaces. Surface layers exhibiting high stiffness and hardness protect the underlying layers from mechanical damage due to contact stresses. Therefore, the deformation and fracture mechanics of surface layers control the lifetime of mechanical systems involving contact interfaces. Even though hard and wear-resistant layers are desirable for reducing sliding wear, the relatively low fracture toughness of most hard materials often leads to unexpected contact fatigue/fracture. Thus, understanding of contact fatigue in layered media subjected to normal and friction surface tractions is critical to the endurance of electromechanical devices possessing contact interfaces.

In early contact mechanics analyses, information about the underlying reasons for surface cracking in layered media was extracted from results for the mechanical stresses and strains produced from sliding contact. King and O'Sulllivan (1987) reported a high tensile stress at the trailing edge of a rigid cylinder sliding over an elastic layered medium. Finite element simulations by Kral and Komvopoulos (1996) confirmed the development of tensile stresses at the surface of a layered medium, revealing a tendency

for the formation of transverse surface cracks in the wake of the sliding indenter. Gong and Komvopoulos (2003) performed a finite element analysis of a rigid sphere sliding over a layered medium with a patterned surface characterized by a high amplitude-to-wavelength ratio and observed the development of a residual tensile stress in the wake of sliding, which intensified with the increase of the sliding cycles.

Although contact stress analysis of layered media has attracted the attention of many researchers, surface contact fatigue and fracture have not been investigated as thoroughly. In fact, the focus in the majority of contact fracture studies has been on homogenous elastic half-spaces. Several fracture analyses of homogenous media (Keer and Worden, 1990; Chen, Farris and Chandrasekar, 1991; Keer and Kuo, 1992; Bower and Fleck, 1994) have shown that surface cracks initiate in the wake of sliding contacts, where the maximum tensile stress is encountered. However, only a few contact fatigue studies of layered media have been conducted to date. Beuth and Klingbeil (1996) performed a plane-strain fracture analysis of an elastic thin film under a residual tensile stress and reported a greater likelihood for film cracking due to substrate yielding that increased the energy available for crack growth. Oliveira and Bower (1996) studied fracture and delamination of thin coatings under contact loads and observed an effect of the elastic property mismatch between the layer and the substrate materials on the fracture load and crack path. Lin and Smith (1999a, 1999b) developed a finite element model to study surface fatigue crack growth in plates and obtained results for the stress intensity factor and the fatigue life. Gong and Komvopoulos (2004b) used the finite element method to analyze surface cracking in a layered medium due to contact with a rigid cylinder and found that surface cracking was dominated by the tensile fracture mode

and that crack growth occurred toward the layer interface at an angle of 57^0 from the normal to the surface.

A major simplification in previous studies was the assumption of ideally smooth contacting surfaces. However, real surfaces exhibit multi-scale roughness and, thus, actual contact is confined between surface summits, hereafter referred to as asperity contacts. Consequently, accurate analysis of surface cracking must include the effect of the surface topography (roughness) on the crack-tip stresses. To avoid biasing of the measurement of surface parameters by the sample size, instrument resolution, and experimental filter, fractal geometry (Mandelbrot, 1983) has been adopted to characterize engineering surfaces (Majumdar and Tien, 1990; Borodich and Onishchenko, 1999). Contact theories based on the fractal description of the surface topography have yielded solutions for the real contact area, contact load, and interfacial temperature rise due to frictional heating for both homogeneous and layered elastic-plastic media (Majumdar and Bhushan, 1991; Wang and Komvopoulos, 1994a, 1994b; Yan and Komvopoulos, 1998; Ciavarella et al. 2000; Komvopoulos and Ye, 2001). However, a contact fatigue analysis of (multi)layered elastic-plastic media in sliding contact with a rough (fractal) surface has not been reported yet. Therefore, the main objective of this study was to perform a contact fatigue analysis that elucidates the role of the surface topography in surface cracking of elastic-plastic (multi)layered media due to sliding against a fractal surface. A contact algorithm and stress intensity factor results from preliminary finite element simulations were used to determine the critical segment of the fractal surface to be used in the contact fatigue analysis. Results for the tensile and shear stress intensity factors and the crack growth direction and dominant fracture mode are presented below in terms of

fractal parameters and position of the critical surface segment with respect to the surface crack.

7.2 Modeling Method

7.2.1 Contact Model and Finite Element Mesh

Figure 7.1 shows a cross-sectional view of the plane-strain problem analyzed in this study. A crack of initial length c_i is modeled perpendicular to the surface of the first layer of thickness h_1. The crack-tip Cartesian coordinates are denoted by x and y and the cylindrical polar coordinates by r and q. A rough (fractal) surface (with a coordinate system (z' x'), $x' = y$) slides over the layered medium from left to right under a load P applied at the middle-point of the profile length, which is at a distance y_P from the crack.

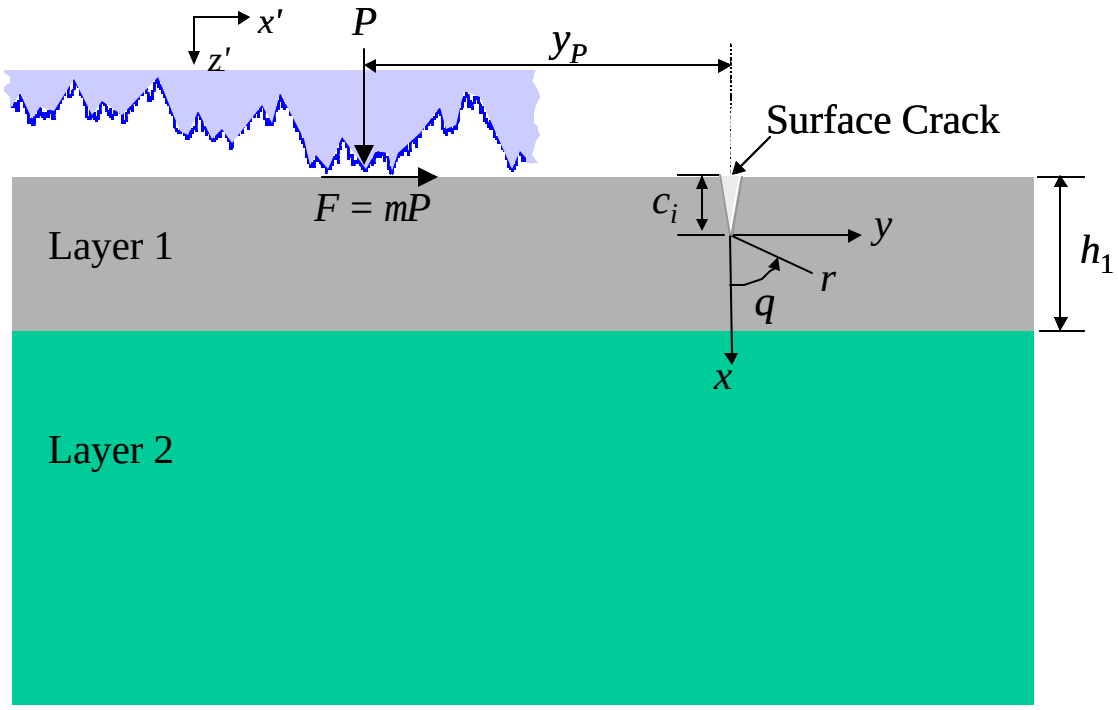

Fig. 7.1 Schematic of a rough surface sliding against a layered medium containing a crack normal to the surface.

Coulomb friction generates a tangential force $F = mP$, where m is the coefficient of friction.

Based on the usual plane strain assumption, quasi-static sliding simulations were performed with the two-dimensional finite element mesh shown in Fig. 7.2(a). The mesh consists of approximately 9,000 eight-node, isoparametric, quadrilateral elements with a specified 3 x 3 integration scheme. The exact number of finite elements used in each simulation depends on the crack growth path. The nodes at the bottom boundary of the mesh were constrained against displacement in the x direction and the nodes at the left boundary against displacement in the y direction. The mesh was refined near the surface, especially around the crack, in order to accurately determine the real contact area and the stress and strain fields adjacent to the surface and the crack-tip vicinity, where high strain gradients occur during sliding. The mesh around the crack, shown in Fig. 7.2(b), consists of 36 eight-node, isoparametric, collapsed quadrilateral, plane-strain elements with their mid-side nodes adjacent to the crack tips shifted to the quarter-point distance in order to simulate the $r^{-1/2}$ singularity of the crack-tip stresses. Since the analysis is based on linear elastic fracture mechanics, the crack-tip nodes were constrained to move together in order to avoid crack-tip blunting in the crack growth simulations.

Contact between the layered medium and the rough surface was modeled by special contact elements that determine contact or separation between surface nodal points of the layered medium and the rigid surface by measuring the local gap. Similar contact elements were used at the crack faces in order to prevent overlapping of the elements. A detailed description of the contact element kinematics and friction formulation has been presented in a previous study (Gong and Komvopoulos, 2003).

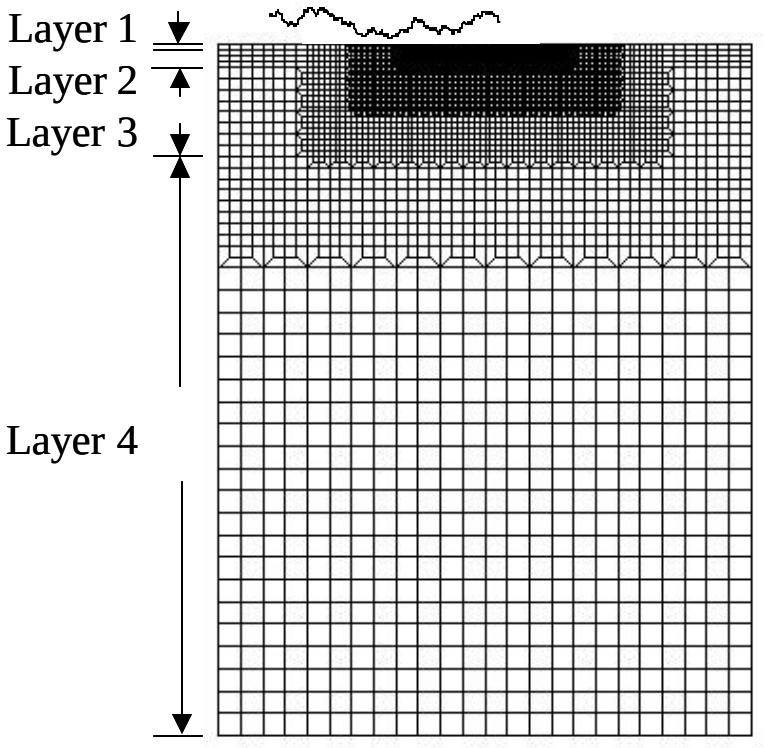

(*a*)

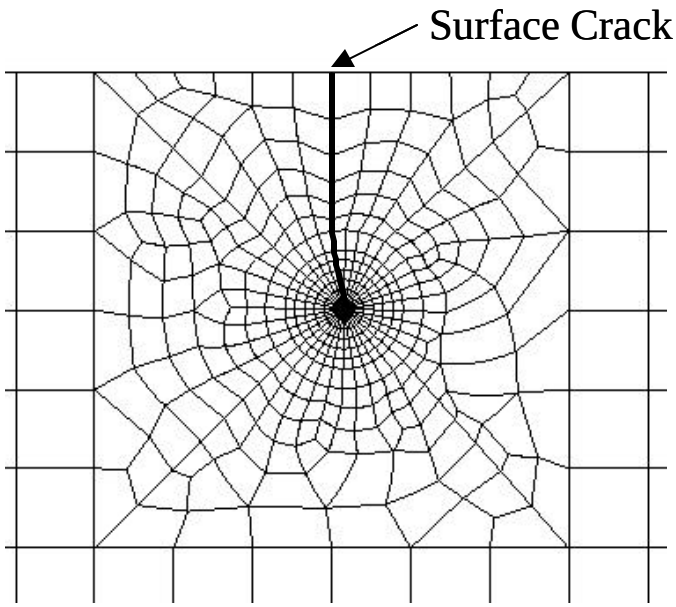

(*b*)

Fig. 7.2 Finite element mesh of a layered medium with a surface crack: (a) mesh of entire layered medium and (b) detail of the mesh around the grown surface crack.

7.2.2 Material Properties and Plasticity Models

Table 7.1 gives the elastic modulus, E, and yield strength, s_Y, of each layer in the layered medium. The first layer was modeled as an elastic material, while all the other layers were modeled as elastic-perfectly plastic materials. All layers were assumed to have a Poisson ratio n = 0.3. The E and s_Y values given in Table 7.1 are typical of layer materials used in magnetic recording rigid disks, i.e., carbon overcoat (layer 1), CoCrPt magnetic medium (layer 2), CrV underlayer (layer 3), and NiP electroplated layer (layer 4). The von Mises yield criterion was used to determine whether yielding occurred at a material point.

7.2.3 Simulation of Sliding Contact and Crack Growth

Quasi-static sliding was simulated in three sequential steps involving loading, sliding, and unloading of a rigid rough surface on the cracked layered medium in an incremental fashion. The rough surface was first displaced toward the layered medium up to a specified maximum global interference, d_g, and, subsequently, displaced laterally to a

Table 7.1. Material properties of layered medium

Medium	E (GPa)	s_Y (Gpa)
Layer 1	260	-
Layer 2	130	2.67
Layer 3	140	2.58
Layer 4	160	2.67

For all layers, n = 0.3.

maximum distance equal to about 100 times the initial crack length while maintaining a constant interference. Finally, the rough surface was unloaded following the same steps as for the loading. In all the simulations, the maximum global interference was fixed, the coefficients of friction at the contact interface and between the crack faces were set equal to 0.5, and the initial crack length was equal to $0.25h_1$. To investigate the effects of surface topography parameters on the stress intensity factor ranges, dominant fracture mode, crack growth rate, and evolution of plasticity, simulations were performed with the finite element code ABAQUS for D = 1.24, 1.34, 1.44, 1.54, and 1.64 and G = 9.46 x 10^{-3}, 9.46 x 10^{-4}, and 9.46 x 10^{-5} nm. In the fatigue simulations, the mesh around the crack tip was modified in order to incorporate the crack increment of the previous sliding cycle. In addition, the effect of the loading history was considered by initiating each sliding cycle from the stress/strain state obtained after the unloading phase of the previous sliding cycle. This was accomplished with a special crack-growth algorithm, described in detail in a previous fracture mechanics analysis (Gong and Komvopoulos, 2004b).

7.3 Results and Discussion

7.3.1 Rough Surface Algorithm

Figure 7.3(a) shows a fractal surface generated from Eq. (4.1) for D = 1.44, G = 9.46 x 10^{-4} nm, g = 1.5, L = 4379 nm, and L_s = 10 nm. Unless otherwise stated, the previous parameters describe the fractal surface used to obtain the finite element results presented in the following sections. The above values of the fractal parameters are representative of the head-disk interface comprising a smooth carbon-coated hard disk

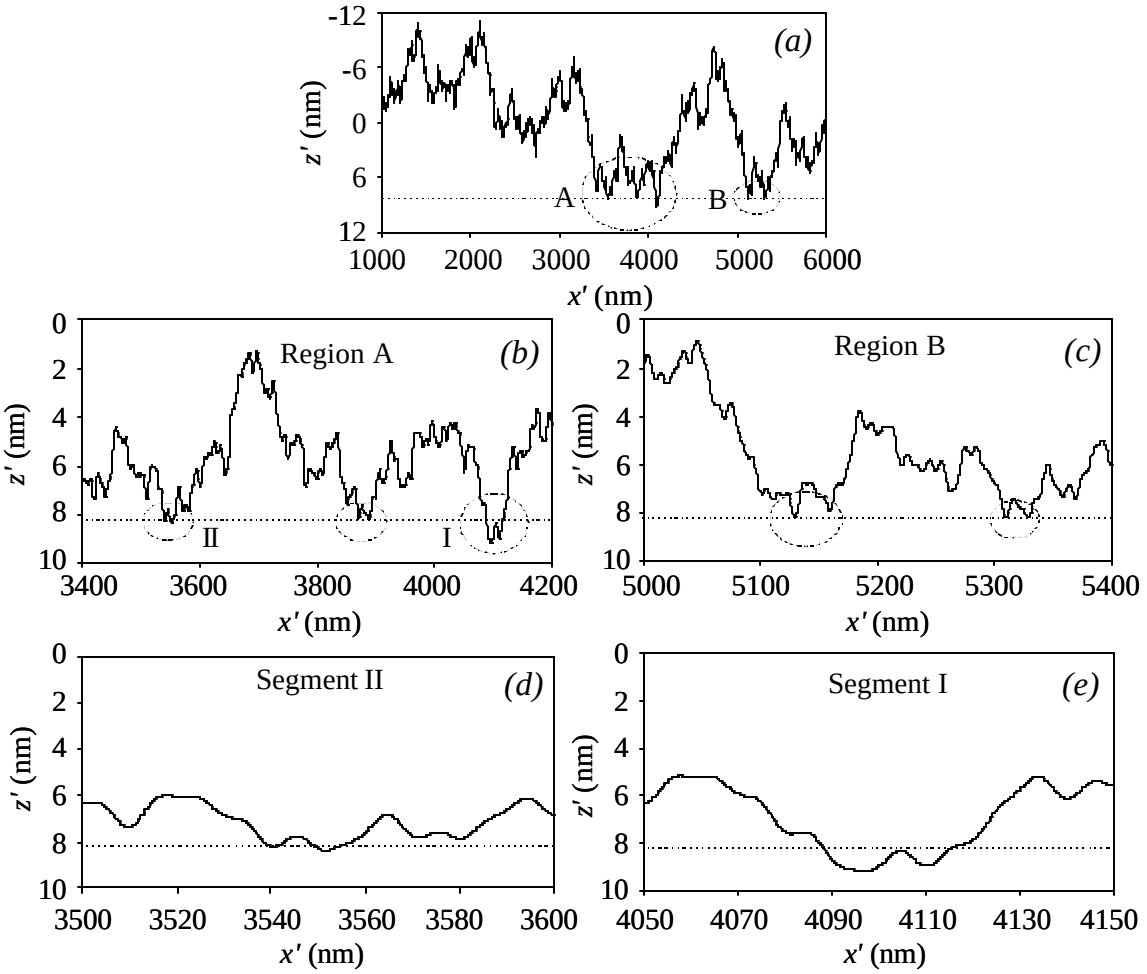

Fig. 7.3 Fractal surface profile (generated from Eq. (4.1) for D = 1.44, G = 9.46 x 10^{-4} nm, g = 1.5, and L = 4379 nm) shown at different scales. A rigid plane (dashed line) truncates the surface profile to a certain maximum global interference, producing two neighboring contact regions A and B consisting of segments with several interacting asperity contacts.

and a relatively rough Al_2O_3-TiC magnetic recording head (Komvopoulos, 2000). Hence, the topography of the surface profile shown in Fig. 7.3(a) is essentially equivalent to that of the rougher surface of the magnetic head. The dashed line represents a rigid plane that truncates the fractal surface at a given global interference. Since modeling of the entire rough surface is impractical, a representative segment of the surface profile was

determined based on the following procedure. First, the entire rough surface was truncated by a rigid plane to a specified maximum global interference in order to determine the critical segment(s) to be used in the fracture analysis. Figure 7.3(a) shows that the truncation of the surface profile by a rigid plane to an interference d_g = 1 nm yielded two potential contact regions (denoted by A and B) consisting of several contact segments (Figs. 7.3(b) and 7.3(c), respectively). From these segments, asperity contacts were encountered only in segments I and II, shown in Figs. 7.3(d) and 7.3(e), respectively. Next, preliminary finite element simulations were performed with the identified contact regions in order to select the (critical) segment with the highest crack-tip stresses (for the given value of d_g). In view of the relatively large spacing of the truncation segments at such small interference, each segment was analyzed separately.

7.3.2 Contact Pressure Distribution

Before proceeding with the analysis of the fatigue results, it is instructive to consider the effect of topography (fractal) parameters on the contact pressure, p, in order to facilitate the interpretation of the crack growth dependence on surface roughness. Figures 7.4 and 7.5 show pressure profiles at asperity contacts due to sliding of a fractal surface possessing different D and G values, respectively. The results were obtained by indenting the layered medium to the same global interference (d_g = 1 nm) and then displacing the rough surfaces over the layered medium by the same distance y_P/c_i = 8. Figure 7.4 shows that, for a given value of G, the real contact area increases and the maximum contact pressure decreases with the increase of D. Figure 7.5 shows that a similar trend occurred with the decrease of G for fixed D. These results can be explained

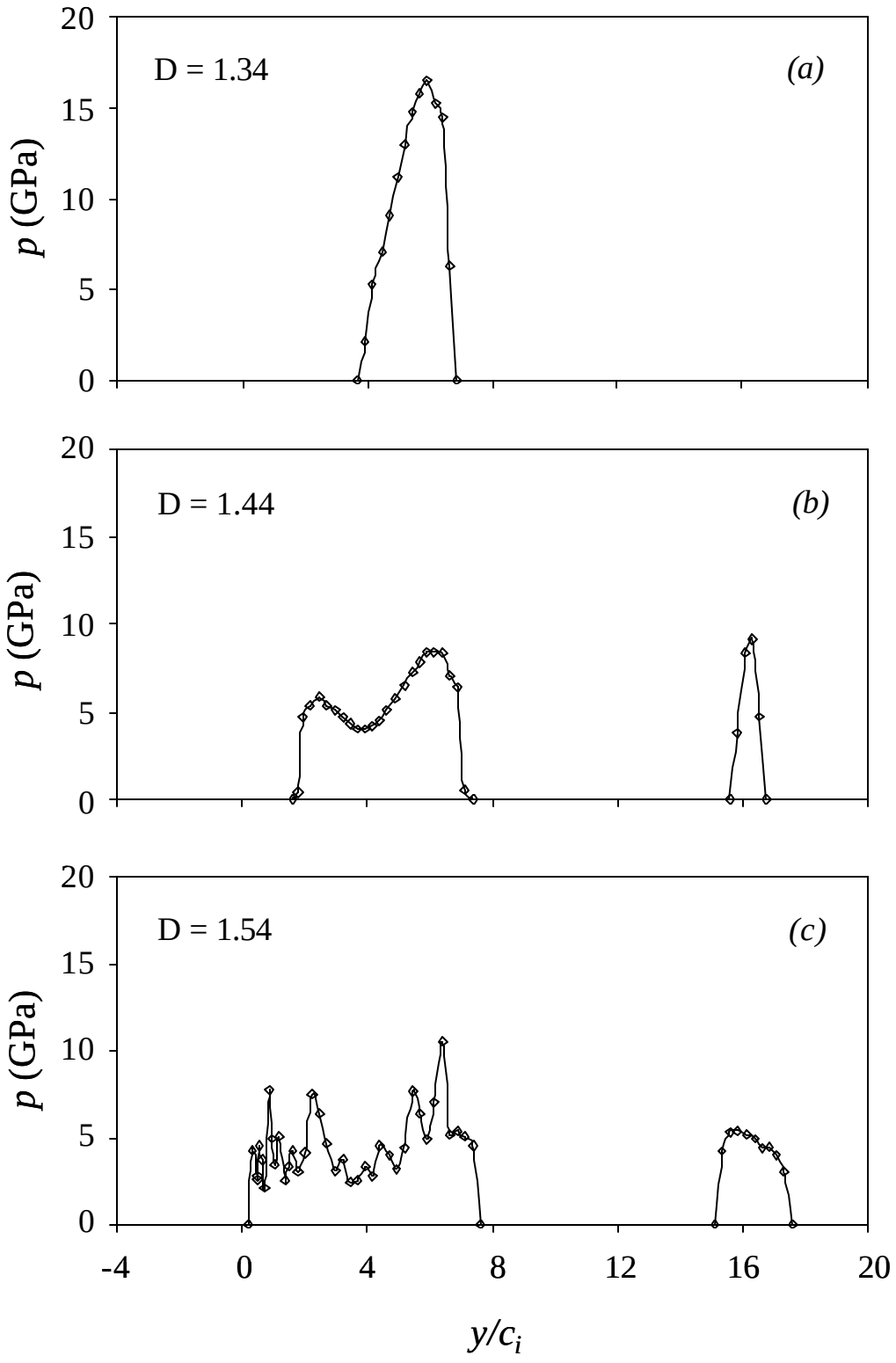

Fig. 7.4 Contact pressure profiles on a layered medium due to sliding contact with a fractal surface at distance $y_P/c_i = 8$: (a) $D = 1.34$, (b) $D = 1.44$, and (c) $D = 1.54$.

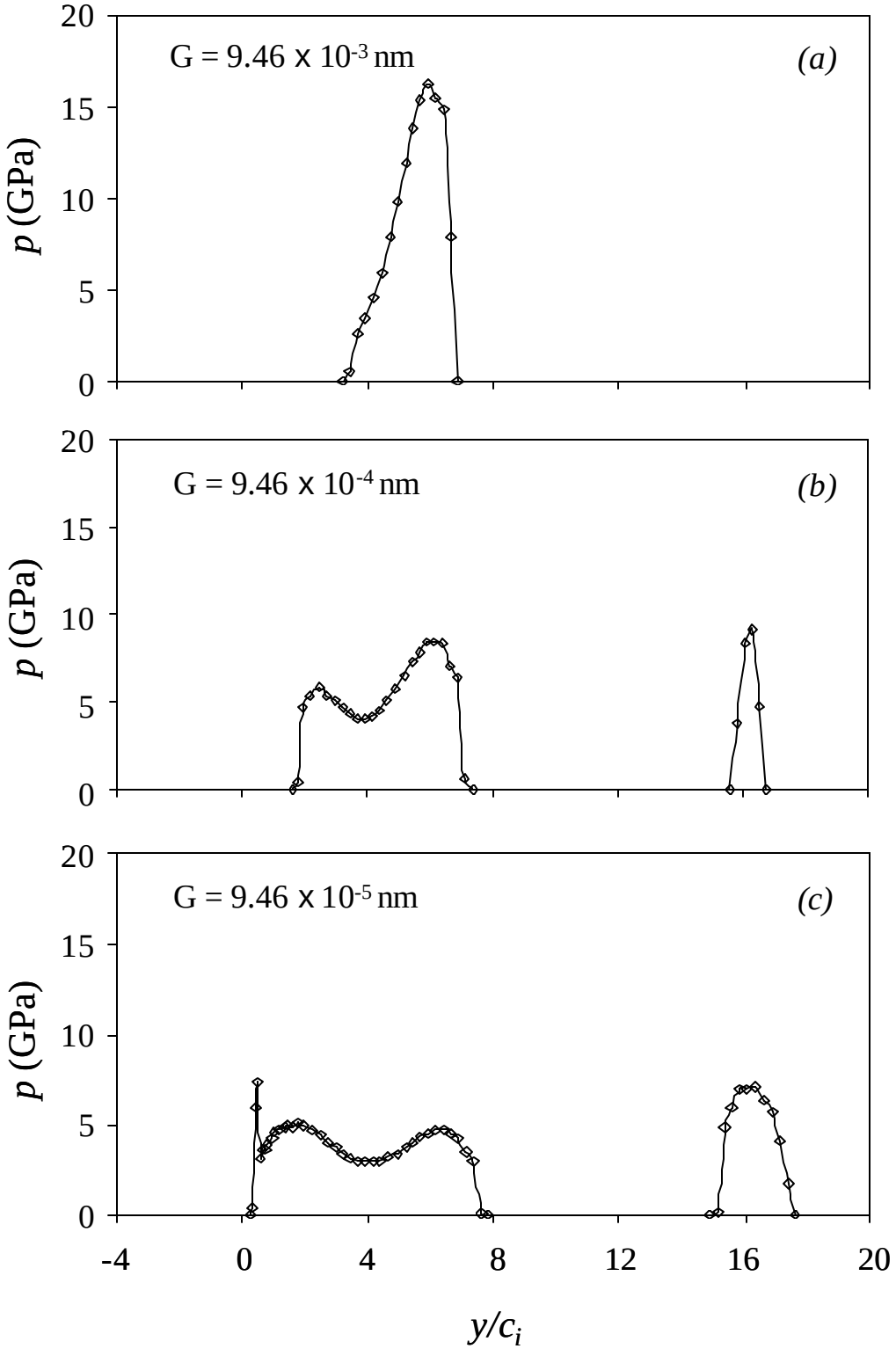

Fig. 7.5 Contact pressure profiles on a layered medium due to sliding contact with a fractal surface at distance $y_P/c_i = 8$: (a) $G = 9.46 \times 10^{-3}$ nm, (b) $G = 9.46 \times 10^{-4}$ nm, and (c) $G = 9.46 \times 10^{-5}$ nm.

by considering the physical meaning of the fractal parameters D and G. Higher D and lower G values are associated with smoother surfaces, yielding a larger number of asperity contacts and lower peak pressures. For relatively smooth surfaces, i.e., D = 1.44 and 1.54 (Figs. 7.4(b) and 7.4(c), respectively), the interface comprises two contact regions. In view of the small lateral spacing, interaction of the stress fields of these neighboring contact regions during sliding (Komvopoulos and Choi, 1992) produces complex variations in the crack-tip stresses. Another important feature is the contact pressure fluctuations obtained for high D values. For instance, the contact pressure profile for D = 1.54 contains several peaks (Fig. 7.4(c)). Despite the similar real contact areas, the surface with D = 1.54 and G = 9.46 x 10^{-4} nm (Fig. 7.4(c)) is not equivalent to the surface with D = 1.44 and G = 9.46 x 10^{-5} nm (Fig. 7.5(c)), as evidenced by the higher pressure peaks shown in Fig. 7.4(c). This is due to the fact that the fractal dimension D determines the contribution of high and low frequency components in the surface profile, while the fractal roughness G does not exhibit this property. However, although a rough surface with a higher D value is not equivalent to a surface with a low G value, it will be shown later that these surfaces yield similar results for the stress intensity factors and plastic strain.

7.3.3 Stress Intensity Factors

The maximum stress intensity factor range, ΔK^{max}, is the driving force for fatigue crack growth. The mode I and mode II stress intensity factors (SIF), K_I and K_{II}, respectively, were used to characterize the stress field in the vicinity of the crack tip. In linear elastic fracture mechanics, K_I and K_{II} are defined as

$$K_I = \lim_{r \to 0} [\sqrt{2pr}\, s_{yy}(r,q)] \tag{7.1}$$

$$K_{II} = \lim_{r \to 0} [\sqrt{2pr}\, t_{xy}(r,q)]. \tag{7.2}$$

The SIFs were determined from the stresses calculated at ten nodes adjacent to the crack tip along the crack plane (q = 0) by linear extrapolation of a least-square line fit through the SIF data.

Figure 7.6 shows the variation of K_I and K_{II} (normalized by $2P/p c_i^{1/2}$) with the position of surface segment I and II (Figs. 7.3(d) and 7.3(e), respectively). When segment I is to the left of the crack, the crack is completely closed due to the predominantly

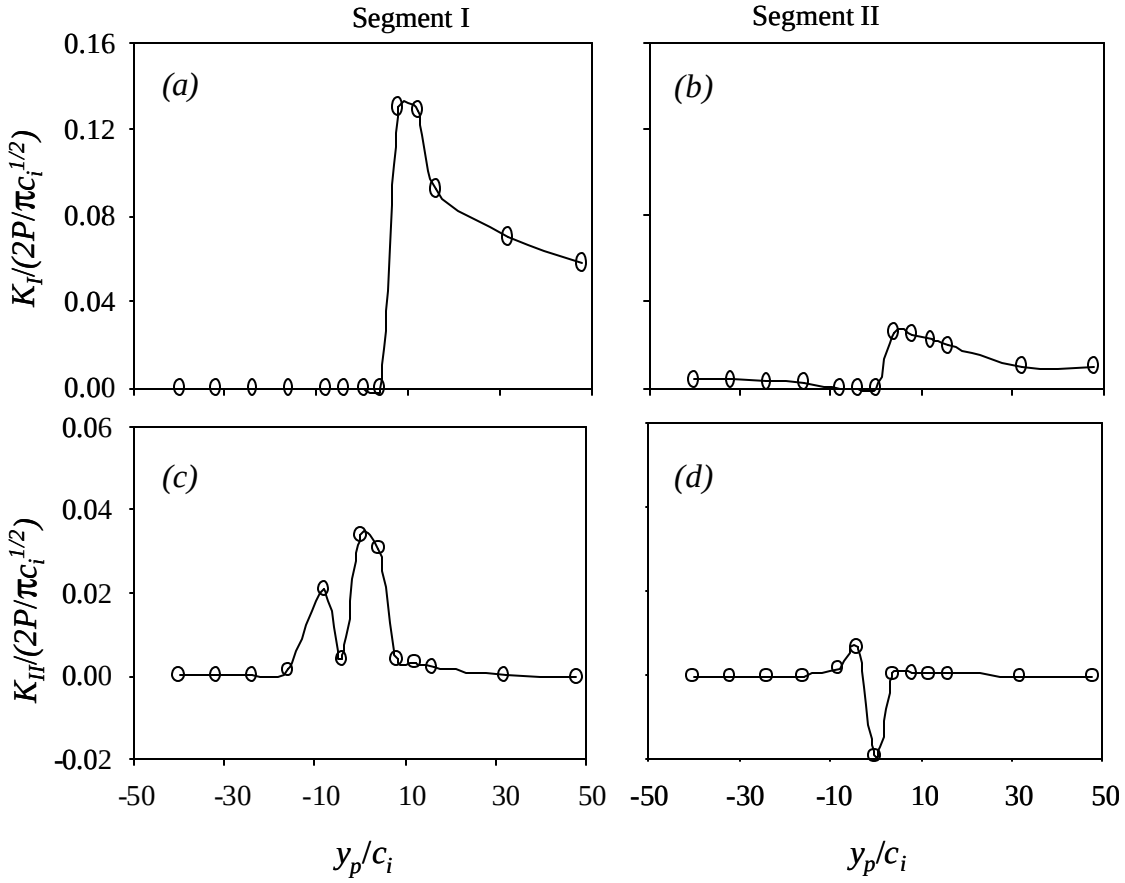

Fig. 7.6 Variation of dimensionless stress intensity factors due to sequential sliding of two different surface segments: (a), (b) K_I and (c), (d) K_{II}.

compressive stress field and, therefore, K_I assumes values close to zero. However, when the surface segment passes over the crack, K_I increases abruptly to a peak value and then decreases gradually as the surface segment moves further to the right. While the subsequent passage of segment II produces a similar variation in K_I (Fig. 7.6(b)), the range of K_I is significantly lower than that due to segment I (Fig. 7.6(a)). Hence, the effect of segment I on the magnitude of K_I is much more pronounced than that of segment II. Figures 7.6(c) and 7.6(d) show different variations of K_{II} with surface segment position. It is noted that the shear mode is dominant when the surface segment approaches the crack from the left, and the tensile mode prevails as soon as the surface segment moves to the right. The normalized $\Delta K_I^{\max}$ and $\Delta K_{II}^{\max}$ due to segment I are equal to 0.1296 and 0.0629, respectively, while the corresponding values for segment II are 0.0262 and 0.0490. Hence, the portion of the surface profile from x' = 4050 nm to x' = 4150 nm (segment I, Fig. 7.3(e)), was used in the fatigue crack growth simulations discussed below.

7.3.4 Fatigue Crack Growth Analysis

Similarly to previous fracture mechanics analysis (Gong and Komvopoulos, 2004b; Komvopoulos and Cho, 1997), fatigue crack growth was studied in terms of the maximum shear and/or tensile SIF range. The dominance of the shear and tensile modes of crack growth depends on the maximum values of ΔK_σ and ΔK_t, defined as

$$\Delta K_s^{\max} = \max[\Delta K_s(q)] = \max[K_{s,\max}\big|_{q=q^*} - K_{s,\min}\big|_{q=q^*}] \tag{7.3}$$

and

$$\Delta K_t^{\max} = \max[\Delta K_t(q)] = \max[K_{t,\max}\big|_{q=q^*} - K_{t,\min}\big|_{q=q^*}], \tag{7.4}$$

where the subscripts max and min denote the maximum and minimum values of K_σ and K_τ, determined at a certain position of the sliding surface segment, and q^* is a given value of angle q ($-180^0 = q^* = 180^0$). In view of the secondary effect of the simulated crack increment, Δc, on the growth direction of a surface crack (Gong and Komvopoulos, 2004b), all the simulations were performed for $\Delta c = h_1/8$.

Results for the crack growth angle, Δq, total deviation angle, q_{total}, and $\Delta K^{\max}$ ($= \max[\Delta K_s^{\max}, \Delta K_t^{\max}]$) at each crack growth cycle are given in Table 7.2. It is

Table 7.2. Crack propagation angles and maximum stress intensity factor range* versus crack growth cycle

N	Δq (deg.)	q_{total} (deg.)	$\Delta K^{\max}/(2P/pc^{1/2})$
1	24	24	0.1597
2	38	62	0.2346
3	-14	48	0.2126
4	18	66	0.2369
5	-21	45	0.2160
6	20	65	0.2333
7	5	70	0.2149
8	4	74	0.2784
9	3	77	0.3225

* Maximum stress intensity factor range: $\Delta K^{\max} = \max[\Delta K_s^{\max}, \Delta K_t^{\max}]$.

noted that q_{total} increases significantly during the first two cycles, fluctuates in the following four cycles, and increases again in the next three cycles when the crack tip approaches the layer interface. The corresponding crack growth path is shown in Fig. 7.7. The similar result for a smooth (cylindrical) surface sliding over the same medium, obtained in a previous study (Gong and Komvopoulos, 2004b), is also plotted in Fig. 7.7 for comparison. These results are in qualitative agreement with the conclusions of a fracture analysis of thin coatings subjected to contact loading (Oliveira and Bower, 1996). When crack growth commences remote from the interface, the two crack paths are nearly parallel to each other. However, when the crack tip is in the proximity of the layer interface, the two crack paths deviate. In the case of the smooth surface, the crack propagates toward the interface, while in the case of the rough surface, the crack tends to

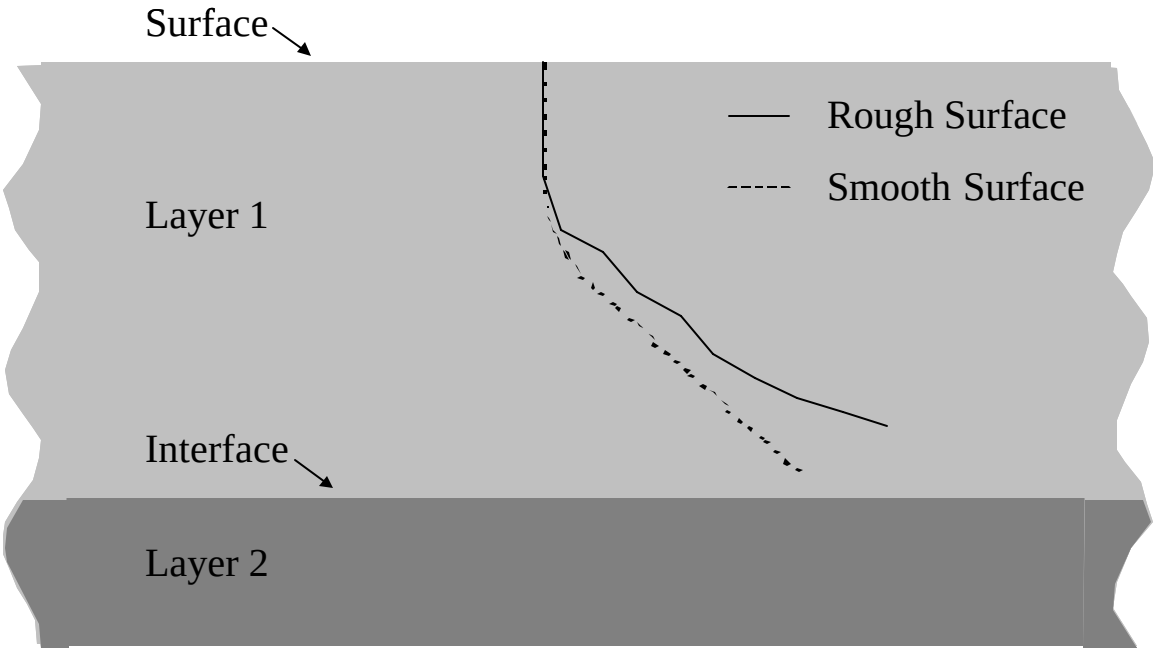

Fig. 7.7 Crack growth paths in a layered medium due to sliding contact with smooth (cylindrical) and rough (fractal) surfaces.

grow approximately parallel to the interface. This finding reveals a roughness effect on the evolution of fatigue in the surface layer, i.e., smooth surfaces are more likely to lead to delamination of the layer along the interface as opposed to rough surfaces that promote delamination within the layer medium.

Figure 7.8(a) shows the normalized maximum stress intensity factor range, $\Delta K^{\max}$, as a function of crack growth cycles, N. The similar result for a smooth (cylindrical) surface is also shown for comparison. The general trend is for $\Delta K^{\max}$ to intensify with the increase of N. The difference in the magnitudes of $\Delta K^{\max}$ of the rough and smooth surfaces is attributed to differences in the interference and surface profile used in each simulation. The dominant crack growth mode can be determined from the magnitudes of the maximum tensile and shear stress intensity factor range, $\Delta K_{\sigma}^{\max}$ and $\Delta K_{\tau}^{\max}$, respectively. Figure 7.8(b) shows the variation of $\Delta K_{\sigma}^{\max} / \Delta K_{\tau}^{\max}$ with the crack growth cycles, N. For the smooth surface case, $\Delta K_{s}^{\max} / \Delta K_{t}^{\max} > 1$ throughout crack growth, indicating the dominance of the tensile fracture mode. However, in the case of the rough surface, the tensile mode is dominant during the first six cycles, when crack growth resembles that in the smooth-surface case (Fig. 7.7), whereas in the subsequent cycles, when crack advancement occurs almost parallel to the interface, crack growth is controlled by the shear mode ($\Delta K_{s}^{\max} / \Delta K_{t}^{\max} < 1$). A similar result has been reported for subsurface crack growth in a homogeneous elastic half-space (Komvopoulos and Cho, 1997).

For the interference range examined in this study, the third and fourth layers

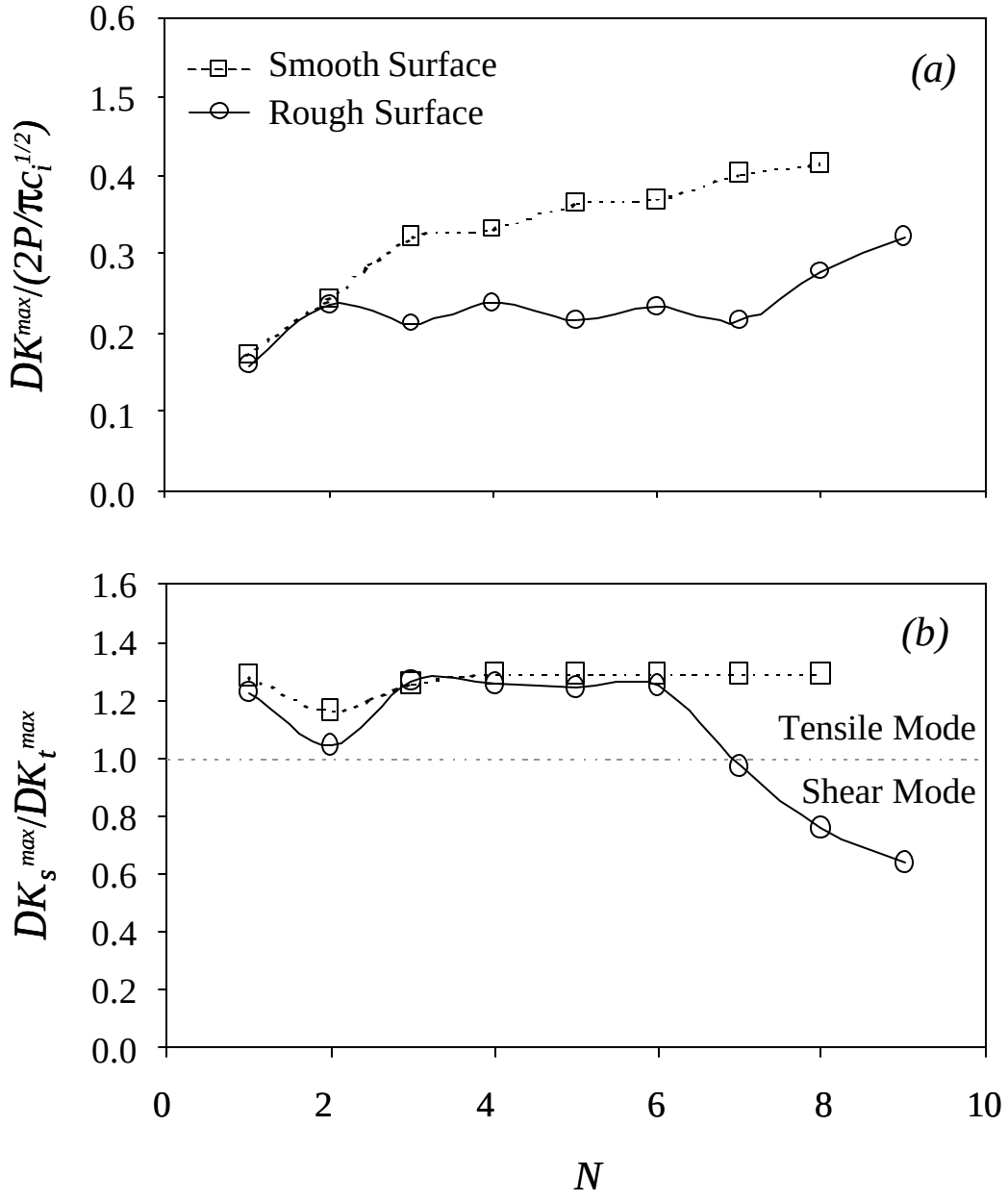

Fig. 7.8 Variation of dimensionless (a) maximum stress intensity factor range $\Delta K^{\max}$ (= max[$\Delta K_s^{\max}$, $\Delta K_t^{\max}$]) and (b) $\Delta K_s^{\max} / \Delta K_t^{\max}$ with crack growth cycles N.

exhibited purely elastic deformation. Therefore, for the sake of brevity, subsurface deformation will be interpreted in light of the evolution of plasticity in the second layer. Figure 7.9(a) shows that the maximum plastic strain, $\bar{e}_p^{\max}$, in the second layer increases with accumulating crack growth cycles. The increment of $\bar{e}_p^{\max}$ at each cycle decreases in the first five cycles because the high stresses in the vicinity of the crack tip do not extend into the second layer. However, notable excursions occurred in the eighth and ninth cycles, in agreement with the results of a previous study (Gong and Komvopoulos, 2004b). These notable increases in $\bar{e}_p^{\max}$ are due to the superposition effect of the crack-tip stresses on the stresses in the second layer, in the region adjacent to the interface. The dependence of plasticity in the second layer on crack growth can be further interpreted by considering the variation of the increment of maximum plastic strain, $\Delta\bar{e}_p^{\max}$, with the crack growth cycles, N, due to sliding of both rough and smooth surfaces (Fig. 7.9(b)). For the smooth surface, $\Delta\bar{e}_p^{\max}$ changes slightly with the evolution of crack growth and increases again when the crack grows in the proximity of the interface. However, in the case of the rough surface, $\Delta\bar{e}_p^{\max}$ decreases monotonically until the fifth cycle and increases gradually with further crack advancement, despite the fact that the crack path is almost parallel to the interface. This is attributed to the significant intensification of the crack-tip stresses by the sliding rough surface. Thus, faster crack growth in the first layer and more plasticity in the second layer occurred in the sliding simulations involving the rough surface.

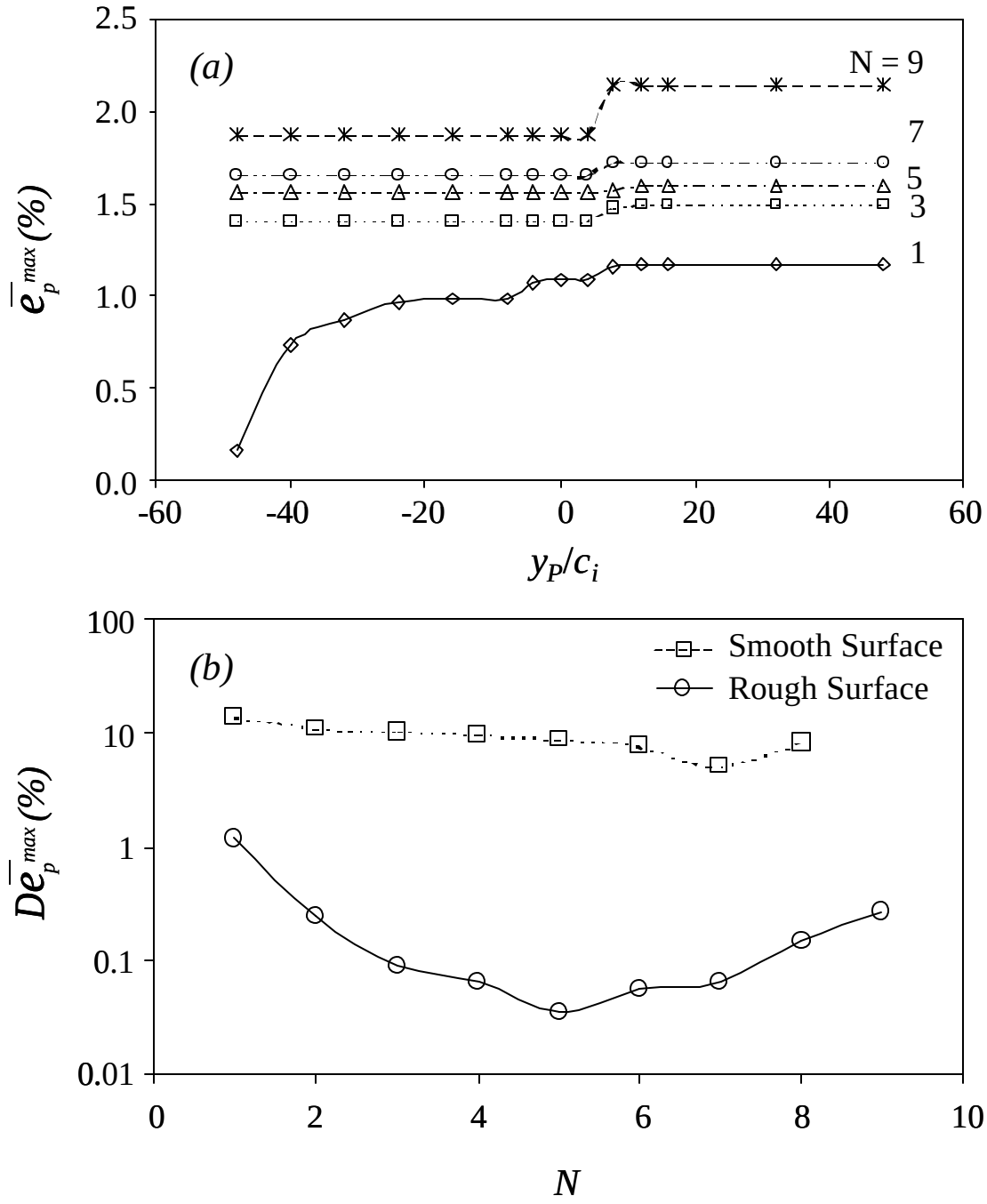

Fig. 7.9 (a) Maximum equivalent plastic strain $\bar{e}_p^{\max}$ and (b) increment of maximum equivalent plastic strain $\Delta\bar{e}_p^{\max}$ in the second layer of a layered medium versus fractal surface position y_P/c_i and crack growth cycles N.

7.3.5 Dependence of Crack Growth on Surface Topography

The effect of the fractal dimension D on the variation of K_I and K_{II} with the position of the sliding fractal surface, y_P/c_i, for fixed G is shown in Figs. 7.10(a) and 7.10(b), respectively. For all D values, K_I increases rapidly from zero to a peak value when the rough surface slides over the crack ($y_P/c_i \sim 0$), and then decreases gradually as the rough surface moves further to the right. The general trend is for K_I to decrease with the increase of D. This is due to the fact that high D values are associated with smooth surfaces, which, for a given global interference, yield lower crack-tip stresses due to the resulting larger asperity contact areas and smaller local interferences. The variation of K_{II} with y_P/c_i and D, shown in Fig. 7.10(b), does not reveal a specific trend except for a slight decrease of maximum K_{II} with the increase of D. The significantly lower magnitudes of K_{II} than those of K_I confirm that initial crack growth is dominated by the tensile mode, in agreement with the results shown in Fig. 7.8.

To illustrate the effect of the fractal dimension on the prevailing fracture mode during initial crack growth, $\Delta K_\sigma^{\max} / \Delta K_\tau^{\max}$ is plotted as a function of D in Fig. 7.11. The dominance of the tensile and shear modes is determined by the magnitude of $\Delta K_\sigma^{\max} / \Delta K_\tau^{\max}$. The results reveal a transition from shear to tensile crack growth when D increases in the range of 1.2-1.7. This stems from the fact that a surface profile characterized by a high D value exhibits a relatively smooth topography. The larger asperity contact areas and higher surface tractions obtained with smoother surfaces promote crack opening and, hence, the dominance of the tensile fracture mode. In view of the results shown in Figs. 7.7, 7.8(b), 7.10, and 7.11, it may be inferred that smoother

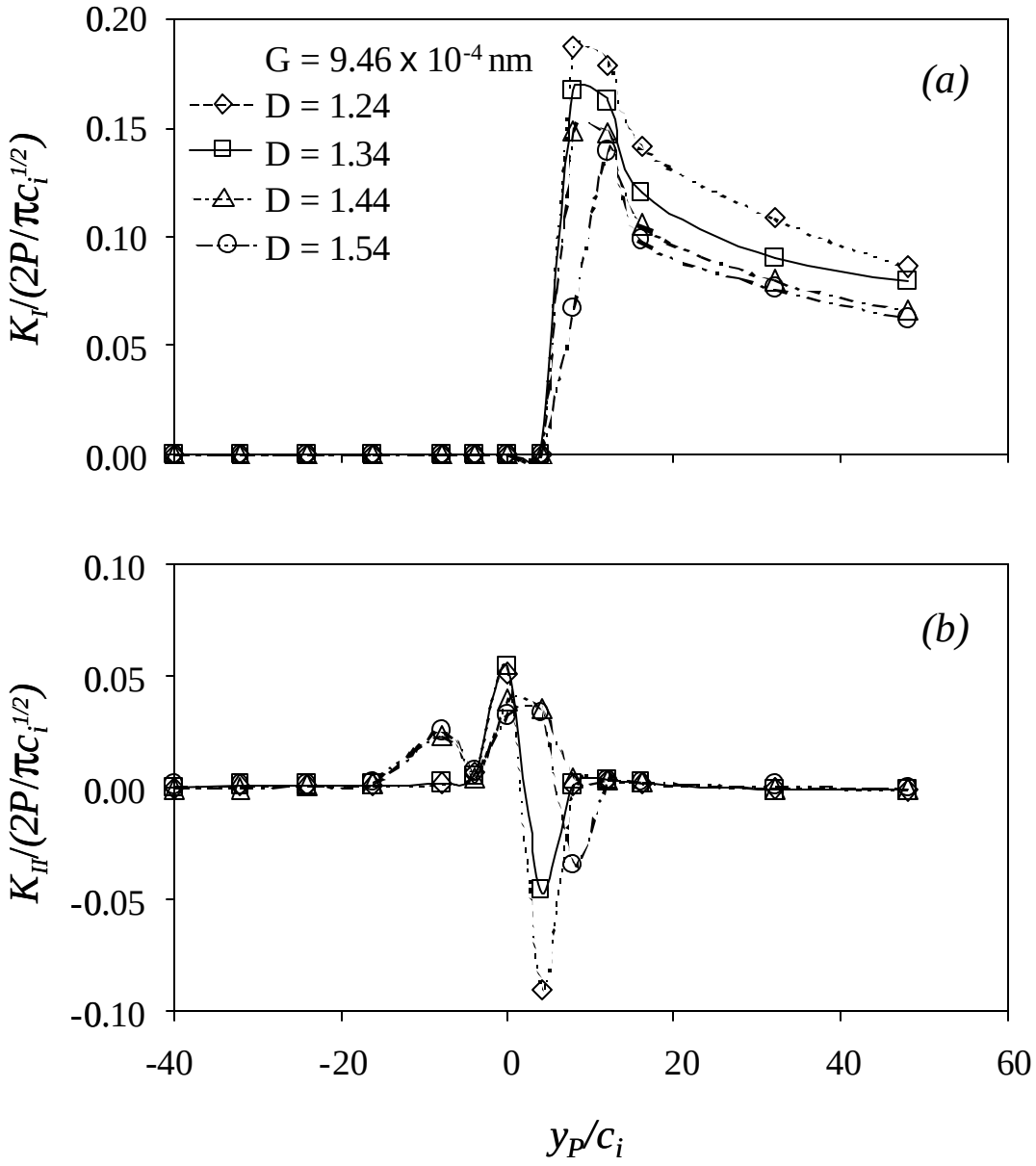

Fig. 7.10 Effect of fractal dimension D on dimensionless stress intensity factor (a) K_I and (b) K_{II} versus fractal surface position y_P/c_i for fixed fractal roughness G.

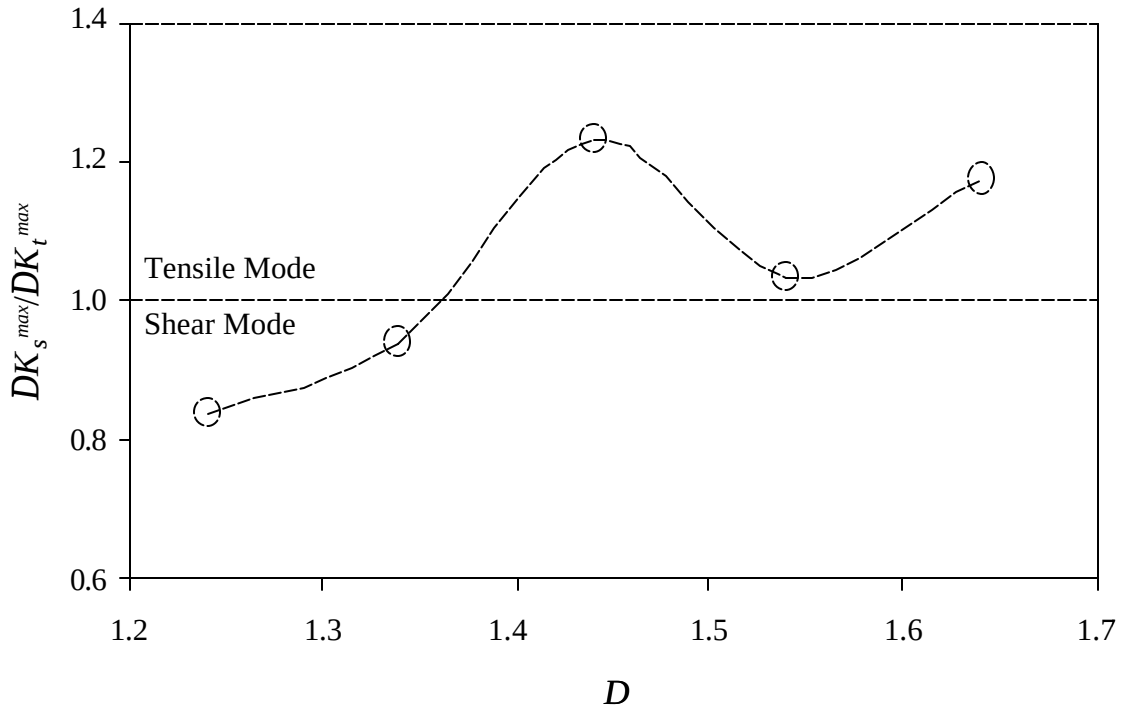

Fig. 7.11 Variation of $\Delta K_s^{\max} / \Delta K_t^{\max}$ with fractal dimension D for fixed fractal roughness G.

surfaces are more likely to lead to tensile mode-dominated crack growth initially and shear mode-dominated crack growth when the crack tip advances in the proximity of the interface.

To provide further evidence for the effect of surface topography on subsurface deformation, $\bar{e}_p^{\max}$ in the second layer is plotted as a function of y_p/c_i for different D values and fixed G in Fig. 7.12. The smoother surface (D =1.54) did not produce plastic deformation. However, the surfaces with D = 1.34 and 1.44 resulted in the accumulation of plasticity during sliding, especially the rougher surface (D = 1.34) after passing over the crack (y_p/c_i = 0). The decrease of the plastic strain with the increase of D is consistent

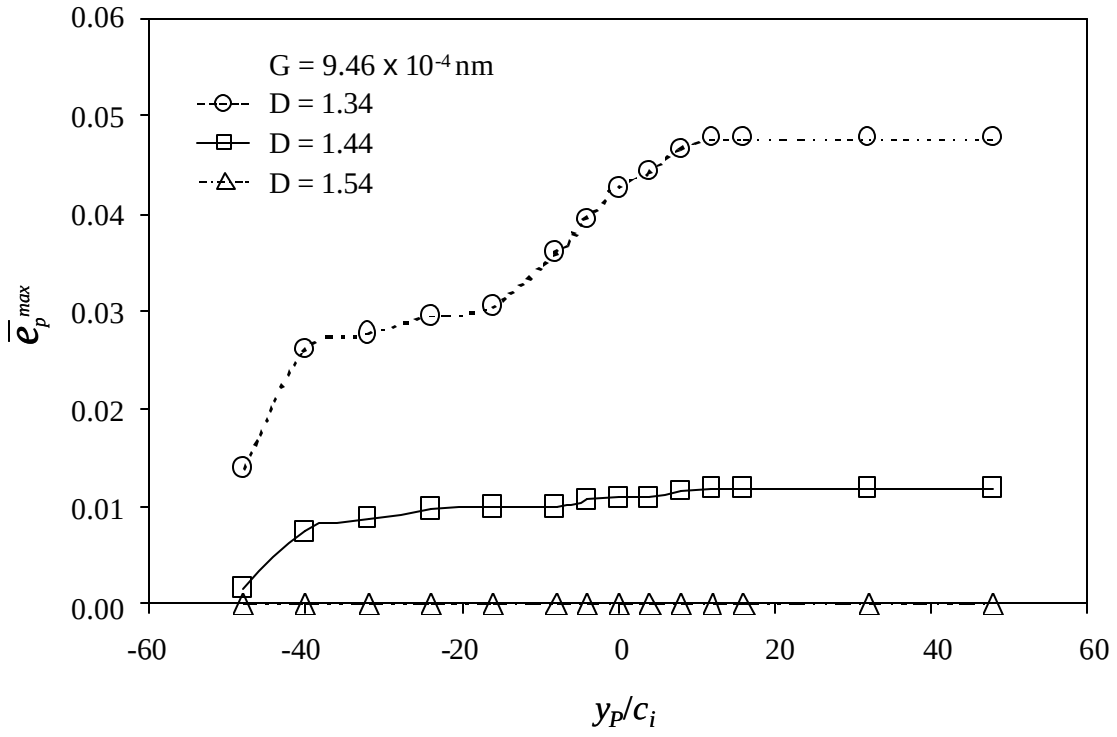

Fig. 7.12 Maximum equivalent plastic strain $\bar{e}_p^{\max}$ in the second layer of a layered medium versus fractal surface position y_P/c_i for different values of fractal dimension D and fixed fractal roughness G.

with the results shown in Fig. 7.10, demonstrating that the SIFs decrease with the increase of D (i.e., smoother surface).

The dependence of the SIFs on the fractal roughness G can be studied in light of the results shown in Fig. 7.13. The increase of the peak value of K_I with the increase of G (Fig. 7.13(a)) is similar to that observed with the decrease of D (Fig. 7.10). As mentioned earlier, this behavior is attributed to the effect of the higher surface roughness associated with the higher value of G. Larger local interferences are obtained with a rougher surface due to the smaller asperity contact areas produced, which intensifies the crack-tip

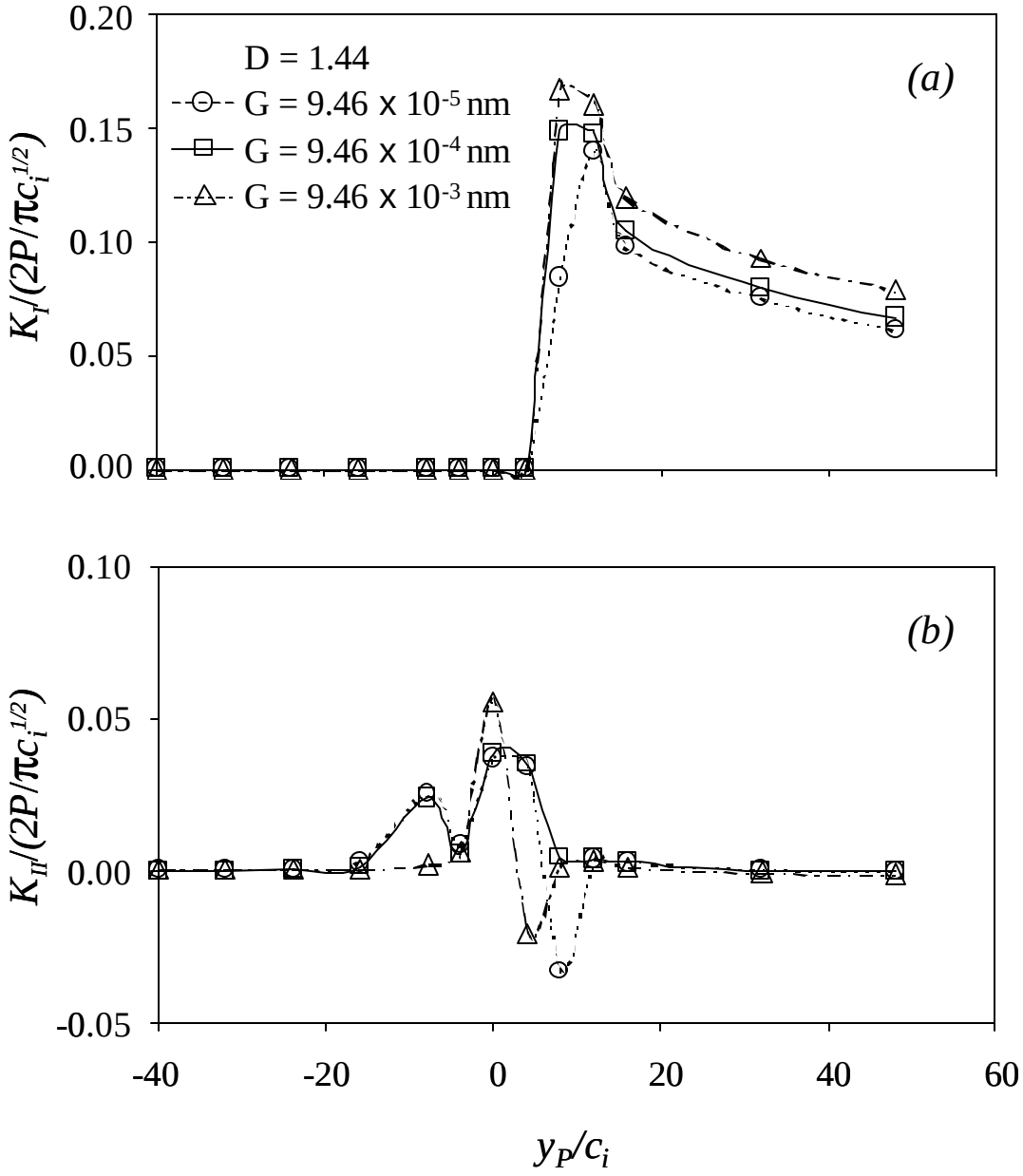

Fig. 7.13 Effect of fractal roughness G on dimensionless stress intensity factor (a) K_I and (b) K_{II} versus fractal surface position y_P/c_i for fixed fractal parameter D.

stresses. The effect of G on the variation of K_{II} is less apparent (Fig. 7.13(b)). A comparison of Figs. 7.13(a) and 7.13(b) shows that ΔK_{II} is significantly less than ΔK_I, similar to the results shown in Figs. 7.6 and 7.10. Therefore, in view of the strong dependence of the crack growth rate on ΔK, it may be concluded that initial crack growth is controlled by the magnitude of ΔK_I, consistent with the results shown in Figs. 7.8(b) and 7.11.

Figure 7.14 shows the dependence of $\bar{e}_p^{\max}$ in the second layer on the magnitude of G for fixed D. The results demonstrate that $\bar{e}_p^{\max}$ intensifies with the increase of G in a fashion similar to that observed with the decrease of D (Fig. 7.12). This is also in

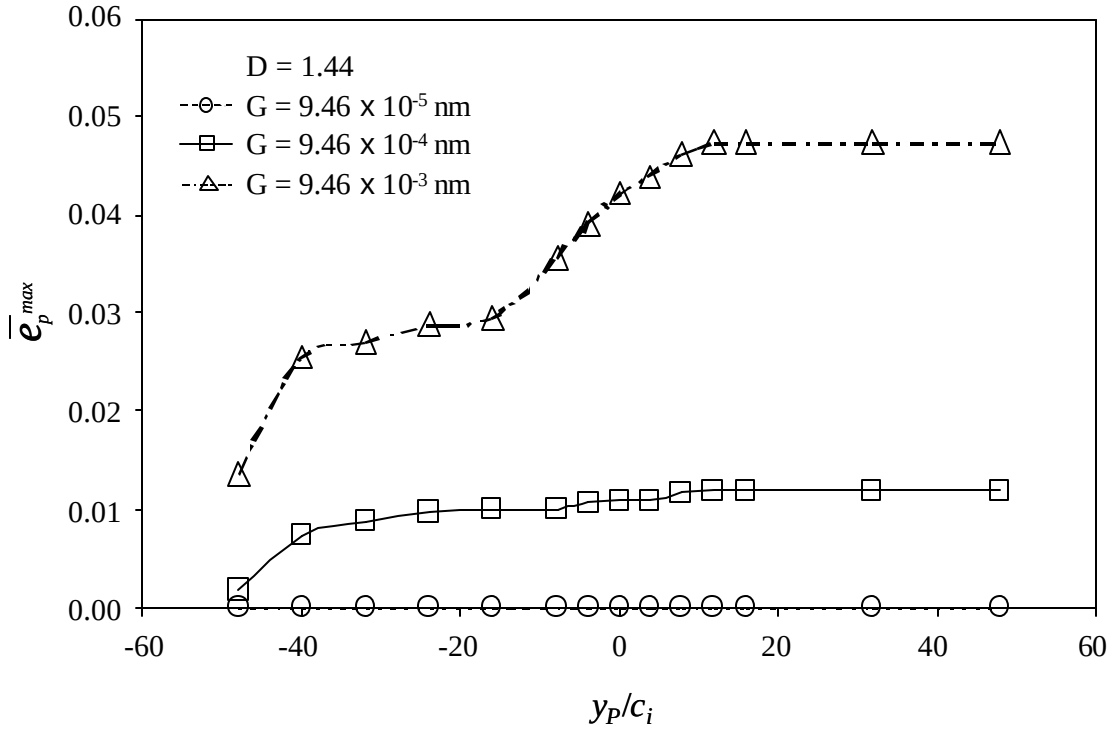

Fig. 7.14 Maximum equivalent plastic strain $\bar{e}_p^{\max}$ in the second layer of a layered medium versus fractal surface position y_P/c_i for different values of fractal roughness G and fixed fractal parameter D.

agreement with the results presented in Fig. 7.13(a), which show that a higher G value enhances K_I due to the surface roughness effect on the crack-tip stresses, as discussed previously. Therefore, from the plastic deformation standpoint, Figs. 7.12 and 7.14 indicate that a surface characterized by a high (low) D value is equivalent to a surface possessing a low (high) G value. For instance, the surfaces with D = 1.54 and G = 9.46 x 10^{-4} nm (Fig. 7.12) and D = 1.44 and G = 9.46 x 10^{-5} nm (Fig. 7.14) resulted in purely elastic deformation in the second layer. Moreover, similar evolutions of $\bar{e}_p^{\max}$ were obtained with surface topographies characterized by fractal parameters D = 1.34 and G = 9.46 x 10^{-4} nm (Fig. 7.12) and D = 1.44 and G = 9.46 x 10^{-3} nm (Fig. 7.14).

7.4 Conclusions

Contact fatigue in a layered medium containing a crack normal to the surface due to sliding of a rigid rough (fractal) surface was analyzed using linear elastic fracture mechanics and the finite element method. The first layer was assumed to be elastic while the other three layers comprising the layered medium were modeled as elastic-perfectly plastic. Based on the presented results and discussion, the following main conclusions can be drawn.

(1) An algorithm for selecting the critical segment of the sliding rough surface was developed in order to enhance the computational efficiency in the finite element simulations.

(2) The increase of the fractal dimension and the decrease of the fractal roughness result in smoother topographies yielding a larger number of interacting asperity contacts with lower contact pressure distributions.

(3) The crack paths corresponding to rough and smooth sliding surfaces are almost parallel to each other when crack growth commences remote from the interface. However, when the crack tip approaches the interface, the stress field produced by the rough surface causes the crack to propagate approximately parallel to the interface. Alternatively, in the case of the smooth surface, the crack growth direction is not affected by the interface. Therefore, the tensile mode controls crack growth in the case of smooth surfaces, whereas rough surfaces promote a tensile-to-shear mode transition when the crack tip approaches the interface.

(4) The tensile and shear stress intensity factors and plastic strain in the second layer (adjacent to the interface) increase with the advancement of the crack and the sliding of the rough surface. The accumulation of plasticity in the second layer decreases during the initial stage of fatigue crack growth, and increases gradually as the crack approaches the layer interface due to the effect of the crack-tip stresses.

(5) The increase of the fractal dimension and the decrease of the fractal roughness lead to the decrease of the stress intensity factors and plastic deformation in the second layer. This is attributed to the effect of fractal parameters on the asperity contact areas and associated local interferences that affect the stresses at the crack tip and the interface.

(6) A transition from shear to tensile dominant mode in contact fatigue and a decrease of plastic deformation in the second layer occur with the increase of the fractal dimension and the decrease of the fractal roughness.

CHAPTER 8

CONCLUSIONS

In this dissertation, contact analyses of semi-infinite media with patterned and rough surfaces were performed in order to shed light into the effects of surface patterning, frictional heating, and surface cracking on the resulting deformation and stresses. In view of the results and discussions presented in previous chapters, the following main conclusions can be drawn.

Surface patterning has a significant effect on the contact pressure, surface tensile stress, surface temperature, and plastic deformation in layered media. The maximum tensile residual stress in layered media with sinusoidal surface patterns occurs at the trailing edge of the contact region. This residual stress is much higher than that obtained with layered media exhibiting flat surfaces and depends on the pattern geometry and friction coefficient. Patterned surfaces yield lower plastic strains and smaller plastic zones than flat surfaces due to the lower stresses resulting from the increased compliance of the top hard layer that can store significant strain energy without undergoing plastic deformation. Nevertheless, this arises at the expense of a higher surface tensile stress at the trailing edge of the contact interface, therefore indicating a greater probability for surface crack initiation for patterned media. Periodic variations in the contact pressure, surface temperature, subsurface stresses, and plastic strain were encountered in the case of patterned layered media and are attributed to the pattern geometry. The similar peak values of the maximum temperature in each layer illustrate that thermal interaction

between neighboring pads is negligible. The steady-state stress/strain fields produced after the first sliding cycle suggest that deformation in the patterned layered medium is insensitive to subsequent similar sliding cycles.

Although the finite element method is the main numerical technique for obtaining solutions for the stresses in both homogenous and layered media in sliding contact with a rough surface, requirements for large number of elements make the finite element approach impractical for analyses involving rough surfaces of relatively large apparent contact areas. For this reason, an analytical procedure was developed that enables the calculation of contact stresses in layered elastic media in contact with a rough surface. A constitutive relation between the mean contact pressure and a representative strain parameter was derived for layered media based on finite element results. The real contact area was obtained as a function of mechanical properties of the layered medium, layer thickness, truncated half-contact width, and asperity radius. It was shown that much higher tensile stresses occur in the case of stiff layers than compliant layers. Numerical results revealed that crack initiation is more likely to occur both at the surface and the interface in the case of the stiff layer and only at the surface in the case of the compliant layer. It was also shown that the stiffer layer increases the likelihood for interface cracking and delamination than the compliant layer.

Knowledge of the surface temperature and thermoelastic stresses in sliding solid bodies with rough surfaces is essential in failure analysis of mechanical systems. A thermomechanical contact model was developed for sliding contact between a semi-infinite elastic medium and a rough (fractal) surface that accounts for the simultaneous effects of thermal and mechanical deformation. For fixed surface interference, frictional

heating increases both the contact area and the contact pressure. This effect was found to be mostly pronounced at asperity microcontacts located at the trailing edge of the contact interface, where the cumulative effect of frictional heating was observed to be most pronounced. It was also found that the maximum temperature at each microcontact occurs always at the surface and increases with the Peclet number. The maximum temperature rise at the surface increases with the decrease of the fractal dimension. Intensification of the temperature gradients with the increase of the Peclet number is responsible for the enhancement of thermoelastic distortion at the surface and the development of high thermal stresses. For low Peclet number, the stress field is dominated by the effect of mechanical stresses. The von Mises equivalent stress is strongly affected by frictional heating, especially at microcontact regions close to the trailing contact edge where the highest thermal stresses are produced due to the cumulative heating effect. The increase of the Peclet number promotes surface plastic deformation and reduces the likelihood for surface cracking.

Surface cracking in a multi-layered medium containing a crack perpendicular to the free surface due to repetitive sliding of a rigid asperity was analyzed based on linear elastic fracture mechanics and the finite element method. The significantly higher values of the tensile stress intensity factor than those of the shear stress intensity factor obtained in all simulation cases indicated that surface cracking in the multi-layered medium due to sliding of a single asperity is controlled by the tensile fracture mode. The surface crack propagated toward the layer interface at an angle of ~57 degrees from the original crack plane, independent of the crack growth increment, in fair agreement with experimental observations. The maximum plastic strain in the second layer increased rapidly as the

crack tip approached the interface due to the effect of the high-stress field at the crack tip. This caused the maximum plastic strain in the second layer to occur always below the crack tip adjacent to the interface rather than below the sliding asperity, as found for uncracked elastic-plastic layered media. Finite element results showed that the coefficient of friction at the contact (sliding) region exhibits a dominant effect on the plastic strain accumulating in the second layer, while the effect of crack-face friction is insignificant. The analysis of surface cracking in layered media due to single asperity sliding was extended to rough-surface sliding to elucidate the surface topography effect on the stress intensity factor and the crack propagation mode. The simulation results show that the crack propagation mode changes from tensile to shear as the crack tip approaches the layer interface. At this juncture, the crack tends to grow approximately parallel to the interface. The stress intensity factors and plastic deformation in the second layer decrease with the increase of the fractal dimension and/or the decrease of the fractal roughness. The increase of the fractal dimension and the decrease of the fractal roughness change the dominant crack growth mode from shear to tensile.

In conclusion, the results of this research contribute to the advancement of the state-of-the-art in contact mechanics of layered media. Specifically, analytical and numerical solutions demonstrated the role of various important factors, such as surface patterning, overcoat properties, frictional heating, and surface cracking, on the mechanical and thermomechanical behavior of half-space homogeneous and layered media with patterned and rough surfaces. The methodologies and models derived in this dissertation can be easily applied to a wide range of length scales, including systems

operating under conditions leading to surface interactions from the nanoscale to the macroscale.

REFERENCES

Alfredsson, B., and Olsson, M., 2000, "Initiation and Growth of Standing Contact Fatigue Cracks," *Engineering Fracture Mechanics*, **65**, pp. 89-106.

Azarkhin, A., and Barber, J. R., 1986, "Thermoelastic Instability for the Transient Contact Problem of Two Sliding Half-Planes," ASME *Journal of Applied Mechanics*, **53**, pp. 565-572.

Bailey, D. M., and Sayles, R. S., 1991, "Effect of Roughness and Sliding Friction on Contact Stresses," ASME *Journal of Tribology*, **113**, pp. 729-738.

Barber, J. R., 1984, "Thermoelastic Displacements and Stresses Due to a Heat Source Moving Over the Surface of a Half Plane," ASME *Journal of Applied Mechanics*, **51**, pp. 636-640.

Barsoum, R. S., 1976, "On the Use of Isoparametric Finite Elements in Linear Fracture Mechanics," *International Journal for Numerical Methods in Engineering*, **10**, pp. 25-37.

Berry, M. V., and Lewis, Z. V., 1980, "On the Weierstrass-Mandelbrot Fractal Function," *Proceedings of the Royal Society* (London), Series A, **370**, pp. 459-484.

Berthe, D., and Vergne, Ph., 1987, "An Elastic Approach to Rough Contact With Asperity Interactions," *Wear*, **117**, pp. 211-222.

Beuth, J. L., and Klingbeil, N. W., 1996, "Cracking of Thin Films Bonded to Elastic-Plastic Substrates," *Journal of Mechanics and Physics of Solids*, **44**, pp. 1411-1428.

Bhushan, B., and Majumdar, A., 1992, "Elastic-Plastic Contact Model of Bifractal Surfaces," *Wear*, **153**, pp. 53-64.

Blok, H., 1937, "Theoretical Study of Temperature Rise at Surfaces of Actual Contact Under Oiliness Lubricating Conditions," *Proceedings General Discussion on Lubrication and Lubricants*, Institute of Mechanical Engineers (London), **2,** pp. 222-235.

Borodich, F. M., and Onishchenko, D. A., 1999, "Similarity and Fractality in the Modeling of Roughness by a Multilevel Profile With Hierarchical Structure," *International Journal of Solids and Structures*, **36**, pp. 2585-2612.

Bower, A. F., and Fleck, N. A., 1994, "Brittle Fracture Under Sliding Line Contact," *Journal of Mechanics and Physics of Solids*, **42**, pp. 1375-1396.

Bryant, M. D., 1988, "Thermoelastic Solutions for Thermal Distributions Moving Over Half Space Surfaces and Application to the Moving Heat Source," ASME *Journal of Applied Mechanics*, **55**, pp. 87-92.

Burmister, D. M., 1945, "The General Theory of Stresses and Displacements in Layered Systems," *Journal of Applied Physics*, **16**, pp. 89-94.

Bush, A. W., Gibson, R. D., and Thomas, T. R., 1975, "The Elastic Contact of a Rough Surface," *Wear*, **35**, pp. 87-111.

Bush, A. W., Gibson, R. D., and Keogh G. P., 1979, "Strongly Anisotropic Rough Surfaces," *ASME Journal of Lubrication Technology*, **101**, pp. 15-20.

Carslaw, H. S., and Jaeger, J. C., 1959, *Conduction of Heat in Solids*, Clarendon Press, Oxford.

Chan, S. K., Tuba, I. S., and Wilson, W. K., 1970, "On the Finite Element Method in Linear Fracture Mechanics," *Engineering Fracture Mechanics*, **2**, pp. 1-17.

Chen, W. T., 1971, "Computation of Stresses and Displacements in a Layered Elastic Medium," *International Journal of Engineering Science*, **9**, pp. 775-800.

Chen, W. T., and Engel, P., 1972, "Impact and Contact Stress Analysis in Mutilayered Media," *International Journal of Solids and Structures*, **8**, pp. 1257-1281.

Chen, L. M., Farris, F. N., and Chandrasekar, S., 1991, "Sliding Microindentation Fracture of Brittle Materials," *Tribology Transactions*, **34**, pp. 161-168.

Cho, S.-S., and Komvopoulos, K., 1997, "Thermoelastic Finite Element Analysis of Subsurface Cracking Due to Sliding Surface Traction," ASME *Journal of Engineering Materials and Technology*, **119**, pp.71-78.

Chou, S. Y., Krauss, P. R., and Kong, L., 1996, "Nanolithographically Defined Magnetic Structures and Quantum Magnetic Disk," *Journal of Applied Physics*, **79**, pp. 6101-6106.

Ciavarella, M., Demelio, G., Barber, J. R., and Jang, Y. H., 2000, "Linear Elastic Contact of the Weierstrass Profile," *Proceedings of the Royal Society* (London), Series A, **456**, pp. 387-405.

Dundurs, J., Tsai, K. C., and Keer, L. M., 1973, "Contact of Elastic Bodies with Wavy Surfaces," *Journal of Elasticity*, **3**, pp. 109-115.

Erdogan, F., and Sih, G. C., 1963, "On the Crack Extension in Plates Under Plane Loading and Transverse Shear," ASME *Journal of Basic Engineering*, **85**, pp. 519-527.

Farhoud, M., Hwang, M., Smith, H. I., Schattenburg, M. L., Bae, J. M., Youcef-Toumi, K., and Ross, C. A., 1998, "Fabrication of Large Area Nanostructured Magnets by Interferometric Lithography," IEEE *Transactions on Magnetics*, **34**, pp. 1087-1089.

Gibson, R. D., 1982, "The Surface as a Random Process," *Rough Surfaces*, Thomas, T. R., ed., Longman, London.

Gong, Z.-Q., and Komvopoulos, K., 2003, "Effect of Surface Patterning on Contact Deformation of Elastic-Plastic Layered Media," ASME *Journal of Tribology*, **125**, pp. 16-24.

Gong, Z.-Q., and Komvopoulos, K., 2004a, "Mechanical and Thermomechanical Elastic-Plastic Contact Analysis of Layered Media with Patterned Surfaces," ASME *Journal of Tribology*, **126**, pp. 9-17.

Gong, Z.-Q., and Komvopoulos, K., 2004b, "Surface Cracking in Elastic-Plastic Multi-Layered Media Due to Repeated Sliding Contact," ASME *Journal of Tribology*, **126**, in press.

Goryacheva, I. G., and Dobychin, M. N., 1991, "Multiple Contact Model in the Problems of Tribomechanics," *Tribology International*, **24**, pp. 29-35.

Graebner, J. E., 1996, "Measurements of Specific Heat and Mass Density in CVD Diamond," *Diamond and Related Materials*, **5**, pp. 1366-1370.

Greenwood, J. A., 1992, "Problems With Surface Roughness," Singer, I. L., Pollock, H. M., ed., *Fundamentals of Friction: Macroscopic and Microscopic Processes*, Kluwer, Dordrecht, pp. 57-76.

Greenwood, J. A., and Williamson, J. B. P., 1966, "Contact of Nominally Flat Surfaces," *Proceedings of the Royal Society* (London), Series A, **295**, pp. 300-319.

Gupta, P. K., and Walowit, J. A., 1974, "Contact Stresses Between an Elastic Cylinder and a Layered Elastic Solid," *ASME Journal of Lubrication Technology*, **96**, pp. 250-257.

Gupta, P. K., Walowit, J. A., and Finkin, E. F., 1973, "Stress Distributions in Plane Strain Layered Elastic Solids Subjected to Arbitrary Boundary Loading," *Journal of Lubrication Technology*, **95**, pp. 427-433.

Gupta, V., Bastias, P., Hahn, G. T., and Rubin, C. A., 1993, "Elastoplastic Finite-Element Analysis of 2-D Rolling-Plus-Sliding Contact With Temperature-Dependent Bearing Steel Material Properties," *Wear*, **169**, pp.251–256.

Henshell, R. D., and Shaw, K. G., 1975, "Crack Tip Finite Elements Are Unnecessary," *International Journal for Numerical Methods in Engineering*, **9**, pp. 495-507.

Hertz, H., 1882, "On the Contact of Elastic Solids," Miscellaneous Papers by H. Hertz, Macmillan, London, UK.

Hertzberg, R. W., 1996, *Deformation and Fracture Mechanics of Engineering Materials*, Wiley, New York.

Huang, J. H., and Ju, F. D., 1985, "Thermomechanical Cracking Due to Moving Frictional Loads," *Wear*, **102**, pp. 81-104.

Jaeger, J. C., 1942, "Moving Sources of Heat and the Temperature at Sliding Contacts," *Proceedings Royal Society of NS Wales*, **76**, pp. 203-224.

Johnson, K. L., 1985, *Contact Mechanic*s, Cambridge University Press, Cambridge, UK.

Johnson, K. L., Greenwood, J. A., and Higginson, J. G., 1985, "The Contact of Elastic Regular Wavy Surfaces," *International Journal of Mechanical Sciences*, **27**, pp. 383-396.

Ju, F. D., and Chen, T. Y., 1984, "Thermomechanical Cracking in Layered Media from Moving Friction Load," AMSE *Journal of Tribology*, **106**, pp. 513-518.

Ju, F. D., and Huang, J. H., 1982, "Heat Checking in the Contact Zone of a Bearing Seal (A Two-Dimensional Model of a Single Moving Asperity)," *Wear*, **79**, pp. 107-118.

Ju, F. D., and Liu, J. C., 1988, "Effect of Peclet Number in Thermomechanical Cracking Due to High-Speed Friction Load," ASME *Journal of Tribology*, **110**, pp. 217-221.

Ju, Y., and Farris, T. N., 1997, "FFT Thermoelastic Solutions for Moving Heat Sources," ASME *Journal of Tribology*, **119**, pp. 156-162.

Kaye, G. W. C., and Laby, T. H., 1986, *Tables of Physical and Chemical Constants and Some Mathematical Functions*, Longman, London, UK.

Keer, L. M., and Kuo, C. H., 1992, "Cracking in a Loaded Brittle Elastic Half-space," *International Journal of Solids and Structures*, **29**, pp. 1819-1826.

Keer, L. M., and Worden, R. E., 1990, "A Qualitative Model to Describe the Microchipping Wear Mode in Ceramic Rollers," *Tribology Transactions*, **33**, pp. 411-417.

King, R. B., 1987, "Elastic Analysis of Some Punch Problems for a Layered Medium," *International Journal of Solids and Structures*, **23**, pp. 1657-1664.

King, R. B., and O'Sullivan, T. C., 1987, "Sliding Contact Stresses in a Two-Dimensional Layered Elastic Half-Space," *International Journal of Solids and Structures*, **23**, pp. 581-597.

Ko, P. L., Iyer, S. S., Vaughan, H., and Gadala, M., 2001, "Finite Element Modelling of Crack Growth and Wear Particle Formation in Sliding Contact," *Wear*, **251**, pp. 1265-1278.

Komvopoulos, K., 1988, "Finite Element Analysis of a Layered Elastic Solid in Normal Contact With a Rigid Surface," ASME *Journal of Tribology*, **110**, pp. 477-485.

Komvopoulos, K., 1989, "Elastic-Plastic Finite Element Analysis of Indented Layered Media," ASME *Journal of Tribology*, **111**, pp. 430-439.

Komvopoulos, K., 2000, "Head-Disk Interface Contact Mechanics for Ultrahigh Density Magnetic Recording," *Wear*, **238**, pp. 1-11.

Komvopoulos, K., and Cho, S. -S., 1997, "Finite Element Analysis of Subsurface Crack Propagation in a Half-Space due to a Moving Asperity Contact," *Wear*, **209**, pp. 57-68.

Komvopoulos, K., and Choi, D.-H., 1992, "Elastic Finite Element Analysis of Multi-Asperity Contacts," ASME *Journal of Tribology*, **114**, pp. 823-831.

Komvopoulos, K., and Yan, W., 1997, "A Fractal Analysis of Stiction in Microelectromechanical Systems," ASME *Journal of Tribology*, **119**, pp. 391-400.

Komvopoulos, K., and Ye, N., 2001, "Three-Dimensional Contact Analysis of Elastic-Plastic Layered Media With Fractal Surface Topographies," *ASME Journal of Tribology*, **123**, pp. 432-640.

Komvopoulos, K., and Ye, N., 2002, "Elastic-Plastic Finite Element Analysis for the Head-Disk Interface With Fractal Topography Description," *ASME Journal of Tribology*, **124**, pp. 775-784.

Kral, E. R., and Komvopoulos, K., 1996, "Three-Dimensional Finite Element Analysis of Surface Deformation and Stresses in an Elastic-Plastic Layered Medium Subjected to Indentation and Sliding Contact Loading," ASME *Journal of Applied Mechanics*, **63**, pp. 365-375.

Kral, E. R., and Komvopoulos, K., 1997, "Three-Dimensional Finite Element Analysis of Subsurface Stress and Strain Fields Due to Sliding Contact on an Elastic-Plastic Layered Medium," ASME *Journal of Tribology*, **119**, pp. 332-341.

Lawn, B., 1992, "Friction Processes in Brittle Fracture," Fundamentals of Friction: Macroscopic and Microscopic Processes, Singer, I. L., and Pollock, H. M., Eds., NATO ASI Series E: *Applied. Science*, **220**, pp. 137-165.

Lee, K., and Barber, J. R., 1993, "Frictionally-Excited Thermoelastic Instability in Automotive Disk Brakes," ASME *Journal of Tribology*, **115**, pp. 607-614.

Leroy, J. M., Floquet, A., and Villechaise, B., 1989, "Thermomechanical Behavior of Multilayered Media: Theory," ASME *Journal of Tribology*, **111**, pp. 538-544.

Lin, X. B., and Smith, R. A., 1999a, "Finite Element Modelling of Fatigue Crack Growth of Surface Cracked Plates, Part I: The Numerical Technique," *Engineering Fracture Mechanics*, **63**, pp. 503-522.

Lin, X. B., and Smith, R. A., 1999b, "Finite Element Modelling of Fatigue Crack Growth of Surface Cracked Plates, Part III: Stress Intensity Factor and Fatigue Crack Growth Life," *Engineering Fracture Mechanics*, **63**, pp. 541-556.

Liu, G., and Wang, Q., 2000, "Thermoelastic Asperity Contacts, Frictional Shear, and Parameter Correlations," ASME *Journal of Tribology*, **122**, pp. 300-307.

Liu, S. B., and Wang, Q., 2001, "A Three-Dimensional Thermomechanical Model of Contact Between Non-Conforming Rough Surfaces," ASME *Journal of Tribology*, **123**, pp. 17-26.

Liu, S. B., and Wang, Q., 2003, "Transient Thermoelastic Stress Fields in a Half-Space," ASME *Journal of Tribology*, **125**, pp. 33-43.

Mageed, A. M. A., and Pandey, R. K., 1992, "Studies on Cyclic Crack Path and the Mixed-Mode Crack Closure Behavior in Al Alloy," *International Journal of Fatigue*, **14**, pp. 21-29.

Majumdar, A., and Bhushan, B., 1991, "Fractal Model of Elastic-Plastic Contact Between Rough Surfaces," *ASME Journal of Tribology*, **113**, pp. 1-11.

Majumdar, A., and Tien, C. L., 1990, "Fractal Characterization and Simulation of rough Surfaces," *Wear*, **136**, pp. 313-327.

Mandelbrot, B. B., 1983, *The Fractal Geometry of Nature*, Freeman, New York.

McCool, J. I., 1986, "Predicting Microfracture in Ceramics via a Microcontact Model," *ASME Journal of Tribology*, **108**, pp. 380-386.

Morath, C. J., Maris, H. J., Cuomo, J. J., Pappas, D. L., Grill, A., Patel, V. V., Doyle, J. P., and Saenger, K. L., 1994, "Picosecond Optical Studies of Amorphous Diamond and Diamondlike Carbon: Thermal Conductivity and Longitudinal Sound Velocity," *Journal of Applied Physics*, **76**, pp. 2636-2640.

Oliveira, S. A. G., and Bower, A. F., 1996, "An Analysis of Fracture and Delamination in Thin Coatings Subjected to Contact Loading," *Wear*, **198**, pp. 15-32.

O'Sullivan, T. C., and King, R. B., 1988, "Sliding Contact Stress Field Due to a Spherical Indenter on a Layered Elastic Half-Space," ASME *Journal of Tribology*, **110**, pp. 235-240.

Paris, P., and Erdogan, F., 1963, "A Critical Analysis of Crack Propagation Laws," ASME *Journal of Basic Engineering*, **85**, pp. 528-534.

Ramachandra, S., and Ovaert, T. C., 2000, "Effect of Coating Geometry on Contact Stresses in Two-Dimensional Discontinuous Coatings," ASME *Journal of Tribology*, **122**, pp. 665-671.

Ritchie, R. O., and Dauskardt, R. H., 1991, "Cyclic Fatigue of Ceramics: a Fracture Mechanics Approach to Subcritical Crack Growth and Life Prediction," *Journal of the Ceramic Society of Japan*, **99**, pp. 1047-1062.

Ross, C., 2001, "Patterned Magnetic Recording Media," *Annual Review of Materials Science*, **31**, pp. 203-235.

Saka, N., Liou, M. J., and Suh, N.P., 1984, "The Role of Tribology in Electrical Contact Phenomena," *Wear*, **100**, pp. 77-105.

Savas, T. A., Farhoud, M., Smith, H. I., Hwang, M., and Ross, C. A., 1999, "Properties of Large-Area Nanomagnet Arrays with 100 nm Period Made by Interferometric Lithography," *Journal of Applied Physics*, **85**, pp. 6160-6162.

Seabra, J., and Berthe, D., 1987, "Influence of Surface Waviness and Roughness on the Normal Pressure Distribution in the Hertzian Contact," ASME *Journal of Tribology*, **109**, pp. 462-470.

Tian, H., and Saka, N., 1991, "Finite Element Analysis of an Elastic-Plastic Two-Layer Half-Space: Sliding Contact," *Wear*, **148**, pp. 261-285.

Tian, H., Saka, N., and Suh, N. P., 1989, "Boundary Lubrication Studies on Undulated Titanium Surfaces," *Tribology Transactions*, **32**, pp. 289-296.

Tian, X. F., and Kennedy, F. E., 1994, "Maximum and Average Flash Temperatures in Sliding Contacts," ASME *Journal of Tribology*, **116**, pp. 167–174.

Tsai, H.-C., and Bogy, D. B., 1987, "Critical Review: Characterization of Diamondlike Carbon Films and Their Application as Overcoats on Thin-Film Media for Magnetic Recording," *Journal of Vacuum Science and Technology A*, **5**, pp. 3287-3312.

Uetz, H., and Föhl, J., 1978, "Wear as an Energy Transformation Process," *Wear*, **49**, pp. 253-264.

Wang, Q., and Liu, G., 1999, "A Thermoelastic Asperity Contact Model Considering Steady-State Heat Transfer," *Tribology Transactions*, **42**, pp. 763–770.

Wang, S. and Komvopoulos, K., 1994a, "A Fractal Theory of the Interfacial Temperature Distribution in the Slow Sliding Regime: Part I - Elastic Contact and Heat Transfer Analysis," ASME *Journal of Tribology*, **116**, pp. 812-823.

Wang, S. and Komvopoulos, K., 1994b, "A Fractal Theory of the Interfacial Temperature Distribution in the Slow Sliding Regime: Part II - Multiple Domains, Elastoplastic Contacts and Applications," *ASME Journal of Tribology*, **116**, pp. 824-832.

Westergaard, H. M., 1939, "Bearing Pressures and Cracks," ASME *Journal of Applied Mechanics*, **6**, pp. 49-53.

White, R. L., New, R. M. H., and Pease, R. F. W., 1997, "Patterned Media: A Viable Route to 50 Gbit/in^2 and Up for Magnetic Recording," IEEE *Transactions on Magnetics*, **33**, pp. 990-995.

Wu, T. W., 1991, "Microscratch and Load Relaxation Tests for Ultra-thin Films," *Journal of Materials Research*, **6**, pp. 407-426.

Yan, W., and Komvopoulos, K., 1998, "Contact Analysis of Elastic-Plastic Fractal Surfaces," *Journal of Applied Physics*, **84**, pp. 3617-3624.

Ye, N., and Komvopoulos, K., 2003, "Three-Dimensional Finite Element Analysis of Elastic-Plastic Layered Media Under Thermomechanical Surface Loading," ASME *Journal of Tribology*, **125**, pp. 52-59.